Summer 2021

Quasiclassical Computations of Compton-Scattered Spectra

Erik Scott Johnson
Old Dominion University, erikscott138@gmail.com

QUASICLASSICAL COMPUTATIONS OF COMPTON-SCATTERED SPECTRA

by

Erik Scott Johnson
B.S. June 2016, Old Dominion University
A.S. June 2012, Tidewater Community College

A Dissertation Submitted to the Faculty of
Old Dominion University in Partial Fulfillment of the
Requirements for the Degree of

DOCTOR OF PHILOSOPHY

PHYSICS

OLD DOMINION UNIVERSITY
August 2021

Approved by:

Balša Terzić (Director)

Geoffrey A. Krafft (Member)

Jean Delayen (Member)

Alexander Godunov (Member)

John Adam (Member)

ABSTRACT

QUASICLASSICAL COMPUTATIONS OF COMPTON-SCATTERED SPECTRA

Erik Scott Johnson
Old Dominion University, 2021
Director: Dr. Balša Terzić

Quality X-ray sources are crucial to fundamental physics research, medical radiology, humanities research, and materials science. While synchrotron radiation (SR) facilities produce the state-of-the-art emissions with respect to brilliance and frequency tunability, the great expense required to build, maintain, and operate these structures greatly limits their accessibility to researchers. Much of the research conducted at SR facilities, however, may be conducted with inverse Compton sources (ICS). Accelerator-based Compton scattering light sources generate high-energy, high-brilliance emissions. Compton scattering is the process by which a photon scatters off an electron. ICS offer an affordable, in-lab alternative to SR facilities. Even though SR facilities produce greater intensity emissions, Compton sources provide the same frequency tunability at the intensities suitable for the purposes of many researchers currently fighting for time at SR facilities, i.e., ICS provides intensities suitable for contrast imaging, X-ray fluorescence, X-ray-diffraction, and X-ray spectroscopy. The focus of this work is to create computational models to simulate Compton-scattered spectra. These models have been used to build a theoretical basis for methods of improving the quality of future Compton sources and to preform diagnostic analysis of existing light sources. The theoretical basis of each model is derived from first principles. The numerical methods employed by each model are defined. A full description of the various functionalities of each code will be addressed. Furthermore, an in-depth analysis of spectral bandwidth sources is discussed. The complex physics arising from an extremely high-intensity, nonlinear laser pulse is explored in detail. Methods of frequency modulation of the incident laser, i.e., a method for correcting the nonlinear broadening effects on the scattered spectrum, will also be discussed. The work will conclude with a an exploration of the ongoing research efforts regarding regimes of operation outside of the limits of these current models.

ACKNOWLEDGMENTS

My heart is full of gratitude, and it is my great pleasure to acknowledge the institutions and, more importantly, the people who have supported my graduate physics work. This undertaking would not have been possible without financial support from the National Science Foundation (NSF), the ODU Graduate School, the ODU Physics Department, the ODU Graduate Physics Students Association, and the Virginia Space Grant Consortium (VSGC). I would also like to thank Jefferson Lab Science Computing as many of the simulations presented within were computed at their cluster.

Funding from the NSF and VSGC came via my principle advisor and mentor, Dr. Balša Terzić, Associate Professor of Physics and Graduate Program Director. Dr. Geoffrey A. Krafft, Director of the Center for Advanced Studies of Accelerators, has been a close advisor whose insight has guided much of my work. Ever since my undergraduate research, Dr. Terzić and Dr. Krafft have both been my steadfast advocates. I have enjoyed the many fruitful years that we have worked together as advisors and student, and I hope to enjoy many more fruitful years working together as colleagues.

The ODU Physics Department has been an incredibly welcoming and nurturing community. Without the support of the faculty, administrators, and my fellow students the curriculum would have been utterly overwhelming. I would specifically like to thank the rest of the professors that have served on my committee: Dr. Jean R. Delayen, Dr. Colm Whelan, Dr. John A. Adam, Dr. Alexander L. Godunov. Thank you, Lisa and Annette: without your patient guidance I never would have gotten any paperwork turned in properly.

Our collaboration with research groups in the global physics community has driven the results presented in this dissertation. I would like to extend my gratitude to our colleagues at the following institutions: L'Istituto Nazionale di Fisica Nucleare (INFN), Milan; University of Rochester Laboratory for Laser Energetics; Eindhoven University of Technology; Munich Compact Light Source at the Technical University of Munich. I would specifically like thank the folks with whom I have had the most direct contact: Gerrit Bruhaug, Linda S. Stoel, and Benedikt Günther. It has been a pleasure working with you all.

Finally, I would like to thank my friends and family that have stood by me through this endeavour. I have been moved by their patience and outpouring of encouragement as I have spent most of the last several years completing this research and writing this dissertation. I thank my parents, Renée and Jim, and my uncle, Jeff. Most importantly, I thank my beautiful wife Heide whose love and insight have driven me to this very moment.

TABLE OF CONTENTS

LIST OF TABLES

LIST OF FIGURES

Figure Page

Figure Page

CHAPTER 1

COMPTON SCATTERING FOR HIGH-BRILLIANCE EMISSIONS

Accelerator-based Compton scattering light sources generate high-energy, high-brilliance scattered spectra. Compton scattering is the process by which a photon scatters off an electron. In accelerator-based Compton scattering, an incident laser pulse collides with a relativistic electron beam. During the collision, momentum from the relativistic electrons is transferred to the incident photons resulting in high-energy photons that are scattered within a tightly collimated cone about the original trajectory of the electron. In a head-on collision configuration, the energy gain in the scattered photon scales with the square of the electrons Lorentz factor γ:

$$E'_{ph} = 4\gamma^2 E_{ph}, \tag{1}$$

where E_{ph} is the incident photon energy and E'_{ph} is the scattered photon energy. This mechanism by which the scattered photons receives the energy gains illustrated in Figure 1. For high-quality electron beams, i.e., when the transverse size of of the beam and the transverse momentum (or emittance) of the electrons are minimized, the resulting Compton-scattered spectrum may be nearly monochromatic. The narrow bandwidth quality of the these emissions together with their tightly collimated propagation result in near laser-like photons in the X-ray and even γ-ray regimes. Furthermore, since the energy of the emissions depends upon the energy of the electron beam, the frequency of these high-energy, laser-like photons is tunable: the energy of the electrons may be adjusted via the accelerator itself to produce the desired wavelength of emitted radiation. Accelerator-based Compton scattering may be used to generate versatile, high quality photons.

Inverse Compton sources may be designed to produce emissions that rival those produced by synchrotron accelerator facilities [2, 3]. Synchrotron radiation is the state-of-the-art when it comes to tunable, high-energy, high intensity emissions with a narrow bandwidth. The drawback to synchrotrons, however, is that the facilities themselves are massive. These facilities consist of rings of magnets and accelerator cavities that are often kilometers in circumference. These Goliaths require the wealth of nations to build and maintain. The operational power demands alone are quite expensive, and therefore, the research opportunities provided by these facilities are quite limited. Additionally, synchrotrons are, by their nature, not mobile. Recent advancement in accelerator technology has made it so compact, mobile Compton sources may be built for applications in which it is not possible to bring the object of interest to a synchrotron facility. For example, a compact Compton source may, in principle, be deployed to examine the hull of a shipping vessel for fatigue. Although a smaller Compton source may not be able to generate the same intensity of emissions that a synchrotron may generate, many applications do not require extreme levels of intensity. The proliferation of accelerator-based Compton sources would greatly increase research opportunities across many fields of study by offering an accessible, affordable alternative to synchrotron facilities.

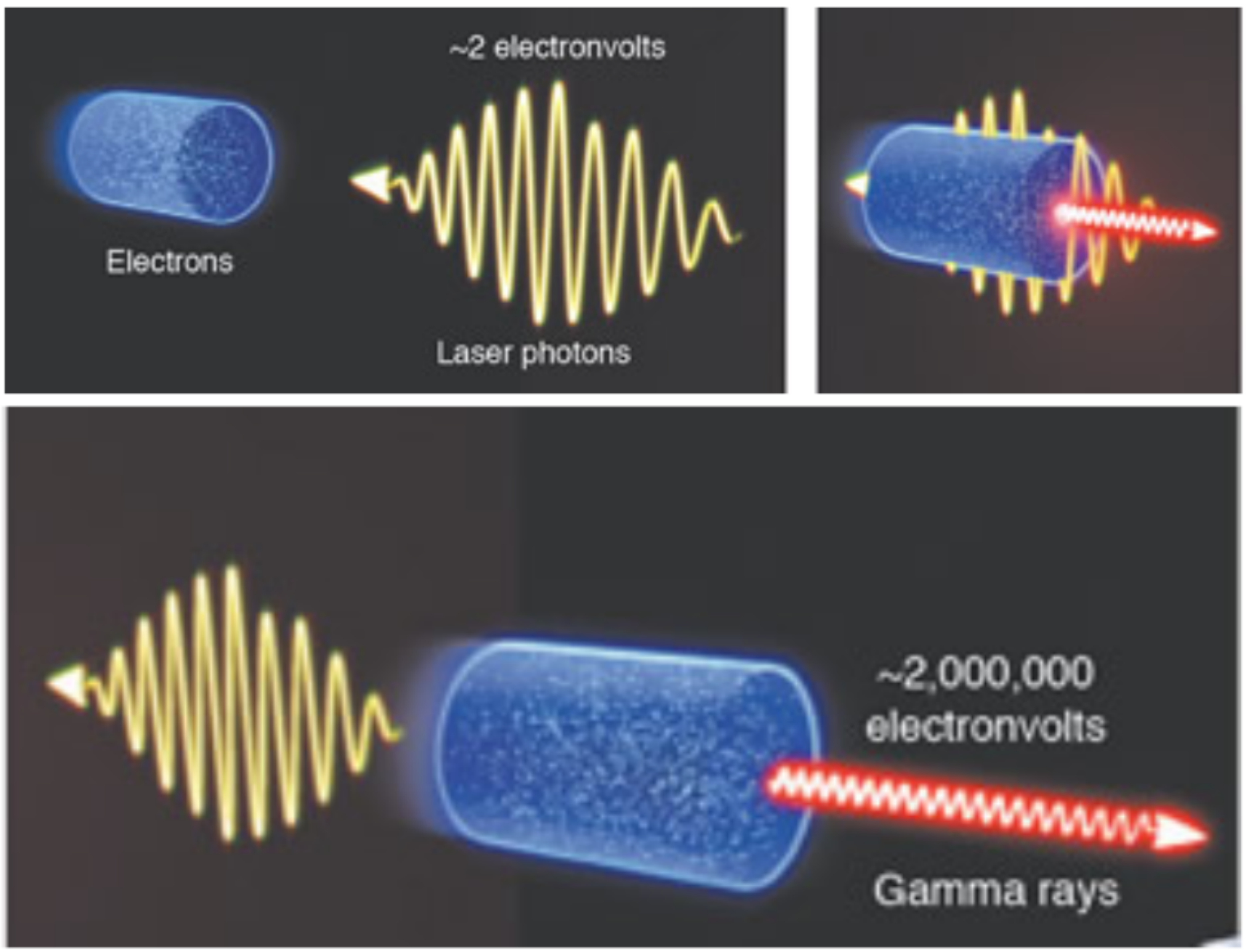

FIG. 1: Photons incident upon a relativistic electron beam are scattered in the direction of the electron trajectory with a substantial boost in energy. The energy increase scales with the square of the electron beams Lorentz factor as per Eq. (1). The electron beam in this diagram has an energy of 255.5 MeV and a Lorentz factor of 500 [1].

The focus of this work is to create computational models to simulate Compton-scattered spectra. These models have been used to build a theoretical basis for methods of improving the quality of future Compton sources and to preform diagnostic analysis of existing light sources.

This first chapter explores several fields of study that make use of high-quality, synchrotron-generated X-rays. The research shown here could, in principle, be conducted using Compton sources instead of synchrotron facilities. The impact of the proliferation of inverse Compton sources is explored with respect to fundamental physics research, medical imaging, humanities research, and materials science.

Chapter 2 is a brief overview of other accelerator sources of electromagnetic radiation. This discussion will develop a context for inverse Compton sources. An explicit comparison to the capabilities of synchrotrons is drawn in this chapter. This section conclude with a brief examination of notable light sources around the world.

Chapter 3 is a brief overview of the general physics underlying the computational models presented in this work. Two models have been developed from distinct physics principles in order to function in two different regimes of operation. These regimes of operation are clearly defined by the qualities of the electron beam and the incident photon pulse. A basic review of the fundamental principles governing these photon-electron collisions is necessary to understand the regimes of operation for inverse Compton scattering events.

Chapters 4 and 5 will serve as a compendium for each of the computational models. The first of these chapters will present the model that functions in the linear Compton regime, and the second of these chapters will present the computational model that functions in the nonlinear Thomson regime. Each chapter will derive the theoretical basis of each model from first principles. The numerical methods employed by each model will be defined. A full description of the various functionalities of each code will be addressed. Furthermore, the chapter regarding the nonlinear code will feature an in-depth discussion of the complex physics arising from an extremely high-intensity laser pulse. Methods of frequency modulation of the incident laser, i.e., a method for correcting the nonlinear broadening effects on the scattered spectrum, will also be discussed.

Chapter 6 features the results of simulations we have conducted using our computational models. The results of thee collaborative efforts will presented with a discussion of the lesson learned from the research.

The work will conclude with Chapter 7. Ongoing research efforts regarding regimes of operation outside of the limits of our current models will be discussed. Possible experimental setups based on the corrective frequency modulation prescriptions will be suggested.

1.1 X-RAYS AND THE HISTORY OF MODERN PHYSICS

Three days before Christmas, 1895, Wilhelm Conrad Röntgen and his wife, Anna Bertha Ludwig, emerged from his laboratory with the very first x-ray image: a photograph of the bones inside Anna's hand. Röntgen would be awarded the first Nobel prize in physics ever awarded for this discovery of bremsstrahlung electromagnetic radiation, i.e., "breaking radiation." Ever since, X-rays have been an integral part of scientific research. Both Röntgen and the first X-ray image taken in public are shown in Figure 2.

X-ray spectroscopy has been of critical importance across the history of modern science [4]. As it has a strong interaction with electrons, X-ray radiation is absorbed by materials consisting of atoms with high electron densities while it passes easily through materials with lower electron densities. This quality makes X-rays incredibly useful for imaging three dimensional objects, both living and inanimate, that are opaque to other lower frequencies of electromagnetic radiation. The great Sir Joseph J. Thomson observed this property in 1897 whilst experimenting with X-rays generated by cathode tubes [5]. During this work he 'discovered' the electron. In 1928, his son, a British physicist named G.P. Thomson, used X-rays to observe the wave nature of matter theorized by M.L de Broglie [6]; Davisson and Germer also observed de Broglie's wave nature using X-rays [7]. Much of this work was made possible by another father-son duo, William Henry Bragg (whose advisor was none other than J.J. Thomson himself) and Lawrence Bragg, who jointly won the Nobel Prize for their advancement of X-ray spectroscopy [8]. Later the double-helix nature of the DNA was discovered via protein crystallography. Under the supervision of Rosalind Franklin in 1952, the X-ray diffraction pattern known as Photo 51, shown in Figure 3, was used to extrapolate the geometry of the DNA molecule [9]. Across many fields throughout the history of modern science, the use of X-rays has been vital to scientific discovery.

X-ray sources are still a crucial tool for researchers today. In this section, the applications of X-ray technology will be explored across several fields of study in order to emphasize the broader societal impact that Compton sources promise. The integral role that tunable, high-quality EM sources play in the clinical application of medical imaging will be discussed. It will be shown how scholars of humanities utilize X-ray sources to study art history and archaeological artifacts. Applications of high-brilliance X-ray sources in the field of material sciences will also be addressed. Large-scale synchrotron radiation (SR) facilities have mostly replaced the cathode tubes of yore. While these SR facilities produce coherent, high-intensity X-rays with narrow bandwidth, the facilities themselves are incredibly expensive to operate. This operational cost greatly limits the number of facilities at which this vital research may be conducted. This section will leave little doubt that the need for affordable, quality EM sources far exceeds the number of sources available in the world today. Compton sources are an affordable alternative to expensive SR facilities.

1.2 MEDICAL RADIOLOGY

Medical radiology utilizes X-rays for practical clinical applications and for biomedical research. Coarse bremsstrahlung techniques are used in most emergency clinics and dentists offices in order to photograph bones and teeth. More advanced imaging may be achieved with higher quality X-ray sources. Medical imaging is based upon the differences in X-ray attenuation. Figure 4 shows how synchrotron radiation may tuned to the attenuation frequency of xenon in order to take an image of a rabbit breathing over time.

Figure 5 clearly illustrates the advantages of using higher brilliance, higher intensity X-rays for

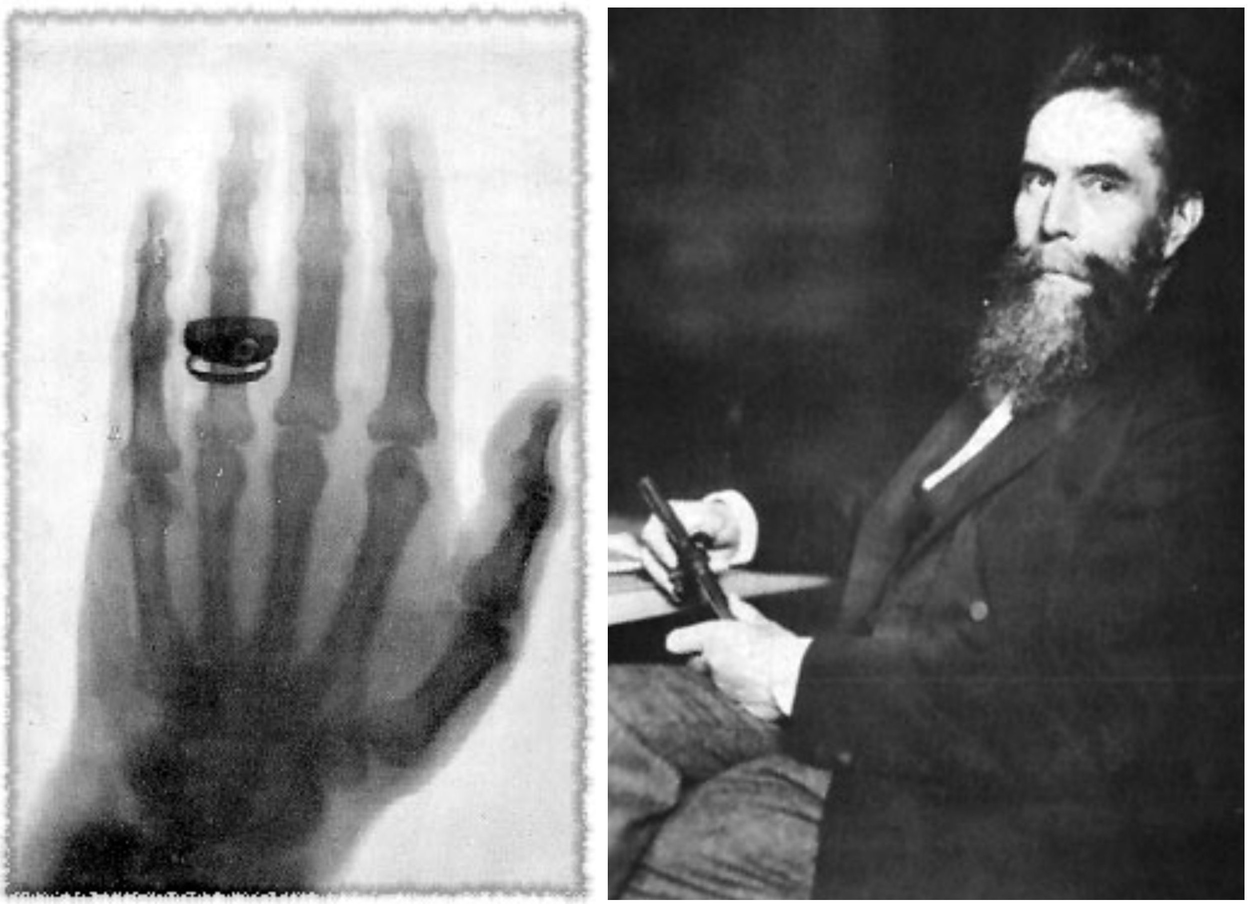

FIG. 2: First X-ray made in public (left). Hand of the famed anatomist, Albert von Kölliker, made during Wilhelm Conrad Röntgen's [10](right) initial lecture before the Würzburg Physical Medical Society, January 23, 1886 [11].

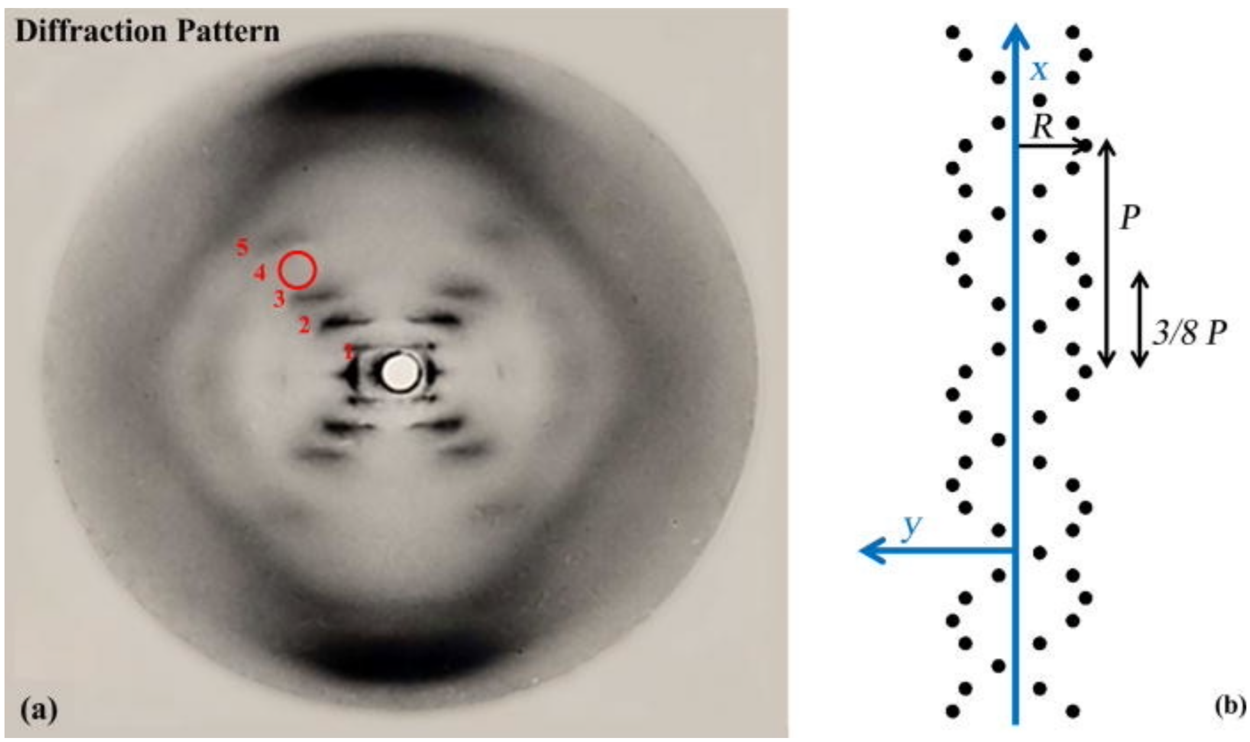

FIG. 3: (a) The well-known Photo 51, the diffraction pattern from DNA in its so-called B configuration. (b) A two-dimensional projection of the phosphate molecules in the DNA backbone [9].

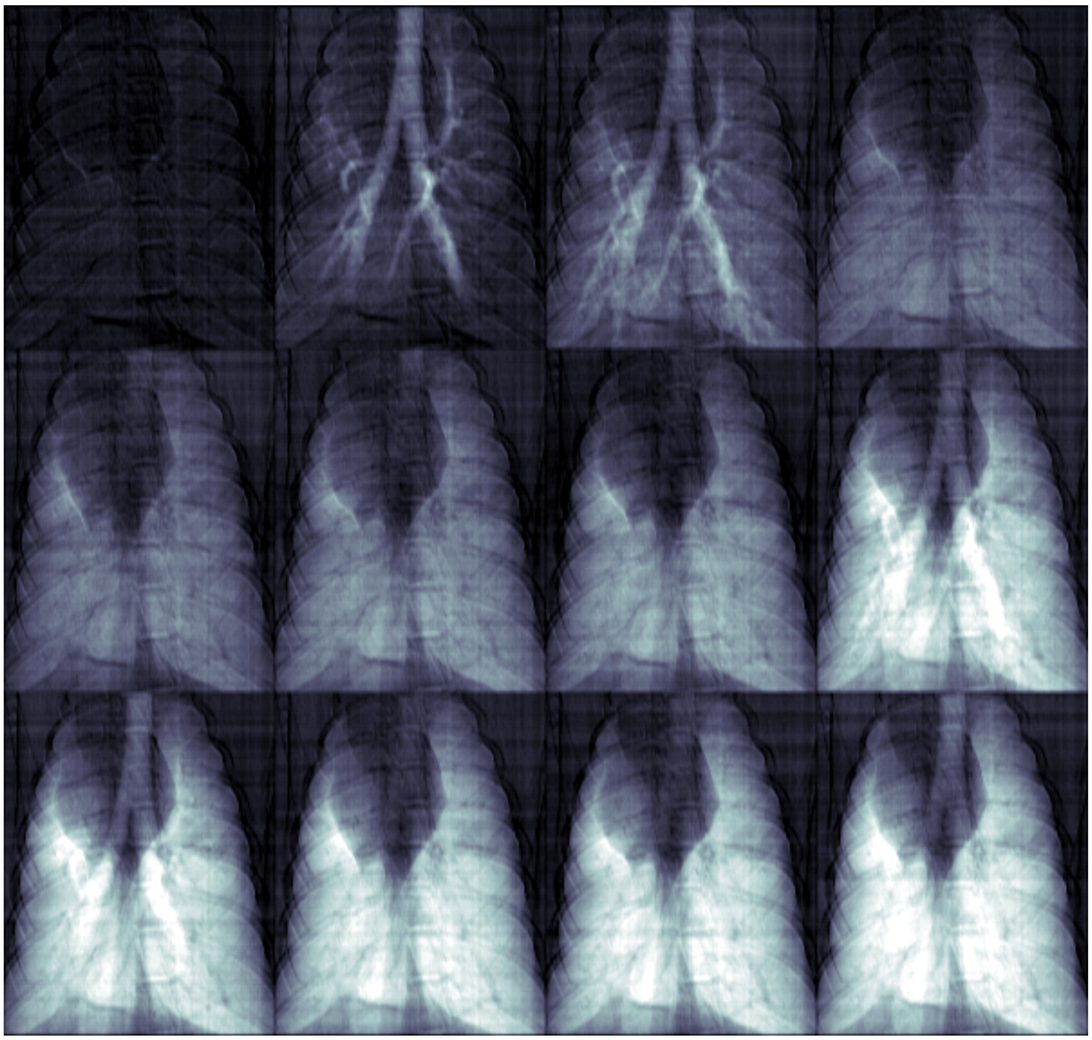

FIG. 4: Projection images of rabbit lung as functions of time. The time difference between subsequent images is 1.3 s. The rabbit is breathing a xenon–oxygen mixture during the wash-in sequence [12, 13].

clinical applications. These photos have been taken from a study in which eight different breast samples with ductal carcinoma were imaged using both the bremsstrahlung-based conal beam breast computed tomography (CBBCT) technique and the propagation-based phase-contrast computed tomography (PB-CT) technique from an SR source. Even to the untrained eye it is very clear the SR-based images have a significantly improved resolution. In fact, the objects of interest, i.e., the lesions caused by the carcinoma, are hardly visible in the bremsstrahlung images [14]. Increasing the number of high-brilliance EM sources increases access to life-changing medical care.

SR sources are useful for imaging vascular stenoses, i.e., the abnormal narrowing of blood vessels. Again, the tunable, high-intensity radiation from the synchrotron allows for more versatile and more relevant imaging. Figure 6 clearly shows that the object of interest, the stenosis in this case, is captured in higher resolution by the SR imaging. Moreover, the stent applied to the stenosis may also be captured by tuning the imaging radiation to the attenuation frequency of the stent.

Although the study presented here and most other vascular imaging has been done experimentally with SR radiation, it has been proposed that the same quality of imaging may be achieved with an inverse Compton source (ICS) [15]. As Compton sources continue to improve in both brilliance and intensity, it is very likely that the quality of medical imaging achieved by SR sources may soon be achieved via ICS.

1.3 HUMANITIES RESEARCH

X-ray fluorescence (XRF) is one of the many tools used by humanities scholars to explore human history [18]. This work will briefly explore the use of XRF in the fields of archaeology and art history. When materials are exposed to X-rays, ionization may occur if the X-ray photons are attenuated to the target atoms, i.e., if the energy of the photons equal to or greater than one of the discrete energy levels of the target atom. Ionization consists of the ejection of one or more electrons from the atom. High-energy X-rays may be specifically attenuated to the tightly held electrons closest to the nucleus of the atom. When an inner orbital electron is removed the structure of the remaining orbiting electrons becomes unstable. Electrons in higher energy orbits descend to fill the lower energy orbits in order to replace the ejected electrons. This decrease in energy level causes photons to be emitted. The emitted photons have energy equal to the difference in energy of the two electron energy levels. Through this process, the target emits photons at wavelengths unique to the energy levels of the atoms within the material. The energy of the emitted photons may be measured to map the presence and distribution of the target atoms. The phenomena is generally called fluorescence. This process is specifically X-ray fluorescence (XRF) since the incident photons are X-rays [19, 20].

XRF is of great use to scholars because the process allows researchers to determine the material makeup of delicate art and artifacts without damaging the target. High-brilliance X-rays may be used to safely image masterpiece paintings to glean insight into the artist and verify the authenticity of lost work. XRF is crucial in restorative practices as it is used to find the deterioration of certain pigments [21].

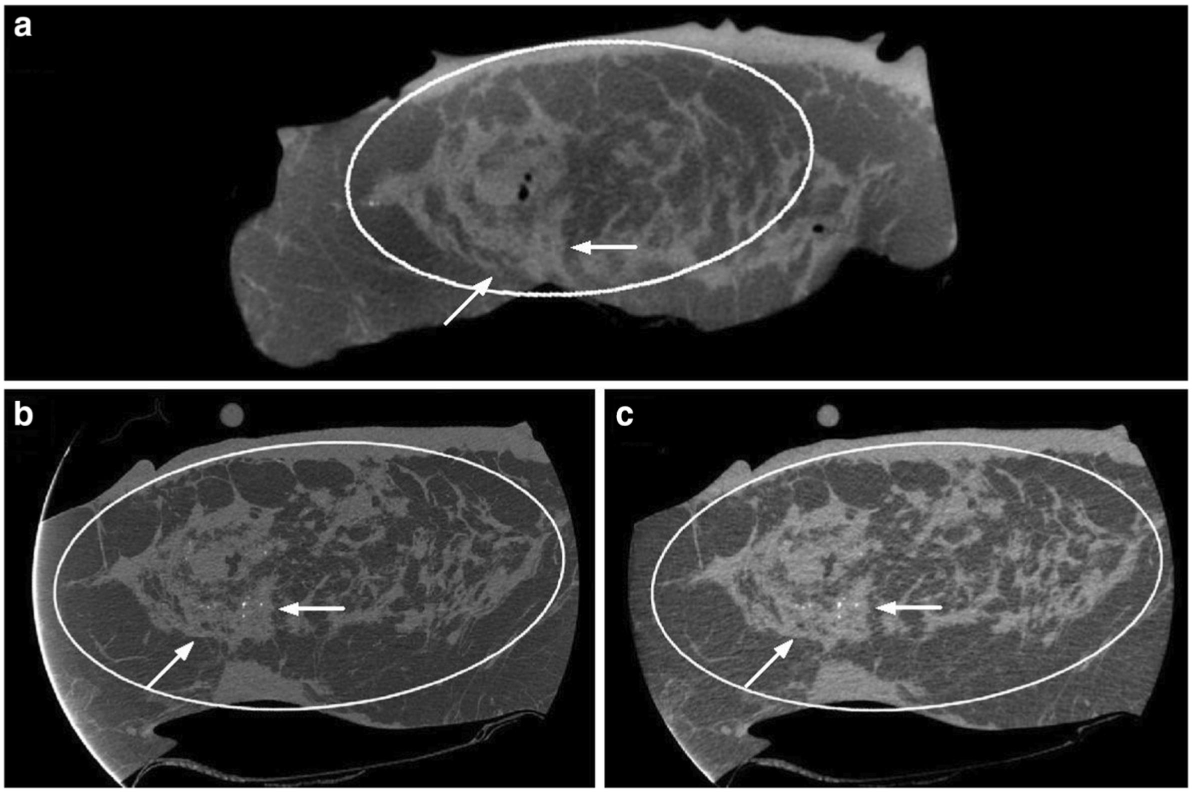

FIG. 5: Tomographic images of sample 6 (after the surgery) with a ductal carcinoma in situ (DCIS), grade 3; the white ovals show the areas of interest for assessment and the arrows indicate the lesion. (a) CBBCT image obtained using a tube voltage of 49 kVp, tube current of 50 mA, MGD of 5.8 mGy, and standard reconstruction mode in Koning CBCT1000. (b) PB-CT image obtained using a beam energy of 35 keV, sample-to-detector distance of 9.31 m, MGD of 5.8 mGy, and iFBP reconstruction method. (c) PB-CT image obtained using a beam energy of 35 keV, sample-to-detector distance of 9.31 m, MGD of 1.5 mGy, and SIRT reconstruction method. The oval shows the area of interest for assessment and the arrows indicate the lesion [14].

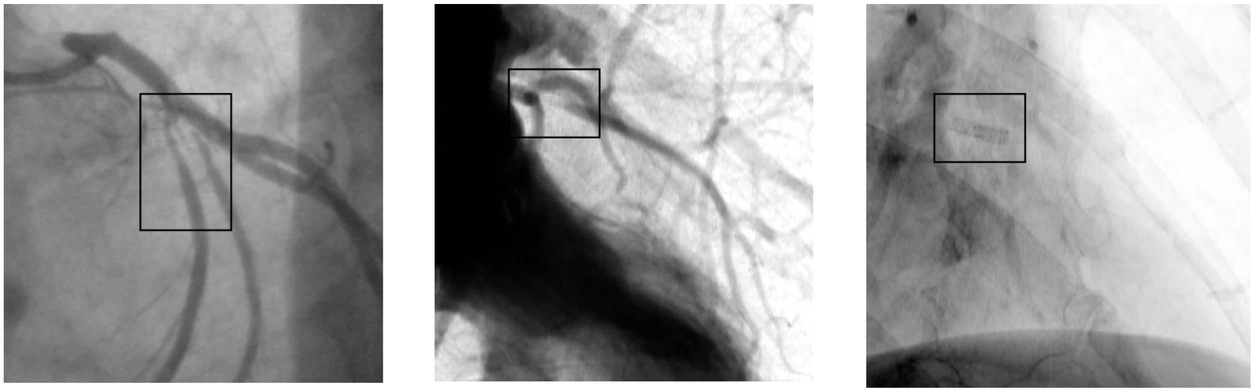

FIG. 6: (left)Bremsstrahlung angiography image, (middle) SR contrast image and (right) tissue attenuated image with stent [16].

XRF has been used to reconstruct the work of Vincent van Gogh. The well-loved 19^{th} Century post-impressionist painter, is known for his vivid colors, his vibrant painting style, and his short but highly productive career. Researchers have discovered that he was far more prolific than originally realized, as many of his known paintings cover a previous works. Van Gogh would often reuse the canvas of an abandoned painting and paint a new or modified composition on top. These previously hidden works have been rediscovered through the clever, gentle application of narrow-bandwidth x-ray radiation. These recovered paintings offer unique insight into the genius of historic artists. Current museum-based imaging tools, however, are unable to reconstruct these hidden works with the resolution required. As shown in Figure 7, SR-based X-ray fluorescence mapping has been applied to visualize a woman's head hidden under the work *Patch of Grass*. Figure 8 shows a reconstruction of the painting beneath *Patch of Grass* compared to similar portraits painted by van Gogh.

Scholars have used these XRF reconstructed images to confirm the authenticity of paintings previously unattributed to the master painter. One such painting shown in Figure 9, *Still life with meadow flowers and roses*, has been confirmed as a Vincent van Gogh original [22]. The artist produced a great quantity of flower pieces during the summer of 1886. During this prolific period he experimented widely with color and a freer application of paint in the fashion of other provincial artists. The 1970 edition of Jacob Baart de la Faille's catalogue raisonné included many of these flower paintings, but the editors doubted the authenticity of *Still life with meadow flowers and roses* since it is an unusually large canvas for van Gogh's work of the era. In 2003 the Kröller-Müller Museum, Otterlo, officially dismissed the painting.

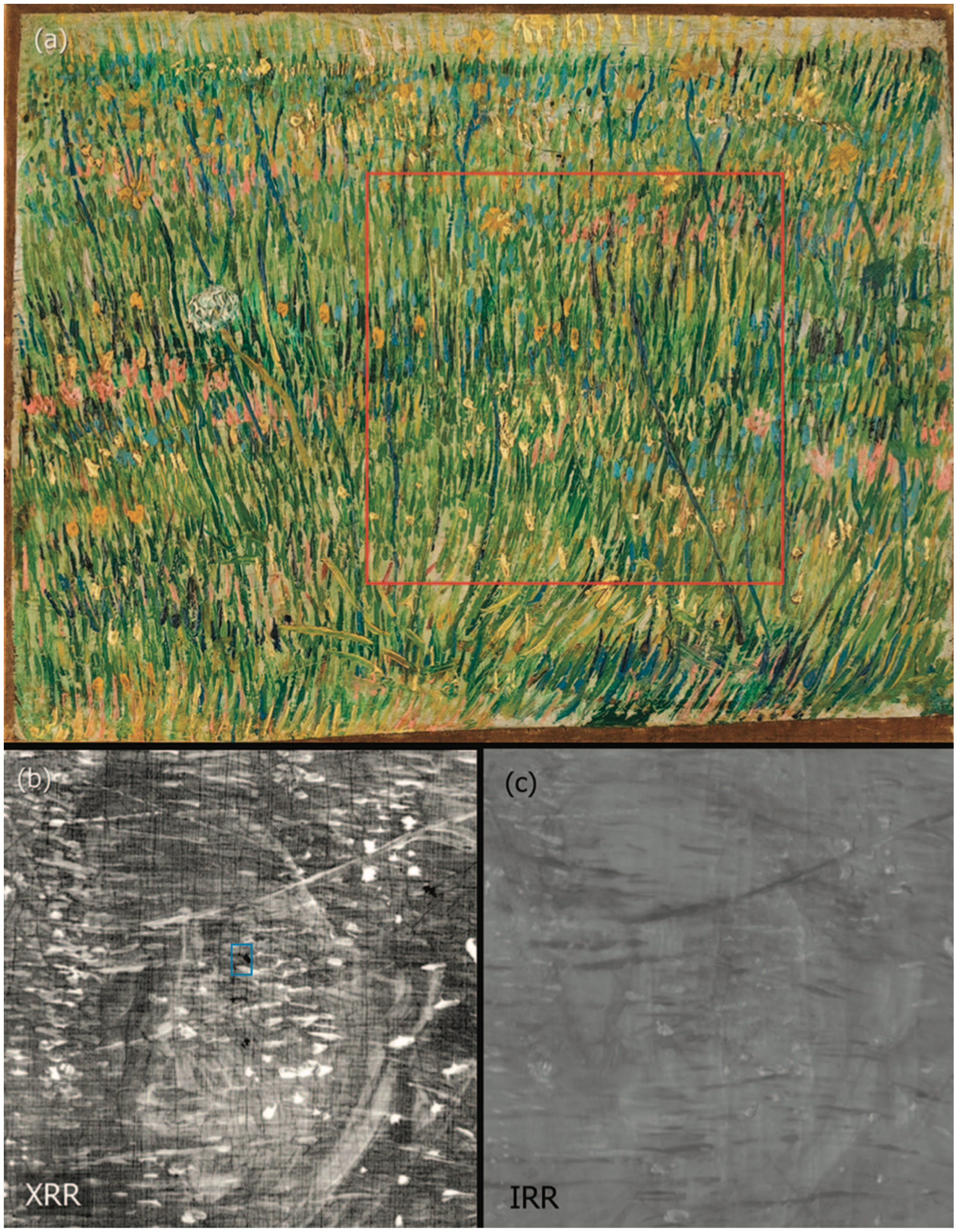

FIG. 7: (a) Vincent van Gogh, *Patch of Grass*, Paris, Apr-June 1887, oil on canvas, 30 cm $\times$ 40 cm, Kröller-Müller Museum, Otterlo, The Netherlands (KM 105.264; F583/JH1263). The red frame indicates the field of view in images (b) and (c) (rotated 90° counter-clockwise). (b) X-ray radiation transmission radiograph (XRR). (c) Infrared reflectograph (IRR) [17].

FIG. 8: (a) Tritonal color reconstruction of Sb (yellowish white) and Hg (red) representing the flesh color of the hidden face. (b) Detail from Vincent van Gogh, *Head of a Woman*, Nuenen, winter 1884-85, oil on canvas, 42 cm × 33 cm, Kröller-Müller Museum, Otterlo (KM 105.591; F154/JH608). (c) Detail from Vincent van Gogh, *Head of a Woman*, Nuenen, winter 1884-85, oil on canvas, 42 cm × 34 cm, Van Gogh Museum, Amsterdam [17].

FIG. 9: Vincent van Gogh, *Still life with meadow flowers and roses*, 1886-87, oil on canvas, 99×79 cm, Kröller-Müller Museum, Otterlo [22].

This decision was based in part on an X-ray image taken of *Still life with meadow flowers and roses* in 1998. This earlier image used conventional X-ray imaging techniques, and it showed that the flowers were painted on a reused canvas. The underlying picture was of two men wrestling. In 2010, the painting was scanned again, this time using XRF at Deutsches Elektronen Synchrotron (DESY) in Hamburg. The resulting images are shown side-by-side in Figure 10. The quality of the XRF image is much greater as there is no interference from the painting of the flowers on the surface. As in medical radiology, the conventional X-ray technique used in 1998 is based on the differences of X-ray attenuation within the material, so this interference from the surface painting is unavoidable. Since different pigments with different molecular makeups were used in the painting of the wrestlers, the fluorescence has been resolved to distinguish the hidden painting from the surface painting.

FIG. 10: (left) (right) Four images showing the distribution of zinc white (ZnO), captured using MA-XRF from the verso at DESY (Hamburg) and the coarser scans at the museum; overlaid with the X-ray image [22].

The results of the XRF scan at DESY revealed two important details to the researchers at the Kröller-Müller Museum. First, the wrestlers in fact wearing loin clothes and not fully nude. Full nudity was not permitted for the live models at the Royal Academy during van Gogh's time there, so this detail is congruent with both the policy of the institution and correspondences from van Gogh himself during this time. The second and perhaps most conclusive detail revealed by the DESY XRF scan is that the paint pigments used in both the painting of the flowers and the wrestlers are consistent with the known works of Vincent van Gogh during this Paris period, i.e., the emitted fluorescence from this XRF scan is of the same characteristic frequency associated with the paints van Gogh would have used. These collections of characteristic wavelengths emitted during an XRF scan act as a 'fingerprint' of sorts for humanities scholars as they are often able to use these combinations to connect the work to a palette that is unique to specific place and era. The results of the XRF were crucial in authenticating the painting and returning *Still life with meadow flowers and roses* to the greater oeuvre of Vincent van Gogh.

Archaeometallurgy is another humanities field that allows scholars to determine the quality and value of ancient metal artifacts in order to find insight into the ancient peoples that crafted them [23]. For civilizations that have left behind metal artifacts but no written history, archaeometallurgy is often one of the best ways to learn about lost cultures. As with the study of masterwork paintings, it is necessary that the analytical techniques employed are non-destructive as these ancient artifacts are unique and irreplaceable. Like XRF and X-ray imaging, many SR techniques meet this requirement. X-ray diffraction (XRD) and X-ray spectroscopy (XRS) are two more SR tools used by archaeologists.

In XRD, the target material is bathed in incident X-rays waves of electromagnetic radiation. The subatomic particles of the target material's molecules (primarily the electrons) scatter these X-ray waves. In the same way that an ocean wave strikes a lighthouse and produces secondary circular waves emanating from the lighthouse, so too does an X-ray wave striking an electron produce secondary spherical electromagnetic waves that emanate from the electron. The scattered X-ray waves create a diffraction pattern that may be resolved in order to reconstruct the locations within the target material [24]. The double helix geometry of DNA was verified using XRD, and the diffraction pattern of the molecule is shown in Figure 3.

In XRS an electron from the inner orbit of an atom is excited by an X-ray photon. This electron then ascends to a higher energy orbit. Ultimately the electron falls from the excited state and returns to the low-energy level. The excitation energy gained from the X-ray photon is emitted as a photon that has an energy that is unique to the difference between the excited energy and the lower energy orbit. These emitted photons, or characteristic photons, are unique to the energy levels of the target element. These characteristic photons are similar to the emissions from XRF, but the mechanism by which they are created does not require the expulsion of an electron from the target [25].

All of these X-ray surveying techniques offer different advantages for different applications in the field of archaeometallurgy. Figure 11 shows an experimental setup for SR survey at the Advanced Photon Source at Argonne National Laboratory. SR X-ray radiology captures 2D and 3D microstructural features of the artifact at very high resolutions. XRD captures the chemical structure of the artifact which gives an indication of the degree of crystallinity, grain size, and texture, that can be used to determine how the artifact was crafted. XRF captures the elemental concentrations near the surface which is important for studying local corrosion layers. XRS reveals the both elemental composition and the chemical and electronic state of specific elements present in the artifact. The artifact being surveyed in Figure 11 is shown in detail in Figure 12. Together these techniques allow archaeologist glean valuable insight into ancient civilizations by surveying

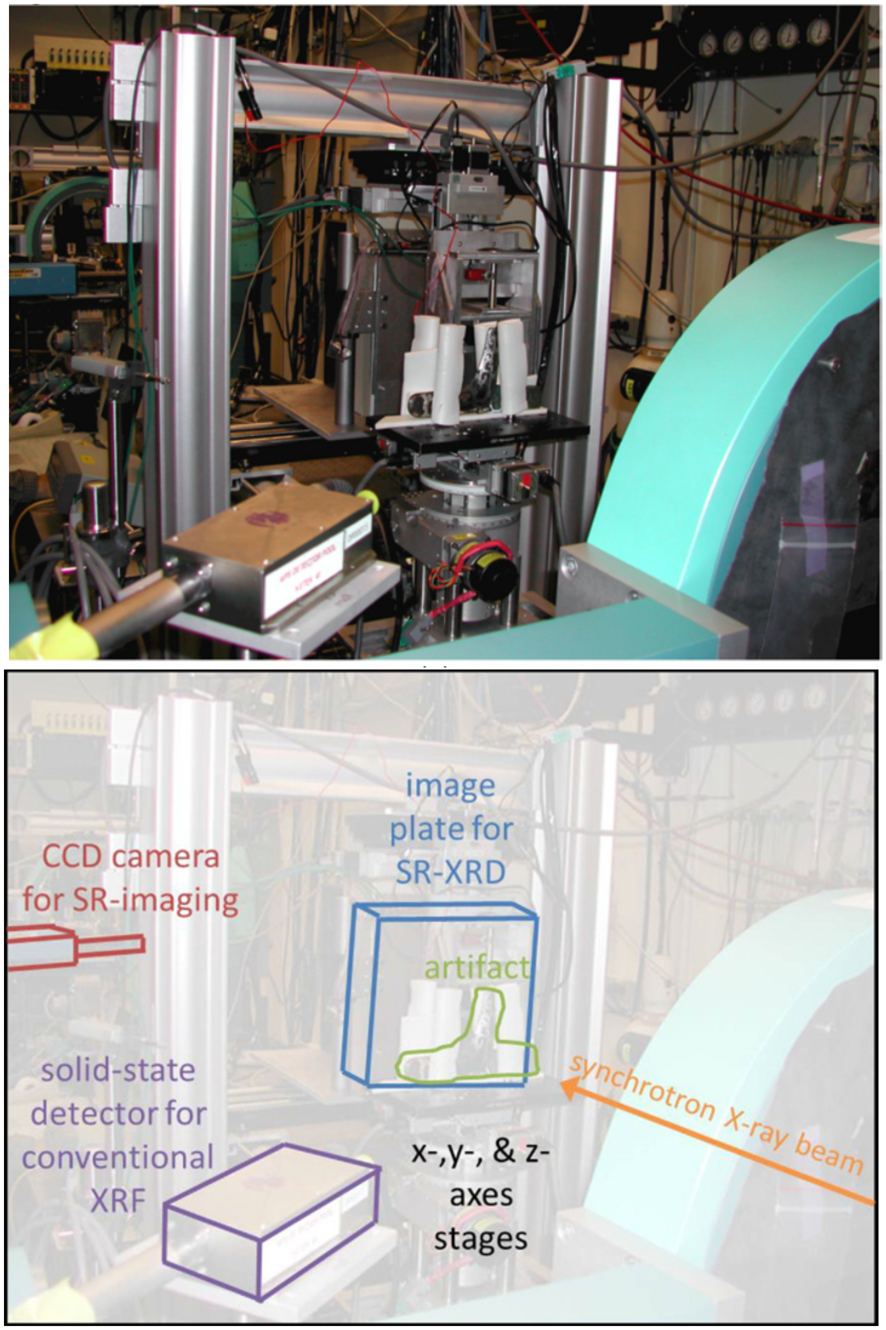

FIG. 11: A typical example of an artifact within an experimental hutch at an SR facility. In this photo, the SR beam is coming from the bottom right corner, the artifact in the middle is an ancient Chinese bronze dagger-axe from the Eastern Zhou dynasty with a silver-inlaid sheath, which was studied at the Advanced Photon Source at Argonne National Laboratory. The image plate is directly behind the artifact and is used to collect SR X-ray radiographic images and SR XRD patterns [23].

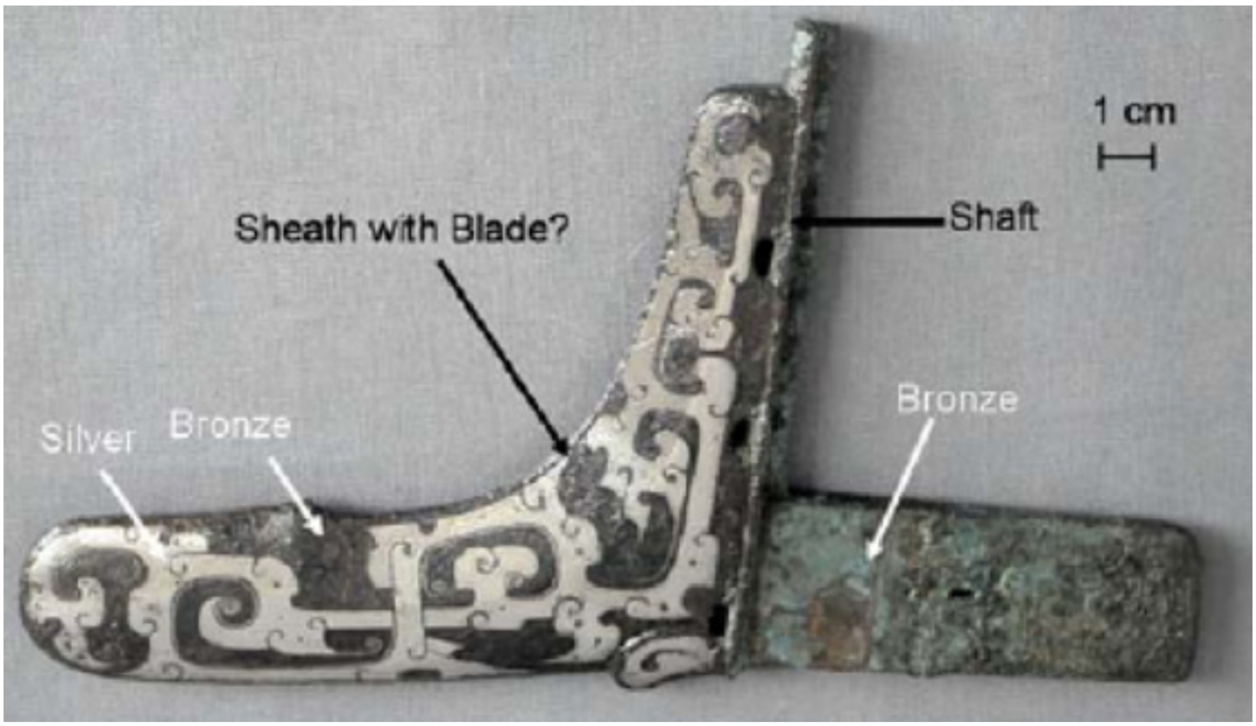

FIG. 12: Image of the ancient Chinese bronze dagger-axe (Ge, Eastern Zhou Dynasty, Warring States period (480-221 B.C.), $3^{rd}/2^{nd}$ century B.C.) with silver-inlaid sheath as pictured in the experimental setup in Figures 11 [23].

the metal artifacts that they have left behind.

1.4 MATERIALS SCIENCE

Materials science is an interdisciplinary field of study that focuses on the design and discovery of new materials and the improvement of existing materials. Researchers in the field of materials science emphasize understanding how the history of a material influences its structure, and thus the material's properties and performance. The materials paradigm is the understanding of processing-structure-properties relationships. This paradigm is used to advance understanding in a variety of research areas, including nanotechnology, biomaterials, and metallurgy [26].

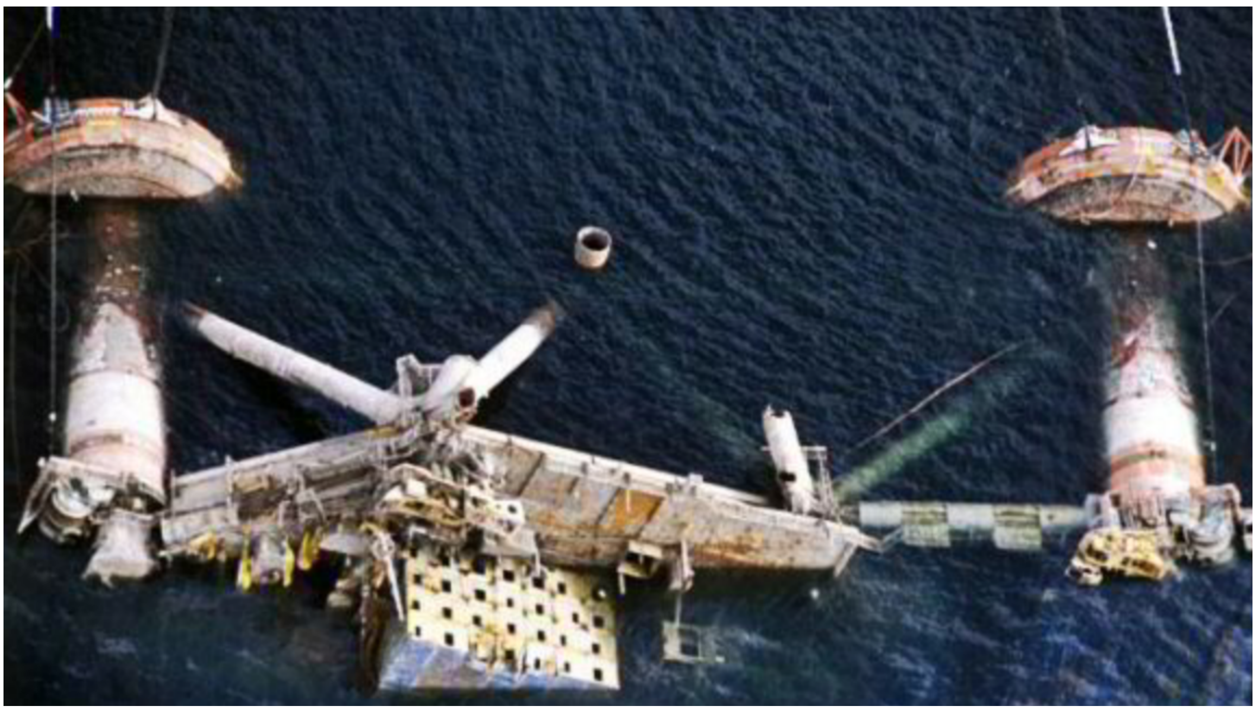

FIG. 13: Alexander L. Kielland oil platform catastrophe, 1980 [27].

Materials science is crucial to the fields of forensic engineering and failure analysis. These fields focus on investigating cases in which manufactured materials, products, structures or components fail causing personal injury or substantial damage to property. These investigations are key to understanding the causes of various industrial accidents and incidents [28].

Materials weaken, or suffer fatigue, as they are subjected to repeated mechanical stress. Fatigue is defined as the development and propagation of fissures in a material as a result of cyclic loading. After a crack has developed, it will continue to grow incrementally every time to the

FIG. 14: On June 17, 2013, Mitsui O.S.K. Lines' 2008-built MOL Comfort began suffering from severe hogging and broke in two while underway from Singapore to Jeddah [29].

material is placed under stress. This process of fatigue often produces striations on the materials surface. A crack continues to grow until it eventually reaches a critical size, which occurs when the stress intensity factor of the crack exceeds the fracture toughness of the material, producing rapid propagation and typically complete fracture of the structure [30].

The results of material failure due to fatigue can be catastrophic [31, 32]. An early example of is the Versailles train crash of 1842: a train, severely overloaded with revelers celebrating the birthday of King Louis Philippe, broke an axle and derailed killing an estimated 55 people. The Boston molasses disaster of 1919 resulted from a fatigue crack near a manhole cover in a 50' tall molasses vat; this resulted in a 25' wave of molasses decimating the local area by knocking building off their very foundations. The de Havilland Comet plane crashes of 1954 were a result of metal fatigue arising from design flaws that ultimately lead to explosive decompression; 56 lives were lost. In 1980, the Alexander L. Kielland oil platform capsized when several anchoring cables snapped due to material fatigue; 120 lives were lost. As shown in Figure 14, the MOL comfort suffered catastrophic hull failure, snapped in half and sank. It is important to note that in the case of the freight ship MOL Comfort, reports show that the stress upon the hull was within engineering specifications thus illustrating that one of he more alarming characteristics of material fatigue is that it can be unpredictable. In order to minimize the probability of these catastrophic events happening again, it is of great importance that researchers continue broadening our understanding of material fatigue processes [33, 34, 35].

SR XRD contrast tomography is a non-destructive surveying technique which images microstructure and grain orientation in polycrystalline materials in three dimensions. By combining this technique with propagation-based phase-contrast tomography researchers are able to get a full picture description for the analysis of local crack growth rate of short fatigue cracks in three dimensions: the three-dimensional crack morphology at different propagation stages, and the shape and orientation of the grains around the crack [36, 37].

CHAPTER 2

A BRIEF REVIEW OF ACCELERATOR-BASED SOURCES OF ELECTROMAGNETIC RADIATION

To highlight the merits of Compton scattering, let us examine this phenomenon within the broader field of X-ray light sources available today. Four other types of light sources will be discussed: common bremsstrahlung sources, synchrotrons, synchrotrons with insertion devices, and free-electron lasers (FEL). As most applications require the greatest possible intensity within the most narrow bandwidth permitted, the average spectral brilliance of these light sources as defined by Wille will be used as a measure of comparison [38]:

$$\mathcal{B} \approx \frac{\gamma^2 \mathcal{F}_{0.1\%}}{4\pi^2 \epsilon^N_{x,\mathrm{RMS}} \epsilon^{\mathrm{N}}_{y,\mathrm{RMS}}}, \tag{2}$$

where γ is the Lorentz factor of the electron beam, $\mathcal{F}_{0.1\%}$ is the flux of the scattered photons within 0.1% of the spectral bandwidth, and $\epsilon^{\mathrm{N}}_{x,\mathrm{rms}}$ and $\epsilon^{\mathrm{N}}_{y,\mathrm{rms}}$ are the normalized horizontal and vertical emittances of the electron beam respectively.

Each light source is defined in this chapter. A full description of the physics underlying the radiation emission is presented here. Each discussion (with the exception of bremsstrahlung) ends with a set of equations that define the spectral intensity distribution and the scaling of each light source. The end of this chapter features a brief discussion of notable light sources.

2.1 BREMSSTRAHLUNG RADIATION

TABLE 1: Comparison of the average brilliance of different light sources [2, 3, 39, 40].

Light Source	$\mathcal{B}$ (ph/(S-mm^2-mrad^2-0.1% BW))
Bremsstrahlung in-lab source	10^{11}
Inverse Compton Source	10^{15}
Synchrotron	10^{16}
Synchrotron with Insertion Device	$10^{17} - 10^{20}$
Free-Electron Laser	$10^{22} - 10^{24}$

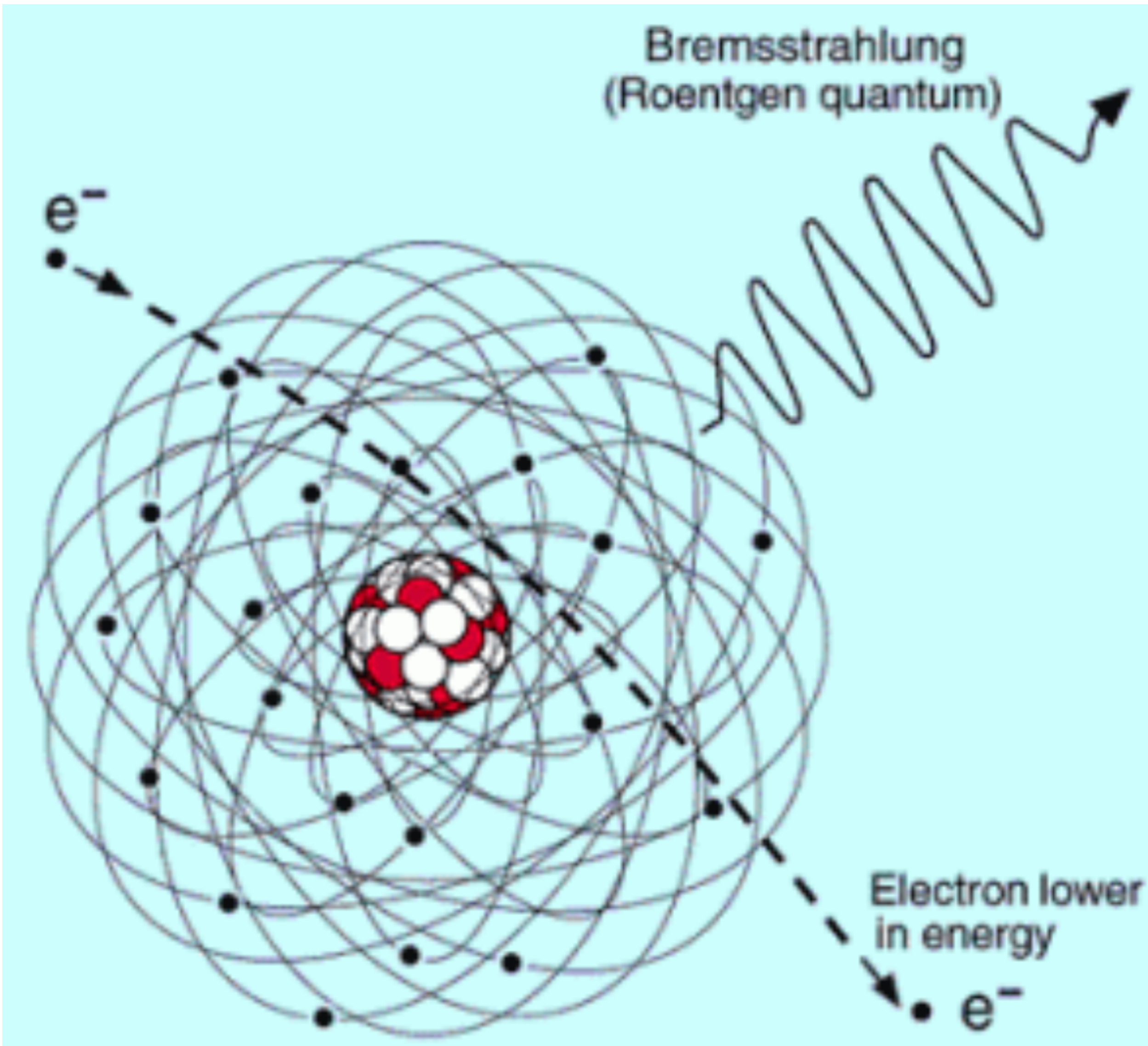

FIG. 15: Bremsstrahlung radiation, or “breaking radiation,” occurs when an accelerated electron is deflected by the strong fields of the atomic nucleus [41, 42].

Bremsstrahlung radiation, as previously discussed, was the earliest mechanism used by physicists to produce X-ray emissions. As illustrated in Figure 15, this form of electromagnetic radiation is generated by a sudden deceleration (a loss of speed or a deflection) of charged particles incident upon the strong electric fields of atomic nuclei. Bremsstrahlung methods are used to create continuous X-ray spectra that spread over a broad range of scattered frequencies. The maximum photon energy emitted through bremsstrahlung methods occurs when the atomic fields bring the electron to rest and all of the electron's energy is emitted as scattered radiation. While passing through the target material, the charged particles may undergo multiple collisions. Each collision emits radiation at some frequency that is less than the maximum emitted energy. The net result is broad bandwidth in the emitted spectrum [41, 43].

While most applications that require high-quality X-rays would benefit from the higher intensity, lower bandwidth emissions available at SR facilities, there is still a need for high-performance reliable systems for in-house experiments. In many cases it is simply impractical to relocate experiments to the SR facility. For example, in crystallography and other branches of pharmaceutical research the delicate substrates of interest may only be available for observation for a very small window of time. The delicate crystals may also be damaged during transit. In the case of humanities research, removing priceless works of art and ancient artifacts from the security of their museums may introduce unacceptable risk. To meet the need for in-house X-ray sources there has been a continuous evolution in their technology. Specifically, the use of liquid gallium in bremsstrahlung sources has lead to a dramatic increase in X-ray brightness for specific emitted X-ray frequencies [39, 40].

2.2 SYNCHROTRONS

Early particle accelerators, such as the cyclotron and microtron, used uniform magnetic fields to keep charged particles bound in circular orbits. This circular orbit was a direct result of the Lorentz force of the magnetic field upon the charged particle

$$\boldsymbol{F} = \dot{\boldsymbol{p}} = \frac{\mathrm{d}}{\mathrm{d}t}(m\boldsymbol{v}) = q(\boldsymbol{E} + \boldsymbol{v} \times \boldsymbol{B}), \tag{3}$$

where $\dot{\boldsymbol{p}}$ is the first time derivative of the momentum vector of the particle, t is time, m is the mass of the particle, $\boldsymbol{v}$ is the velocity vector of the particle, q is the charge of the particle, $\boldsymbol{E}$ is the vector of the external electric field, and $\boldsymbol{B}$ is the vector of the external magnetic field. A stable orbit with a fixed radius R may be established by setting the Lorentz force equal to the centripetal force and solving for R

$$R = \frac{vE}{qc^2B}, \tag{4}$$

where v and E are the magnitudes of the previous vectors and E is the energy of the electron. For

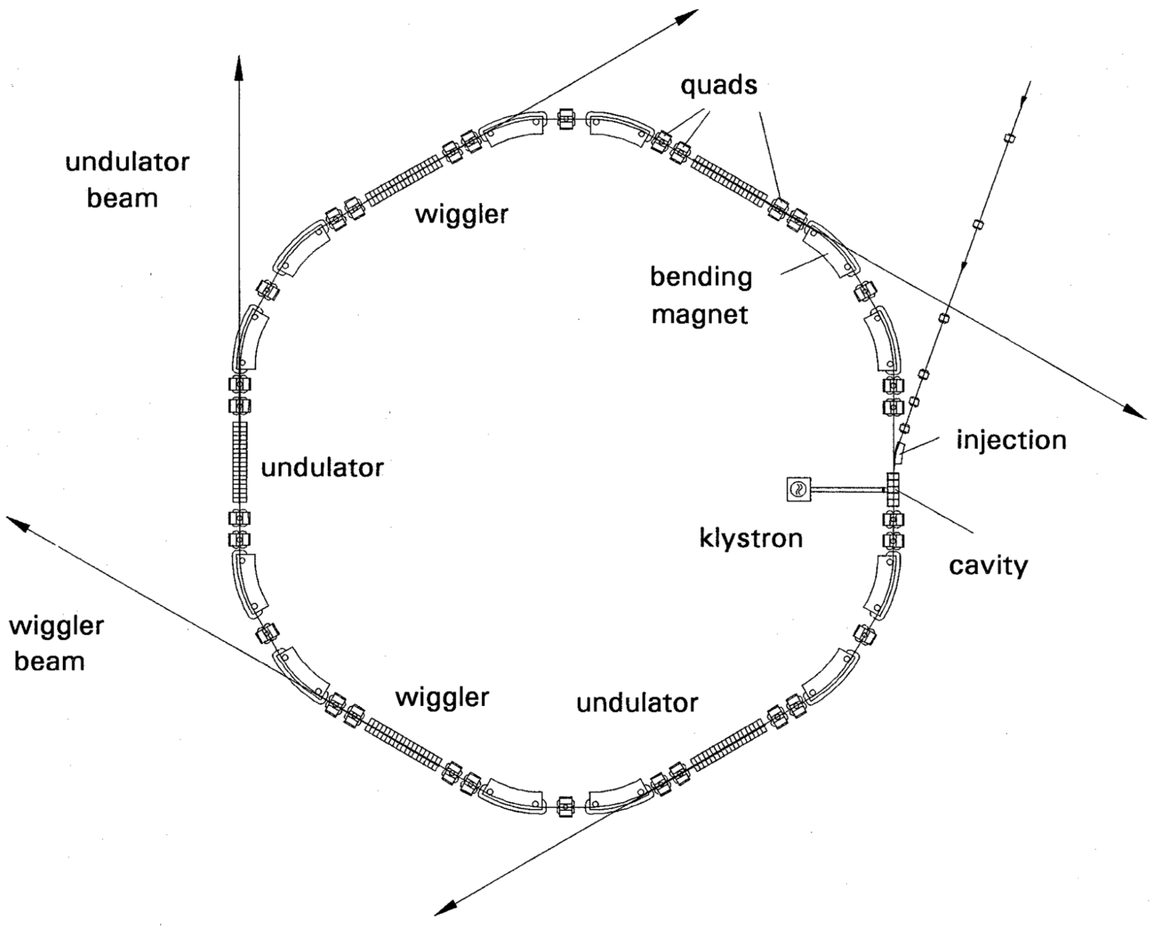

FIG. 16: General layout of a modern synchrotron light source [38].

a relativistic electron ($v \approx c$) in a stable orbit [38],

$$R = \frac{E}{ecB}. \tag{5}$$

Eq. (5) shows how the energy of the electron is limited by the magnitude of the uniform magnetic field for a fixed radius. In practice, the magnetic field is limited to about 1.5 T in conventional magnets and about 5 T in superconducting magnets. In order to overcome this limit, the broad uniform magnetic fields were removed and then replaced by short bending magnets that only generate field in the region of the electron beam. In order to maintain a fixed radius, the magnitude of the bending magnets and the energy of the electron beam would have to increase at the same rate as per Eq. (5), i.e., the field magnitude and the energy of the electrons would increase *synchronously*. Hence, these high-energy accelerators are called synchrotrons. A diagram of a typical synchrotron accelerator is shown in Figure 16.

The increase in energy as well as the placement of the sharp, narrow-field magnets leads to the emission of high-quality X-rays. In contrast to a linear particle accelerator (linac), synchrotrons emit much more radiation. In both types of accelerators, the energy gains from the accelerating cavities themselves contributes little to the emitted radiation. As a particle approaches the speed of light, it gains less linear acceleration from a given force. The change in direction imposed on the electrons by the bending magnets, however, causes a tremendous amount of high-energy radiation. The highest intensity radiation is emitted as the electron is transversely accelerated through the bending magnets of the synchrotron. The electron emits radiation in a fan shape throughout the curved motion, but the general trajectory of the emitted radiation is indicated with arrows in Figure 16. The emitted radiation makes up the energy loss of the electron orbiting the accelerator and it scales with the fourth power of the electron energy $\Delta E_{\text{loss}} \propto E^4$ [38, 41, 44].

The spectral photon density for synchrotron radiation is well-documented. J. Schwinger was first to publish the expression in 1954 [45]:

$$\frac{\mathrm{d}\dot{N}}{\mathrm{d}\epsilon/\epsilon} = I_{\text{beam}} \frac{e\gamma^4}{3\epsilon_0 R \omega_c \hbar} \frac{9\sqrt{3}}{8\pi} \frac{\omega}{\omega_c} \int_{\omega/\omega_c}^{\infty} K_{5/3}\left(\omega/\omega_c\right) \mathrm{d}[\omega/\omega_c], \tag{6}$$

where I_{beam} is the electron beam current, ϵ_0 is the permittivity of free space, $K_{5/3}$ is the modified Bessel function, and ω_c is the characteristic frequency of the emitted radiation:

$$\omega_c = \frac{3\pi c\gamma^3}{2R}. \tag{7}$$

2.3 SYNCHROTRONS WITH INSERTION DEVICES

As presented in Section 2.2, SR is emitted when the particle beam is deflected by bending magnets. This emitted radiation is characterized by a wide spectrum that spreads from microwaves up to through X-rays. This range of frequencies is determined by the critical photon energy

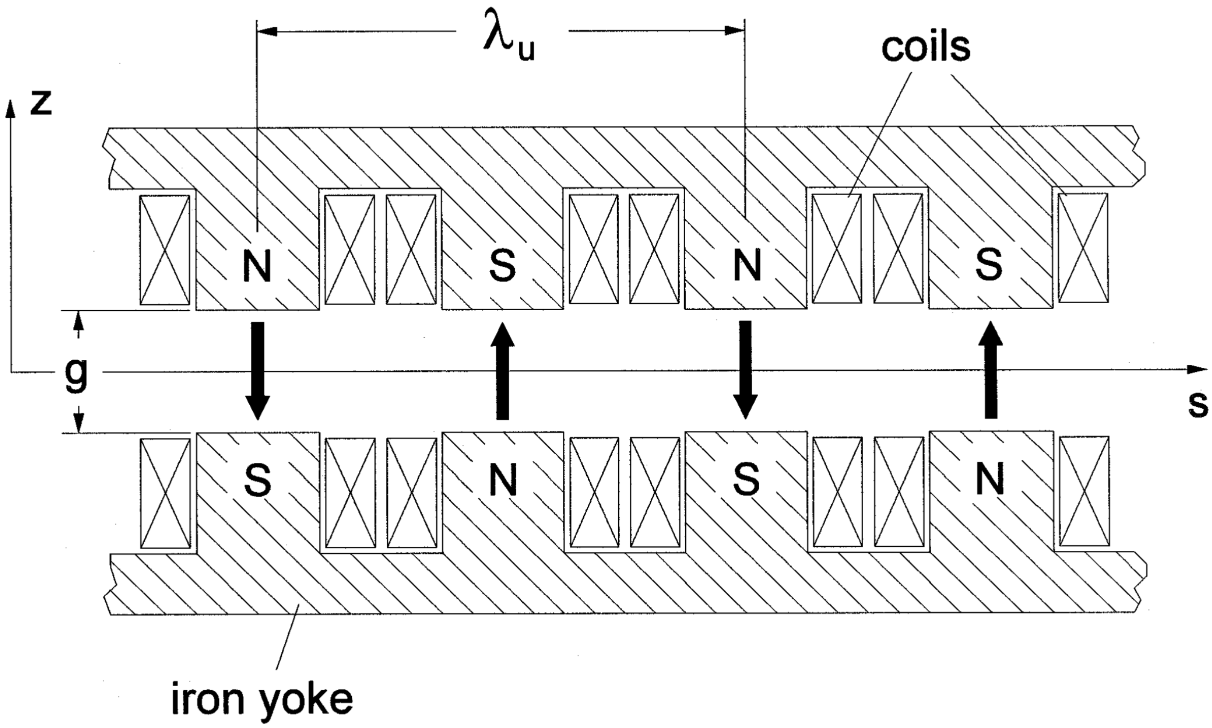

FIG. 17: Principal design of an electromagnetic wiggler or undulator [38].

$E_c = \omega_c \hbar$, where ω_c is the characteristic frequency from Eq. (7). To meet the growing demands of fundamental research, it is necessary to further refine the quality of SR to provide radiation characteristics that cannot be generated from narrow bending magnets alone. As defined in Eq. (5), the magnitude of the bending magnets and the electron beam energy in circular accelerators is fixed. These stuck parameters leave little room for optimizing SR for desired output spectra unique to the needs of specific experiments. To create SR with a particular set of desired characteristics, insertion devices are installed along the particle beam path as shown in Figure 16. Undulators and wigglers are the most commonly used insertion devices. Both of these devices consist of an array of alternating magnet poles that deflect the particle beam periodically in opposite directions, i.e., these devices induce a wiggling motion in the electron trajectory [46]. The only difference between undulators and wigglers is the energy at which they operate: undulators are for low-energy beams and wigglers are for high-energy beams. A diagram of a typical undulator/wiggler is shown in Figure 17. Since these devices do not cause any net deflection in the particle beam, they do not change the beam line geometry when they are incorporated into the accelerator [38, 41, 44].

The spectral photon density emitted by synchrotrons with insertion devices depends on both the energy of the electron beam and the properties of the undulator/wiggler. The dimensionless quantity K is known as the undulator/wiggler parameter:

$$K = \frac{\lambda_{\mathrm{u}} e\tilde{B}}{2\pi mc}, \tag{8}$$

where λ_{u} is the undulator period (see Figure 17) and $\tilde{B}$ is the magnitude of the Fourier transform of the magnetic field in the undulator. The parameter K quantifies the difference between undulators and wigglers: all undulators meet the condition $K \ll 1$ and wigglers have all other values of K. Harmonics appear in the scattered spectra in wiggler radiation. The wavelength of the photon emitted from the undulator within the k^{th} harmonic λ_k is a function of the undulator parameter K and the observation angle Θ

$$\lambda_k = \frac{\lambda_u}{2\gamma^2 k}\left(1 + \frac{1}{2}K^2 + \gamma^2\Theta^2\right). \tag{9}$$

The spectral photon density emitted in the direction of the electron beam axis ($\Theta = 0$) is a function of the undulataor parameter K

$$\left.\frac{\mathrm{d}N}{\mathrm{d}\Omega}\right|_{\Theta=0} = \alpha\gamma^2 N_{\mathrm{p}}^2 \frac{\Delta\omega}{\omega} \frac{K^2}{\left(1+\frac{1}{2}K^2\right)^2} \sum_{k=1}^{\infty} \left(\frac{\sin \pi N_{\mathrm{p}} \Delta\omega_k/\omega_1}{\pi N_{\mathrm{p}} \Delta\omega_k/\omega_1}\right)^2 \tilde{\boldsymbol{J}}^2, \tag{10}$$

where α is the fine structure constant, N_{p} is the number of photons passing through the undulator, $\Delta\omega/\omega$ is the spectral linewidth, and $\tilde{\boldsymbol{J}}$ is a function defined by Bessel functions

$$\tilde{\boldsymbol{J}} = \left[\boldsymbol{J}_{\frac{1}{2}(k-1)}\left(\frac{kK^2}{4+2K^2}\right) - \boldsymbol{J}_{\frac{1}{2}(k+1)}\left(\frac{kK^2}{4+2K^2}\right)\right]. \tag{11}$$

2.4 FREE-ELECTRON LASERS

In a conventional laser setup, an incident electromagnetic wave stimulates emission from some medium that acts as an energy reservoir. The emitted frequency has the same frequency as the incident wave, but the amplitude of the stimulated waves has been amplified by the energy reservoir. Emissions from an undulator may be amplified in a similar fashion by replacing the laser medium with a relativistic electron beam passing through an undulator magnet. Here the free electrons of the beam become the lasing material, and thus we have a free-electron laser (FEL). FELs emit quasi-monochromatic, spontaneous radiation that is captured and recycled into an optical cavity. This process is shown in Figure 18. Within the optical cavity, the captured radiation interacts with the electron beam causing accelerations which are periodic with the frequency of the undulator radiation. The path of the electrons is modulated by periodic deflections in the undulator field to generate transverse velocity components to couple the particle motion to transverse field: the undulator magnet serves both as the source of radiation and the means to couple to the electric field to the electron motion. This coupling results in a gain or loss of energy from/to the electromagnetic

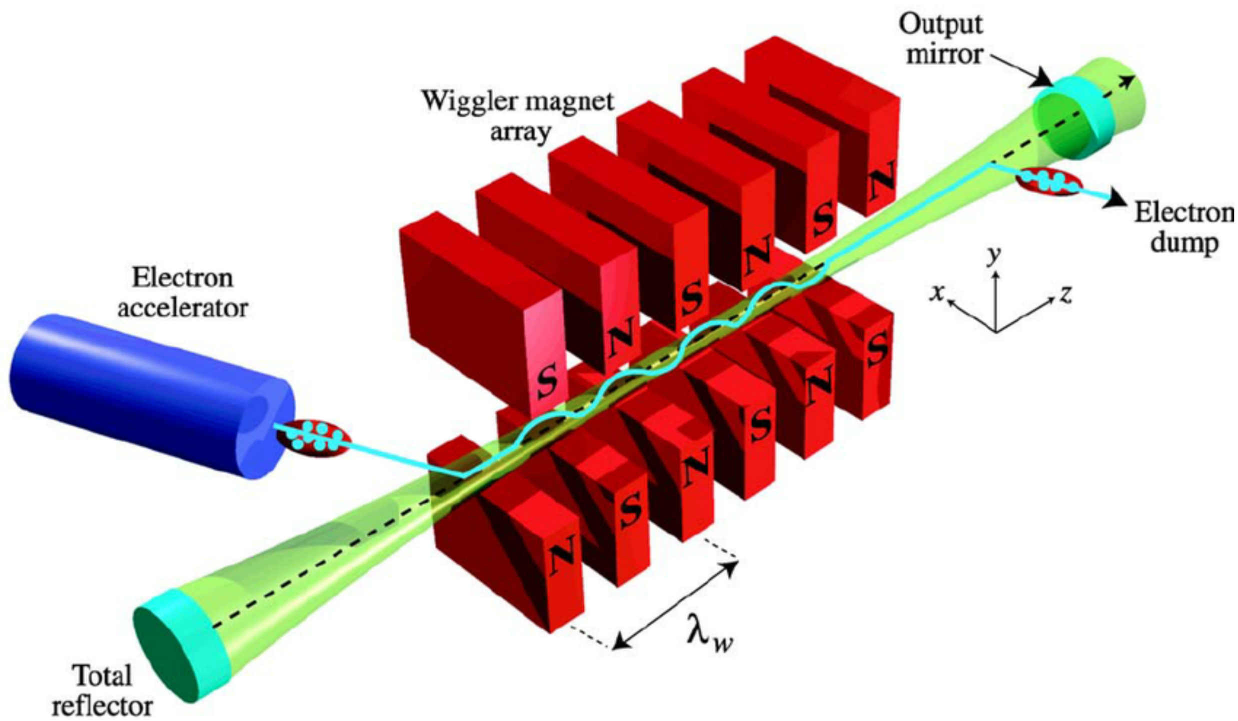

FIG. 18: Diagram of a free-electron laser [47].

field depending on the location of the particle with respect to the to the phase of the external radiation field [38, 41, 48, 49].

This model for FEL works well from infrared up to the ultraviolet regime, but the lack of a material that can reflect extreme ultraviolet and X-rays means that FELs must be modified to work around a mirror-less optical cavity. The X-ray FEL (XFEL) is therefore designed with an elongated undulator and no optical cavity. The entire emitted radiation must be generated through a single pass through the undulator magnet, so the desired emission brightness must be achieved in one pass. Self-amplified spontaneous emission (SASE) is the process by which these coherent, high-brilliance emissions are generated. When the electrons first enter the undulator they are distributed evenly and emit only incoherent spontaneous radiation. As the electrons interact with both the oscillating undulator magnetic field and the radiation that their own transverse motion creates, these fields force the electrons to drift into microbunches that are separated by a distance that approaches the exact wavelength of the emitted radiation. For a sufficiently long undulator, this interaction forces the electrons into an oscillatory motion that generates only coherent radiation. All emitted radiation reinforces itself. The electromagnetic waves emitted by the electrons and by the undulator become superimposed on one another. This results in an exponential increase of emitted radiation power, leading to high beam intensities and laser-like properties [50, 51, 52].

In the small gain regime of FEL operation,

$$G \propto -\frac{\mathrm{d}}{\mathrm{d}w}\left(\frac{\sin w}{w}\right)^2. \tag{12}$$

w is defined

$$w = 2\pi h N_\mathrm{p}\frac{\gamma - \gamma_\mathrm{r}}{\gamma_\mathrm{r}}, \tag{13}$$

where h is the harmonic of the radiation frequency, N_p is the total number of wavelengths in the undulator magnet, and γ_r is the resonance energy of the undulator

$$\gamma_\mathrm{r}^2 = \frac{\gamma^2}{h}. \tag{14}$$

In the high-gain regime,

$$I_\mathrm{ph} \propto I_0 \exp\left(\frac{z}{L_\mathrm{G}}\right), \tag{15}$$

where z is the position along the length of the undulator, L_G is the power gain length, and I_0 is the spontaneous coherent intensity for and undulator of length L_G.

CHAPTER 3

AN OVERVIEW OF COMPTON AND THOMSON SCATTERING

A brief overview of the fundamental physics underlying the mechanics of Compton scattering is presented in this chapter. Later chapters present the computational models that make up the primary focus of this work: the theoretical basis of each model will be derived from first principles, and then the numerical methods utilized by the computational models will also be presented in great detail. In this chapter the physics principles common to both models are discussed in order to build a foundation of understanding for the discussions that will come later. The basic parameters that characterize the electron beam and laser pulse are defined here.

The collision geometry is discussed first. The calculations required to compute the simulated spectra occur in several frames of reference: most notably the lab frame in which the observer resides and the relativistic beam frame in which the electrons reside. The coordinate systems used in the computations later is clearly and concisely defined here.

This discussion begins by clearly defining Thomson and Compton scattering. It shows how the work presented here depends directly on the early work of these Nobel Prize winners, both of whom are shown in Figure 19. These two regimes of photon-electron collisions, which still bear the names of these physics titans, are compared and contrasted. Understanding Thomson and Compton scattering is critical to understanding the computational models presented in this work.

The most important parameters of the incident laser pulse are discussed in this chapter as well. First the field strength parameter, a constant that scales with the square root of the laser pulse intensity, a is defined. The field strength parameter is critical to simulating the photon-electron collisions as it used to predict complicated, nonlinear effects that arise from Compton scattering from a high-intensity laser pulse. The field strength parameter is also defined here, and the nonlinear effects will be discussed in detail in Chapter 5.

The second important parameter of the incident laser pulse is its transverse width, i.e., the dimension of the laser pulse fields perpendicular to the photons trajectory. In the simplest treatment, the plane-wave approximation, this width is infinite, and the amplitude of the vector potential does not depend upon transverse position. A more sophisticated treatment of the field in which the laser pulse has finite transverse width is also presented in this work. The different treatments of the incident laser fields used by the computational models is clearly defined in this section.

The models in this work are limited to photon-electron collisions in which only one photon is emitted. The conditions for single photon emissions are discussed in this chapter. Developing the theoretical basis for incorporating multi-photon emissions, i.e., accounting for the radiation reaction, is a challenge that requires further research. Chapter 7 will offer suggestions for how to best attack this problem.

The different calculations presented in this work are derived from considering the scattered

FIG. 19: (left) Sir Joseph John Thomson, 1856-1940; (right) Arthur Holly Compton, 1892-1962 (Courtesy of the A.I.P. Niels Bohr Library)[11].

radiation from two very different perspectives. One way of viewing the photon-electron collision is through 4-vector conservation laws. In this perspective both the incident and scattered are treated as particles with 4-vector momentum. This method is necessary for capturing the electron recoil. The second perspective regarding the scattered radiation is to treat it as a field generated by the motion of a charged particle. This method is necessary to capture nonlinear effects that arise from a high intensity laser pulse. In this chapter, both perspectives will be presented. 4-vector momentum is used to define the angular frequency of the scattered photon in terms of the scattering parameters. An energy density equation for the general motion of a charged particle is also derived in this chapter. These discussions serves as a primer for the involved derivation of the computational models that will be discussed at length in Chapters 4 and 5. It is important to note that even thought these perspectives are quite different, the calculation derived from them reduce to equivalent expressions during in the appropriate limits. This is demonstrated in Chapter 6 when the computational models are used to replicate experimental data.

This chapter concludes with a discussion about the inherent sources of bandwidth in all Compton scattering events. Bandwidth (also referred to as "spread" in the scattered spectra) refers to the range of frequencies in which the photons are scattered. An ideal emission would be monochromatic, i.e., all scattered photons would have the same frequency. Since generating high-quality light sources demands that the scattered bandwidth is minimized, it is vitally important to understand the electron beam and laser pulse qualities that exacerbate bandwidth.

3.1 COLLISION GEOMETRY

A general layout of the collision between an electrons and photons is shown in Figure 20. The positive z-axis is defined by the trajectory of the electron beam. The origin is generally fixed at the point of the photon-electron collision. The scattered photon trajectory is defined by the polar angle θ and the azimuthal angle ϕ. In some of the calculations presented later in the work, however, the photon-electron collision will be slightly offset from the origin of the lab frame. This offset is referred to as the source size. This source size is much, much smaller than the distance from the collision to the observer in all of the cases presented in this work, so for simplicity the source will be treated as zero. The correction to this approximation will be presented in the appendix to show that the correction to the spot size treatment is a very high order correction indeed.

The angle between the electron trajectory and the laser beam is Φ. When Φ is near zero, the laser pulse and the electron beam are moving in nearly the same direction: along the z-axis. Side scattering occurs when the two beams are near perpendicular, i.e., $\Phi \approx \pi/2$. The head-on orientation is most often used in Compton radiation sources since these collisions yield a greater intensity of scattered, high-energy photons within a narrow spectral bandwidth. Additionally, most of the calculation presented here will use an incident laser pulse that is linearly polarized in the x direction. For all values of Φ it is important to align the sensor aperture in the direction of the electron beam, i.e., the aperture must be located on the positive z-axis. The light scattered off a relativistic electron beam strongly favors the direction of the electron beam. In fact, the majority

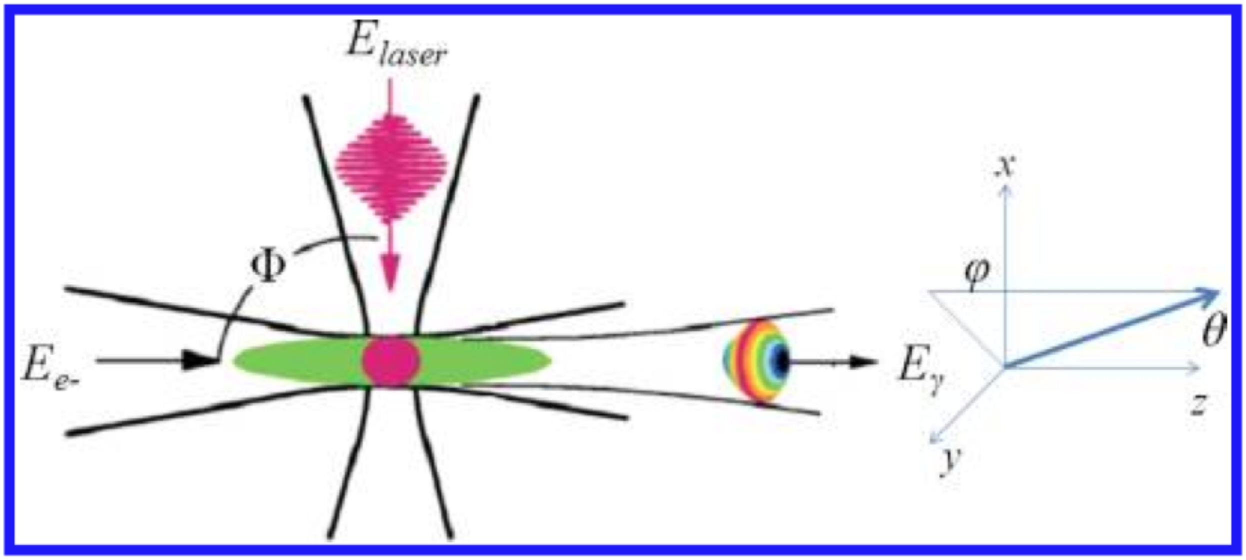

FIG. 20: This diagram shows a laser pulse of photon energy E_{laser} incident on an electron of energy E_{e-} that travels along the z-axis. E_γ is the energy of the scattered photon whose trajectory is expressed by the angles ϕ and θ [53].

of the photons will be scattered through a cone whose side makes an angle $1/10\gamma$ with electron trajectory.

3.2 THOMSON VERSUS COMPTON SCATTERING

Toward the end of the 19$^{\text{th}}$ century, as the scientific world grappled with the particle-wave duality of cathode-rays and X-rays, J.J. Thomson observed that a moving electric field accelerates charged particles. In Thomson scattering a charged particle is subject to the electric field of a propagating electromagnetic wave. This oscillating field causes the the charged particle to oscillate at the same exact frequency as the passing electric field. This induced oscillation causes the charged particle to emit dipole radiation that is, again, at the same frequency as the incident field. Thus the electromagnetic waves are scattered off the charged particle. Thomson was the first to classically calculate the radiation emitted by this acceleration [54, 55, 11]. The spectral energy density for a Thomson scattering event involving a head-on collision between a relativistic electron beam and the laser (crossing angle $\Phi = \pi$)is well-documented [53]:

$$\frac{d^2 E_\gamma}{d\omega' d\Omega} = \frac{r_e^2 \epsilon_0}{2\pi c} \left|\tilde{E}(k')\right|^2 \frac{\sin^2\phi\,(1-\beta\cos)^2 + \cos^2\phi\,(\cos\theta - \beta)^2}{\gamma^2\,(1-\beta\cos\theta)^4}, \tag{16}$$

where $k' = k(1-\beta\cos\theta)/(1+\beta)$, r_e is the classical electron radius and $\tilde{E}(k')$ is the Fourier transform of the electric field as a function of the angular frequency of the incident photon.

These observed properties of Thomson scattering, however, only hold for photon-electron collisions that occur at relatively low energies. In Thomson scattering, the momentum loss for the electron is nearly zero, i.e., the electron sustains no recoil. In order to quantify the bounds of Thomson scattering we define the unitless parameter X [57]

$$X = \frac{4E_e E_L}{(mc^2)^2}, \tag{17}$$

where E_e is the energy of the electron, E_L is the energy of the photon, m is the electron mass and c is the speed of light. Thomson scattering occurs when $X \ll 1$. This known as the Thomson regime (or the classical limit).

As X increases the electron recoil can no longer be neglected. A.H. Compton collaborated with J.J. Thomson at Cambridge's Cavendish Laboratory to study photon-electron collisions with high-energy photons. In the experiment, X-rays were scattered off stationary targets. The spin averaged differential cross section was measured to be [58]

$$\frac{d\sigma}{d\Omega} = \frac{r_e^2}{2}\left(\frac{\omega'}{\omega}\right)^2\left[\frac{\omega'}{\omega} + \frac{\omega}{\omega'} - \sin^2\theta\right], \tag{18}$$

which gives the probability that a photon would be scattered into a given solid angle $d\Omega$. They also deduced the relationship between the incident and scattered photon angular frequency to be

$$\omega' = \frac{\omega}{1 + \frac{\omega\hbar}{mc^2}(1-\cos\theta)}, \tag{19}$$

in contrast to the classical result, $\omega' = \omega$. As the energy of the incident X-ray was increased, the energy of the scattered photon began to develop a dependence upon the scattering angles as shown in Figure 21. As the collision energies grow beyond the classical limit, the 4-vector momentum analysis must be introduced to account for the electron recoil. Section 3.6 introduces the 4-vector analysis used in this work in much greater detail [59].

In contrast to the the full Compton calculation, the recoil of the electron due to the momentum transfer from the photon may be neglected in the Thomson calculation. In other words, the Thomson regime is a specific, energy-limited case of Compton scattering. Since Thomson scattering maybe thought of as a subset of Compton scattering, it is common practice to refer to all accelerator-based photon-electron collisions and Compton scattering events.

3.3 FIELD STRENGTH PARAMETER: LINEAR VERSUS NONLINEAR

A photon moving through space has an electromagnetic field that accelerates electrons and other charged particles. The acceleration of the electron is related to the photon density by the

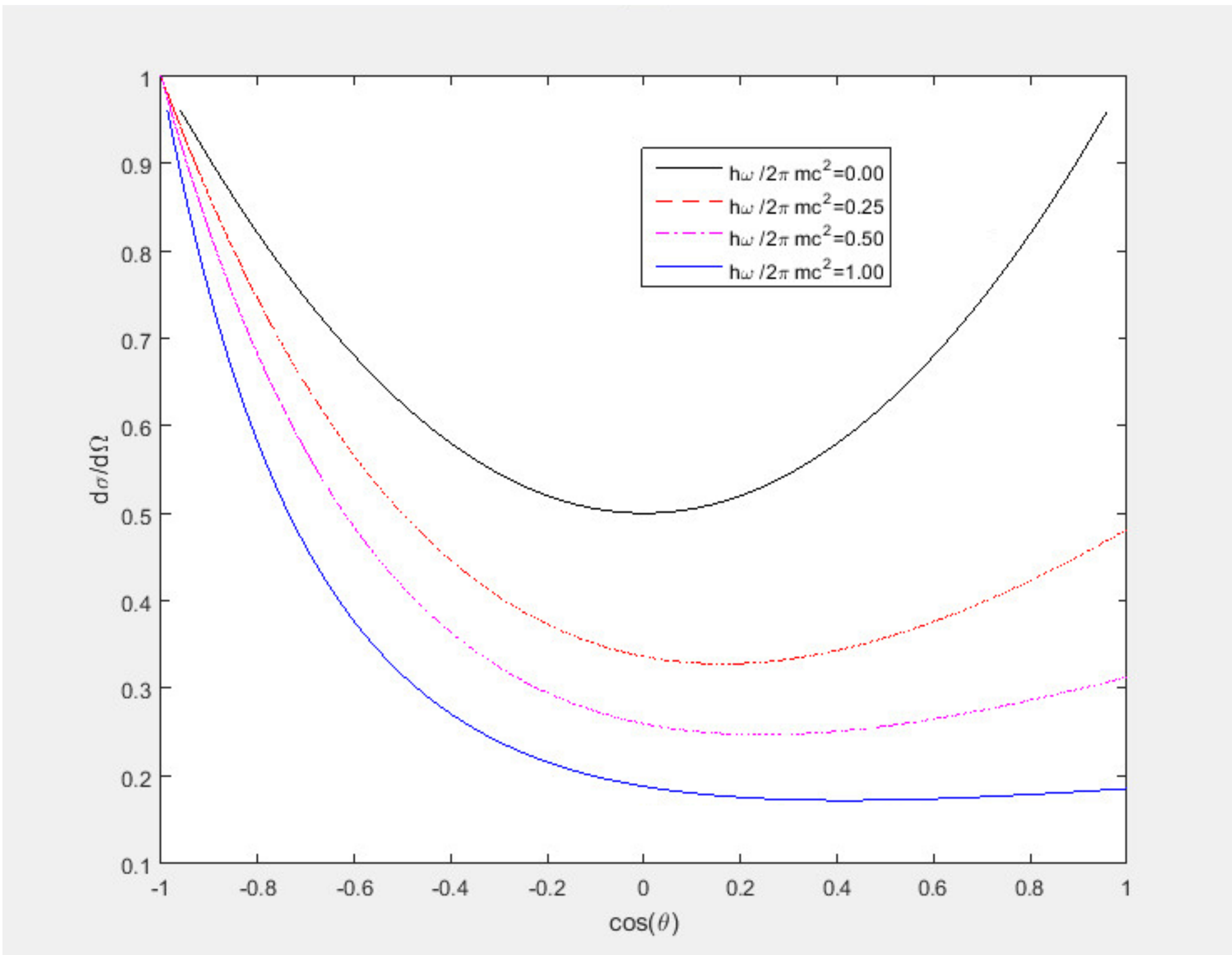

FIG. 21: Spin averaged differential cross-section for Compton scattering as a function of $X = 4E_e\hbar\omega/(mc^2)^2$ [56].

field strength parameter, a_0 [60]:

$$a_0 \equiv \frac{eA_0}{mc}. \tag{20}$$

Here, e is the fundamental charge and A_0 is the maximum amplitude of the vector potential of all the photons. This unitless parameter gives the normalized, transverse vector potential for the photon plane-wave, and it scales with the square root of the intensity of the laser pulse. In terms of the electric field of the laser

$$a_0 \equiv \frac{eE_0\lambda}{2\pi mc^2}, \tag{21}$$

where λ is the incident laser wavelength and E_0 is the maximum amplitude of the electric field. The total energy of the laser pulse scales with the normalized length of the laser pulse σ times the square of the field strength parameter $E_{ph\,total} \propto a_0^2\sigma$. In general, the field strength parameter should be expressed locally, i.e., with a spatial dependence such as $a(\xi = z + ct)$, but most often it is treated as a peak amplitude envelope for an oscillating function. The magnitude of the field strength parameter divides photon-electron collisions into two regimes: the linear regime, where $a_0 \ll 1$, and the nonlinear regime for all other values of a_0. As the intensity of the laser pulse increases, the field strength causes the electron to oscillate at relativistic velocities. This induced relativistic motion causes several nonlinear effects to occur in the scattered spectra including substantial ponderomotive broadening. These problematic nonlinear effects will be addressed in Chapter 5.

3.4 TREATMENT OF THE INCIDENT LASER FIELDS

In these simulations, the laser pulse is either modeled as a 1D plane-wave or as a 3D laser pulse. The simplest method, i.e., the plane-wave approximation, is used in the earlier models. The normalized vector potential is defined:

$$\tilde{A}(\xi) = \frac{eA(\xi)}{mc} = a(\xi)\cos\left(\frac{2\pi\xi}{\lambda}\right), \tag{22}$$

where $a(\xi)$ is the laser envelope. As shown by Eq. (22), the field does not depend on the transverse position of the electron. This approximation may be used whenever the transverse size of the laser pulse is far greater than the spot size of the electron beam.

Since infinite plane-waves do not, in fact, exist in particle accelerators, the 3D laser pulse model is a much more comprehensive modeling method for calculating scattered spectra. A 3D approximation of the laser pulse may be expressed in terms of vector potential in a form similar to Eq. (22) by simply allowing the laser envelope to have a three dimensional dependence, i.e., $a(\xi) \to a(x, y, z)$. Within this work, however, the phase of the vector potential is not dependent upon the transverse coordinates. The phase only depends upon the parameter ξ.

3.5 REGIMES OF OPERATION

It has been the purpose of this work to develop a comprehensive computational model to calculate the the radiated spectra for Compton sources. As previously discussed, Compton scattering events can be generally classified by two parameters: the energy of the electron beam and the intensity of the laser pulse. As shown in Figure 22, photon-electron collisions with a relatively low laser intensity, i.e., with a relatively low field strength parameter a_0, are described as linear, while collisions with higher intensities are nonlinear. Photon-electron collisions with relatively low electron beam energy, i.e. with a relatively low Lorentz factor γ, are called Thomson scattering events while collisions with high electron energy are called Compton scattering events (It is, however, common practice to broadly refer to all of these types of photon-electron collisions as Compton scattering regardless of the electron beam energy). Two unique computational models have been developed to operate in specific regimes of operation. The first model derived from conservation laws simulates photon-electron collisions in the linear Thomson and Compton regimes; this first model is valid for collisions that fall into sections I and IV of Figure 22. The second model derived by solving the Hamilton-Jacobi for the electron's equations of motion simulates photon-electron collisions in the linear and nonlinear Thomson regime; this second model is valid for collisions that fall into sections I and II of Figure 22.

The number of photons emitted per electron is another important consideration that further divides the operational regimes of Compton scattering models. The models presented in this work are limited to a single photon emission per collision event. Two parameters must be limited in order to ensure that only photon is emitted: the field strength parameter and the duration of the laser pulse. A higher intensity of the incident laser pulse increases the probability that multiple photons from that field will interact with the electron. The probability for multiple collisions and emissions also increases with the duration of time that the electron is subjected to the incident field. The regime of operation in which only one photon is emitted form the collision event is explicitly defined by the inequality

$$a_0 < \sqrt{\frac{3\lambda_0}{2\sqrt{\pi}\alpha\sigma_{l,z}}}, \tag{23}$$

where λ_0 is the wavelength of the incident photon, α is the fine structure constant, and $\sigma_{l,z}$ is the longitudinal length of the laser pulse. As multiple photons are emitted from the electron, the recoil of the electron becomes significant. As a result, the scattered radiation is emitted into broader ranger of angular frequencies. The green line at n_γ in Figure 22 denotes the boundary between the single and multiple photon emission regimes of operation. Ongoing efforts will be required to expand the operation of these computational model into the nonlinear Compton regime.

3.6 4-VECTOR PHOTON-ELECTRON COLLISIONS

In relativistic photon-electron collisions, the dependence of the scattered angular frequency upon the scattering angle that Compton observed can be understood through a 4-vector analysis of the collision. In this section, the angular frequency will be calculated for a simple model in which one electron collides with a photon in a true backscattering orientation, i.e., the electron has no

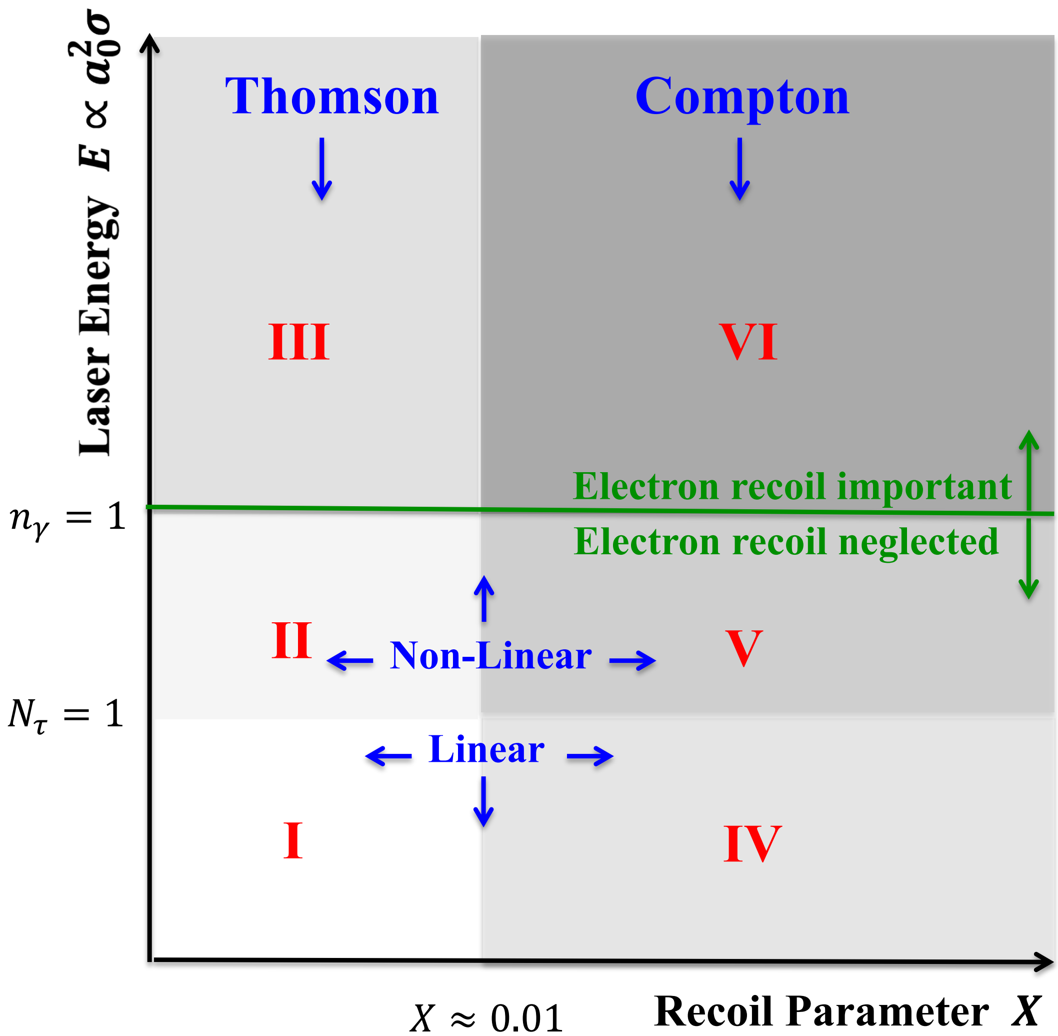

FIG. 22: Regimes of operation of inverse Compton sources, given in terms of the electron recoil parameter X on the horizontal axis, and the total energy of the laser $E \propto a_0^2\sigma$ [61].

transverse motion, and the photon collides withe the electron head-on. The analysis presented here will serve two purposes: it will concisely demonstrate the the 4-vector analysis that will be used at length later while touching base with the well-documented results of A.H. Compton. A more general scattered angle will be calculated in Chapter 4.

Before proceeding, let us define the vector notation that will be used in this work. The notation for vectors in three dimensional space will be bold font and italicized, e.g., $\boldsymbol{a}$ is some vector in three dimensional space. The 4-vector notation will be bold font with no italics, e.g., $\mathbf{a}$ is some 4-vector. With this notation the 4-vector $\mathbf{a}$ is defined

$$\mathbf{a} = (a_t, \boldsymbol{a}) = (a_t, a_x, a_y, a_z)\,, \tag{24}$$

where a_t is the time component of the 4-vector and $a_{x,y,z}$ are the space components of the 4-vector. 4-vector multiplication for any two general 4-vectors $\mathbf{a}$ and $\mathbf{b}$ is defined

$$\mathbf{a} \cdot \mathbf{b} = a_t b_t - \boldsymbol{a} \cdot \boldsymbol{b} = a_t b_t - (a_x b_x + a_y b_y + a_z b_z)\,. \tag{25}$$

Consider first the energy-momentum four-vector before the collision of a single photon from the laser pulse,

$$\mathbf{k} = \left(\frac{\hbar\omega}{c},\ 0,\ 0,\ -\frac{\hbar\omega}{c}\right), \tag{26}$$

and the four-vector of a single electron from the beam,

$$\mathbf{p} = (E_e/c, \boldsymbol{p_e}) = (\gamma mc,\ 0,\ 0,\ -\gamma\beta mc)\,, \tag{27}$$

where $\boldsymbol{p_e}$ is the relativistic 3-vector momentum of the electron before the collision, m is the electron mass, $\hbar$ is the reduced Planck's constant, and γ and β are the conventional relativistic variables

$$\gamma = \frac{E_e}{mc^2}, \tag{28}$$

where E_e is the relativistic energy of the electron, and

$$\beta = \sqrt{1 - \frac{1}{\gamma^2}}. \tag{29}$$

After the collision, the scattered photon has momentum

$$\mathbf{k}' = \left(\frac{\hbar\omega'}{c},\ \frac{\hbar\omega'}{c}\sin\theta\cos\phi,\ \frac{\hbar\omega'}{c}\sin\theta\sin\phi,\ \frac{\hbar\omega'}{c}\cos\theta\right), \tag{30}$$

and the electron has the momentum

$$\mathbf{p}' = (E_e'/c, \boldsymbol{p_e'}), \tag{31}$$

where E_e' is the energy of the electron after the collision and $\boldsymbol{p_e'}$ is the relativistic 3-vector momentum of the electron after the collision. E_e also satisfies

$$E_e^2 = |\boldsymbol{p_e}|^2 c^2 + m^2 c^4. \tag{32}$$

By the law of conservation of momentum the total initial momentum must equal the total scattered momentum:

$$\mathbf{p} + \mathbf{k} = \mathbf{p}' + \mathbf{k}', \tag{33}$$

which can be rewritten as

$$\mathbf{p}' = \mathbf{p} + \mathbf{k} - \mathbf{k}'. \tag{34}$$

Taking the square of each side of Eq. (34) under four-vector multiplication yields

$$\mathbf{p}' \cdot \mathbf{p}' = \mathbf{p} \cdot \mathbf{p} + \mathbf{p} \cdot \mathbf{k} - \mathbf{p} \cdot \mathbf{k}' + \mathbf{k} \cdot \mathbf{p} + \mathbf{k} \cdot \mathbf{k} - \mathbf{k} \cdot \mathbf{k}' - \mathbf{k}' \cdot \mathbf{p} - \mathbf{k}' \cdot \mathbf{k} + \mathbf{k}' \cdot \mathbf{k}'. \tag{35}$$

All of these product may be calculated:

$$\mathbf{k} \cdot \mathbf{k} = \mathbf{k}' \cdot \mathbf{k}' = 0, \tag{36}$$

$$\mathbf{p} \cdot \mathbf{k} = \gamma m \hbar \omega \left(1 + \beta\right), \tag{37}$$

$$\mathbf{p} \cdot \mathbf{k}' = \gamma m \hbar \omega' \left(1 - \beta \cos\theta\right), \tag{38}$$

$$\mathbf{k} \cdot \mathbf{k}' = \frac{\hbar \omega \omega'}{c^2} \left(1 + \cos\theta\right), \tag{39}$$

$$\mathbf{p} \cdot \mathbf{p} = m^2 c^2 \gamma^2 \left(1 - \beta^2\right) = m^2 c^2, \tag{40}$$

and

$$\mathbf{p}' \cdot \mathbf{p}' = E_e'^2 - \left|\boldsymbol{p_e'}\right|^2 = m^2 c^2. \tag{41}$$

Regrouping Eq. (35) produces

$$\mathbf{p}' \cdot \mathbf{p}' - \mathbf{p} \cdot \mathbf{p} = 2\left(\mathbf{p} \cdot \mathbf{k}\right) - 2\left(\mathbf{p} \cdot \mathbf{k}'\right) - 2\left(\mathbf{k} \cdot \mathbf{k}'\right), \tag{42}$$

and then substituting the products yields

$$0 = \gamma m \hbar \omega \left(1 + \beta\right) - \gamma m \hbar \omega' \left(1 - \beta \cos\theta\right) - \frac{\hbar^2 \omega \omega'}{c^2} \left(1 + \cos\theta\right). \tag{43}$$

Solving Eq. (33) for ω' gives

$$\omega' = \frac{\omega \left(1 + \beta\right)}{1 - \beta \cos\theta + \frac{\omega \hbar}{\gamma m c^2} \left(1 + \cos\theta\right)}. \tag{44}$$

Recall from Section 3.2 that this expression is in agreement with Compton's original calculation in Eq. (19) within the limit of a stationary, non-relativistic electron, i.e., $\gamma \to 1$ and $\beta \to 0$. Here, the usual $(1-\cos\theta)$ from Compton's formula for scattering from a stationary target becomes $(1+\cos\theta)$ in the backscattered geometry [59, 2].

3.7 ENERGY DENSITY SPECTRUM RADIATED BY AN ACCELERATED CHARGE

The radiation generated by a moving charge particle may be expressed as the energy per scattering frequency per solid angle into which the radiation is scattered [58]

$$\frac{\mathrm{d}^2 E'}{\mathrm{d}\omega' \mathrm{d}\Omega} = \frac{e^2 \omega'^2}{16\pi^3 \epsilon_0 c^3} \left| \int_{-\infty}^{\infty} \mathbf{n} \times (\mathbf{n} \times \boldsymbol{\beta})\, e^{i\omega(t - \mathbf{n}\cdot\mathbf{r}(t)/c)}\, \mathrm{d}t \right|^2, \tag{45}$$

where E' is the radiated photon energy, ω' is the angular frequency of the radiated photons, $\mathrm{d}\Omega$ is the solid angle into which the photons are radiated, e is the charge of the particle, c is the speed of light, $\boldsymbol{n}$ is the unit vector of the observation vector, and $\boldsymbol{\beta}$ is the relativistic velocity of the particle. The the vectors in the expression are defined geometrically in Figure 23, where $\boldsymbol{\beta} = \dot{\boldsymbol{r}}/c$. This expression is an energy density spectrum. The spectrum radiated by the charged particle may be found by integrating an energy density spectrum of an area of interest. The total emitted spectrum may be found by integrating a spherical shell around the origin. For the purpose of this work, the integration will be computed over the area of a sensor aperture.

3.8 INHERENT SOURCES OF BANDWIDTH IN COMPTON SCATTERING

In this section, the innate sources of spread in all Compton scattering events will be introduced. While these sources of spread may be found in all Compton scattering, different regimes of operation may present sources of bandwidth unique to their specific regime. Regime-specific sources of spectral broadening will be discussed in Chapters 4 and 5.

There are four basic sources of energy spread in the scattered pulse: (i) energy spread in the electron beam σ_{E_e}/E_e, (ii) energy spread in the incident laser photons σ_{E_p}/E_p(this distribution is known as the incident laser linewdith), (iii) energy spread from the limited solid angle of the aperture of the scattered photon sensor σ_a/E_a, and (iv) energy spread due to the transverse momentum of the electrons within beam $\sigma_\epsilon/E_\epsilon$. The total inherent broadening in any Compton-scattered spectra can be approximated [57, 62],

$$\frac{\sigma_{E'}}{E'} = \sqrt{\left(\frac{\sigma_{\theta_{\mathrm{MAX}}}}{E_{\theta_{\mathrm{MAX}}}} + \frac{\sigma_\epsilon}{E_\epsilon}\right)^2 + \left(\frac{\sigma_L}{E_L}\right)^2 + \left(\frac{\sigma_\gamma}{E_\gamma}\right)^2}, \tag{46}$$

where $\sigma_{\theta_{\mathrm{MAX}}}/E_{\theta_{\mathrm{MAX}}}$ is the spread from the maximum aperture opening, $\sigma_\epsilon/E_\epsilon$ is the spread from emittance, σ_L/E_L is the spread from the longitudinal photon spread, and σ_γ/E_γ is the energy spread in the electron beam. The spectral broadening due to the electron beam energy spread is doubled due to the γ^2 dependence of the scattered radiation in the forward direction, i.e. when $\theta = 0$. The effect of varying electron energy spread on the emitted photon spectra is illustrated in

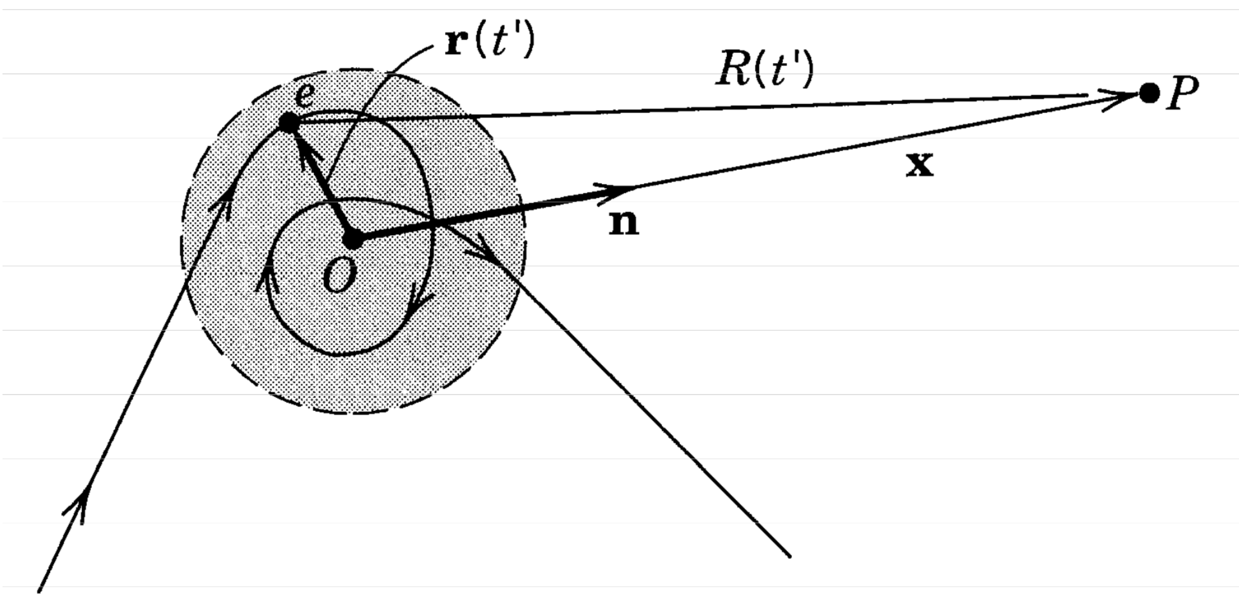

FIG. 23: This diagram defines the geometry in Jackson's general expression for the energy density spectrum generated by the motion of a charge particle. The origin is at O and the observation is taken at point P. The position vector of the observation point is $\boldsymbol{x}$ and the unit vector of the observation. vector is defined as $\boldsymbol{n}$. The vector $\boldsymbol{r}$ is the vector from the origin to the charge. The vector $\boldsymbol{R}$ is from the charge to the observation point [58].

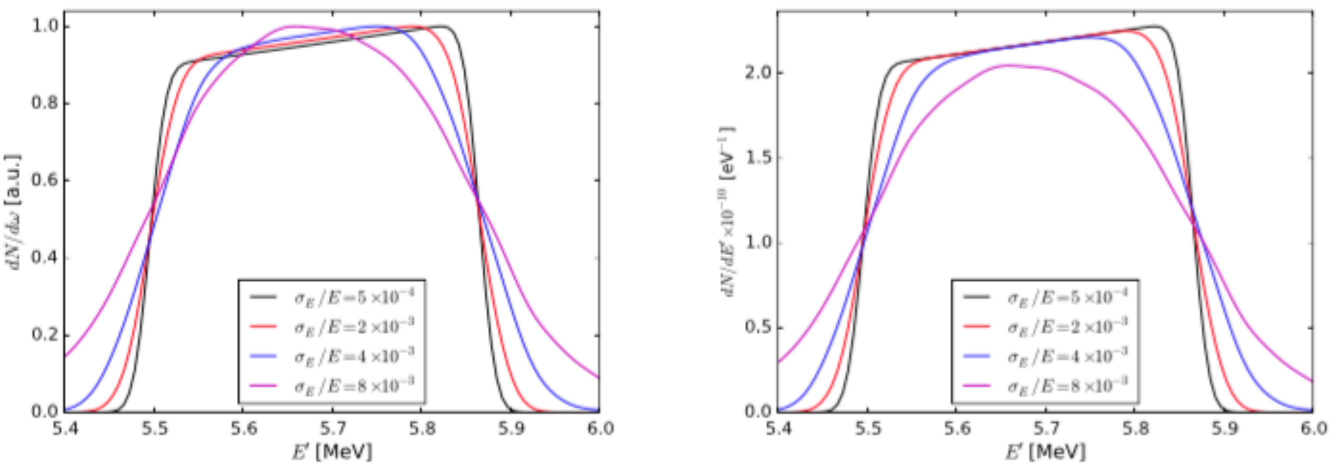

FIG. 24: The number density of the energy spectrum of a Compton gamma-ray beam produced by the head-on collision of a 500 MeV electron with a 800 nm pulsed laser beam, for different relative energy spread of the electron beam σ_E. The laser is collimated by an aperture with radius of 16 mm, placed 60 m downstream from the collision point. The horizontal emittance ϵ_E is held constant at 0.05 nm rad. Here a Gaussian laser pulse with $\sigma = 50$ is used. Each curve is generated by averaging 400 electrons sampling the prescribed distribution. Left panel: Spectra scaled to their respective peak values. Right panel: Spectra in physical units [2].

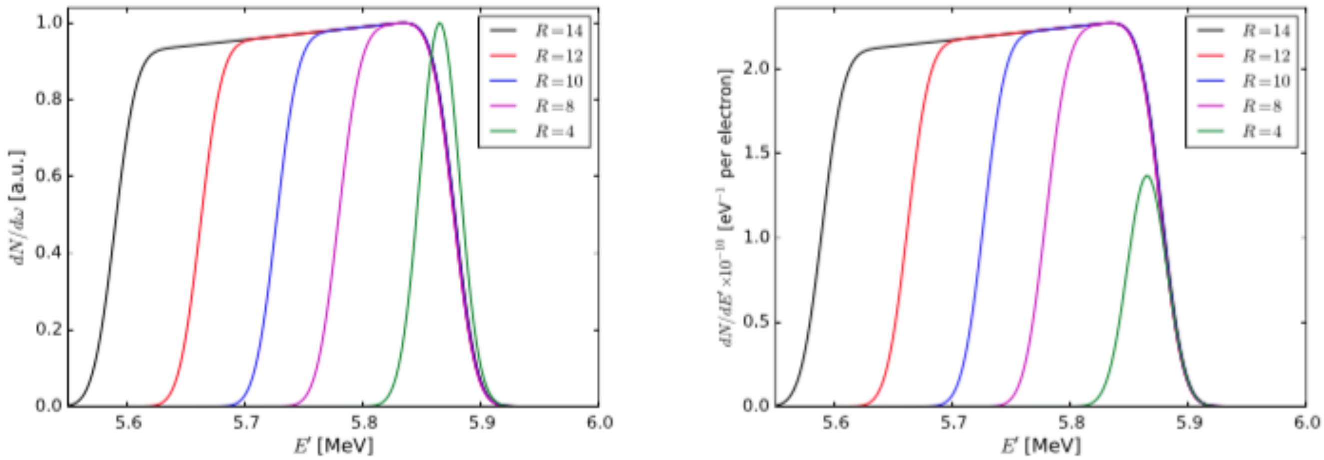

FIG. 25: The number density of the energy spectrum of a Compton gamma-ray beam produced by the head-on collision of a 500 MeV electron with a 800 nm pulsed laser beam, for different radii R of the collimation point (in mm). The aperture is 60 m downstream from the collision point. The horizontal emittance and energy spread of the electron beam are held constant at 0.05 nm rad and 2×10^3, respectively. Here a Gaussian laser pulse with $\sigma = 50$ is used. Each curve is generated by averaging 400 electrons sampling the prescribed distribution. Left panel: Spectra scaled to their respective peak values. Right panel: Spectra in physical units [2].

Figure 24.

The energy spread in the scattered photons due to the incident laser linewidth is equivalent to the relative energy spread in the laser linewidth itself. This is due to the double Doppler upshift of the emissions observed in any solid angle. In the specific case of a longitudinal Gaussian photon distribution in the incident pulse, the spectral broadening may be calculated

$$\frac{\sigma_{E_L}}{E_L} = \frac{1}{2\sqrt{2}\pi\sigma}, \tag{47}$$

where σ is the longitudinal variance in the Gaussian distribution of the incident photons.

The energy spread due to a circular, on-axis aperture is a function of the most energetic frequency $\omega'_{\rm max}$ and least energetic frequency $\omega_{\rm min}$ emitted through the opening:

$$\frac{\sigma_{\theta_{\rm MAX}}}{E_{\theta_{\rm MAX}}} = \frac{\omega'_{\rm max} - \omega'_{\rm min}}{\sqrt{12}\omega'_{\rm mid}}, \tag{48}$$

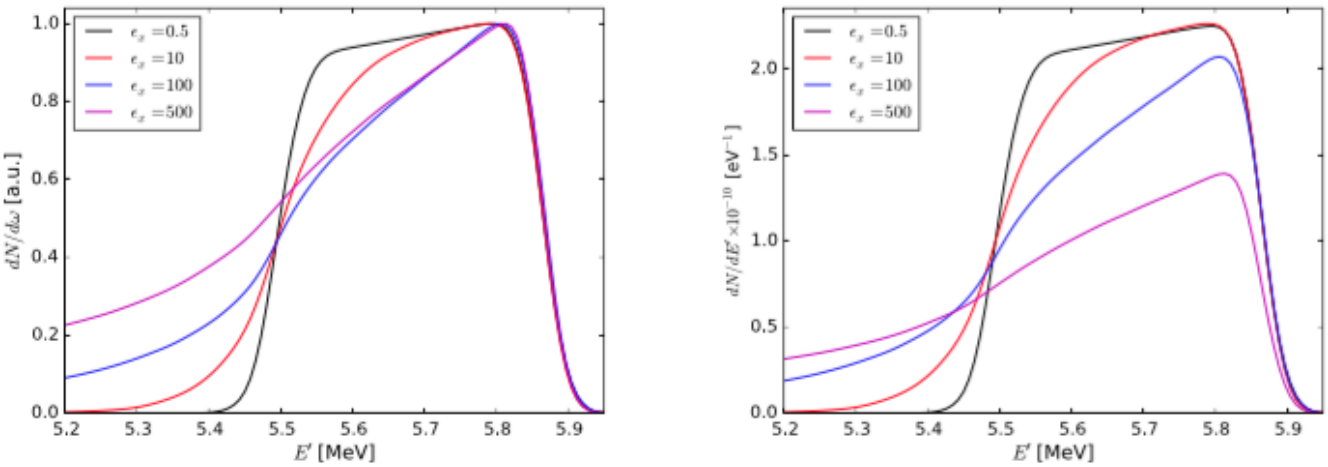

FIG. 26: The number density of the energy spectrum of a Compton gamma-ray beam produced by the head-on collision of a 500 MeV electron with a 800 nm pulsed laser beam, for different horizontal emittances ϵ_x. The laser is collimated by an aperture with radius of 16 mm, placed 60 m downstream from the collision point. The relative energy spread of the electron beam σ_E is held constant at 2×10^3. Here a Gaussian laser pulse with $\sigma = 50$ is used. Each curve is generated by averaging 400 electrons sampling the prescribed distribution. Left panel: Spectra scaled to their respective peak values. Right panel: Spectra in physical units [2].

where

$$\omega'_{\text{max}} = \omega'(\theta = 0) = \frac{\omega(1+\beta)}{1 - \beta + (2\hbar\omega/\gamma mc^2)}, \tag{49}$$

$$\omega'_{\text{min}} = \omega'(\theta = \theta_a) = \frac{\omega(1+\beta)}{1 - \beta\cos(\theta_a) + (\hbar\omega/\gamma mc^2)(1 + \cos(\theta_a))}, \tag{50}$$

and

$$\omega'_{\text{mid}} = \frac{(\omega'_{\text{max}} + \omega'_{\text{min}})}{2}. \tag{51}$$

the factor of $1/\sqrt{12}$ in Eq. (48) represents the RMS width of a variable uniformly distributed between 0 and 1. The effect of varying the aperture on the emitted photon spectra is illustrated in Figure 25.

The last source of emission broadening is generated by the electron beam emittance, or the transverse motion of the electrons relative to the propagation of the electron beam. This energy spread arises from the angle dependence of the Doppler shift in the scattered photons which, in turn, causes the forward radiation through the aperture to be red-shifted. It is calculated by

$$\frac{\sigma_\epsilon}{E_\epsilon} = \sqrt{\left(\frac{\sigma_{\epsilon_x}}{E_{\epsilon_x}}\right)^2 + \left(\frac{\sigma_{\epsilon_y}}{E_{\epsilon_y}}\right)^2} = \sqrt{2}\gamma\sqrt{\left(\frac{\epsilon_x}{\beta_x^*}\right)^2 + \left(\frac{\epsilon_y}{\beta_y^*}\right)^2}, \tag{52}$$

where ϵ is the emittance and β^* is is the electron beta function at the point of collision. The electron beta function describes the amplitude of the electrons displacement as it oscillates about its orbit in the accelerator. In the case of a circular beam in which the the vertical emittance and horizontal emittance are equal, Eq.(52) reduces to

$$\frac{\sigma_{E_\epsilon}}{E_\epsilon} = \frac{2\gamma^2\epsilon}{\beta^*}. \tag{53}$$

Unlike the other sources of energy spread discussed, the broadening from emittance generates an asymetrical low-energy tail. The effect of varying electron emittance on the emitted photon spectra is illustrated in Figure 26.

CHAPTER 4

LINEAR COMPTON SCATTERING

In this chapter, we introduce a model which simulates the radiation emitted through the head-on collision of a visible light laser pulse and a high-energy, relativistic electron beam. Both the energy and scattered angle of the photons after the collision have probabilistic distributions. These distributions can be calculated via the energy density spectrum [2]:

$$\frac{\mathrm{d}^2 E'}{\mathrm{d}\omega' \mathrm{d}\Omega} = \frac{\epsilon_0 c}{2\pi} \left| \tilde{E}\left(\omega\left(\omega'\right)\right) \right|^2 \frac{\mathrm{d}\sigma}{\mathrm{d}\Omega} \left[\frac{\omega'}{\omega} \frac{\mathrm{d}\omega}{\mathrm{d}\omega'} \right], \tag{54}$$

where ϵ_0 is the permittivity of free space, c is the speed of light, $\tilde{E}(\omega(\omega'))$ is the space Fourier transform of the electric field of the incident laser pulse, ω' and ω are the scattered and incident photon angular frequencies, respectively, and $\mathrm{d}\sigma/\mathrm{d}\Omega$ is the differential cross section for Compton scattering.

Imagine that the collision of a single electron and a single photon is centered inside a spherical shell. The photon enters the shell through the north pole and the electron enters the shell through the south pole. The energy density spectrum maps both the energy of the scattered photon and also the likelihood of where the scattered photon will exit the spherical shell. The computational model presented here is able to predict the light spectrum generated through this type of photon-electron collision by integrating the energy density over the surface of this shell; more specifically, the model integrates Eq. (54) over a finite area on the surface of this shell where sensors are located. This energy density spectrum is not tractable analytically, so it is necessary to develop computational models to implement numerical methods to calculate these integrals.

This chapter begins with a brief discussion of the numerical methods implemented to compute the above energy density spectrum for the linear Compton regime. The energy density spectrum, Eq. (54), is then derived from first principles. The discussion continues on to an in-depth look at each component of the energy density spectrum. The angular frequency expressions are derived from a rigorous 4-vector momentum analysis of the photon-electron collision. The Klein-Nishina cross section is calculated generally for an electron with transverse momentum. This cross section is calculated for both linear and circular polarizations of the incident laser pulse. The incident laser field treatments are well-defined for both the plane-wave approximation and for fields with finite transverse size. This chapter concludes with a recalculation of the inherent sources of bandwidth that arise from the electron recoil that is specific to the high-energy photon-electron collisions of the Compton regime.

4.1 LINEAR COMPTON COMPUTATIONAL MODEL

This linear Compton computational model, called ICCS3D [2, 57], is coded in Python [63] and utilizes Cython [64] modules for computational efficiency. Likewise, the script takes full advantage of the Python multiprocessing library in order to run the calculations in parallel: the calculations are distributed across many processing cores and allowed to run simultaneously. The linear Compton spectra are generated by integrating Eq. (54) over the solid angle of a sensor aperture

$$\frac{\mathrm{d}E'}{\mathrm{d}\omega'} = \frac{\epsilon_0 c}{2\pi} \int\int_{\Omega} \left|\tilde{E}\left(\omega\left(\omega'\right)\right)\right|^2 \frac{\mathrm{d}\sigma}{\mathrm{d}\Omega} \left[\frac{\omega'}{\omega}\frac{\mathrm{d}\omega}{\mathrm{d}\omega'}\right] \mathrm{d}\Omega. \tag{55}$$

This double integral is computed numerically using the `dblquad` quadrature function from Cython's scipy library. The integral is calculated for every single electron in the beam, and then summed. Because of the efficiency of both `dblquad` and the parallel processing features of Python, the non-analytic integral in Eq. (55) may be computed for tens of thousands of electrons in a matter of minutes.

4.2 DERIVATION OF THE ENERGY DENSITY SPECTRUM

In this section, the energy density spectrum resulting from inverse Compton scattering in the linear regime is derived from first principles. As with nearly all of the Compton scattering calculations presented in this work, this derivation proceeds form the backscattering orientation in which a relativistic electron beam collides head-on with a laser pulse. The recoil of the high-energy electron will be calculated via conservation laws. Since this is a linear regime calculation for a low-intensity laser pule, the electron oscillates in its own average rest frame at the frequency of the incident laser pulse, i.e., the electron emits dipole radiation by the same mechanism originally observed by J.J. Thomson. Additionally, this energy density spectrum calculation requires that each electron is permitted to emit only one photon. This limits both the intensity and the duration of the incident laser pulse. A plane-wave approximation is assumed for the incident laser such that the phase of the photon fields is independent from the position perpendicular to the trajectory of photon propagation. The amplitude of the incident photons, however, may depend on the transverse position. This allows for scattering simulations in which a laser pulse with finite transverse dimensions may be modeled.

The development of this novel energy density spectrum is built upon a semiclassical treatment of the incident laser fields, a 4-vector analysis of the photon-electron collision, and a clever application of the Klein-Nishina cross section. In this derivation electron is first treated as object at rest in its own frame. Using this orientation, the Klein-Nishina cross section may be invoked to build a weighted probability density for the trajectory of the scattered photon. The Klein-Nishina and the change of frame required for this model is discussed at length in Section 4.4. As previously demonstrated in Section 3.6, the angular frequency of the scattered photon will be derived using conservation laws. This time, however, the solution will be generalized for an electron with any incident 3D momentum $\boldsymbol{p_e}$. This application of the conservation laws is crucial to this expression as it captures the recoil of the electron, i.e., it captures the effects upon the scattered spectrum that is unique to the Compton regime. The semiclassical treatment of the incident laser fields will be used to build a distribution of incident photon frequencies. Together these calculations will be used to build an expression that gives the total radiated energy scattered through a given solid angle Ω at a given frequency ω' [2].

The derivation begins by defining the fields of the incident laser pulse. As stated previously, the plane-wave approximation will be used where the electric field is generally defined

$$E_x(z,t) = -\frac{1}{2\pi}\int_{-\infty}^{\infty} i\omega\tilde{A}_x(\omega)e^{i\omega(z/c+t)}d\omega, \tag{56}$$

where $\tilde{A}_x$ is the Fourier transform of the vector potential. The derivation presented here is valid for any function $\tilde{A}(\omega)$, i.e., any field shape, that is true for Eq. (56). The power per unit area in the wave packet may be calculated

$$c\left[\frac{\epsilon_0}{2}E_x^2(z,t) + \frac{B_y^2(z,t)}{2\mu_0}\right] = \epsilon_0 c E_x^2(z,t). \tag{57}$$

Parseval's completeness relation is used to calculate the time-integrated intensity or energy per area in the pulse passing by an electron moving along the z-axis of the coordinate system [65]:

$$\int_{-\infty}^{\infty} E_x^2(z=0,t)dt = \frac{1}{2\pi}\int_{-\infty}^{\infty}\left|\tilde{E}_x(\omega)\right|^2 d\omega, \tag{58}$$

where $\tilde{E}(\omega)$ now denotes the Fourier time transform of the incident pulse. The incident energy per unit angular frequency per unit area is thus

$$\frac{\epsilon_0 c}{2\pi}\left|\tilde{E}_x(\omega)\right|^2 = \frac{\epsilon_0 c}{2\pi}\left|\omega\tilde{A}_x(\omega)\right|^2. \tag{59}$$

Within a quasiclassical analysis the number of incident photons per unit angular frequency per area is consequently

$$\frac{\epsilon_0 c}{2\pi}\frac{\left|\tilde{E}_x(\omega)\right|^2}{\hbar|\omega|}. \tag{60}$$

The number of scattered photons generated into a given solid angle $\mathrm{d}\Omega$ is

$$\frac{\mathrm{dN_{scat}}}{\mathrm{d}\Omega} = \int_{-\infty}^{\infty}\frac{\epsilon_0 c}{2\pi}\frac{\left|\tilde{E}_x(\omega)\right|^2}{\hbar|\omega|}\frac{\mathrm{d}\sigma}{\mathrm{d}\Omega}d\omega, \tag{61}$$

and, because the scattered photon has energy $\hbar\omega'$, the total scattered energy is

$$\frac{\mathrm{d}E'}{\mathrm{d}\Omega} = \int_{-\infty}^{\infty}\frac{\epsilon_0 c}{2\pi}\left|\tilde{E}_x[\omega(\omega')]\right|^2\frac{\omega'}{\omega}\frac{\mathrm{d}\sigma}{\mathrm{d}\Omega}d\omega, \tag{62}$$

where the Klein-Nishina differential cross section $\mathrm{d}\sigma/\mathrm{d}\Omega$ will be used in the computations. In any particular direction there is a unique monotonic relationship between ω' and ω and so a change of variables is possible yielding the energy density spectrum for the linear Compton model in Eq. (54):

$$\frac{\mathrm{d}^2 E'}{\mathrm{d}\omega' \mathrm{d}\Omega} = \frac{\epsilon_0 c}{2\pi} \left| \tilde{E}_x[\omega(\omega')] \right|^2 \frac{\mathrm{d}\sigma}{\mathrm{d}\Omega} \left[\frac{\omega'}{\omega} \frac{\mathrm{d}\omega}{\mathrm{d}\omega'} \right].$$

4.3 SCATTERED ANGULAR FREQUENCY

In this section the angular frequency of the Compton-scattered photon is derived from 4-vector conservation laws. This calculation is generalized for an electron with transverse momentum. This derivation proceeds in a similar fashion as the simpler on-axis-electron solution from Section 3.6, but the electron now has non-zero momentum in the x and y components. This progression is necessary as all accelerators produce electron beams with some emittance, and this transverse motion has a substantial impact upon the scattered spectrum. This calculation captures the effects unique to photon-electron collisions in the Compton regime. The first derivative of the incident angular frequency with respect to the scattered frequency, which is required to compute the linear Compton energy density spectrum, Eq. (54), is also calculated here.

As before the calculation begins by defining the 4-vector momentum of the incident photon

$$\mathbf{k} = \left(\frac{\hbar\omega}{c},\ 0,\ 0,\ -\frac{\hbar\omega}{c} \right) = \frac{\hbar\omega}{c} \hat{\mathbf{k}} = \frac{\hbar\omega}{c} (1, \hat{\boldsymbol{k}}). \tag{63}$$

The photon 4-vector is also defined in terms of the unit vector as this will be convenient for the proceeding calculation. After the collision, the scattered photon momentum is defined by the polar scattering angles

$$\mathbf{k}' = \left(\frac{\hbar\omega'}{c},\ \frac{\hbar\omega'}{c} \sin\theta\cos\phi,\ \frac{\hbar\omega'}{c} \sin\theta\sin\phi,\ \frac{\hbar\omega'}{c} \cos\theta \right) = \frac{\hbar\omega'}{c} \hat{\mathbf{k}}' = \frac{\hbar\omega'}{c} (1, \hat{\boldsymbol{k}}'). \tag{64}$$

As previously stated the electron momentum is generalized to include transverse momentum, and it is defined by its relativistic velocity in three components $\boldsymbol{\beta}$

$$\mathbf{p} = (E_e/c, \boldsymbol{p_e}) = (E_e/c, \gamma mc\boldsymbol{\beta}) = (\gamma mc,\ \gamma mc\beta_x,\ \gamma mc\beta_y,\ \gamma mc\beta_z). \tag{65}$$

Recall from Eq. (33) that the law of conservation of momentum demands that the total initial momentum must equal the total scattered momentum:

$$\mathbf{p} + \mathbf{k} = \mathbf{p}' + \mathbf{k}'.$$

As before, this may be rewritten

$$\mathbf{p}' = \mathbf{p} + \mathbf{k} - \mathbf{k}'.$$

Taking the square of each side s under four-vector multiplication yields

$$\mathbf{p}' \cdot \mathbf{p}' = \mathbf{p} \cdot \mathbf{p} + \mathbf{p} \cdot \mathbf{k} - \mathbf{p} \cdot \mathbf{k}' + \mathbf{k} \cdot \mathbf{p} + \mathbf{k} \cdot \mathbf{k} - \mathbf{k} \cdot \mathbf{k}' - \mathbf{k}' \cdot \mathbf{p} - \mathbf{k}' \cdot \mathbf{k} + \mathbf{k}' \cdot \mathbf{k}'.$$

Again, regrouping this expression gives the equation

$$\mathbf{p}' \cdot \mathbf{p}' - \mathbf{p} \cdot \mathbf{p} = 2\left(\mathbf{p} \cdot \mathbf{k}\right) - 2\left(\mathbf{p} \cdot \mathbf{k}'\right) - 2\left(\mathbf{k} \cdot \mathbf{k}'\right).$$

As shown in Eq. (40) and Eq. (41), any 4-vector momentum that multiplied by itself will produce a constant that scales with the square of the objects mass

$$\mathbf{p} \cdot \mathbf{p} = \mathbf{p}' \cdot \mathbf{p}' = m^2c^2; \quad \mathbf{k} \cdot \mathbf{k} = \mathbf{k}' \cdot \mathbf{k}' = 0. \tag{66}$$

Using the 4-vectors from Eq. (63) and Eq. (64), the previous relation may be rewritten in terms of the incident and scattered angular frequencies

$$\begin{aligned} 0 &= \frac{\omega\hbar}{c}\mathbf{p} \cdot \hat{\mathbf{k}} - \frac{\omega'\hbar}{c}\mathbf{p} \cdot \hat{\mathbf{k}}' - \frac{\omega\omega'\hbar^2}{c^2}\hat{\mathbf{k}} \cdot \hat{\mathbf{k}}', \\ \omega'\left(\mathbf{p} \cdot \hat{\mathbf{k}}' + \frac{\omega\hbar}{c}\hat{\mathbf{k}} \cdot \hat{\mathbf{k}}'\right) &= \omega\mathbf{p} \cdot \hat{\mathbf{k}}, \\ \omega' &= \frac{\omega\mathbf{p} \cdot \hat{\mathbf{k}}}{\mathbf{p} \cdot \hat{\mathbf{k}}' + \frac{\omega\hbar}{c}\hat{\mathbf{k}} \cdot \hat{\mathbf{k}}'}. \end{aligned}$$

This expression can be written in terms of the 3-vector momentum of the incident photon, scattered photon, and the initial relativistic velocity of the electron

$$\omega' = \frac{\omega\left(1 - \boldsymbol{\beta} \cdot \hat{\boldsymbol{k}}\right)}{1 - \boldsymbol{\beta} \cdot \hat{\boldsymbol{k}}' + \frac{\omega\hbar}{\gamma mc^2}\left(1 - \hat{\boldsymbol{k}} \cdot \hat{\boldsymbol{k}}'\right)}. \tag{67}$$

The following dot products are used to calculate the scattered angular frequency ω' in terms of the initial relativistic velocity of the electron $\boldsymbol{\beta}$, the angular frequency of the incident photon ω, and the scattering angles θ, ϕ:

$$\boldsymbol{\beta} \cdot \hat{\boldsymbol{k}} = -\beta_z, \tag{68}$$

$$\boldsymbol{\beta} \cdot \hat{\boldsymbol{k}}' = \beta_x \sin\theta\cos\phi + \beta_y \sin\theta\sin\phi + \beta_z \cos\theta, \tag{69}$$

and

$$\hat{\boldsymbol{k}} \cdot \hat{\boldsymbol{k}}' = -\cos\theta. \tag{70}$$

The scattered angular frequency may now be expressed in terms of the initial conditions and the scattering angles

$$\omega' = \frac{\omega\left(1 + \beta_z\right)}{1 - \left(\beta_x \sin\theta\cos\phi + \beta_y \sin\theta\sin\phi + \beta_z \cos\theta\right) + \frac{\omega\hbar}{\gamma mc^2}\left(1 + \cos\theta\right)}. \tag{71}$$

The linear Compton energy density spectrum, Eq. (54), also requires an expression for the first derivative of the incident photon angular frequency with respect to the scattered photon angular frequency $\mathrm{d}\omega/\mathrm{d}\omega'$. After a little algebra, Eq. (67) may be rewritten so that incident angular frequency, ω, is a function of scattered angular frequency, ω

$$\omega = \frac{\omega' \left(1 - \boldsymbol{\beta} \cdot \hat{\boldsymbol{k}}'\right)}{1 - \boldsymbol{\beta} \cdot \hat{\boldsymbol{k}} + \frac{\omega' \hbar}{\gamma m c^2} \left(1 - \hat{\boldsymbol{k}} \cdot \hat{\boldsymbol{k}}'\right)}. \tag{72}$$

The derivative with respect to the scattered photon angular frequency may now be solved

$$\frac{\mathrm{d}\omega}{\mathrm{d}\omega'} = \frac{\left(1 - \boldsymbol{\beta} \cdot \hat{\boldsymbol{k}}'\right)}{1 - \boldsymbol{\beta} \cdot \hat{\boldsymbol{k}} + \frac{\omega' \hbar}{\gamma m c^2} \left(1 - \hat{\boldsymbol{k}} \cdot \hat{\boldsymbol{k}}'\right)} - \frac{\frac{\omega' \hbar}{\gamma m c^2} \left(1 - \boldsymbol{\beta} \cdot \hat{\boldsymbol{k}}'\right) \left(1 - \hat{\boldsymbol{k}} \cdot \hat{\boldsymbol{k}}'\right)}{\left(1 - \boldsymbol{\beta} \cdot \hat{\boldsymbol{k}} + \frac{\omega' \hbar}{\gamma m c^2} \left(1 - \hat{\boldsymbol{k}} \cdot \hat{\boldsymbol{k}}'\right)\right)^2}. \tag{73}$$

Applying the dot product solutions as before gives a solution to the derivative $\mathrm{d}\omega/\mathrm{d}\omega'$ in terms of the initial conditions and the scattering angles.

$$\begin{aligned} \frac{\mathrm{d}\omega}{\mathrm{d}\omega'} = & \frac{(1 - (\beta_x \sin\theta \cos\phi + \beta_y \sin\theta \sin\phi + \beta_z \cos\theta))}{1 + \beta_z + \frac{\omega' \hbar}{\gamma m c^2} (1 + \cos\theta)} - \\ & \frac{\frac{\omega' \hbar}{\gamma m c^2} (1 - (\beta_x \sin\theta \cos\phi + \beta_y \sin\theta \sin\phi + \beta_z \cos\theta)) (1 + \cos\theta)}{\left(1 + \beta_z + \frac{\omega' \hbar}{\gamma m c^2} (1 + \cos\theta)\right)^2}. \end{aligned} \tag{74}$$

4.3.1 REDUCTION TO ON-AXIS CALCULATION

The general expression for the angular frequency of the scattered photon should reduce to the on-axis calculation in the appropriate limit, i.e., $\beta_x, \beta_y \to 0$. In this section, the general angular frequency, Eq. (72), will be reduced to the on-axis calculation, Eq. (44), as a means of checking the calculation:

$$\begin{aligned} \lim_{\beta_x, \beta_y \to 0} & \frac{\omega (1 + \beta_z)}{1 - (\beta_x \sin\theta \cos\phi + \beta_y \sin\theta \sin\phi + \beta_z \cos\theta) + \frac{\omega \hbar}{\gamma m c^2} (1 + \cos\theta)} = \\ & \frac{\omega (1 + \beta)}{1 - ((0) \sin\theta \cos\phi + (0) \sin\theta \sin\phi + \beta \cos\theta) + \frac{\omega \hbar}{\gamma m c^2} (1 + \cos\theta)} = \\ & \frac{\omega (1 + \beta)}{1 - (\beta \cos\theta) + \frac{\omega \hbar}{\gamma m c^2} (1 + \cos\theta)}. \end{aligned} \tag{75}$$

Eq. (75) is indeed equivalent to Eq. (44), so the two calculations are in agreement. Furthermore, this generalized form also reduces to Compton's original expression for the scattered angular frequency, Eq. (19) within the limit of a stationary, non-relativistic electron source.

4.3.2 COMPTON PARAMETER X

It is important to introduce the unitless Compton parameter X from Eq. (17) from Section 3.2 into the analysis. The X parameter quantifies the effects on the spectra that arise from operating in the Compton regime. The spectral red-shift that arise from highly relativistic collisions, i.e., $X \gg 1$, will be discussed in detail in Section 4.6. Recall that X is defined

$$X = \frac{4E_{\mathrm{e}}E_{\mathrm{L}}}{(mc^2)^2}.$$

From the relativistic energy relation,

$$E_{\mathrm{e}} = \gamma mc^2 \rightarrow \gamma = \frac{E_{\mathrm{e}}}{mc^2}. \tag{76}$$

The unitless Compton parameter X appears in Eq. (67) in the denominator

$$\frac{\omega\hbar}{\gamma mc^2}\frac{X(mc^2)^2}{E_{\mathrm{e}}E_{\mathrm{L}}} = \frac{X}{4\gamma^2}. \tag{77}$$

The scattered angular frequency expressions may be rewritten in terms of X:

$$\omega' = \frac{\omega\left(1+\beta_z\right)}{1-\left(\beta_x\sin\theta\cos\phi+\beta_y\sin\theta\sin\phi+\beta_z\cos\theta\right)+\frac{X}{4\gamma^2}\left(1+\cos\theta\right)}. \tag{78}$$

Multiplying the numerator and denominator by $\gamma^2(1+\beta)$ yields

$$\omega' = \frac{\gamma^2\omega\left(1+\beta_z\right)\left(1+\beta\right)}{\gamma^2\left(1-\left(\beta_x\sin\theta\cos\phi+\beta_y\sin\theta\sin\phi+\beta_z\cos\theta\right)\right)\left(1+\beta\right)+\frac{X}{4}\left(1+\cos\theta\right)\left(1+\beta\right)}. \tag{79}$$

Let us consider the impact of the Compton factor X on the maximum scattered angular frequency ω'. The maximum scattered angular frequency occurs for the on-axis electron, i.e., $\beta_x, \beta_y \rightarrow 0$ and $\beta_z \rightarrow \beta$,

$$\omega' = \frac{\gamma^2\omega(1+\beta)^2}{\gamma^2\left(1-\beta\cos\theta\right)\left(1+\beta\right)+\frac{X}{4}\left(1+\cos\theta\right)\left(1+\beta\right)}. \tag{80}$$

Using the first order expansion $\cos\theta \approx 1-\theta^2/2$

$$\omega' = \frac{\gamma^2\omega(1+\beta)^2}{1+\frac{\beta(1+\beta)\gamma^2\theta^2}{2}+\frac{X(1+\beta)(2-\theta^2/2}{4}}. \tag{81}$$

For a relativistic electron, $\beta \rightarrow 1$ and $\gamma^2 \gg X/4$

$$\omega' = \frac{4\omega\gamma^2}{1+X+\theta^2\gamma^2}. \tag{82}$$

Again, since the highest energy occurs on-axis ($\theta = 0$), the Compton edge of the scattered spectrum

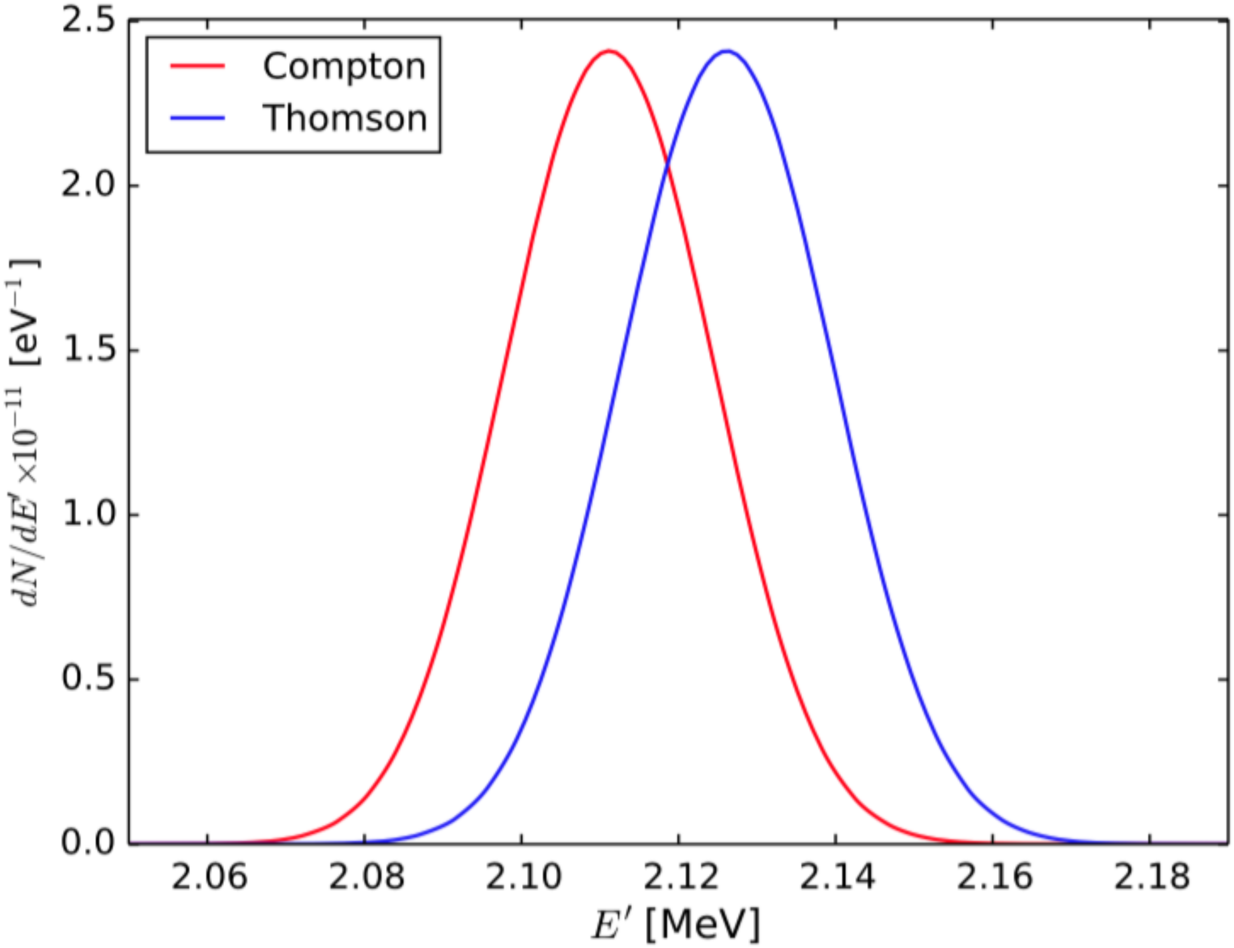

FIG. 27: Frequency shift between the spectra of Compton and Thomson scattering of a single electron with $E_b = 300$ MeV, with a laser pulse with $a_0 = 0.01$, $\lambda = 800$ nm, $\sigma = 20.3$, captured by aperture of $\theta = 1/10\gamma$ [2]. For these parameters, the Compton factor is still rather small $X = 7.12 \times 10^{-3}$, but notice that the red-shift is substantial relative to the total bandwidth of the spectrum.

can be calculated as a function of the Compton parameter

$$E'_{\mathrm{ph,max}} = \frac{4\gamma^2 E_{\mathrm{L}}}{1+X}. \tag{83}$$

This expression quantifies the spectral red-shift that is indicative of highly relativistic photon-electron collisions within the Compton regime. Eq. (83) is consistent with the analysis of Curatolo et al. [62]. $E_{\mathrm{ph,max}}$ has been used to to study how the Compton parameter X impacts the inherent sources spectral bandwidth. These changes to the scaling laws are defined in Section 4.6.

4.4 KLEIN-NISHINA CROSS SECTION

In 1928, Klein and Nishina investigated Compton scattering based on the Dirac equation just proposed in the same year, and derived the Klein–Nishina formula for the scattering cross section of a photon. This differential cross section is used to calculate the spectrum of the scattered radiation for a single electron. The entire energy scattered from an electron beam is obtained by summing the spectra for each individual electron, each generated using the relativistic factors for each electron. The expression presented in this section correctly accounts for a linearly, circularly, or elliptically polarized incident laser pulse [2, 66, 67, 68].

The Klein-Nishina cross section in the rest frame of the electron is often represented as [58, 69]

$$\frac{d\sigma}{d\Omega_b} = \frac{r_e^2}{4}\left(\frac{\omega'_b}{\omega_b}\right)^2 \left[\frac{\omega'_b}{\omega_b} + \frac{\omega_b}{\omega'_b} - 2 + 4\left(\boldsymbol{\epsilon_b}\cdot\boldsymbol{\epsilon'_b}\right)^2\right], \tag{84}$$

where ϵ_b and ϵ'_b are the polarization vectors of incident and scattered radiation respectively. The more general expression that is valid for both linear and circular polarizations is given by Stedman and Pooke [70]

$$\frac{d\sigma}{d\Omega_b} = \frac{r_e^2}{4}\left(\frac{\omega'_b}{\omega_b}\right)^2 \left[\left(\frac{\omega'_b}{\omega_b} + \frac{\omega_b}{\omega'_b}\right)\left(1 - \left|\boldsymbol{\epsilon}_b\cdot\boldsymbol{\epsilon}'_b\right|^2 + \left|\boldsymbol{\epsilon}_b\cdot\boldsymbol{\epsilon}'^*_b\right|^2\right) + 2\left(\left|\boldsymbol{\epsilon}_b\cdot\boldsymbol{\epsilon}'_b\right|^2 + \left|\boldsymbol{\epsilon}_b\cdot\boldsymbol{\epsilon}'^*_b\right|^2 - 1\right)\right]. \tag{85}$$

The Klein-Nishina transformed into the lab frame serves as the differential cross section for the linear Compton model presented in this chapter [2]

$$\begin{aligned}\frac{d\sigma}{d\Omega} = \frac{r_e^2}{2\gamma^2\left(1-\boldsymbol{\beta}\cdot\hat{\boldsymbol{k}}\right)^2}\left(\frac{\omega'}{\omega}\right)^2 \Bigg[&\left(\frac{\omega'\left(1-\boldsymbol{\beta}\cdot\hat{\boldsymbol{k}}'\right)}{\omega\left(1-\boldsymbol{\beta}\cdot\hat{\boldsymbol{k}}\right)} + \frac{\omega\left(1-\boldsymbol{\beta}\cdot\hat{\boldsymbol{k}}\right)}{\omega'\left(1-\boldsymbol{\beta}\cdot\hat{\boldsymbol{k}}'\right)}\right) \\ &- \frac{2(mc)^2\left(\mathbf{k}'\cdot\boldsymbol{\epsilon}\right)\left(\mathbf{k}'\cdot\boldsymbol{\epsilon}^*\right)}{\left(\mathbf{p}\cdot\mathbf{k}'\right)^2} \\ &+ 2(mc)^2\frac{\left(\mathbf{p}\cdot\boldsymbol{\epsilon}\right)\left(\mathbf{k}'\cdot\boldsymbol{\epsilon}^*\right) + \left(\mathbf{k}'\cdot\boldsymbol{\epsilon}\right)\left(\mathbf{p}\cdot\boldsymbol{\epsilon}^*\right)}{\left(\mathbf{p}\cdot\mathbf{k}\right)\left(\mathbf{p}\cdot\mathbf{k}'\right)^2}\left(\mathbf{k}\cdot\mathbf{k}'\right) \\ &- 2(mc)^2\frac{\left(\mathbf{p}\cdot\boldsymbol{\epsilon}\right)\left(\mathbf{p}\cdot\boldsymbol{\epsilon}^*\right)}{\left(\mathbf{p}\cdot\mathbf{k}\right)^2\left(\mathbf{p}\cdot\mathbf{k}'\right)^2}\left(\mathbf{k}\cdot\mathbf{k}'\right)^2\Bigg],\end{aligned} \tag{86}$$

where r_e is the electron radius, γ is the Lorentz factor of the electron, $\boldsymbol{\beta}$ is the relativistic velocity of the electron, $\mathbf{k}$ is the 4-vector momentum of the incident photon, $\mathbf{k}'$ is the 4-vector momentum of the scattered photon, ω is the angular frequency of the incident photon, ω' is the angular frequency of the scattered photon, m is the electron mass, c is the speed of light, $\boldsymbol{\epsilon}$ is the polarization vector of the incident laser pulse, and $\mathbf{p}$ is the relativistic momentum of the electron. The photon and electron momenta are defined in Section 4.3.

4.4.1 LINEAR POLARIZATION

The incident laser pulse is linearly polarized in the $\hat{\boldsymbol{x}}$ orientation, the polarization vector is defined $\boldsymbol{\epsilon}$:

$$\boldsymbol{\epsilon} = \boldsymbol{\epsilon}^* = \hat{\boldsymbol{x}}. \tag{87}$$

The first two dot products were solved Section 4.3:

$$\boldsymbol{\beta} \cdot \hat{\boldsymbol{k}} = -\beta_z,$$

and

$$\boldsymbol{\beta} \cdot \hat{\boldsymbol{k}}' = \beta_x \sin\theta \cos\phi + \beta_y \sin\theta \sin\phi + \beta_z \cos\theta.$$

The photon-electron dot products are calculated:

$$\mathbf{p} \cdot \mathbf{k} = \hbar\omega \left(\gamma m + \frac{p_z}{c} \right), \tag{88}$$

and

$$\mathbf{p} \cdot \mathbf{k}' = \hbar\omega' \left(\gamma m - \frac{1}{c} \left(p_x \sin\theta \cos\phi + p_y \sin\theta \sin\phi + p_z \cos\theta \right) \right). \tag{89}$$

The photon-photon dot product is calculated:

$$\mathbf{k} \cdot \mathbf{k}' = \frac{\hbar^2 \omega \omega'}{c^2} \left(1 + \cos\theta \right). \tag{90}$$

Now, the ϵ dot products from Eq. (86) are solved

$$\mathbf{p} \cdot \boldsymbol{\epsilon} = \mathbf{p} \cdot \boldsymbol{\epsilon}^* = p_x, \tag{91}$$

and

$$\mathbf{k}' \cdot \boldsymbol{\epsilon} = \mathbf{k}' \cdot \boldsymbol{\epsilon}^* = \frac{\omega' \hbar}{c} \sin\theta \cos\phi. \tag{92}$$

Substituting these dot products back into Eq. (86) gives the Klein-Nishina cross section in terms of the initial conditions of the collision and the photon scattering angle

$$
\begin{aligned}
\frac{d\sigma}{d\Omega} =& \frac{r_e^2}{2\gamma^2\left(1+\beta_z\right)^2}\left(\frac{\omega'}{\omega}\right)^2\left[\left(\frac{\omega'\left(1-\left(\beta_x\sin\theta\cos\phi+\beta_y\sin\theta\sin\phi+\beta_z\cos\theta\right)\right)}{\omega\left(1+\beta_z\right)}\right.\right. \\
&+\left.\frac{\omega\left(1+\beta_z\right)}{\omega'\left(1-\left(\beta_x\sin\theta\cos\phi+\beta_y\sin\theta\sin\phi+\beta_z\cos\theta\right)\right)}\right) \\
&-\frac{2(mc)^2\left(\frac{\omega'\hbar}{c}\sin\theta\cos\phi\right)^2}{\left(\hbar\omega'\left(\gamma m-\frac{1}{c}\left(p_x\sin\theta\cos\phi+p_y\sin\theta\sin\phi+p_z\cos\theta\right)\right)\right)^2} \\
&+\frac{4(mc)^2p_x\left(\frac{\omega'\hbar}{c}\sin\theta\cos\phi\right)\left(\frac{\hbar^2\omega\omega'}{c^2}\left(1+\cos\theta\right)\right)}{\left(\hbar\omega\left(\gamma m+\frac{p_z}{c}\right)\right)\left(\hbar\omega'\left(\gamma m-\frac{1}{c}\left(p_x\sin\theta\cos\phi+p_y\sin\theta\sin\phi+p_z\cos\theta\right)\right)\right)^2} \\
&-\left.\frac{2(mc)^2p_x^2\left(\frac{\hbar^2\omega\omega'}{c^2}\left(1+\cos\theta\right)\right)^2}{\left(\hbar\omega\left(\gamma m+\frac{p_z}{c}\right)\right)^2\left(\hbar\omega'\left(\gamma m-\frac{1}{c}\left(p_x\sin\theta\cos\phi+p_y\sin\theta\sin\phi+p_z\cos\theta\right)\right)\right)^2}\right],
\end{aligned} \tag{93}
$$

Reduction of the Linearly Polarized Klein-Nishina to the On-Axis Calculation

The Klein-Nishina cross section for the case of an on-axis electron has previously been solved [56]:

$$
\begin{aligned}
\frac{d\sigma}{d\Omega} =& \frac{r_e^2}{2\gamma^2(1+\beta)^2}\left(\frac{\omega'}{\omega}\right)^2 \\
&\times\left[\frac{\omega'}{\omega}\frac{1-\beta\cos\theta}{1+\beta}+\frac{\omega}{\omega'}\frac{1+\beta}{1-\beta\cos\theta}-2+\frac{2\left(\cos\theta-\beta\right)^2\cos^2\phi}{\left(1-\beta\cos\theta\right)^2}+2\sin^2\phi\right].
\end{aligned} \tag{94}
$$

Subjecting Eq. (93) to the on-axis limit gives the following equation:

$$
\begin{aligned}
\lim_{p_x,p_y\to 0}\frac{d\sigma}{d\Omega} =& \frac{r_e^2}{2\gamma^2(1+\beta)^2}\left(\frac{\omega'}{\omega}\right)^2 \\
&\times\left[\frac{\omega'}{\omega}\frac{1-\beta\cos\theta}{1+\beta}+\frac{\omega}{\omega'}\frac{1+\beta}{1-\beta\cos\theta}-\frac{2(mc)^2\left(\frac{\omega'\hbar}{c}\sin\theta\cos\phi\right)^2}{\left(\hbar\omega'\left(\gamma m-\frac{p_z\cos\theta}{c}\right)\right)^2}\right].
\end{aligned} \tag{95}
$$

The subtrahend in the square brackets can be rearranged:

$$
\begin{aligned}
&\frac{2(mc)^2\left(\frac{\omega'\hbar}{c}\sin\theta\cos\phi\right)^2}{\left(\hbar\omega'\left(\gamma m-\frac{p_z\cos\theta}{c}\right)\right)^2}= \\
&\qquad\frac{2\sin^2\theta\cos^2\phi}{\gamma^2\left(1-\beta\cos\theta\right)^2} \\
&\qquad\frac{2\left(1-\beta^2\right)\left(1-\cos^2\theta\right)\cos^2\phi}{\left(1-\beta\cos\theta\right)^2} \\
&\qquad-\frac{2\left(\cos^2\theta-2\beta\cos\theta+\beta^2-1+2\beta\cos\theta-\beta^2\cos^2\theta\right)\cos^2\phi}{\left(1-\beta\cos\theta\right)^2} \\
&\qquad-\frac{2\left(\cos\theta-\beta\right)^2\cos^2\phi}{\left(1-\beta\cos\theta\right)^2}+2-2\sin^2\phi.
\end{aligned}
\tag{96}
$$

Substituting Eq. (96) back into Eq. (95) gives

$$
\begin{aligned}
\frac{d\sigma}{d\Omega}=&\frac{r_e^2}{2\gamma^2(1+\beta)^2}\left(\frac{\omega'}{\omega}\right)^2 \\
&\times\left[\frac{\omega'}{\omega}\frac{1-\beta\cos\theta}{1+\beta}+\frac{\omega}{\omega'}\frac{1+\beta}{1-\beta\cos\theta}-2+\frac{2\left(\cos\theta-\beta\right)^2\cos^2\phi}{\left(1-\beta\cos\theta\right)^2}+2\sin^2\phi\right],
\end{aligned}
$$

which is equivalent to the summed differential cross section used in the previous work. Therefore the differential cross section of the electron beam with transverse momentum is equivalent to the differential cross section of the previous model when $|\boldsymbol{p}| = p_z$.

4.4.2 CIRCULAR POLARIZATION

The general form of an electric field from circularly polarized laser pulse is defined [58]:

$$
\boldsymbol{E}(\boldsymbol{x},t)=E_0(\boldsymbol{\epsilon}_1\pm i\boldsymbol{\epsilon}_2)e^{i\boldsymbol{k}\cdot\boldsymbol{x}-i\omega t}, \tag{97}
$$

where E_0 is the magnitude of the electric field and the vectors $\boldsymbol{\epsilon}_1$, $\boldsymbol{\epsilon}_2$ are the transverse unit vectors, $\boldsymbol{k}$ is the propagation vector of the laser pulse, $\boldsymbol{x}$ is the position vector, ω is the angular frequency of the laser pulse, and t is time. For the inverse linear Compton scattering model, the propagation vector and the transverse unit vectors are defined $\boldsymbol{k} = -zbm\hat{z}$, $\boldsymbol{\epsilon}_1 = \hat{\boldsymbol{x}}$, and $\boldsymbol{\epsilon}_2 = \hat{\boldsymbol{y}}$. Using the parameter $\xi = z + tc$ the unit vector of the circular polarization becomes

$$
\boldsymbol{\epsilon}=\frac{1}{\sqrt{2}}\left(\left[\cos\left(\frac{\omega}{c}\xi\right)\hat{\boldsymbol{x}}\pm\sin\left(\frac{\omega}{c}\xi\right)\hat{\boldsymbol{y}}\right]+i\left[-\sin\left(\frac{\omega}{c}\xi\right)\hat{\boldsymbol{x}}\pm\cos\left(\frac{\omega}{c}\xi\right)\hat{\boldsymbol{y}}\right]\right). \tag{98}
$$

The linear Compton model has been used primarily for linear polarization, i.e., $\boldsymbol{\epsilon} = \boldsymbol{\epsilon}^* = \hat{\boldsymbol{x}}$. To generate the scattered spectra for a circularly polarized laser pulse, the scalar products from

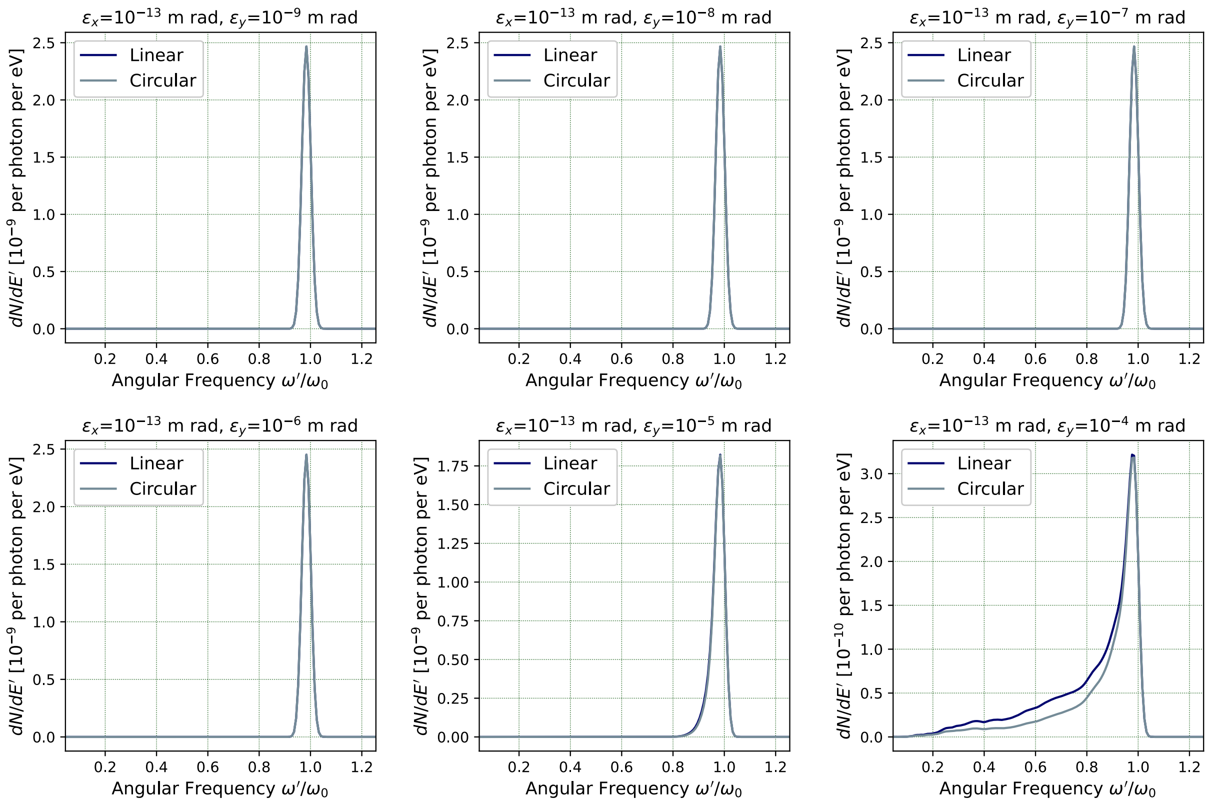

FIG. 28: Comparison of scattered spectra within the linear Compton regime generated by a linearly polarized laser pulse and by a circularly polarized laser pulse for differing horizontal and vertical normalized emittance values. The following parameters were used in the simulations: $E_\mathrm{e} = 23$ MeV; $\sigma_{E_\mathrm{e}}/E_\mathrm{e} = 0.175\%$; $\sigma_x = 41\ \mu$m; $\sigma_y = 81\ \mu$m; $\lambda = 800$ nm; $a_0 = 0.05$; $\sigma = 5.57$; $\theta_\mathrm{A} = 0.004$. The scattered frequency is scaled by the normalizing frequency $\omega_0 = 2\pi c/\lambda$.

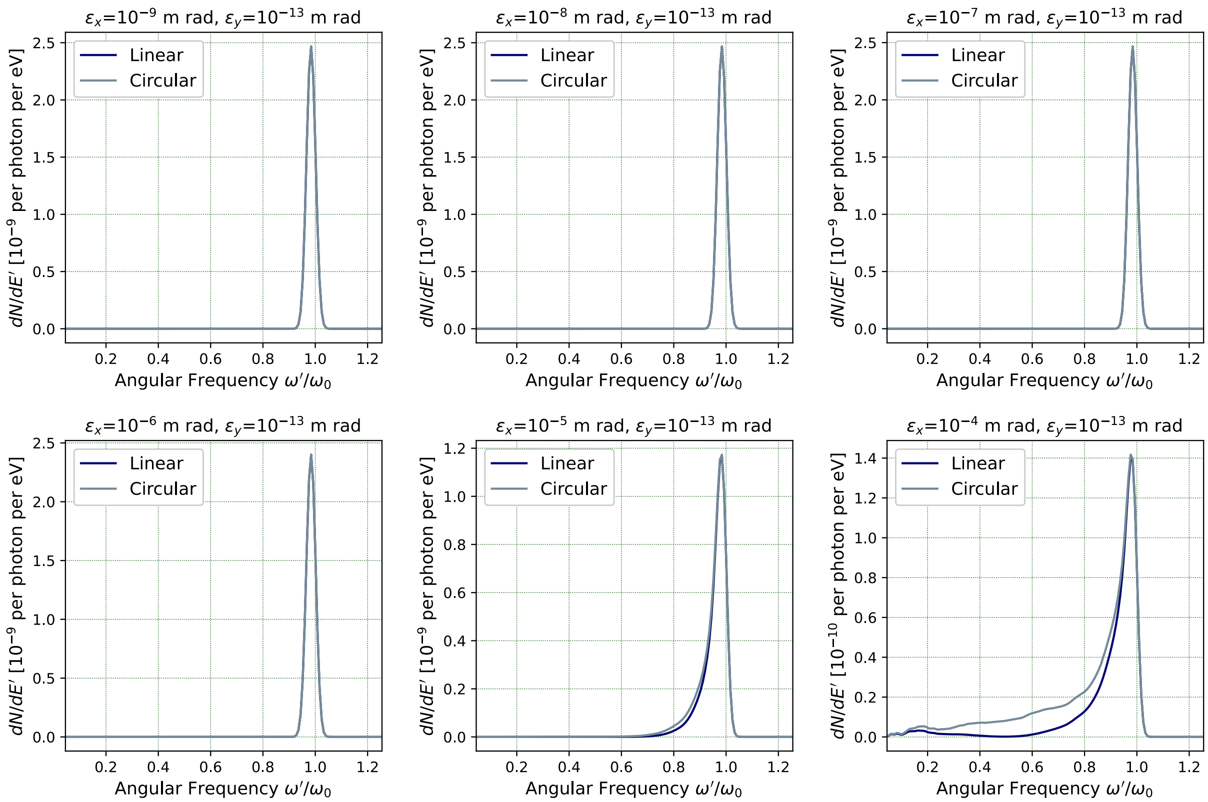

FIG. 29: Comparison of scattered spectra within the linear Compton regime generated by a linearly polarized laser pulse and by a circularly polarized laser pulse for differing horizontal and vertical normalized emittance values. The following parameters were used in the simulations: $E_\mathrm{e} = 23$ MeV; $\sigma_{E_\mathrm{e}}/E_\mathrm{e} = 0.175\%$; $\sigma_x = 41$ μm; $\sigma_y = 81$ μm; $\lambda = 800$ nm; $a_0 = 0.05$; $\sigma = 5.57$; $\theta_\mathrm{A} = 0.004$. The scattered frequency is scaled by the normalizing frequency $\omega_0 = 2\pi c/\lambda$.

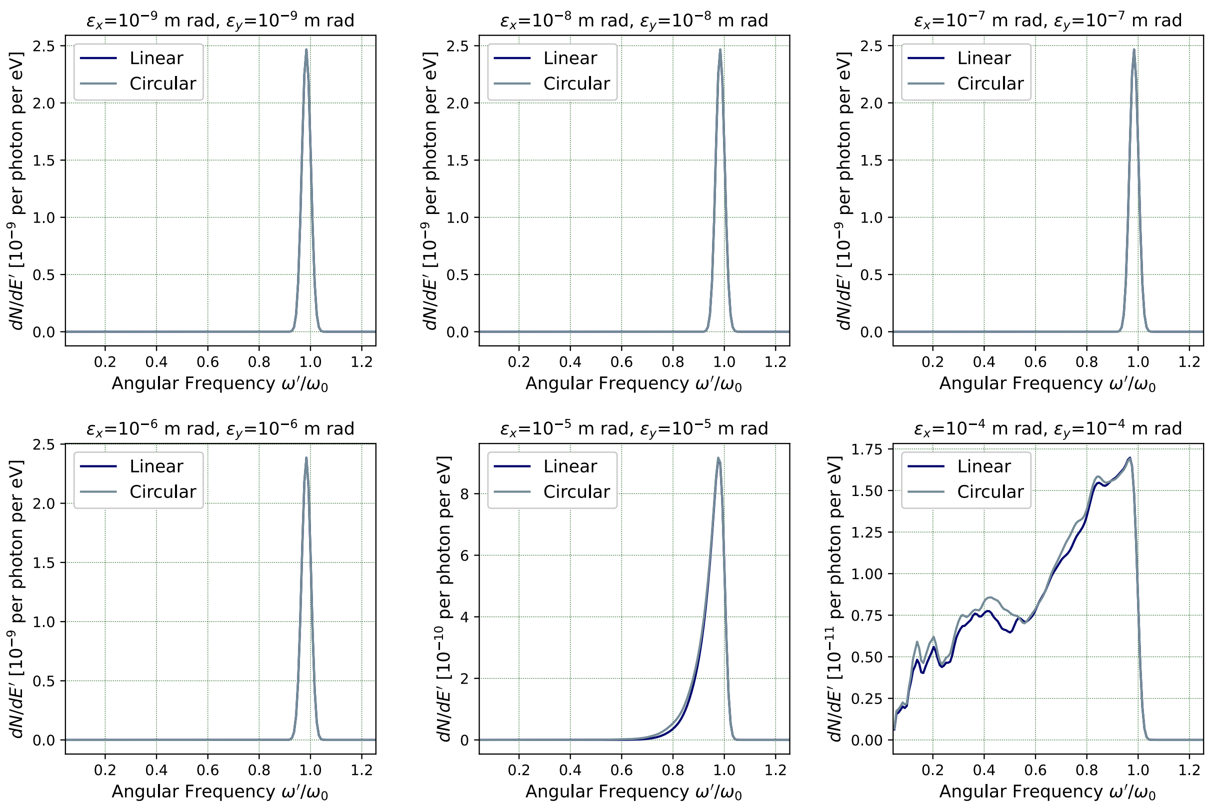

FIG. 30: Comparison of scattered spectra within the linear Compton regime generated by a linearly polarized laser pulse and by a circularly polarized laser pulse for differing horizontal and vertical normalized emittance values. The following parameters were used in the simulations: $E_\mathrm{e} = 23$ MeV; $\sigma_{E_\mathrm{e}}/E_\mathrm{e} = 0.175\%$; $\sigma_x = 41$ μm; $\sigma_y = 81$ μm; $\lambda = 800$ nm; $a_0 = 0.05$; $\sigma = 5.57$; $\theta_\mathrm{A} = 0.004$. The scattered frequency is scaled by the normalizing frequency $\omega_0 = 2\pi c/\lambda$.

Eq. (86) must be calculated using Eq. (98):

$$\mathbf{k}'\cdot\boldsymbol{\epsilon} = \frac{\hbar\omega'}{\sqrt{2}c}\left[\sin\theta\cos\phi\left(\cos\left(\frac{\omega}{c}\xi\right) - i\sin\left(\frac{\omega}{c}\xi\right)\right) + \sin\theta\sin\phi\left(\pm\sin\left(\frac{\omega}{c}\xi\right) \pm i\cos\left(\frac{\omega}{c}\xi\right)\right)\right], \quad (99)$$

$$\mathbf{k}'\cdot\boldsymbol{\epsilon}^* = \frac{\hbar\omega'}{\sqrt{2}c}\left[\sin\theta\cos\phi\left(\cos\left(\frac{\omega}{c}\xi\right) + i\sin\left(\frac{\omega}{c}\xi\right)\right) + \sin\theta\sin\phi\left(\pm\sin\left(\frac{\omega}{c}\xi\right) \mp i\cos\left(\frac{\omega}{c}\xi\right)\right)\right], \quad (100)$$

$$\mathbf{p}\cdot\boldsymbol{\epsilon} = \frac{1}{\sqrt{2}}\left[p_x\left(\cos\left(\frac{\omega}{c}\xi\right) - i\sin\left(\frac{\omega}{c}\xi\right)\right) + p_y\left(\pm\sin\left(\frac{\omega}{c}\xi\right) \pm i\cos\left(\frac{\omega}{c}\xi\right)\right)\right], \quad (101)$$

and

$$\mathbf{p}\cdot\boldsymbol{\epsilon}^* = \frac{1}{\sqrt{2}}\left[p_x\left(\cos\left(\frac{\omega}{c}\xi\right) + i\sin\left(\frac{\omega}{c}\xi\right)\right) + p_y\left(\pm\sin\left(\frac{\omega}{c}\xi\right) \mp i\cos\left(\frac{\omega}{c}\xi\right)\right)\right]. \quad (102)$$

Substituting these dot product solutions into Eq. (86) gives the correct scattering angle distribution for Compton scattering from a circularly polarized laser pulse. First, the products of the dot products must be calculated:

$$(\mathbf{k}'\cdot\boldsymbol{\epsilon})(\mathbf{k}'\cdot\boldsymbol{\epsilon}^*) = \frac{\hbar^2\omega'^2}{2c^2}\sin^2\theta, \quad (103)$$

$$(\mathbf{p}\cdot\boldsymbol{\epsilon}^*)(\mathbf{k}'\cdot\boldsymbol{\epsilon}) + (\mathbf{p}\cdot\boldsymbol{\epsilon})(\mathbf{k}'\cdot\boldsymbol{\epsilon}^*) = \frac{\hbar\omega'}{c}\sin\theta\left(p_x\cos\phi + p_y\sin\phi\right), \quad (104)$$

and

$$(\mathbf{p}\cdot\boldsymbol{\epsilon})(\mathbf{p}\cdot\boldsymbol{\epsilon}^*) = \frac{1}{2}(p_x^2 + p_y^2). \quad (105)$$

Finally, these expressions are substituted into Eq. (86) to complete the Klein-Nishina cross section for a circularly polarized incident laser pulse:

$$\begin{aligned}
\frac{d\sigma}{d\Omega} =& \frac{r_e^2}{2\gamma^2\left(1+\beta_z\right)^2}\left(\frac{\omega'}{\omega}\right)^2\Bigg[\Bigg(\frac{\omega'\left(1-\left(\beta_x\sin\theta\cos\phi+\beta_y\sin\theta\sin\phi+\beta_z\cos\theta\right)\right)}{\omega\left(1+\beta_z\right)} \\
&+\frac{\omega\left(1+\beta_z\right)}{\omega'\left(1-\left(\beta_x\sin\theta\cos\phi+\beta_y\sin\theta\sin\phi+\beta_z\cos\theta\right)\right)}\Bigg) \\
&-\frac{2(mc)^2\frac{\hbar^2\omega'^2}{2c^2}\sin^2\theta}{\left(\hbar\omega'\left(\gamma m-\frac{1}{c}\left(p_x\sin\theta\cos\phi+p_y\sin\theta\sin\phi+p_z\cos\theta\right)\right)\right)^2} \\
&+\frac{2(mc)^2\frac{\hbar\omega'}{c}\sin\theta\left(p_x\cos\phi+p_y\sin\phi\right)\left(\frac{\hbar^2\omega\omega'}{c^2}\left(1+\cos\theta\right)\right)}{\left(\hbar\omega\left(\gamma m+\frac{p_z}{c}\right)\right)\left(\hbar\omega'\left(\gamma m-\frac{1}{c}\left(p_x\sin\theta\cos\phi+p_y\sin\theta\sin\phi+p_z\cos\theta\right)\right)\right)^2} \\
&-\frac{2(mc)^2\frac{1}{2}(p_x^2+p_y^2)\left(\frac{\hbar^2\omega\omega'}{c^2}\left(1+\cos\theta\right)\right)^2}{\left(\hbar\omega\left(\gamma m+\frac{p_z}{c}\right)\right)^2\left(\hbar\omega'\left(\gamma m-\frac{1}{c}\left(p_x\sin\theta\cos\phi+p_y\sin\theta\sin\phi+p_z\cos\theta\right)\right)\right)^2}\Bigg].
\end{aligned} \quad (106)$$

Figures 28-30 show sets of scattered spectra calculated by the linear Compton model. In each plot, there is a spectrum representing the linear Klein-Nishina and the circular Klein-Nishina. Unsurprisingly as both expressions Eq. (86) and Eq. (106) are very similar, in all cases the linear and circular spectra are very similar. The difference between the polarization geometries increases

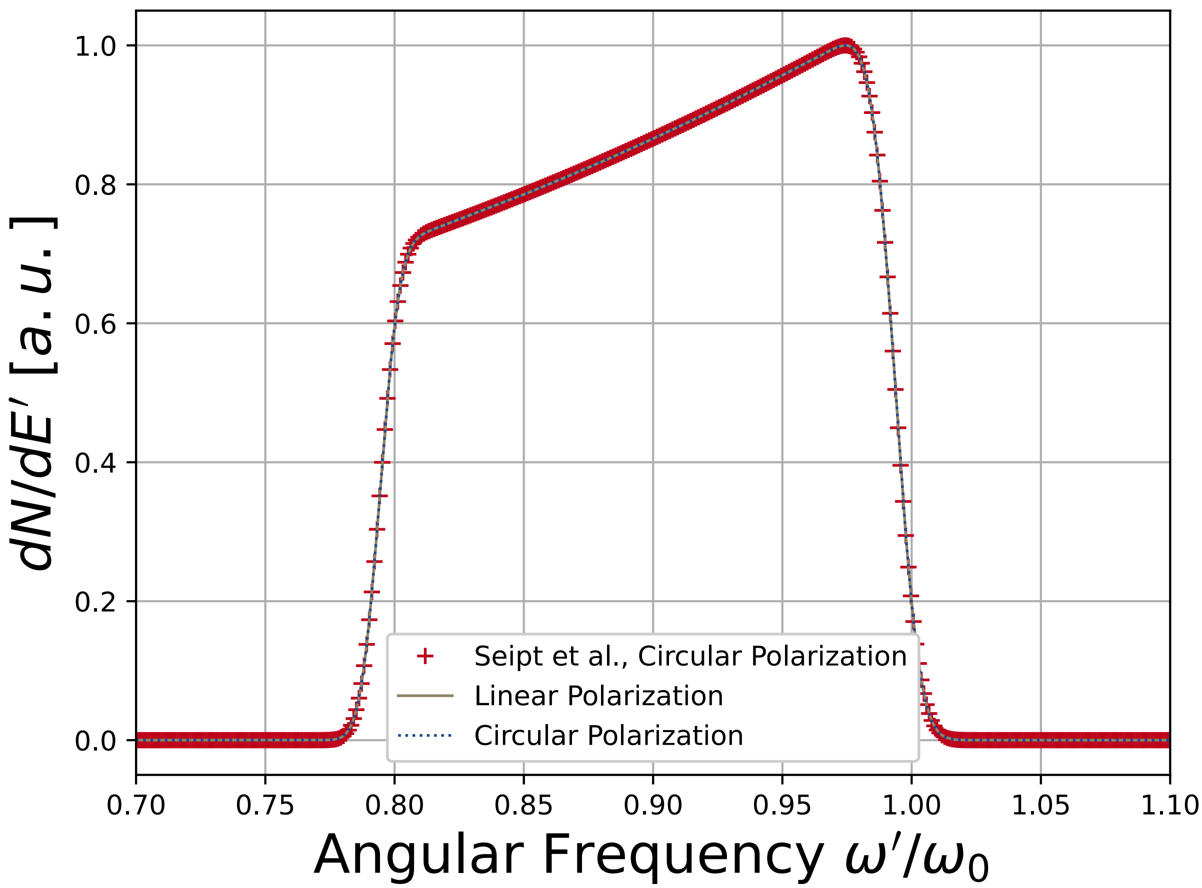

FIG. 31: Benchmarking ICCS against Figure 3 (c), $a_0 = 0.01$, from Seipt et al. [71]. The scattered frequency is scaled by the normalizing frequency $\omega_0 = 2\pi c/\lambda$.

with emittance, so the differences between the two will manifest more obviously in cases extremely high emittance.

Figure 31 shows the linear Compton model replication of the scattered spectra from reference [71] compared to the original figure. Since emittance has been minimized for this plot, the transverse momenta p_x, p_y go to zero. Therefore, Eq. (104) and Eq. (105) also go to zero, so the peak normalized spectrum is the same for the linear and nonlinear cases. Furthermore, the Klein-Nishina cross section for circular polarization, Eq. (106), reduces to the on-axis calculation in exactly the same way as the linear polarization.

4.5 FREQUENCY REPRESENTATION OF THE LASER PULSE ELECTRIC FIELD

The frequency representation of the laser pulse electric field $\left|\tilde{E}\left(\omega(\omega')\right)\right|^2$ may be calculated generally by taking the modulus squared of the Fourier transform of the localized vector potential of the incident laser in real space $A(\xi)$ multiplied by the incident angular frequency

$$\left|\tilde{E}\left(\omega(\omega')\right)\right|^2 = \left|\omega(\omega')\mathscr{F}\left\{A(\xi)\right\}\right|^2, \tag{107}$$

where $\xi = z + ct$ is the spacial parameter that describes the position along the laser pulse. As previously stated in Section 4.5, any plane-wave vector potential envelope shape that satisfies Eq. (56) is valid for this energy density spectrum calculation. For example, the vector potential of a plane-wave laser pulse with a Gaussian photon distribution is defined

$$A\left(\xi\right) = A_0 e^{\frac{-\xi^2}{2(\sigma\lambda)^2}} \cos\left(\frac{2\pi\xi}{\lambda}\right), \tag{108}$$

where A_0 is the amplitude of the vector potential, λ is the wavelength of the incident photon, and σ is the normalized length of the laser pulse. The normalized pulse length is derived from the time duration of the laser pulse T. The normalized length of the pulse can be taken as a root mean square (RMS)

$$\sigma_{\text{RMS}} = \frac{cT}{\lambda}, \tag{109}$$

or the normalized length of the pulse can be taken as full width at half max (FWHM)

$$\sigma_{\text{FWHM}} = \frac{cT}{\lambda}2.35. \tag{110}$$

Unless otherwise stated, the RMS length will be assumed for the context of this work, i.e., $\sigma = \sigma_{\text{RMS}}$. The Fourier transform of Eq. (108) has been completed in previous work [56], and so applying Eq. (107) to that solution yields the frequency representation of the laser pulse electric field:

$$\tilde{E}\left(\omega(\omega')\right) = \frac{\omega(\omega')ca_0 m\sigma\lambda\sqrt{\pi}}{e\sqrt{2}} e^{\frac{-(\sigma\lambda)^2}{2c^2}\left(\omega(\omega')-\frac{2\pi c}{\lambda}\right)^2}\left[e^{\frac{-4\pi\lambda\sigma^2\omega}{c}}+1\right]. \tag{111}$$

4.5.1 3D LINEAR COMPTON

Earlier versions of the linear Compton computation model [57] also calculated the scattered energy spectra by numerically integrating over the solid angle of a sensor aperture. This earlier code, however, only simulated the fields of the laser pulse as an infinite plane-wave. For all simulations in which the transverse size of the laser is much larger than the transverse size of the electron beam (also known as the spot size), this approximation is valid and will not adversely impact the spectrum calculation. Eq. (22) shows that in this 1D plane-wave approximation, the field does not depend on the transverse position of the electron.

A more sophisticated treatment of these fields must be developed in order to capture the physics relevant to the transverse size of the laser pulse. Let us define the spatial dependence of the field strength using 3D Cartesian coordinates, i.e., $a(\xi) \to a(x, y, z)$.

The improved representation of the laser pulse fields assumes a laser pulse of finite transverse size. The photons are given a Gaussian distribution in all three spacial dimensions ($\hat{x}, \hat{y}$, and $\hat{z}$) [72]:

$$a(x, y, z) = a_0 \exp\left\{-\frac{x^2}{2\sigma_{x,l}^2} - \frac{y^2}{2\sigma_{y,l}^2} - \frac{z^2}{2\sigma_{z,l}^2}\right\}, \tag{112}$$

where a_0 is the field strength parameter and $\sigma_{x,l}$, $\sigma_{y,l}$, and $\sigma_{z,l}$ represent the Gaussian spread in the laser pulse for each coordinate. For convenience, Eq. (112) may be parameterized to a single spatial coordinate in order to calculate the energy density spectrum. To facilitate the parameterization it must be assumed that the path of the electron remains a straight line as it passes through the field of the laser pulse; in other words, the momentum of the electron is kept constant as it passes through the laser pulse. Under this assumption, both time and the Cartesian coordinates may be defined in terms of the location ξ of the electron along its straight path through the laser field (Note that at $\xi = 0$, the electron is in the center of its path through the field.):

$$x = x_0 + \frac{p_x}{m}\frac{\xi - z_0}{c}, \quad y = y_0 + \frac{p_y}{m}\frac{\xi - z_0}{c}, \quad z = z_0 + cr_0 t, \quad t = \frac{\xi - z_0}{c}, \tag{113}$$

where x_0, y_0, and z_0 are the initial Cartesian coordinates of the electron when it enters the field of the laser pulse, p_x, p_y, and p_z represent the electron's momentum in each Cartesian coordinate, and r_0 is a parameter derived from the electrons momentum and the electron's Lorentz factor γ:

$$r_0 = \frac{(p_z/\gamma)}{\sqrt{p_x^2 + p_y^2 + (p_z/\gamma)^2}}. \tag{114}$$

After the application of a little algebraic rigor, Eq. (112) may be parameterized as a Gaussian distribution in terms of the initial conditions and ξ,

$$a(\xi) = \bar{a}_0 \exp\left(-\frac{(\xi + \eta)^2}{2\tilde{\sigma}_{z,l}^2}\right), \tag{115}$$

where the magnitude of this Gaussian distribution $\bar{a}_0$ is

$$\bar{a}_0 = a_0 \exp\left\{-\frac{x_0^2}{2\sigma_{x,l}^2} - \frac{y_0^2}{2\sigma_{y,l}^2} - \frac{z_0^2}{2\sigma_{z,l}^2}\right\} \exp\left\{\frac{\eta}{2\tilde{\sigma}_{z,l}^2}\right\}, \tag{116}$$

and the other constants are defined thusly:

$$\eta = \tilde{\sigma}_{z,l}^2 \left(\frac{x_0 \tilde{p}_x}{\sigma_{x,l}^2} + \frac{y_0 \tilde{p}_x}{\sigma_{y,l}^2} + \frac{z_0 r_0}{\sigma_{z,l}^2} \right), \; \tilde{\sigma}_{z,l}^2 = \frac{\sigma_{z,l}^2}{r_0^2} \left(\frac{\tilde{p}_x^2 \sigma_{z,l}^2}{r_0^2 \sigma_{x,l}^2} + \frac{\tilde{p}_y^2 \sigma_{z,l}^2}{r_0^2 \sigma_{y,l}^2} + 1 \right)^{-1}, \; \tilde{p}_x = \frac{p_x}{mc}, \; \tilde{p}_y = \frac{p_y}{mc}. \quad (117)$$

This parameterization may be used in two distinct ways to calculate the frequency representation of the laser pulse. First, Eq. (107) may be applied to the newly parameterized vector potential, and the Fourier transform of Eq. (115) must be completed. The second way is to make an approximation in which the new frequency representation has the same form as the plane-wave Gaussian, Eq. (111), but in the 3D approximation, the field strength parameter a_0 is replaced by the effective field strength parameter $\bar{a}_0$ from Eq. (116).

Fourier Transform for 3D Gaussian Vector Potential

As detailed in Appendix A, the Fourier transform of Eq. (115) leads to the new field treatment for the linear Compton computational model:

$$\left| \tilde{E}(\omega(\omega')) \right|^2 = \omega^2(\omega') a_\omega^2 \exp\left\{ \frac{-\left(\omega(\omega') - \omega_0\right)^2}{2\sigma_\omega^2} \right\}, \quad (118)$$

where the new constants are defined:

$$a_\omega^2 = \frac{\pi m^2 c^2 \bar{a}_0^2 \tilde{\sigma}_{z,l}^2}{2e^2}, \quad \omega_0 = \frac{2\pi c}{\lambda}, \quad \sigma_\omega^2 = \frac{c^2}{2\tilde{\sigma}_{z,l}^2}. \quad (119)$$

The new modality was benchmarked in order to test its functionality. First, the improved model was made to replicate the spectra generated by the origin plane-wave model in the appropriate limit, i.e., $\sigma_x << \sigma_{x,l}$. When the transverse size of the laser pulse is much greater than the spot size of the electron beam, the two computational models should produce the same spectra. Define the parameter r as the ratio of the electron beam spot size to the transverse width of the laser pulse:

$$r_x = \frac{\sigma_x}{\sigma_{x,l}}; r_y = \frac{\sigma_x}{\sigma_{y,l}}. \quad (120)$$

Figure 32 shows that for $r \leq 1$, the 3D model does indeed replicate the spectra generated by the earlier model. In these plots, all parameters are kept constant over these various plots except for the r value. The two major consequences of increased r are clearly illustrated in these plots: as r increases, the maximum peak of the spectrum decreases and the variance increases. In other words, as the laser pulse width becomes smaller than the electron spot size, the generated spectrum becomes both shorter and wider.

Second, the 3D functionality was benchmarked against data published in a refereed journal. Figure 33 shows two plots of the total spread in the scattered spectra as function of the spread due to the incident laser photon distribution. The first plot was generated by the 3D model, and

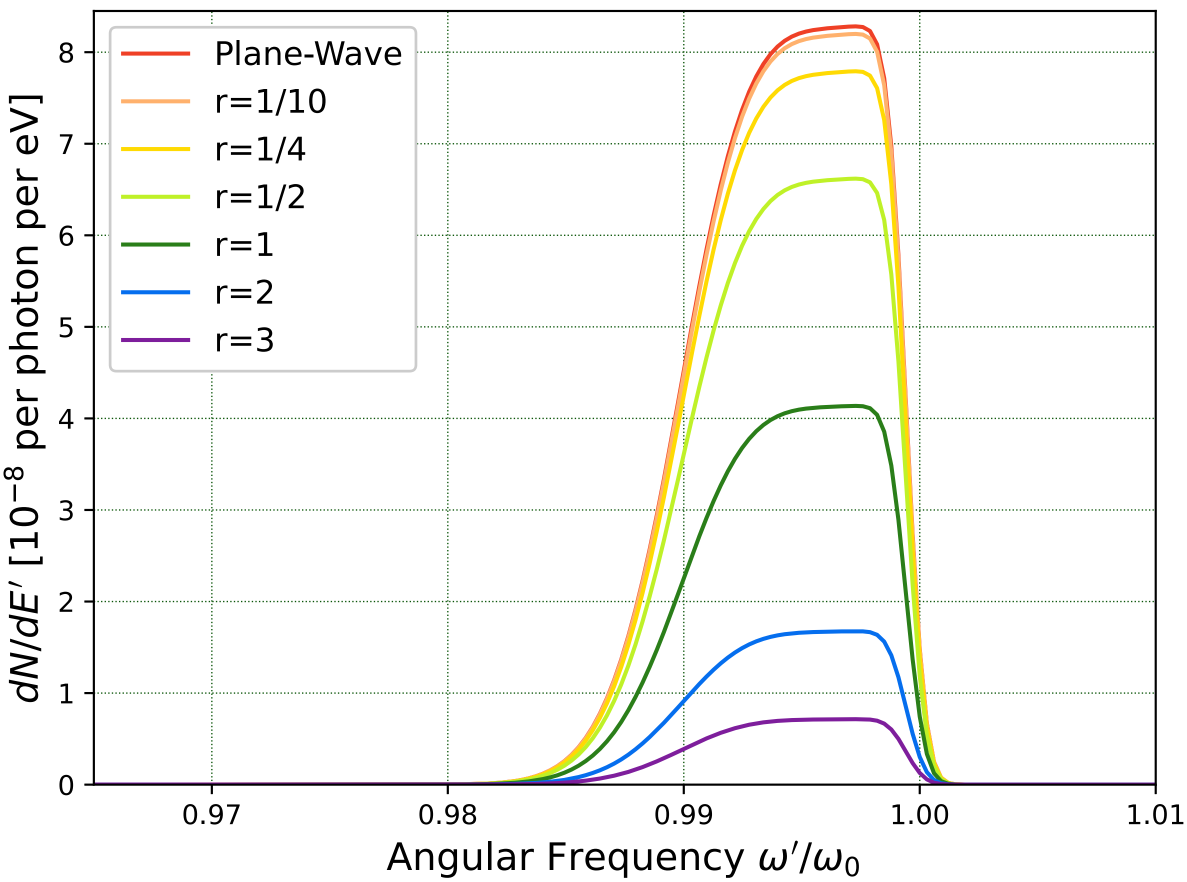

FIG. 32: Spectra of Compton-scattered photons incident through a circular, on-axis aperture for the following parameters: $E_\mathrm{e} = 25.5$ MeV; $\sigma_{E_\mathrm{e}}/E_\mathrm{e} = 1.376 \times 10^{-4}$; $\lambda = 1,000$ nm; $a_0 = 0.0113$; $\sigma_{z,l} = 1.4 \times 10^{-4}$ m; $\epsilon_x = 10^{-7}$ m rad; $\epsilon_y = 1.3 \times 10^{-7}$ m rad; $\theta_\mathrm{A} = 0.003$. These spectra have been produced by the original computational model [57], and the expanded 3D computational model. For a smaller ratio of transverse electron beam size to transverse laser field size, i.e., $r \leq 1$, the 3D laser treatment reproduces the spectra generated by the original computational model. This observation carries two significant implications: first, the new code replicates the calculations of the plane-wave approximation in the appropriate limit, so it is thereby benchmarked against the original model; second, the difference between the transverse sizes of the electron beam and the laser pulse have the most meaningful impact on the scattered radiation when the laser field is much smaller than the electron beam. The scattered frequency is scaled by the normalizing frequency $\omega_0 = 2\pi c/\lambda$.

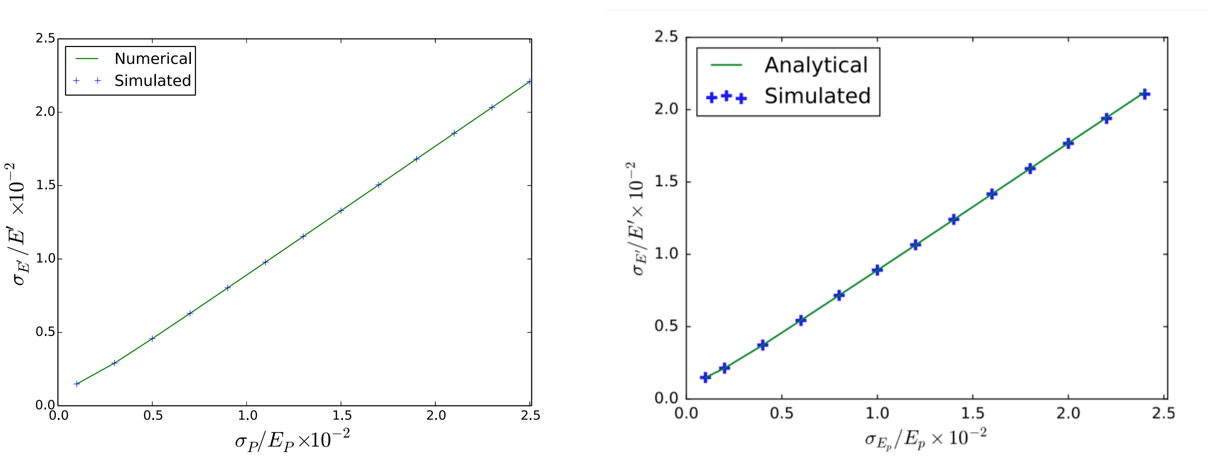

FIG. 33: Benchmarking the 3D laser treatment against data from a refereed publication for the following parameters: $E_\mathrm{e} = 7,000$ MeV; $\sigma_{E_\mathrm{e}}/E_\mathrm{e} = 0$; $\sigma_x = \sigma_y = 1.0 \times 10^{-5}$ m; $\lambda = 1,000$ nm; $a_0 = 0.0113$; $\sigma_{z,l} = 1.4 \times 10^{-4}$ m; $\epsilon_x = \epsilon_y = 0$; $\theta_\mathrm{A} = 0.003$. Both plots show the total normalized spread in spectra generated from Compton scattering $\sigma_{E'}/E'$ as a function of the normalized spread due to longitudinal photon distribution in the laser pulse σ_P/E_P. The left figure was produced by the 3D model using the parameters cited by Ranjan et al. 2018 [57]. The right figure is Figure 2 from Ranjan et al. [57]. The strong agreement of the two plots shows that the new model successfully replicated the calculation. Since the emittance of the electron beam is zero, the top plot generated by ICCS3D is independent of r.

the second plot was published in the journal article [57]. The strong agreement of the two plots confirms that the new functionality is benchmarked against the published data.

Gaussian Magnitude Approximation $a_0 \rightarrow \bar{a}_0$

It is known that a Fourier transform of a Gaussian function is itself another Gaussian function. This simple premise leads to the approximation of reusing the 1D Gaussian solution for the frequency representation of the electric field of the incident laser. In this approximation the field strength modifier a_0 is replaced with the effective field strength parameter $\bar{a}_0$. The normalized length of the laser pulse is also solved from the longitudinal Gaussian spread in the laser photons $\sigma_{z,l}$

$$\sigma = \frac{\sigma_{z,l}}{\lambda}. \tag{121}$$

The amplitude of the frequency representation of the laser field from Eq. (111) changes $a_0 \rightarrow \bar{a}_0$:

$$\frac{\omega(\omega')ca_0 m\sigma\lambda\sqrt{\pi}}{e\sqrt{2}} \rightarrow \frac{\omega(\omega')c\bar{a}_0 m\sigma_{z,l}\sqrt{\pi}}{e\sqrt{2}}. \tag{122}$$

The difference between this approximation and the amplitude of the Fourier transform from Eq. (119) is incredibly small

$$\begin{gathered}
\sigma_{z,l}^2 \approx \tilde{\sigma}_{z,l}^2, \\
1 \approx \frac{1}{r_0^2}\left(\frac{\tilde{p}_x^2\sigma_{z,l}^2}{r_0^2\sigma_{x,l}^2} + \frac{\tilde{p}_y^2\sigma_{z,l}^2}{r_0^2\sigma_{y,l}^2} + 1\right)^{-1}, \\
r_0^2\left(\frac{\tilde{p}_x^2\sigma_{z,l}^2}{r_0^2\sigma_{x,l}^2} + \frac{\tilde{p}_y^2\sigma_{z,l}^2}{r_0^2\sigma_{y,l}^2} + 1\right) \approx 1, \\
\frac{\tilde{p}_x^2\sigma_{z,l}^2}{\sigma_{x,l}^2} + \frac{\tilde{p}_y^2\sigma_{z,l}^2}{\sigma_{y,l}^2} + r_0^2 \approx 1.
\end{gathered}$$

The difference in the Gaussian spread scales by the same factor, so they are also approximately equivalent even for extremely high emittance. The agreement of the two calculations is shown in Figure 34.

Spread from 3D Linear Compton

After benchmarking, ICCS3D was used to explore the contribution of r to the total spread in the energy spectrum. Figure 35 shows the total spread in the scattered energy spectrum as a function of r. The parameters for this plot were chosen to minimize other sources of spectral broadening. Assuming that the contribution to spread from r combines with the other sources of spread, the

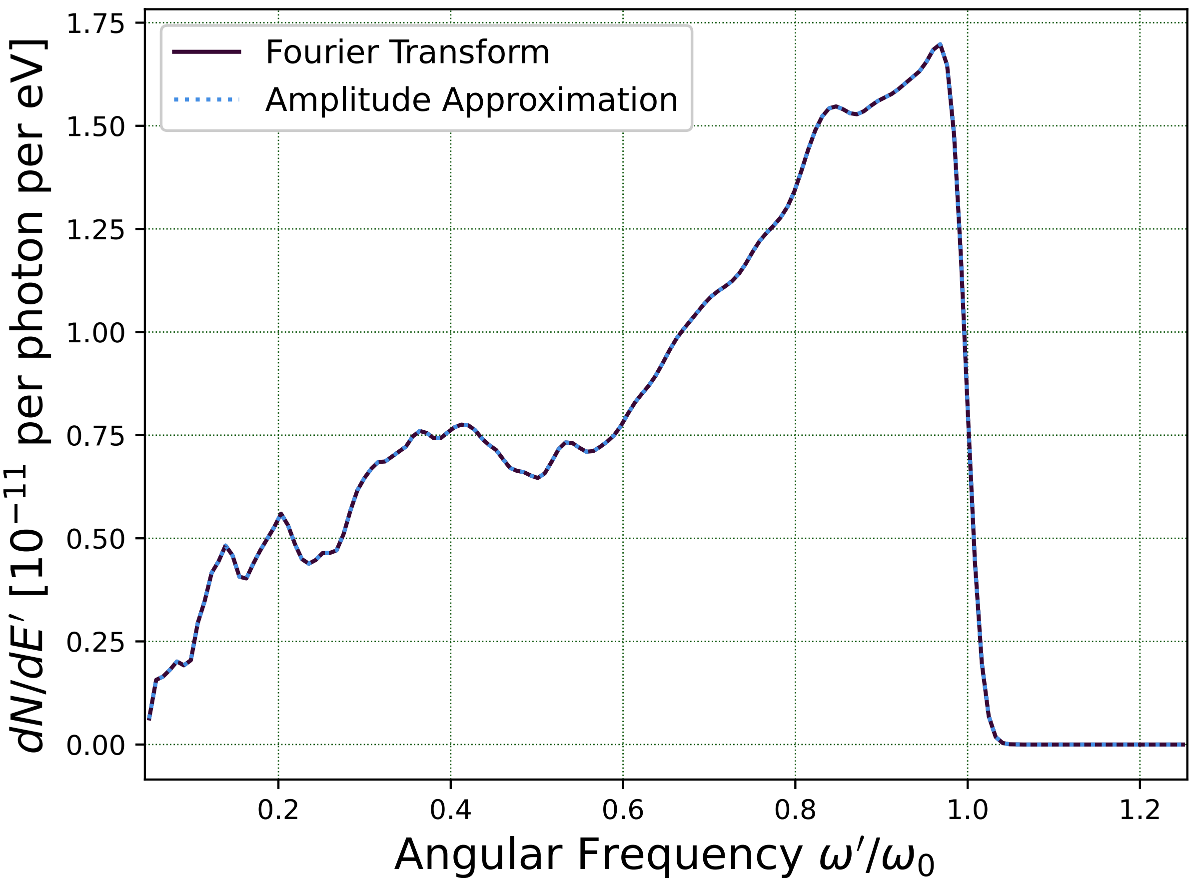

FIG. 34: Scattered spectra in the linear Compton regime using the Fourier transform and the magnitude approximation of the frequency representation of the incident laser pulse electric field. The following parameters were used in the simulations: $E_\mathrm{e} = 23$ MeV; $\sigma_{E_\mathrm{e}}/E_\mathrm{e} = 0.175\%$; $\sigma_x = 41 \times 10^{-6}$ m; $\sigma_y = 81 \times 10^{-6}$ m; $\lambda = 800$ nm; $a_0 = 0.05$; $\sigma = 5.57$; $\epsilon_x = \epsilon_y = 10^{-4}$ m rad; $\theta_\mathrm{A} = 0.004$. The scattered frequency is scaled by the normalizing frequency $\omega_0 = 2\pi c/\lambda$.

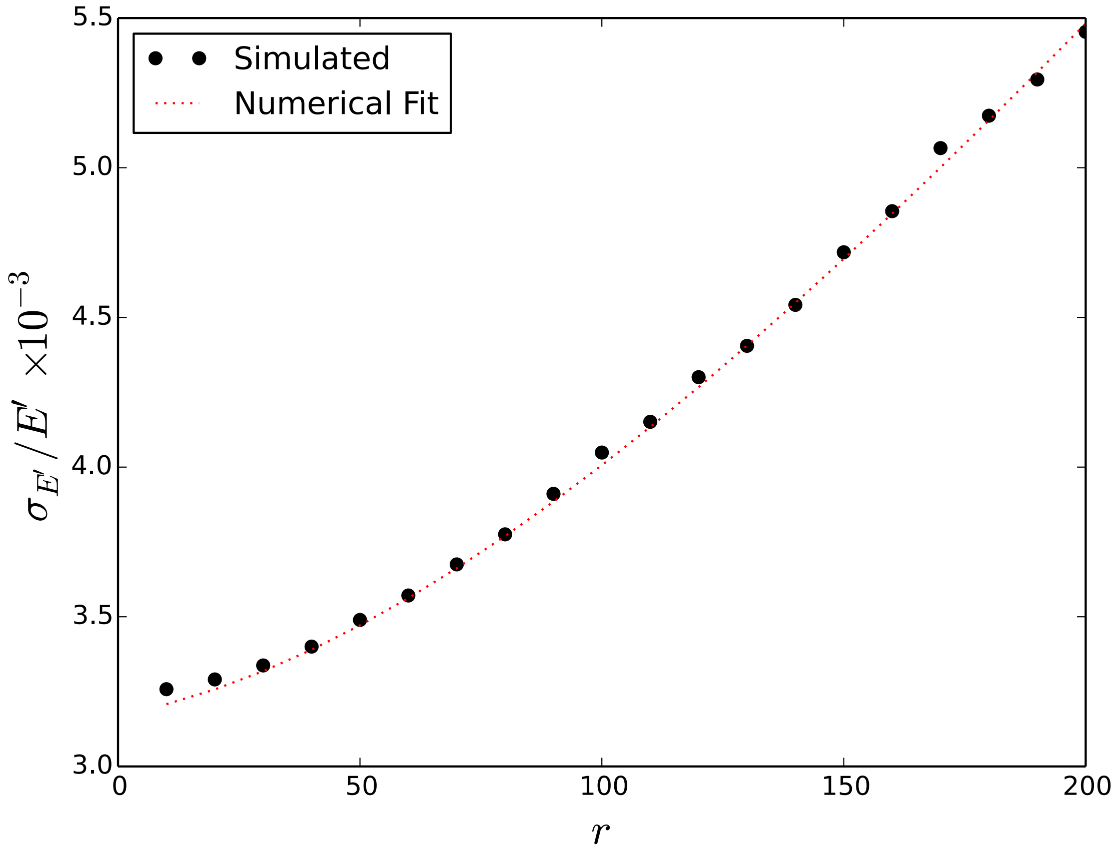

FIG. 35: Total normalized spread in spectra generated from Compton scattering $\sigma_{E'}/E'$ as a function of ratio of transverse electron beam size to transverse laser field size $r = \sigma_x/\sigma_{x,l}$ for the following parameters: $E_\mathrm{e} = 500$ MeV; $\sigma_{E_\mathrm{e}}/E_\mathrm{e} = 5.0 \times 10^{-4}\%$; $\sigma_x = \sigma_y = 1.0 \times 10^{-5}$ m; $\lambda = 800$ nm; $a_0 = 0.0113$; $\sigma_{z,l} = 28.3 \times 10^{-6}$ m; $\epsilon_x = \epsilon_y = 5.0 \times 10^{-11}$ m rad; $\theta_\mathrm{A} = 8.8 \times 10^{-5}$. All sources of spectral broadening other than r have been minimized. As r increases, i.e., as the transverse size becomes small relative to the transverse electron beam size, the total spread increases. For r greater than 50, the spectral broadening from r dominates the total spectral broadening, and the dependence of r on total spread becomes linear.

total spread in the scattered spectrum may be given by

$$\frac{\sigma_{E'}}{E'} = \sqrt{\left(\frac{\sigma_{\theta_{MAX}}}{E_{\theta_{MAX}}} + \frac{\sigma_\epsilon}{E_\epsilon}\right)^2 + \left(\frac{\sigma_L}{E_L}\right)^2 + \left(\frac{\sigma_\gamma}{E_\gamma}\right)^2 + \left(\frac{\sigma_r}{E_r}\right)^2}, \tag{123}$$

where $\sigma_{\theta_{MAX}}/E_{\theta_{MAX}}$ is the spread from the maximum aperture opening, $\sigma_\epsilon/E_\epsilon$ is the spread from emittance, σ_L/E_L is the spread from the longitudinal photon spread, and σ_γ/E_γ is the energy spread in the electron beam. From the simulation data in Figure 35, the energy spread as a function of r becomes linear for higher r values. Figure 36 shows plots using the same parameters from Figure 35 for various emittance values. The plots show that the slope increases as emittance increases; therefore, the spread from r depends on emittance.

4.6 SCALING LAWS FOR SPECTRAL BROADENING FOR THE COMPTON REGIME

One of the driving purposes for modeling Compton scattering is to develop methods for minimizing the bandwidth of the scattered radiation. As previously stated in Section 3.8, spectral broadening arises form the energy spread and emittance of the electron beam, energy spread in the incident photons, and from viewing the scattered radiation through a finite aperture. These expressions governing bandwidth in photon-electron collisions will be readdressed for the Compton regime using the previously derived expression for the angular frequency of the scattered photon as a function of the Compton parameter X, Eq. (82) [57, 73]. Here the Planck constant will be used to transform the expression from frequency to energy

$$E'_{\text{ph,max}} = \frac{4\gamma^2 E_{\text{L}}}{1 + X + \theta^2\gamma^2}. \tag{124}$$

By implementing a computational model that incorporates the full Compton recoil, it is confirmed through simulation that the influence of the laser bandwidth and aperture vanishes in collision regimes where electron recoil is substantial. Both the analysis and the simulations will show that the bandwidth arising from the electron beam emittance also decreases as the electron recoil is increased. For convenience, the parameter Ψ will be used

$$\Psi = \gamma\theta_{\text{MAX}}. \tag{125}$$

The amended scaling laws for the energy spread in the the electron beam and the photon beam may be found by taking the derivative of Eq. (83) and Eq. (124). First, consider the derivative of the Compton edge expression

$$\mathrm{d}E'_{\text{ph,max}} = \frac{8\gamma E_L \mathrm{d}\gamma}{1+X} + \frac{4\gamma^2 \mathrm{d}E_L}{1+X} - \frac{4\gamma^2 E_L \mathrm{d}X}{(1+X)^2}. \tag{126}$$

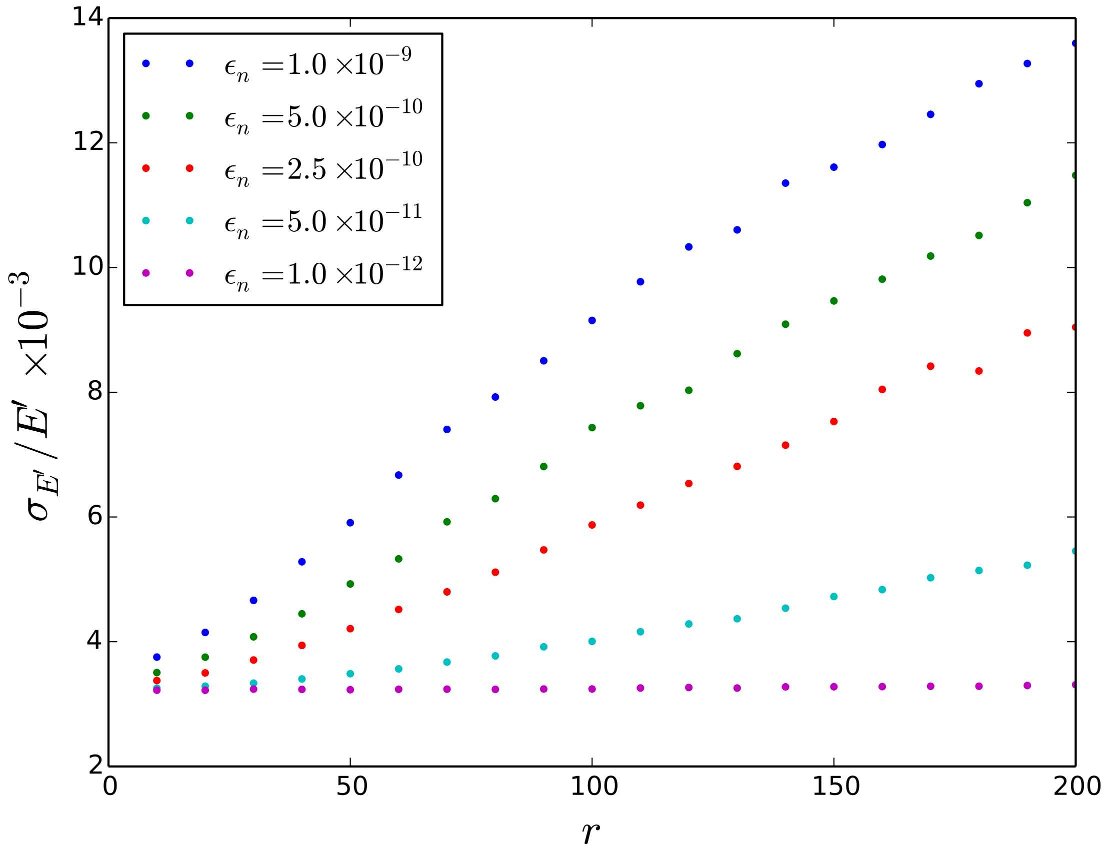

FIG. 36: Total normalized spread in spectra generated from Compton scattering $\sigma_{E'}/E'$ as a function of ratio of transverse electron beam size to transverse laser field size $r = \sigma_x/\sigma_{x,l}$ for various values of normalized emittance ϵ_n for the following parameters: $E_{\mathrm{e}} = 500$ MeV; $\sigma_{E_{\mathrm{e}}}/E_{\mathrm{e}} = 5.0 \times 10^{-4}\%$; $\sigma_x = \sigma_y = 1.0 \times 10^{-5}$ m; $\lambda = 800$ nm; $a_0 = 0.0113$; $\sigma_{z,l} = 28.3 \times 10^{-6}$ m; $\epsilon_x = \epsilon_y = 5.0 \times 10^{-11}$ m rad; $\theta_{\mathrm{A}} = 8.8 \times 10^{-5}$. From previous work [57], one expects an increased emittance to affect the curved portion of these plots for low values of r. It is important to note, however that increased emittance also increases the slope of the plot for higher r values; this suggests that the spectral broadening due to r is also dependent upon ϵ_n.

This expression may be normalized by dividing both sides by E'_{ph}:

$$\frac{\mathrm{d}E'_{\text{ph}}}{E'_{\text{ph}}} = \frac{2+X}{1+X}\frac{\mathrm{d}\gamma}{\gamma} + \frac{1}{1+X}\frac{\mathrm{d}E_L}{E_L}, \tag{127}$$

where $\mathrm{d}\gamma/\gamma$ is the energy spread in the electron beam and $\mathrm{d}E_L/E_L$ is the energy distribution in the photon pulse. Since this derivation uses Eq. (83), it proceeds from the assumption that the radiation is scattered on-axis, i.e., $\theta = 0$. To generalize the result for all scattered angles, take the derivative of Eq. (124) and evaluate the total error:

$$\frac{\mathrm{d}E'_{\text{ph}}}{E'_{\text{ph}}} = \frac{\sigma_\gamma}{E_\gamma} + \frac{\sigma_L}{E_L} - \frac{2\Psi^2}{1+X+\Psi^2}\frac{\mathrm{d}\theta}{\theta}. \tag{128}$$

This expression is solved for the new, Compton-scaled treatments of bandwidth from electron and photon energy spread:

$$\frac{\sigma_\gamma}{E_\gamma} = \frac{2+X}{1+X+\Psi^2}\frac{\mathrm{d}\gamma}{\gamma} + \frac{1}{1+X}\frac{\mathrm{d}E_L}{E_L}, \tag{129}$$

and

$$\frac{\sigma_L}{E_L} = \frac{1+\Psi^2}{1+X+\Psi^2}\frac{1}{2\sqrt{2}\pi\sigma}. \tag{130}$$

Consider next Eq. (48) from Section 3.8, the expression for the linewidth due to a circular, on-axis sensor aperture in the Thomson regime:

$$\frac{\sigma_{\theta_{\text{MAX}}}}{E_{\theta_{\text{MAX}}}} = \frac{\omega'_{\text{max}} - \omega'_{\text{min}}}{\sqrt{12}\omega'_{\text{mid}}}.$$

In the Compton regime, the angular frequency expression are changed: $\omega'_{\text{max}} \to 4\omega\gamma^2/(1+X)$ and $\omega'_{\text{min}} \to 4\omega\gamma^2/(1+X+\Psi^2)$. Using these properly scaled frequencies, the bandwidth due to the aperture opening may be properly scaled for the Compton regime

$$\frac{\sigma_{\theta_{\text{MAX}}}}{E_{\theta_{\text{MAX}}}} = \frac{1}{\sqrt{12}}\frac{\Psi^2}{1+X+\Psi^2/2}. \tag{131}$$

The Compton-scaled linewidth due to emittance may be calculated analytically using the definition of normalized variance [74]

$$\frac{\sigma_\epsilon^2}{E_\epsilon^2} = \frac{\left\langle E'^2_{\text{ph}}\right\rangle - \left\langle E'_{\text{ph}}\right\rangle^2}{\left\langle E'_{\text{ph}}\right\rangle^2}. \tag{132}$$

In order to solve the expected values with respect to emittance ϵ, the scattered energy must be redefined in terms of emittance. Consider some angle $\theta_r = \sqrt{\theta_x^2 + \theta_y^2}$ by which the individual photon angle is misaligned from the electron beam trajectory. It is important to break the emittance dependence into horizontal x and vertical y components so that the analysis is general for asymmetric beams. The misalignment angles have some distribution $\rho(\theta_x, \theta_y)$ within the electron beam. A bivariate normal distribution is a reasonable assumption for a high quality electron beam:

$$\rho(\theta_x, \theta_y) = \frac{1}{2\pi\sigma_{\theta_x}\sigma_{\theta_y}} \exp\left(-\frac{\theta_x^2}{2\sigma_{\theta_X}^2} - \frac{\theta_y^2}{2\sigma_{\theta_y}^2}\right). \tag{133}$$

The spread in this distribution describes the transverse size, or spot size, of the electron beam. These variable are related to the electron beam emittance through the beta function of the acclerator β^*

$$\sigma_{\theta_x} = \sqrt{\frac{\epsilon_x}{\beta_x^*}}; \quad \sigma_{\theta_y} = \sqrt{\frac{\epsilon_y}{\beta_y^*}}. \tag{134}$$

Eq. (124) may be rewritten

$$E'_{\mathrm{ph,max}} = \frac{4\gamma^2 E_{\mathrm{L}}}{1 + X + \left(\theta_x^2 + \theta_y^2\right)^2 \gamma^2}. \tag{135}$$

The expected values in Eq. (132) may be calculated up to the fourth order:

$$\begin{aligned}\left\langle E'_{\mathrm{ph}}\right\rangle &= \int\int_{-\infty}^{\infty} E'_{\mathrm{ph}}(\theta_x, \theta_y)\rho(\theta_x, \theta_y)\mathrm{d}\theta_x\mathrm{d}\theta_y \\ &\approx E'_{\mathrm{ph,max}}\left(1 - \frac{\gamma^2\left(\theta_x^2 + \theta_y^2\right)}{1 + X} + \frac{\gamma^4\left(3\sigma_{\theta_x}^4 + 2\sigma_{\theta_x}^2\sigma_{\theta_y}^2 + 3\sigma_{\theta_y}^4\right)}{(1 + X)^2}\right),\end{aligned} \tag{136}$$

and

$$\begin{aligned}\left\langle E'^2_{\mathrm{ph}}\right\rangle &= \int\int_{-\infty}^{\infty} E'^2_{\mathrm{ph}}(\theta_x, \theta_y)\rho(\theta_x, \theta_y)\mathrm{d}\theta_x\mathrm{d}\theta_y \\ &\approx E'^2_{\mathrm{ph,max}}\left(1 - \frac{2\gamma^2\left(\theta_x^2 + \theta_y^2\right)}{1 + X} + \frac{3\gamma^4\left(3\sigma_{\theta_x}^4 + 2\sigma_{\theta_x}^2\sigma_{\theta_y}^2 + 3\sigma_{\theta_y}^4\right)}{(1 + X)^2}\right).\end{aligned} \tag{137}$$

After substituting these solutions back into Eq. (132), the linewidth from emittance may be calculated

$$\frac{\sigma_\epsilon}{E_\epsilon} = \frac{\sqrt{2}\gamma}{1 + X}\sqrt{\left(\frac{\epsilon_x}{\beta_x^*}\right)^2 + \left(\frac{\epsilon_y}{\beta_y^*}\right)^2}. \tag{138}$$

CHAPTER 5

NONLINEAR THOMSON SCATTERING

For a laser pulse in the plane-wave approximation and for an electron that is limited to on-axis motion, i.e., the electron has no transverse motion ($p_x = p_y = 0$), the total energy density spectrum for a photon-electron collision in the nonlinear Thomson regime may be calculated

$$\begin{aligned}\frac{\mathrm{d}^2 E'}{\mathrm{d}\omega'\mathrm{d}\Omega} = \frac{e^2\omega'^2}{16\pi^3\epsilon_0 c^3}\Bigg(&\left|D_1\Big(\omega(\omega')\Big)\right|^2 \sin^2\phi \\ &+\left|D_1\Big(\omega(\omega')\Big)\left(\frac{\cos\theta-\beta_z}{1-\beta_z\cos\theta}\right)\cos\phi + D_2\Big(\omega(\omega')\Big)\sin\theta\right|^2\Bigg),\end{aligned} \tag{139}$$

where e is the electron charge, ω is the incident photon angular frequency, c is the speed of light, θ, ϕ are the polar coordinates centered on the point of collision, and the functions $D_{1,2}(\omega(\omega'))$ are the effective motion of the electron as it passes through the laser pulse field. Eq. (139) has been derived by first calculating the electron's equations of motion by solving the Hamilton-Jacobi. Then the equations of motion were applied to Eq. (45), the general expression for the energy density spectrum generated by a moving charged particle from Section 3.7.

In the nonlinear regime, the high intensity of the incident laser pulse induces relativistic, oscillatory motion in the electron. The electron takes on a figure-eight-type orbit within its average rest frame that causes the charged particle to emit dipole radiation. The intensity causes several nonlinear effects to manifest in the scattered radiation including a significant spectral broadening. Borrowing the term from Wolfgang Pauli's review article, this increased bandwidth is referred to as *ponderomotive* broadening as it scales with square of the field strength a_0^2 [75]. These effects are discussed in detail in this chapter.

As with the previous chapter, this chapter will begin with a brief discussion of the numerical methods implemented to integrate the nonlinear Thomson energy density spectrum. The energy density spectrum presented above will be derived using the Hamilton-Jacobi method. The Hamilton-Jacobi will also be used to derive the energy density spectrum for an electron with transverse motion. Through a clever parameterization similar to that found in Section 4.5.1, Eq. (139) will also be generalized for a collision that involves an incident photon field with a finite transverse size. These derivations are followed by an in-depth survey of the ponderomotive effects that degrade emitted spectra in the nonlinear regime. Frequency modulation of the incident laser pulse, or chirping, is the method by which the incident frequency of the laser pulse is manipulated over the length of the pulse to minimize the ponderomotive effects on the scattered spectra. Chirping will be well-defined, and the optimal chirping prescriptions will be given for plane-waves and incident laser fields with finite transverse size. The nonlinear Thomson chapter will conclude with a discussion of a new functionality to the computational model: the incident laser fields may be represented by discrete data sets instead of analytic functions. This new functionality has been developed to accommodate state-of-the-art nonlinear, high-intensity lasers whose measured fields do not neatly conform to the shape of analytic functions.

5.1 NONLINEAR THOMSON COMPUTATIONAL MODEL

This nonlinear Thomson computational model, called SENSE [72], is coded in Python [63] and utilizes Cython [64] modules for computational efficiency. Likewise, the script takes full advantage of the Python multiprocessing library in order to run the calculations in parallel: the calculations are distributed across many processing cores and allowed to run simultaneously. The nonlinear Thomson spectra are generated by integrating Eq. (139) over the solid angle of a sensor aperture [60, 72]

$$\begin{aligned}\frac{\mathrm{d}E'}{\mathrm{d}\omega'} = \frac{e^2\omega'^2}{16\pi^3\epsilon_0 c^3}\int\int_\Omega \Bigg(&\left| D_1\Big(\omega(\omega')\Big)\right|^2 \sin^2\phi \\ &+ \left| D_1\Big(\omega(\omega')\Big)\left(\frac{\cos\theta-\beta_z}{1-\beta_z\cos\theta}\right)\cos\phi + D_2\Big(\omega(\omega')\Big)\sin\theta\right|^2\Bigg)\mathrm{d}\Omega.\end{aligned} \tag{140}$$

There are, however, additional integrals in the effective motion functions $D_{1,2}$ that are also not analytically tractable [72]

$$D_{1,2} \propto \int_{-\infty}^{\infty} \tilde{A}^{1,2}(\xi)\exp\left\{ i\omega\left(\xi\kappa_0 + \kappa_1\int_{-\infty}^{\xi}\tilde{A}(\xi')\mathrm{d}\xi' + \kappa_2\int_{-\infty}^{\xi}\tilde{A}^2(\xi')\mathrm{d}\xi'\right)\right\}\mathrm{d}\xi, \tag{141}$$

where $\kappa_{0,1,2}$ are constant relative to the integrals and $\tilde{A}(\xi)$ is the normalized field vector for the incident laser pulse. These integrals within the effective motion functions are calculated numerically using the Simpson method [76]:

$$\int_{x_0}^{x^2} f(x)\mathrm{d}x = \frac{h}{3}\left(y_0 + 4y_1 + y_2\right) - \frac{h^5}{90}f^{(4)}(c), \tag{142}$$

where $h = x_2 - x_1 = x_1 - x_0$ and c is between x_0 and x_2.

The highly oscillatory nature of the effective motion functions introduces a significant challenge to the quadrature. Because of this, the outer double integral over the solid angle of the aperture cannot be completed efficiently using the scipy `dblquad` function. Monte Carlo is used to complete the integration: values for the polar coordinates θ, ϕ are generated randomly for the bounds of the sensor aperture and then averaged over some number of iterations n_{MC}. For a sufficiently high number of iterations, the error of this quadrature is negligible to our spectrum calculation

$$\mathrm{ERROR} \propto n_{\mathrm{MC}}^{-1/2}. \tag{143}$$

As with the linear Compton model, the integrals in Eq. (140) are calculated for every single electron in the beam and then summed in order to generate the total scattered spectrum. Due to the additional integrations and the highly oscillatory nature of the nonlinear energy density spectrum, the nonlinear Thomson computational model requires significantly more run time than the linear Compton model. The run time scales directly with the resolution of the integrations, and so so higher field strength simulations require much more processing time.

5.2 DERIVATION OF THE NONLINEAR THOMSON ENERGY DENSITY SPECTRUM

The ponderomotive effects unique to the nonlinear regime arise from the motion of the electron in its own center of mass frame. In order to capture these effects with the computational model, this motion must be accounted for in the energy density spectrum. The relativistic velocity $\boldsymbol{\beta}$ in Eq. (45), the general expression for the energy density spectrum emitted from a moving charged particle, captures that motion:

$$\frac{\mathrm{d}^2 E'}{\mathrm{d}\omega' \mathrm{d}\Omega} = \frac{e^2 \omega'^2}{16\pi^3 \epsilon_0 c^3} \left| \int_{-\infty}^{\infty} \mathbf{n} \times (\mathbf{n} \times \boldsymbol{\beta})\, e^{i\omega(t - \mathbf{n}\cdot\mathbf{r}(t)/c)}\, \mathrm{d}t \right|^2 .$$

Calculating the equations of motion for the Thomson scattered electron, i.e., calculating the relativistic velocity $\boldsymbol{\beta}$, may be achieved through the Hamilton-Jacobi method. In Section 5.2.1, the Hamilton-Jacobi method theory for a charged particle is defined. The general equations of motion are solved for the Thomson scattered electron in Appendix B. The linear Thomson energy density spectra for an on-axis electron and for an electron with transverse motion are presented here. The energy density spectrum for the on-axis electron will also be generalized for an electron with three dimensional momentum through a clever paramertization of the incident laser field.

5.2.1 HAMILTON-JACOBI THEORY FOR A CHARGED PARTICLE WITH RELATIVISTIC VELOCITY

Hamilton-Jacobi theory uses canonical transforms to provide a general procedure for solving mechanical problems [77, 78]. Specifically, this method seeks a transformation from the coordinates $\boldsymbol{q}$ and the momenta $\boldsymbol{p}$ at time t into a new set of *constant* quantities which may be the initial values $\boldsymbol{q}_0 = \boldsymbol{q}(t = 0)$ and $\boldsymbol{p}_0 = \boldsymbol{p}(t = 0)$. This powerful method solves general equations of motion in terms of the initial coordinates and momenta for Hamiltonian systems that evolve with time. This method may be used for any Hamiltonian $\mathscr{H}$ that solves the Hamilton-Jacobi equation

$$-\frac{\partial S}{\partial t} = \mathscr{H}\left(q_i, \frac{\partial S}{\partial q_i}, t\right), \tag{144}$$

for a general function S known as *Hamilton's principle function.* Hamilton's principle function also has the following properties

$$p_i = \frac{\partial S}{\partial q_i}, \tag{145}$$

$$Q_i = \beta_i = \frac{\partial S}{\partial P_i}, \tag{146}$$

where the constants $\boldsymbol{Q}$ and $\boldsymbol{P}$ will reduce to the initial coordinate and initial momentum in this problem. The power in the Hamilton-Jacobi theory comes from these conditions: once an appropriate function S has been found for a known Hamiltonian $\mathscr{H}$, then the equations of motion may be solved through first order derivatives.

Hamilton-Jacobi theory has been used to solve the equations of motion of for a Thomson scattered electron. If the intensity of the incident laser pulse is appropriately high, the electron will begin to oscillate at a relativistic velocity within its own average rest frame. This oscillatory motion causes the electron to emit dipole radiation. By applying these equations of motion to the fundamental principles of electrodynamics, the effective motion of the electron $D_{1,2}$ may be solved, and this effective motion $D_{1,2}$ may be used to calculate the energy density spectrum of the scattered radiation in the lab frame [79].

In order to calculate the effective motion $D_{1,2}$ of the electron, the Hamiltonian $\mathscr{H}$ and the appropriate form of Hamilton's principle function S must be established first. The Lagrangian $\mathscr{L}$ for an electron passing through an electromagnetic filed with relativistic motion is defined

$$\mathscr{L} = -mc^2\sqrt{1-\beta^2} + e\varphi - \frac{e}{c}\boldsymbol{v}\cdot\boldsymbol{A}. \tag{147}$$

where m is the electron mass, c is the speed of light, β is the relativistic speed of the electron, e is the elementary charge, φ is the electric potential, $\boldsymbol{v}$ is the velocity of the electron, and $\boldsymbol{A}$ is the vector potential. The canonical momentum of the electron is the first derivative of the Lagrangian $\mathscr{L}$ with respect to the velocity of the electron:

$$\boldsymbol{P} = \frac{\partial \mathscr{L}}{\partial \boldsymbol{v}} = \gamma m\boldsymbol{v} - \frac{e}{c}\boldsymbol{A}. \tag{148}$$

The Hamiltonian $\mathscr{H}$ of the relativistic electron is the difference of the relativistic and potential energies of the electron

$$\mathscr{H} = \gamma mc^2 - e\varphi. \tag{149}$$

Eq. (149) may be expanded using the relativistic energy-momentum equation and the canonical momentum of the electron, i.e., Eq. (148)

$$(\mathscr{H} + e\varphi)^2 = m^2c^4 + \left(\boldsymbol{P} + \frac{e}{c}\boldsymbol{A}\right)^2 c^2. \tag{150}$$

Using Eq. (144) and Eq. (145), this expression may be expressed in terms of the Hamilton-Jacobi equation and the definition of the electron momentum in terms of Hamilton's principle function S

$$\left(-\frac{\partial S}{\partial t} + e\varphi\right)^2 = m^2c^4 + \left(\frac{\partial S}{\partial \boldsymbol{r}} + \frac{e}{c}\boldsymbol{A}\right)^2 c^2. \tag{151}$$

This equation is valid for any charged particle passing through an electromagnetic field at a relativistic speed. The Hamilton-Jacobi method may be used to find the equations of motion for any vector potential $\boldsymbol{A}$ for which there is some function S that makes Eq. (151) true.

5.2.2 ON-AXIS ELECTRON ENERGY DENSITY SPECTRUM

The equations of motion for the Thomson scattered electron are calculated in Appendix B by solving the Hamilton-Jacobi equation. This solution is for an electron with transverse initial momentum, but the on-axis equations of motion may be found by simply taking the limit where the initial transverse momentum and the initial transverse position are zero, i.e., $k_x, k_y \to 0$ and $x_0, y_0 \to 0$. The velocity components from the equations of motion are solved in terms of the initial relativistic velocity of the electron β

$$\frac{v_x}{c} = \frac{1}{c}\frac{\mathrm{d}x}{\mathrm{d}\xi}\frac{\mathrm{d}\xi}{\mathrm{d}t} = \frac{1}{\gamma\,(1+\beta)}\tilde{A}(\xi), \tag{152}$$

$$\frac{v_y}{c} = \frac{1}{c}\frac{\mathrm{d}y}{\mathrm{d}\xi}\frac{\mathrm{d}\xi}{\mathrm{d}t} = 0, \tag{153}$$

and

$$\frac{v_z}{c} = \frac{1}{c}\frac{\mathrm{d}z}{\mathrm{d}\xi}\frac{\mathrm{d}\xi}{\mathrm{d}t} = -\frac{1}{\gamma^2\,(1+\beta)^2}\tilde{A}^2(\xi) + \frac{\beta}{1+\beta}, \tag{154}$$

where $\tilde{A}(\xi) = eA(\xi)/mc$ is the normalized vector potential envelope. The phase argument from Eq. (45) has also been calculated for the far-field approximation

$$\begin{aligned} t - \frac{\mathbf{n}\cdot\mathbf{r}(t)}{c} &= \frac{\xi}{c(1+\beta)}\,(1-\beta\cos\theta) + \left[-\frac{\sin\theta\cos\phi}{c\gamma(1+\beta)}\right]\int_{-\infty}^{\xi}\tilde{A}(\xi')\mathrm{d}\xi' \\ &\quad + \left[\frac{1+\cos\theta}{c\gamma^2\,(1+\beta)^2}\right]\int_{-\infty}^{\xi}\tilde{A}^2(\xi')\mathrm{d}\xi'. \end{aligned} \tag{155}$$

By introducing a change of variable from time to the independent variable ξ, the energy density spectrum may be defined by completing the cross products in Eq. (45). The component of the energy density spectrum radiating in the plane of collision is

$$\frac{\mathrm{d}^2E'_\sigma}{\mathrm{d}\omega'\mathrm{d}\Omega} = \frac{e^2\omega'^2}{16\pi^3\epsilon_0c^3}\,|D_1(\omega)|^2\sin^2\phi, \tag{156}$$

and the component of the energy density spectrum radiating perpendicular to the plane of collision is

$$\frac{\mathrm{d}^2E'_\pi}{\mathrm{d}\omega'\mathrm{d}\Omega} = \frac{e^2\omega'^2}{16\pi^3\epsilon_0c^3}\left|D_1(\omega)\left(\frac{\cos\theta-\beta}{1-\beta\cos\theta}\right)\cos\phi + D_2(\omega)\sin\theta\right|^2, \tag{157}$$

where the effective motion functions are defined

$$
\begin{aligned}
D_1 = \int \frac{\mathrm{d}\xi}{\gamma(1+\beta)} \frac{eA_x(\xi)}{mc^2} & \\
\times \exp \Bigg[i\omega \Bigg(& \frac{\xi(1-\beta\cos\theta)}{c(1+\beta)} - \frac{\sin\theta\cos\phi}{c\gamma(1+\beta)} \int_{-\infty}^{\xi} \frac{eA_x(\xi')}{mc^2}\mathrm{d}\xi' \\
& + \frac{(1+\cos\theta)}{c\gamma^2(1+\beta)^2} \int_{-\infty}^{\xi} \frac{e^2A_x^2(\xi')}{2m^2c^4}\mathrm{d}\xi' \Bigg) \Bigg],
\end{aligned} \tag{158}
$$

and

$$
\begin{aligned}
D_2 = \frac{1+\beta}{(1-\beta\cos\theta)} \int \frac{\mathrm{d}\xi}{\gamma^2(1+\beta)^2} \frac{e^2A_x^2(\xi)}{2m^2c^4} & \\
\times \exp \Bigg[i\omega \Bigg(& \frac{\xi(1-\beta\cos\theta)}{c(1+\beta)} - \frac{\sin\theta\cos\phi}{c\gamma(1+\beta)} \int_{-\infty}^{\xi} \frac{eA_x(\xi')}{mc^2}\mathrm{d}\xi' \\
& + \frac{(1+\cos\theta)}{c\gamma^2(1+\beta)^2} \int_{-\infty}^{\xi} \frac{e^2A_x^2(\xi')}{2m^2c^4}\mathrm{d}\xi' \Bigg) \Bigg].
\end{aligned} \tag{159}
$$

These $D(\omega)$ functions include the nonlinear effective frequency considerations generated by the vector potential induced electron motion. They also include the effects of a finitely extended vector potential that occurs in a short laser pulse. This calculation for the scattered spectrum is quite general within the Thomson limit since the only approximation relied upon is the far-field approximation, i.e., when the observation occurs at a distance much greater than the source size ($\boldsymbol{R}(t') \gg \boldsymbol{r}(t')$ from Figure 23).

By applying the limit that the field strength vanishes $a_0 \to 0$, these polarization of the nonlinear energy density spectrum have been reduced to the well documented linear Thomson calculations in previous work [60, 56],

$$
\frac{\mathrm{d}^2E'_\sigma}{\mathrm{d}\omega'\mathrm{d}\Omega} = \frac{r_e^2}{16\pi^3\epsilon_0 c} \frac{\left|\tilde{E}\left[\omega(1-\beta\cos\theta)/c(1+\beta)\right]\right|^2}{\gamma^2(1-\beta\cos\theta)^2} \sin^2\phi, \tag{160}
$$

and spectral density perpendicular to the plane of scattering

$$
\frac{\mathrm{d}^2E'_\pi}{\mathrm{d}\omega'\mathrm{d}\Omega} = \frac{r_e^2}{16\pi^3\epsilon_0 c} \frac{\left|\tilde{E}\left[\omega(1-\beta\cos\theta)/c(1+\beta)\right]\right|^2}{\gamma^2(1-\beta\cos\theta)^2} \left(\frac{\cos\theta-\beta}{1-\beta\cos\theta}\right)^2 \cos^2\theta. \tag{161}
$$

3D Laser Treatment

The nonlinear Thomson computational model may be generalized to include 3D laser field treatments using the magnitude approximation technique implemented in the linear Compton model in Section 4.5.1. As in the previous analysis, the field strength parameter for a 3D Gaussian distribution is path-dependent, and thereby computed for each electron using its initial momentum and initial coordinate:

$$\bar{a}_0 = a_0 \exp\left\{-\frac{x_0^2}{2\sigma_{x,l}^2} - \frac{y_0^2}{2\sigma_{y,l}^2} - \frac{z_0^2}{2\sigma_{z,l}^2}\right\} \exp\left\{\frac{\eta}{2\tilde{\sigma}_{z,l}^2}\right\}.$$

In principle, the spread in the Gaussian is also changed in this approximation, but as previously stated, the impact on the scattered spectrum due to the parameterization of the Gaussian variance is negligible, even for cases of extreme emittance.

In order to integrate over the area of the sensor aperture, the nonlinear Thomson model creates a Monte Carlo distribution centered around the coordinate where the electron trajectory pierces the plane in which the aperture lies. The aperture lies some distance R from the collision in the longitudinal $\hat{z}$ dimension. Since the electron has non-zero angles, the electron will be offset from the z-axis by some small dimension that is a function of its relativistic velocity. The offset in $\hat{x}$ and $\hat{y}$ directions respectively are defined

$$x_0 = R\frac{\beta_x}{\beta_z}, \qquad y_0 = R\frac{\beta_y}{\beta_z}. \tag{162}$$

By changing the field strength parameter to the 3D Gaussian parameterized, path-dependent calculation and by accounting for the aperture offset, the on-axis nonlinear Thomson energy density spectrum may be generalized for electrons with transverse motion and 3D laser field treatments.

5.2.3 TRANSVERSE ELECTRON ENERGY DENSITY SPECTRUM

The equations of motion for the Thomson scattered electron is calculated in Appendix B by solving the Hamilton-Jacobi equation. This solution is for an electron with transverse initial momentum. The velocity components from the equations of motion are solved in terms of the initial relativistic velocity components of the electron $\beta_{x,y,z}$

$$\frac{v_x}{c} = \frac{1}{c}\frac{\mathrm{d}x}{\mathrm{d}\xi}\frac{\mathrm{d}\xi}{\mathrm{d}t} = \frac{1}{\gamma(1+\beta_z)}\left(\tilde{A}(\xi) + \gamma\beta_x\right), \tag{163}$$

$$\frac{v_y}{c} = \frac{1}{c}\frac{\mathrm{d}y}{\mathrm{d}\xi}\frac{\mathrm{d}\xi}{\mathrm{d}t} = \frac{\beta_y}{1+\beta_z}, \tag{164}$$

and

$$\frac{v_z}{c} = \frac{1}{c}\frac{\mathrm{d}z}{\mathrm{d}\xi}\frac{\mathrm{d}\xi}{\mathrm{d}t} = -\frac{1}{\gamma^2\left(1+\beta_z\right)^2}\left[\gamma\beta_x\tilde{A}(\xi) + \tilde{A}^2(\xi)\right] + \frac{\beta_z}{1+\beta_z}. \tag{165}$$

The phase argument from Eq. (45) has also been calculated for the far-field approximation

$$\begin{aligned} t - \frac{\mathbf{n}\cdot\mathbf{r}(t)}{c} &= \frac{\xi}{c(1+\beta_z)}\left(1 - \beta_x \sin\theta\cos\phi - \beta_y \sin\theta\sin\phi - \cos\theta\beta_z\right) \\ &+ \left[\frac{\beta_x(1+\cos\theta)}{c\gamma\,(1+\beta_z)^2} - \frac{\sin\theta\cos\phi}{c\gamma(1+\beta_z)}\right]\int_{-\infty}^{\xi}\tilde{A}(\xi')\mathrm{d}\xi' \\ &+ \left[\frac{1+\cos\theta}{c\gamma\,(1+\beta_z)^2}\right]\int_{-\infty}^{\xi}\tilde{A}^2(\xi')\mathrm{d}\xi'. \end{aligned} \tag{166}$$

By introducing a change of variable from time to the independent variable ξ, the energy density spectrum may be defined by completing the cross products in Eq. (45). The component of the energy density spectrum radiating in the plane of collision is

$$\begin{aligned} \frac{\mathrm{d}^2E'_\sigma}{\mathrm{d}\omega'\mathrm{d}\Omega} &= \frac{e^2\omega'^2}{16\pi^3\epsilon_0c^3}\times \\ &\left|D_1\sin\theta - \beta_x\frac{\left[\beta_x(1+\cos\theta)/(1+\beta_z) - \sin\theta\cos\phi\right]D_1 + (1+\cos\theta)D_2}{1-\beta_x\cos\phi\sin\theta - \beta_y\sin\phi\sin\theta - \beta_z\cos\theta}\sin\phi\right. \\ &\left.+\beta_y\frac{\left[\beta_x(1+\cos\theta)/(1+\beta_z) - \sin\theta\cos\phi\right]D_1 + (1+\cos\theta)D_2}{1-\beta_x\cos\phi\sin\theta - \beta_y\sin\phi\sin\theta - \beta_z\cos\theta}\cos\phi\right|^2, \end{aligned} \tag{167}$$

and the component of the energy density spectrum radiating perpendicular to the plane of collision is

$$\begin{aligned} \frac{\mathrm{d}^2E'_\pi}{\mathrm{d}\omega'\mathrm{d}\Omega} &= \frac{e^2\omega'^2}{16\pi^3\epsilon_0c^3}\left|D_1\cos\phi\cos\theta\right. \\ &-\beta_x\frac{\left[\beta_x(1+\cos\theta)/(1+\beta_z) - \sin\theta\cos\phi\right]D_1 + (1+\cos\theta)D_2}{1-\beta_x\cos\phi\sin\theta - \beta_y\sin\phi\sin\theta - \beta_z\cos\theta}\cos\phi\cos\theta \\ &-\beta_y\frac{\left[\beta_x(1+\cos\theta)/(1+\beta_z) - \sin\theta\cos\phi\right]D_1 + (1+\cos\theta)D_2}{1-\beta_x\cos\phi\sin\theta - \beta_y\sin\phi\sin\theta - \beta_z\cos\theta}\sin\phi\cos\theta \\ &+\beta_z\frac{\left[\beta_x(1+\cos\theta)/(1+\beta_z) - \sin\theta\cos\phi\right]D_1 + (1+\cos\theta)D_2}{1-\beta_x\cos\phi\sin\theta - \beta_y\sin\phi\sin\theta - \beta_z\cos\theta}\sin\theta \\ &\left.D_2\sin\theta + D_1\sin\theta\frac{\beta_x}{1+\beta_z}\right|^2. \end{aligned} \tag{168}$$

This off-axis solutions will be reduced to the on-axis calculations. As the initial transverse relativistic velocity of the electron goes to zero $\beta_x, \beta_y \to 0$, it is clear that Eq. (167) and Eq. (167) reduce to the on-axis energy density spectrum polarizations.

5.2.4 COMPARISON BY SIMULATION OF THE NONLINEAR ENERGY DENSITY SPECTRA

Though the energy density spectra for the on-axis electron motion that has been generalized for a 3D incident laser field, i.e., the energy density spectrum presented in Section 5.2.2, is quite different from the energy density spectrum calculated from the Hamilton-Jacobi solution for an electron with transverse motion, simulations show that both expressions produce nearly identical spectra. Figures 37-42 contain the spectra from this comparison study. For this work, a slightly amended version of SENSE, called NLTX, was written with the changed effective motion expressions. Every other aspect of the script remained unchanged. Each figure in the set contains nine pair of plots, one SENSE spectrum and one NLTX spectrum. The only parameters manipulated in the study were the horizontal emittance, vertical emittance, and field strength. The emittance was varied because the only difference in the calculations arises from the initial transverse relativistic velocity of the electron β_x, β_y. In the limit that they go to zero, the on-axis solution is recovered. The field strength parameter was changed to observe what role, if any, the nonlinear effects would play in the difference between these calculations. It is plainly clear from the results that even for extremely high emittance values– emittance values far beyond most operating accelerators– both models, SENSE and NLTX, produce nearly identical spectra, even at high field strength values.

There are two very important observations to take away from this study. First and most importantly, any approximations made in the parameterization of SENSE for the 3D envelope model did not undermine the accuracy of the generated spectrum: it is nearly exactly the same as the full transverse calculation. As SENSE has been thoroughly benchmark, this is not a surprise for the lower emittance calculations. The agreement of the two models at absurdly high emittance values, however, is a new benchmark for the original code.

The second important observation is that the new calculation is done in the lab frame. In the work presented so far, this has not been an issue as the the transform that allows for the use of the on-axis electron motion energy density spectrum is a simple rotation, and it is not computationally expensive. If there is ever a need to use since outside of a true backscattering orientation, however, the new Hamilton-Jacobi solution will be quite useful. The time resolution required to capture the photon-electron interaction will be significantly easier to compute in the lab frame. This is especially true if multiple photon beams are introduced into the collision– an interesting concept that may be used to cool the electron beam and reduce spectral broadening. These possible uses are beyond the scope of this work.

5.3 NONLINEAR EFFECTS UPON THE SCATTERED SPECTRA

As the field strength parameter increases from the linear regime, $a_0 \ll 1$, into higher field strengths, the motion of the electron is affected in four ways. The first effect is that the average velocity in the forward direction is reduced to

$$\beta_{\text{average}} = 1 - \frac{1 + \frac{a_0^2}{2}}{2\gamma^2}. \tag{169}$$

This reduced speed red-shifts the scattered radiation by a factor of $1 + a_0^2/2$ for a linearly polarized laser pulse. The second and third effects of the increased field strength arise from an induced a longitudinal and transverse modulation in the electron which causes a figure-eight motion in the rest frame of the electron. This induced oscillatory acceleration on the axis of travel generates

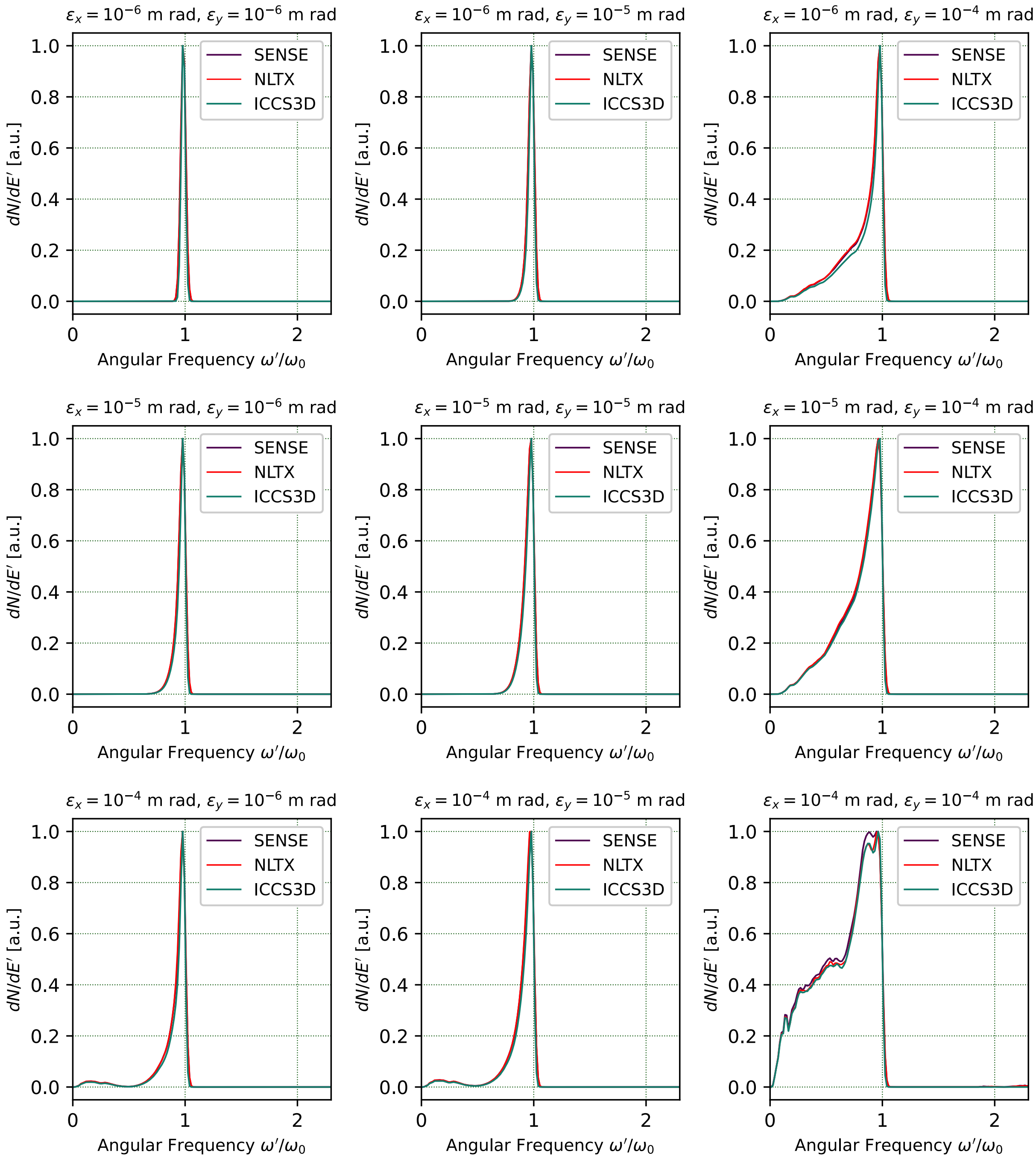

FIG. 37: Peak normalized simulated spectra from SENSE, ICCS3D, and NLTX for field strength $a_0 = 0.05$ and a range of normalized horizontal emittance ϵ_x and normalized vertical emittance ϵ_y values with the following parameters: $E_e = 23$ MeV; $\Delta E_e/E_e = 0.175\%$; $\sigma_x = 41$ μm; $\sigma_y = 81$ μm; $\lambda = 800$ nm; $\sigma_{x,l} = 13.59$ μm; $\sigma_{y,l} = 13.59$ μm; $\sigma = 5.57$.

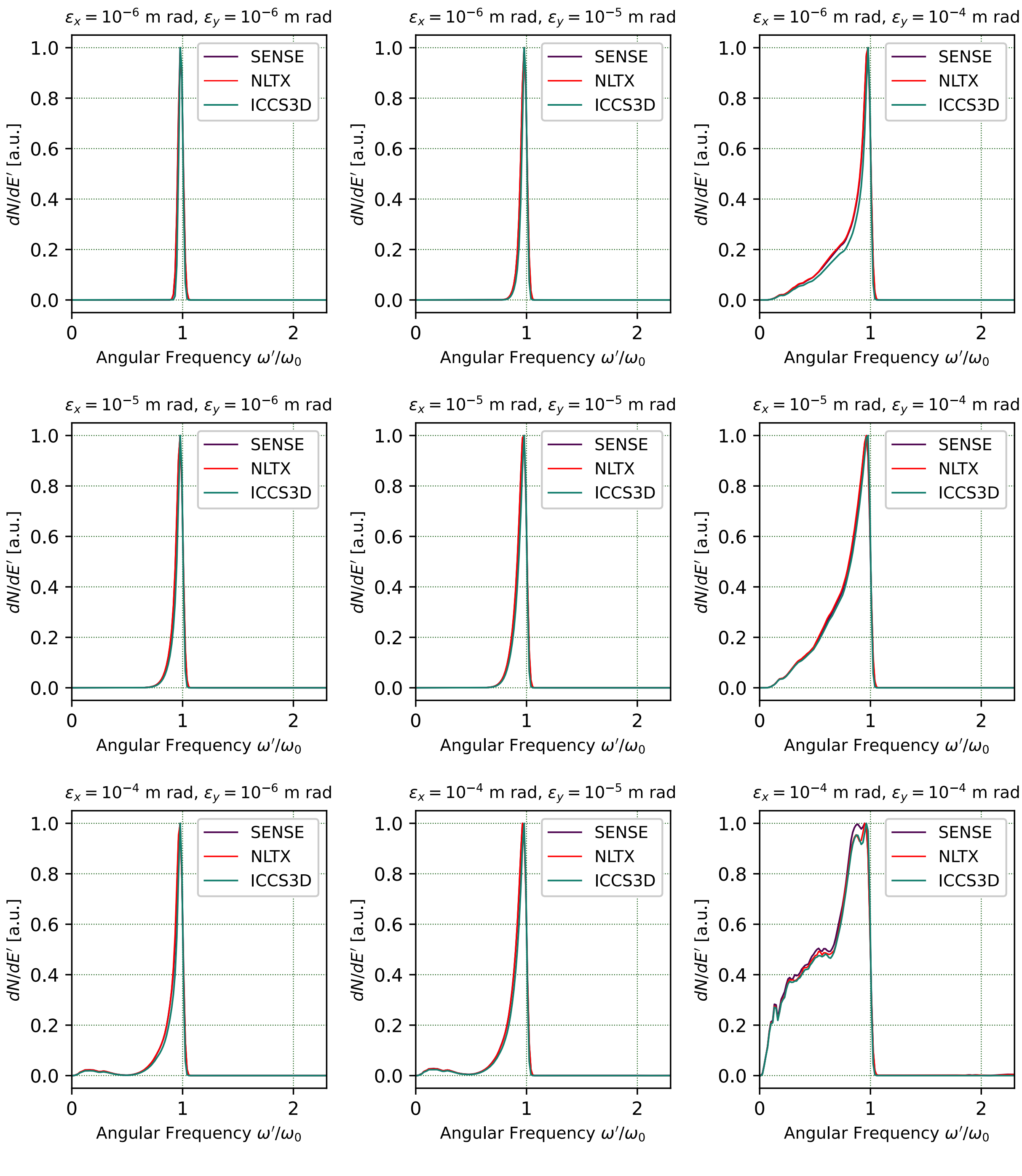

FIG. 38: Peak normalized simulated spectra from SENSE, ICCS3D, and NLTX for field strength $a_0 = 0.1$ and a range of normalized horizontal emittance ϵ_x and normalized vertical emittance ϵ_y values with the following parameters: $E_e = 23$ MeV; $\Delta E_e/E_e = 0.175\%$; $\sigma_x = 41$ μm; $\sigma_y = 81$ μm; $\lambda = 800$ nm; $\sigma_{x,l} = 13.59$ μm; $\sigma_{y,l} = 13.59$ μm; $\sigma = 5.57$.

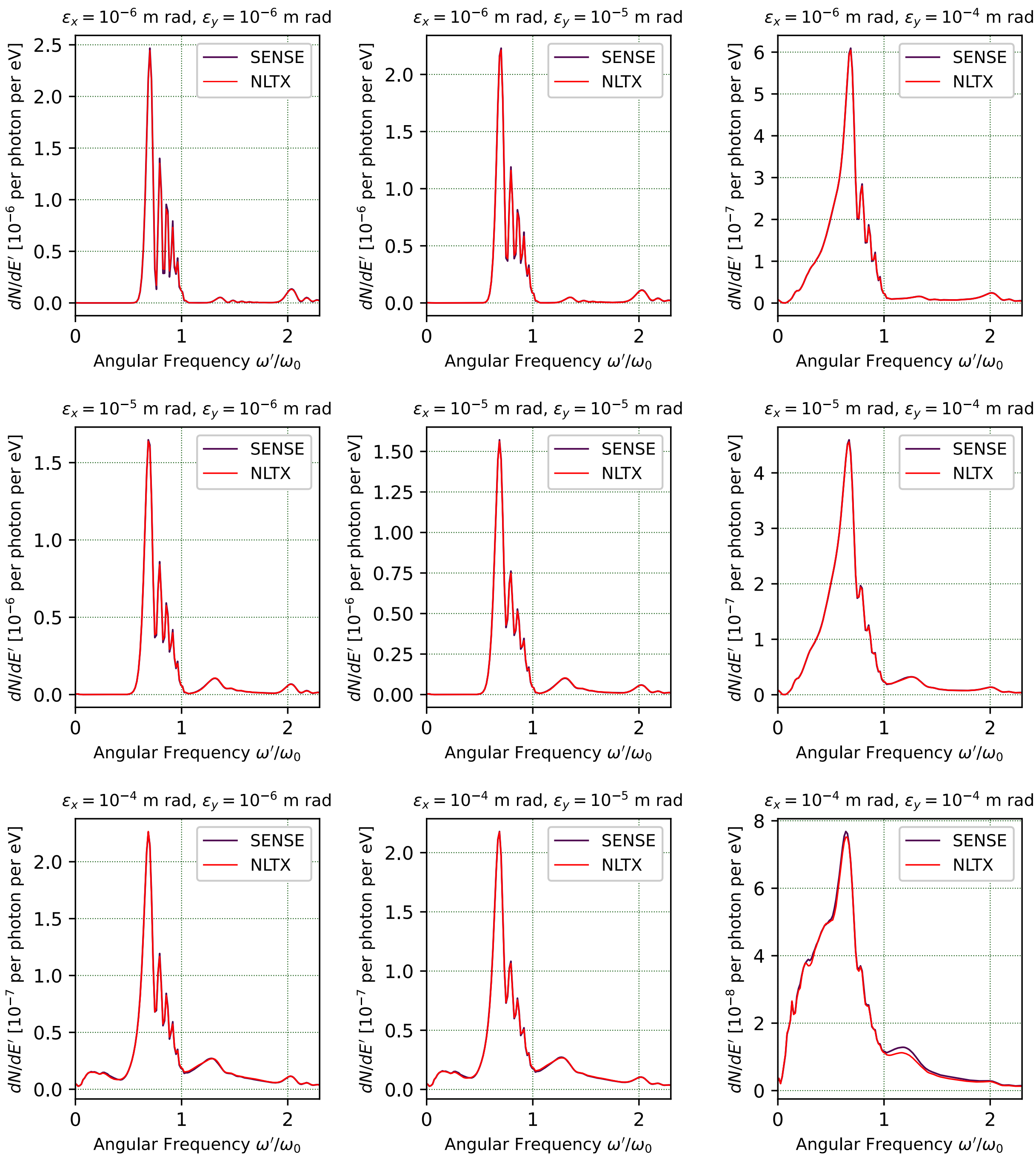

FIG. 39: Simulated spectra from SENSE and NLTX for field strength $a_0 = 1.0$ and a range of normalized horizontal emittance ϵ_x and normalized vertical emittance ϵ_y values with the following parameters: $E_e = 23$ MeV; $\Delta E_e/E_e = 0.175\%$; $\sigma_x = 41$ μm; $\sigma_y = 81$ μm; $\lambda = 800$ nm; $\sigma_{x,l} = 13.59$ μm; $\sigma_{y,l} = 13.59$ μm; $\sigma = 5.57$.

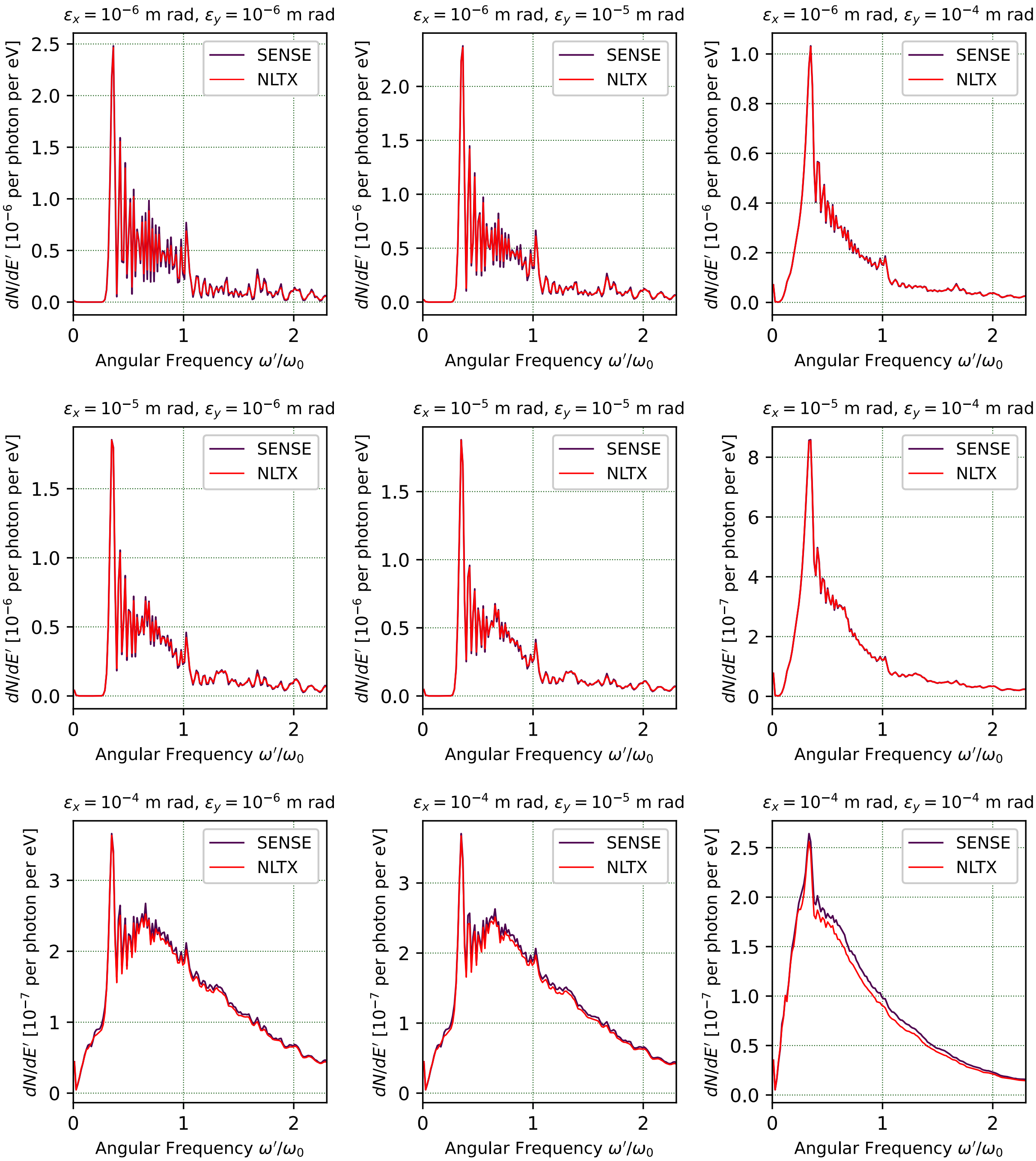

FIG. 40: Simulated spectra from SENSE and NLTX for field strength $a_0 = 2.0$ and a range of normalized horizontal emittance ϵ_x and normalized vertical emittance ϵ_y values with the following parameters: $E_e = 23$ MeV; $\Delta E_e/E_e = 0.175\%$; $\sigma_x = 41$ μm; $\sigma_y = 81$ μm; $\lambda = 800$ nm; $\sigma_{x,l} = 13.59$ μm; $\sigma_{y,l} = 13.59$ μm; $\sigma = 5.57$.

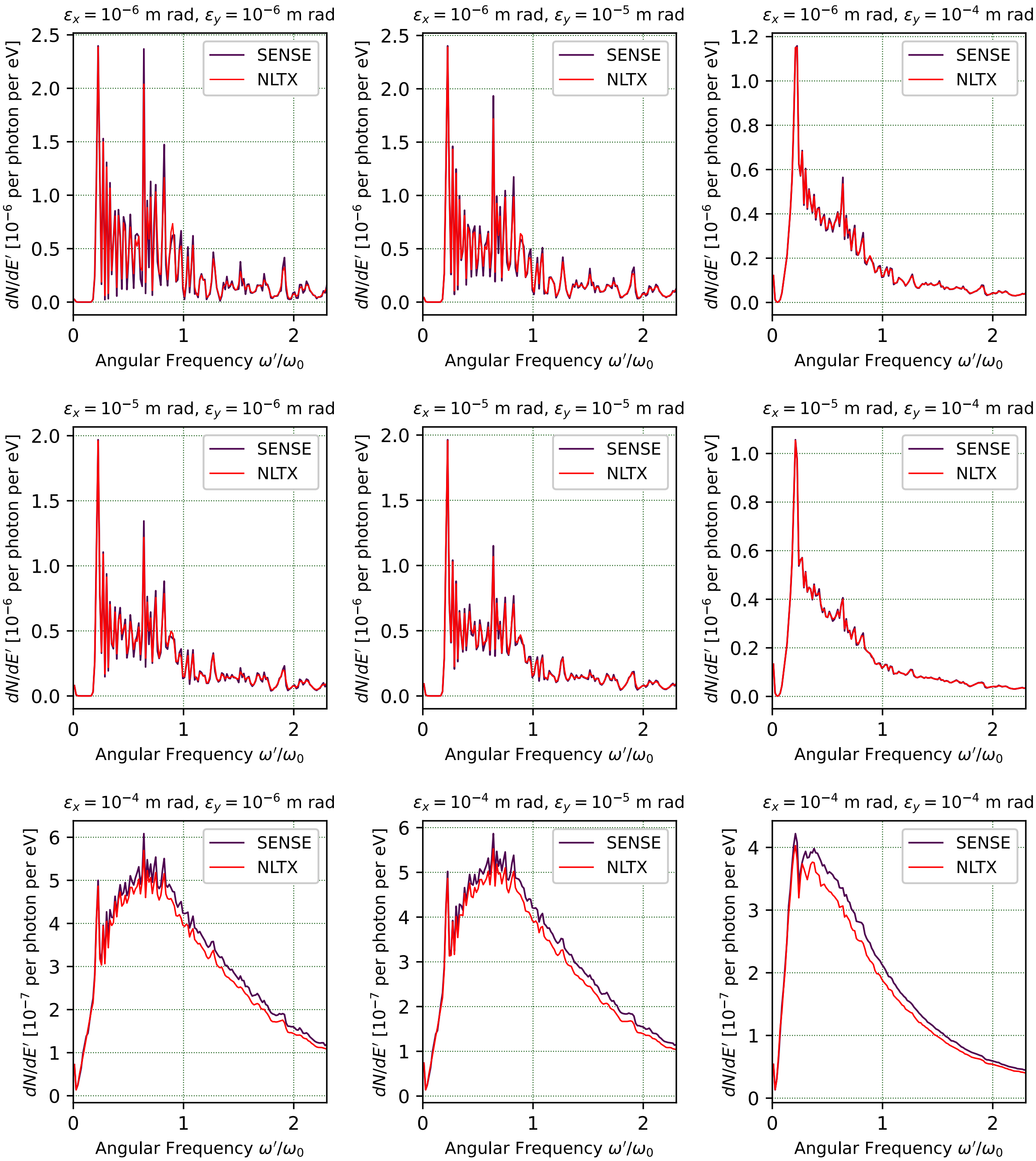

FIG. 41: Simulated spectra from SENSE and NLTX for field strength $a_0 = 2.75$ and a range of normalized horizontal emittance ϵ_x and normalized vertical emittance ϵ_y values with the following parameters: $E_e = 23$ MeV; $\Delta E_e/E_e = 0.175\%$; $\sigma_x = 41$ μm; $\sigma_y = 81$ μm; $\lambda = 800$ nm; $\sigma_{x,l} = 13.59$ μm; $\sigma_{y,l} = 13.59$ μm; $\sigma = 5.57$.

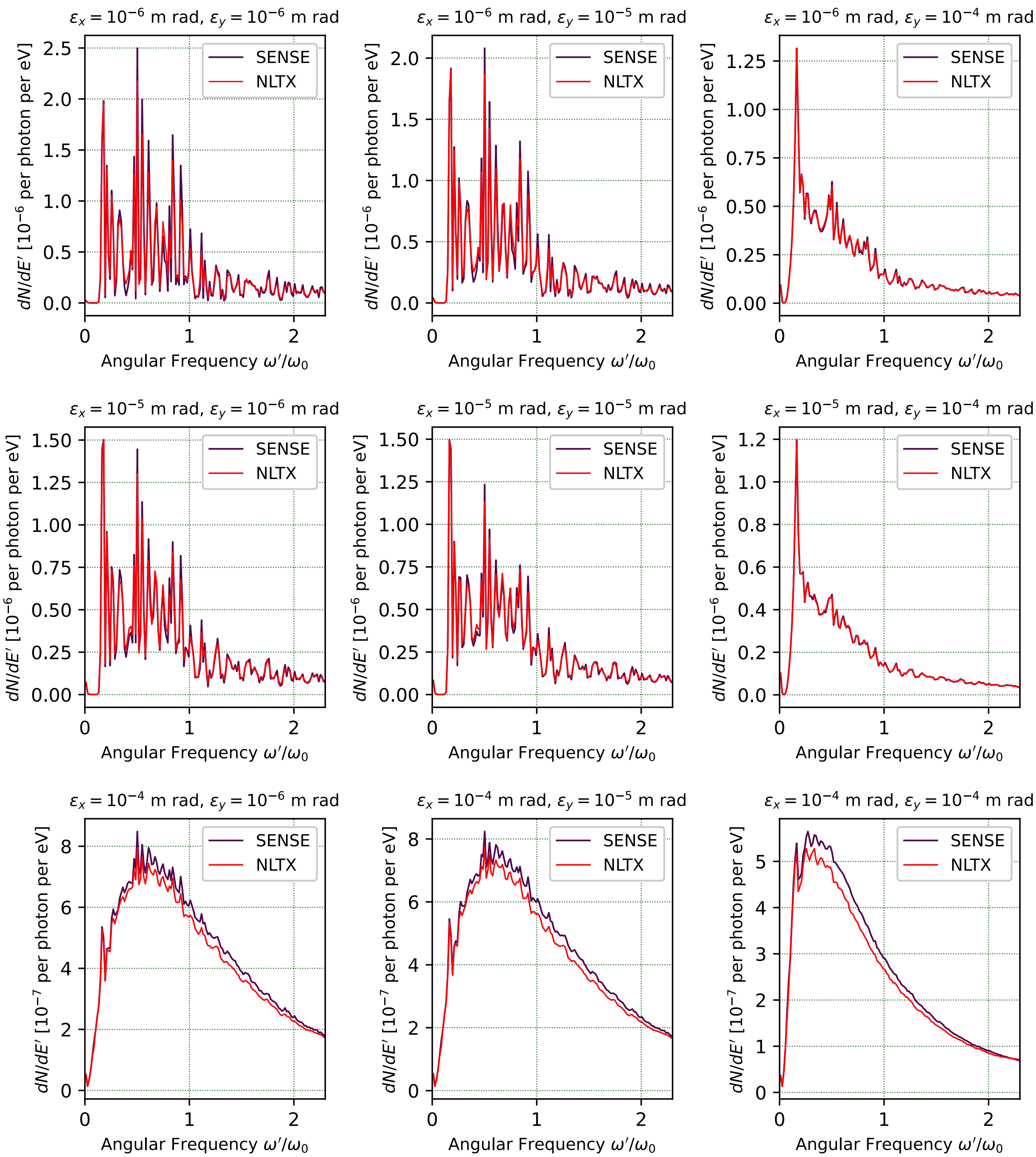

FIG. 42: Simulated spectra from SENSE and NLTX for field strength $a_0 = 3.25$ and a range of normalized horizontal emittance ϵ_x and normalized vertical emittance ϵ_y values with the following parameters: $E_e = 23$ MeV; $\Delta E_e/E_e = 0.175\%$; $\sigma_x = 41$ μm; $\sigma_y = 81$ μm; $\lambda = 800$ nm; $\sigma_{x,l} = 13.59$ μm; $\sigma_{y,l} = 13.59$ μm; $\sigma = 5.57$.

TABLE 2: Parameters for the numerical integration of the nonlinear Thomson effective motion spectrum, Eq. (158).

Parameter	Figure 43	Figure 44
Vector Potential Amplitude	$\alpha_x = a$	$\alpha_x = A \exp\left[-\xi^2/2(8.156\lambda_0)^2\right]$
Electron Lorentz Factor	$\gamma = 100$	$\gamma = 100$
Number of Wavelengths	N=20	N=20
Scattered Angle	$\theta = 0$	$\theta = 0$

dipole emissions from the electron. The motion causes the total bandwidth in the spectrum to be dramatically broadened, and it causes dips in the spectral peaks. The fourth effect arises as the field strength approaches unity. The oscillating motion of the electron in its rest frame becomes relativistic, and the electron radiates harmonics of the fundamental emission frequency. In the case of a linearly polarized incident laser pulse, the magnitude of these harmonics can be described by "Bessel function factors." The flux factor of the nth harmonic is

$$F_n(a) = \frac{n^2 a^2}{(1 + a^2/2)^2} \left\{ J_{(n-1)/2} \left[\frac{na^2}{4(1 + a^2/2)} \right] - J_{(n+1)/2} \left[\frac{na^2}{4(1 + a^2/2)} \right] \right\}. \tag{170}$$

By integrating the effective motion spectrum, one may observe the nonlinear affects of the vector potential on the scattered spectra. Figure 43 plots Eq. (158) integrated numerically using a $10^5 - 10^6$ Simpson method with the parameters from Table 2. This plot shows two spectra at different values of the field strength parameter a. The fundamental peak of the spectrum with the greater field strength (the blue plot) is significantly red-shifted. The dipole emissions from the motion of the electron due to the field oscillations in the transverse ($\hat{x}$) direction are evident in the rapid oscillations of the spectra. Notice that the relative width of each spectrum is the same for the two field strengths since the vector potential is constant in the longitudinal direction ($\hat{z}$).

The same integration over a Gaussian laser pulse, as shown in Figure 44, better illustrates the three nonlinear effects described above. Besides the photon distribution and the increased field strength in the blue plot, the parameters in this calculation are kept the same as the parameters in Figure 43, and they are listed in Table 2. At the lower field strength (the black plot) the main peaks of the spectrum are similar to the peaks in the previous example, but the high-field case (the blue plot) presents a much lower peak and a significantly broadened spectrum. This high-field induced phenomenon may be called "ponderomotive broadening," as the phenomenon is induced by the square of the vector potential function in the integral of Eq. (158). Figure 46 shows the vector potential of a Gaussian distribution squared. As the photon passes through the potential

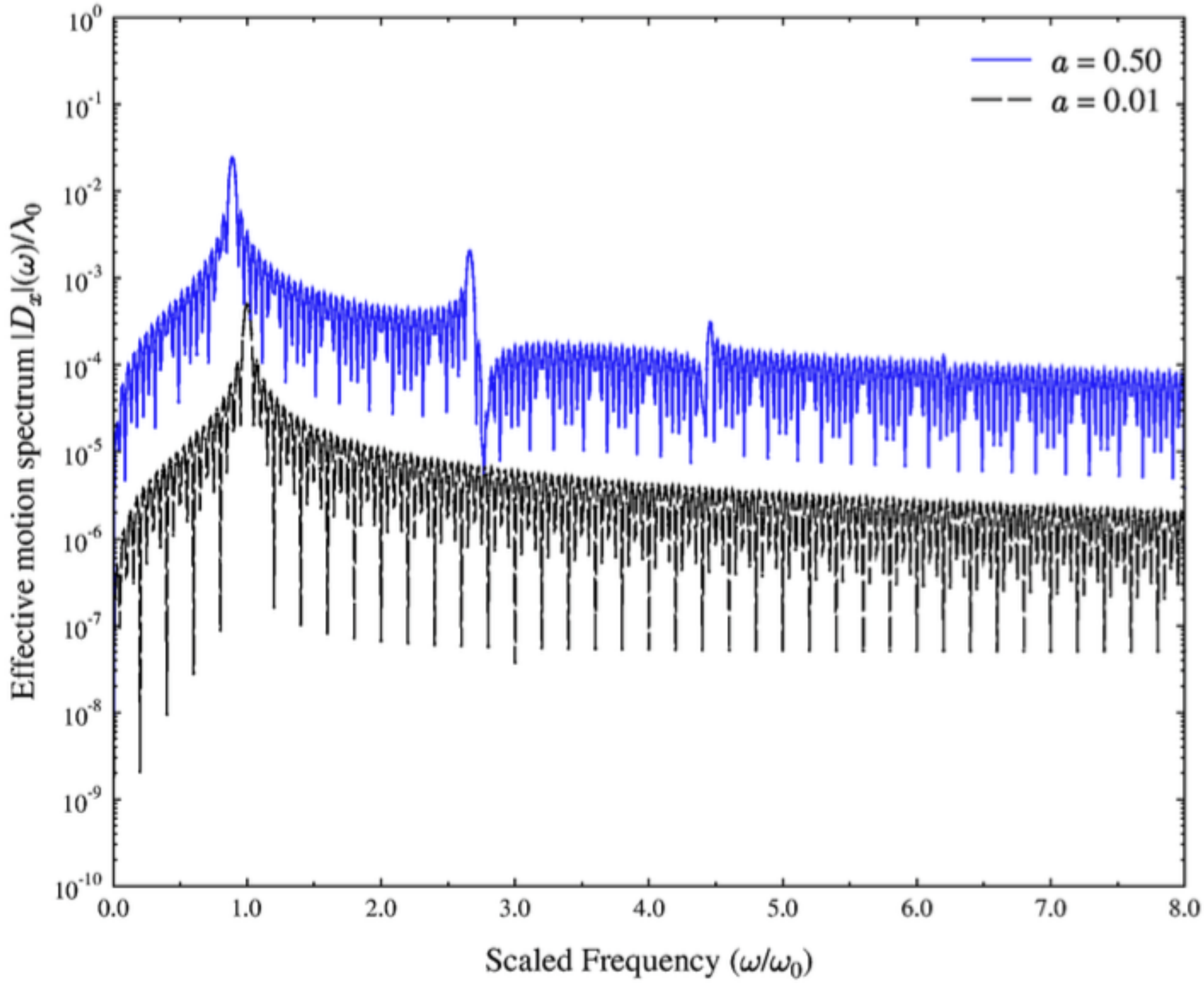

FIG. 43: Effective motion spectra for a 20 oscillation flat laser pulse at two values of field strength for a $\gamma = 100$ electron beam. In order to reduce confusion in the $a = 0.50$ plot, data at $\omega = 0.4i\omega_0$, for $i = 1, ..., 19$, have been omitted from the plot. At these frequencies $D_x = D_1$ vanishes due to constructive interference [60].

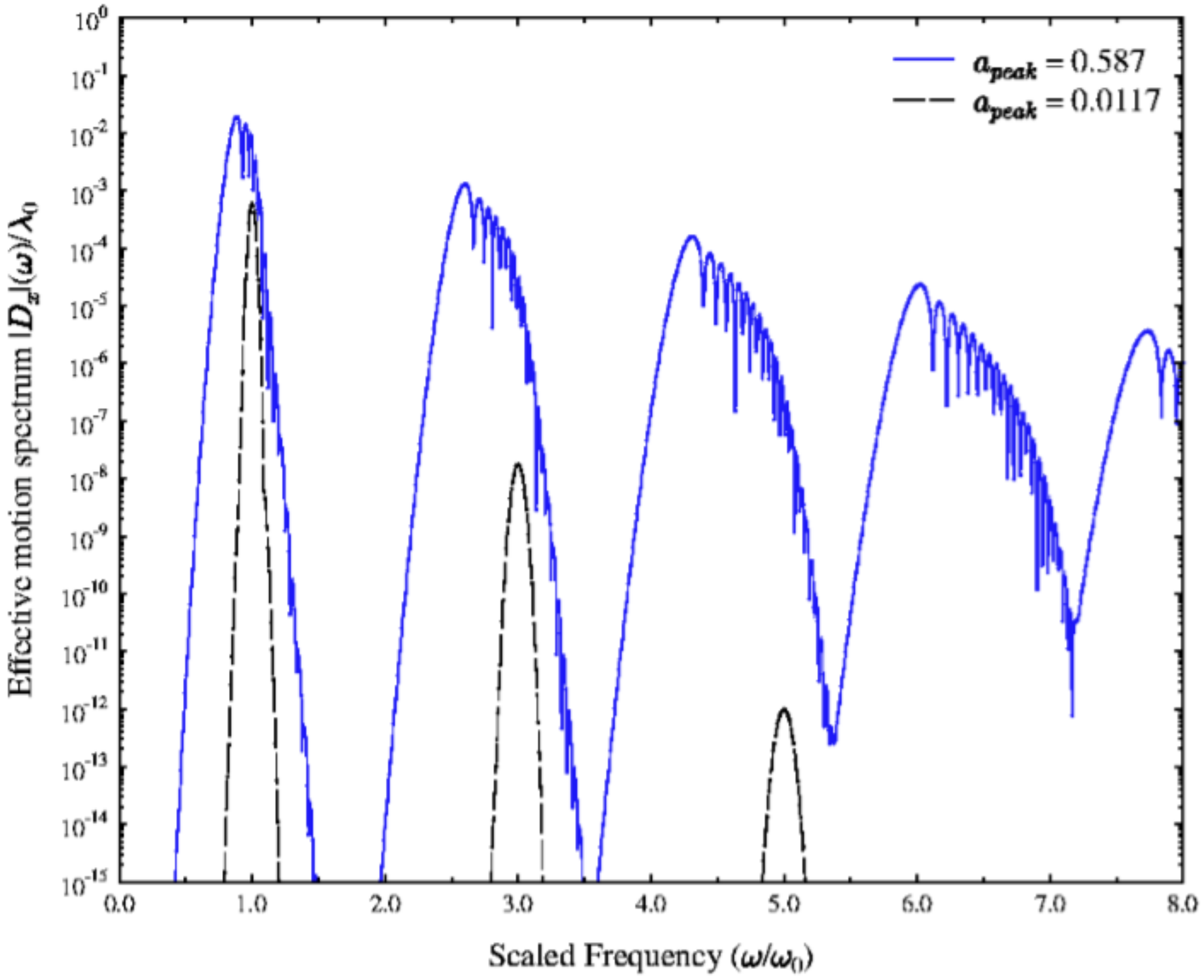

FIG. 44: Effective motion spectra for a Gaussian pulse. The spectrum is broadened at high-field strength due to ponderomotive effects which change the electron longitudinal velocity. The dips within the spectral peaks are not numerical. They are due to the destructive interference of the induced emission from various longitudinal locations within the laser pulse [60].

envelope, its speed is reduced as $A_x^2(\xi)$ increase, but the speed of the electron is increased as the potential decreases. These sudden, oscillatory changes in velocity cause the electron to radiate at shifting frequencies, which in turn, broadens the observed scattered spectrum. The electron will radiate the most at the red shifted frequency because it spends the most time in the "high-field" portion of the potential envelope, i.e. where the magnitude of the field is greatest. Notice that this ponderomotive broadening and the relative frequency shift affects all harmonics, so at high enough harmonics the peaks will begin to overlap.

The ponderomotive broadening effect has direct relevance to experimental data. In Figure 45, three effective motion spectra for three different field strengths are plotted for photon-electron collisions in which the electron source is stationary. Therefore, the harmonic frequency scale is determined solely by the incident laser frequency. In the lowest field strength (black plot), the individual harmonic lines are distinguishable. In the middle field strength plot (blue plot), the spectrum is nearly continuous after the first harmonic line, which is much more subtle than in the lower field strength. At the greatest field strength, the plot becomes continuous. The frequencies of the harmonics dominate the spectrum over the corresponding synchrotron radiation.

5.4 CHIRPING: CORRECTION TO PONDEROMOTIVE BROADENING

While the basic sources of energy spread in Section 3.8 are unavoidable in Compton scattering, the ponderomotive broadening may be corrected through frequency modulation (FM) of the incident laser pulse. This process is commonly called "chirping." Frequency modulation is simply changing the frequency of the incident laser pulse over its duration, i.e. $\omega \to \omega(\xi)$. Even though changing the incident frequency over the duration of the pulse does *increase* the total energy spread of the incident laser pulse itself σ_{E_p}/E_p, proper tuning of this FM may be used to compensate for the changing longitudinal velocity of the electron. The correction arises from the dependence of the effective motion spectrum in Eq. (158) upon the vector potential of the laser pulse, which itself is dependent upon the incident laser frequency.

5.4.1 2013 GHEBREGZIABHER ET AL. CHIRPING PRESCRIPTION

Ghebregziabher, Shadwick, and Umstadter (GSU) [80] first suggested that chirping could be used to correct ponderomotive broadening of nonlinear, inverse Compton scattering in the Thomson limit. GSU developed a a three-dimensional, relativistic model to simulate the scattered spectra from an electron beam with a high-intensity laser pulse, and then they used this model to demonstrate the effects of their chirping prescription. In their model, the number of oscillations in the vector potential as a function of the temporal duration τ of the pulse was calculated

$$N_\tau = 0.24 a_0^2 \tau, \tag{171}$$

where a_0 is the maximum amplitude of the oscillating potential. From this calculation, GSU

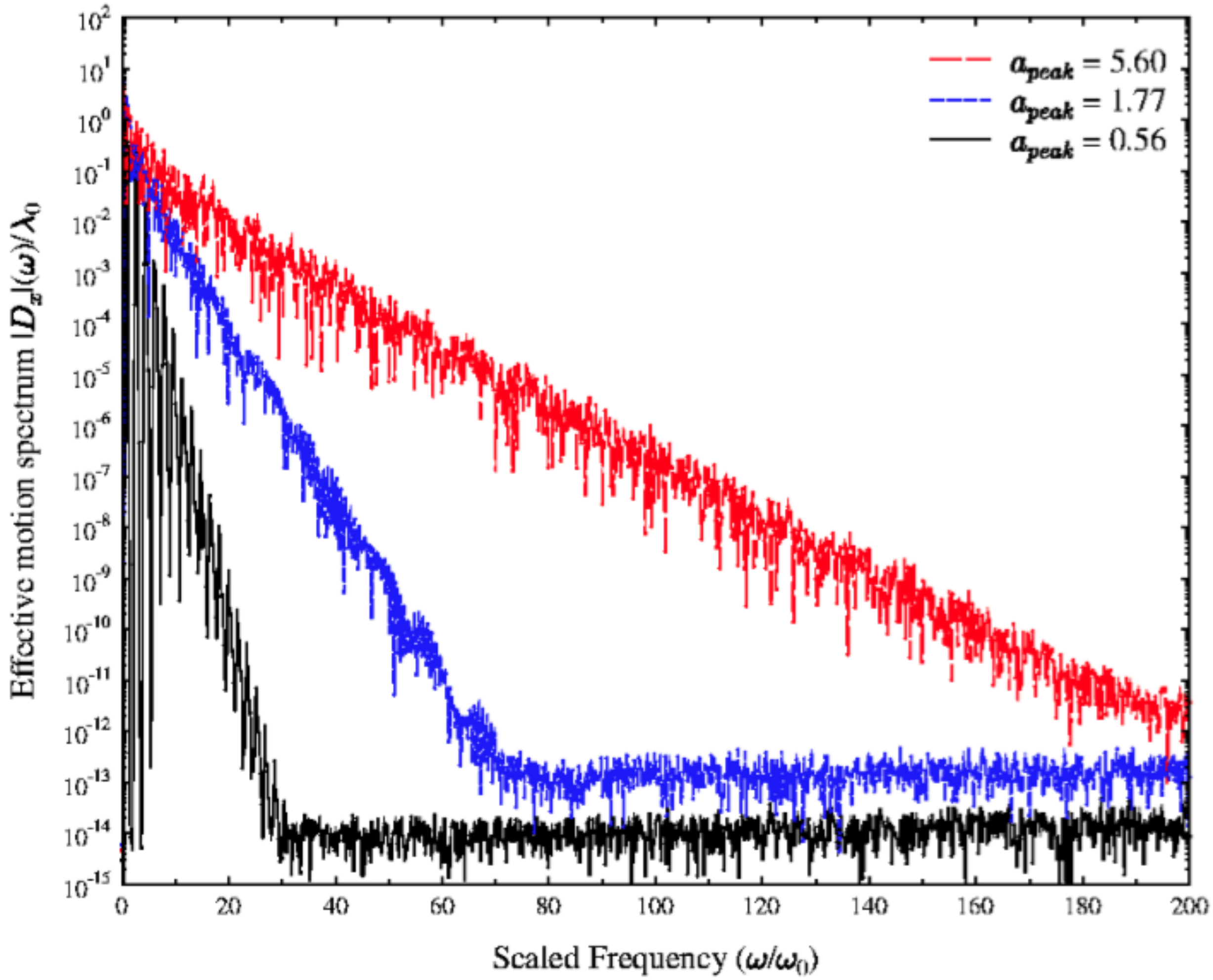

FIG. 45: Thomson forward scattered spectrum from an experiment. The lowest field strength case has individual harmonic peaks as in Fig. (44). The higher field spectra oscillate, are not harmonic, and scale as synchrotron radiation spectrum above critical frequency. Flat regions are at the noise floor of the numerical calculations [60].

TABLE 3: Parameters used in the inverse-Compton scattering in Figures 27 & 47.

Parameter	Symbol	Value
Aperture semi-angle	A	$1/(\gamma \times 10)$
Electron Beam Energy	E_b	300 MeV
Lorentz Factor	γ	587
Field Strength Parameter	a_0	0.01
Peak Laser Pulse Wavelength	λ	800nm
Standard Deviation of $a(t)$	σ	20.3

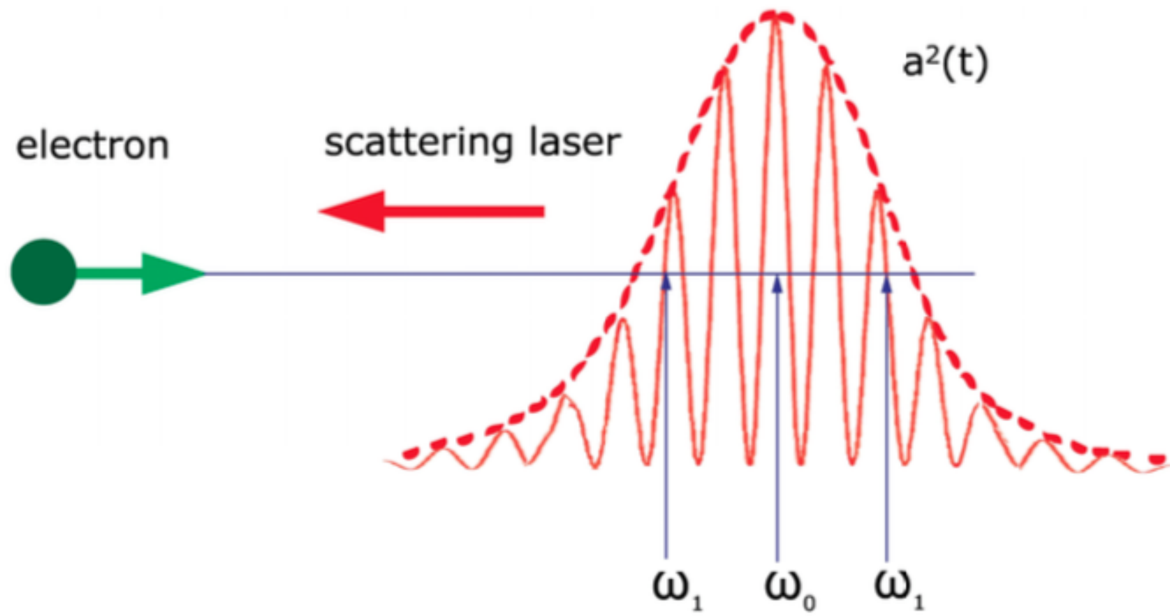

FIG. 46: Schematic diagram illustrating the time varying ponderomotive potential experienced by an electron as it collides with a counter propagating laser pulse [80].

proposed that the correct FM for a Gaussian distribution would be

$$\omega(t) = \frac{2}{3}\omega_0 \left\{ 1 + \left[a(t)/\sqrt{2}a_0 \right]^2 \right\}, \tag{172}$$

where ω_0 is the frequency in the beam frame when the wave envelope is at the maximum potential. The results of the GSU calculation are presented in Figure (47): the amplitude of the energy density spectrum of the corrected spectrum is increased by a factor of five, and the bandwidth is greatly reduced. It is important to note, however, that this model has inappropriately used the Thomson approximation for scattered angular frequency when the full Compton treatment is required as discussed in Section 3.2. While the geometry of the spectrum in Figure 47 is correct, the entire spectrum should be red shifted as shown in Figure 27.

5.4.2 EXACT CHIRPING CALCULATION FOR A PLANE-WAVE WITH LINEAR POLARIZATION IN THE THOMSON LIMIT

Since the introduction of chirping, the general prescription for calculating the FM that correctly

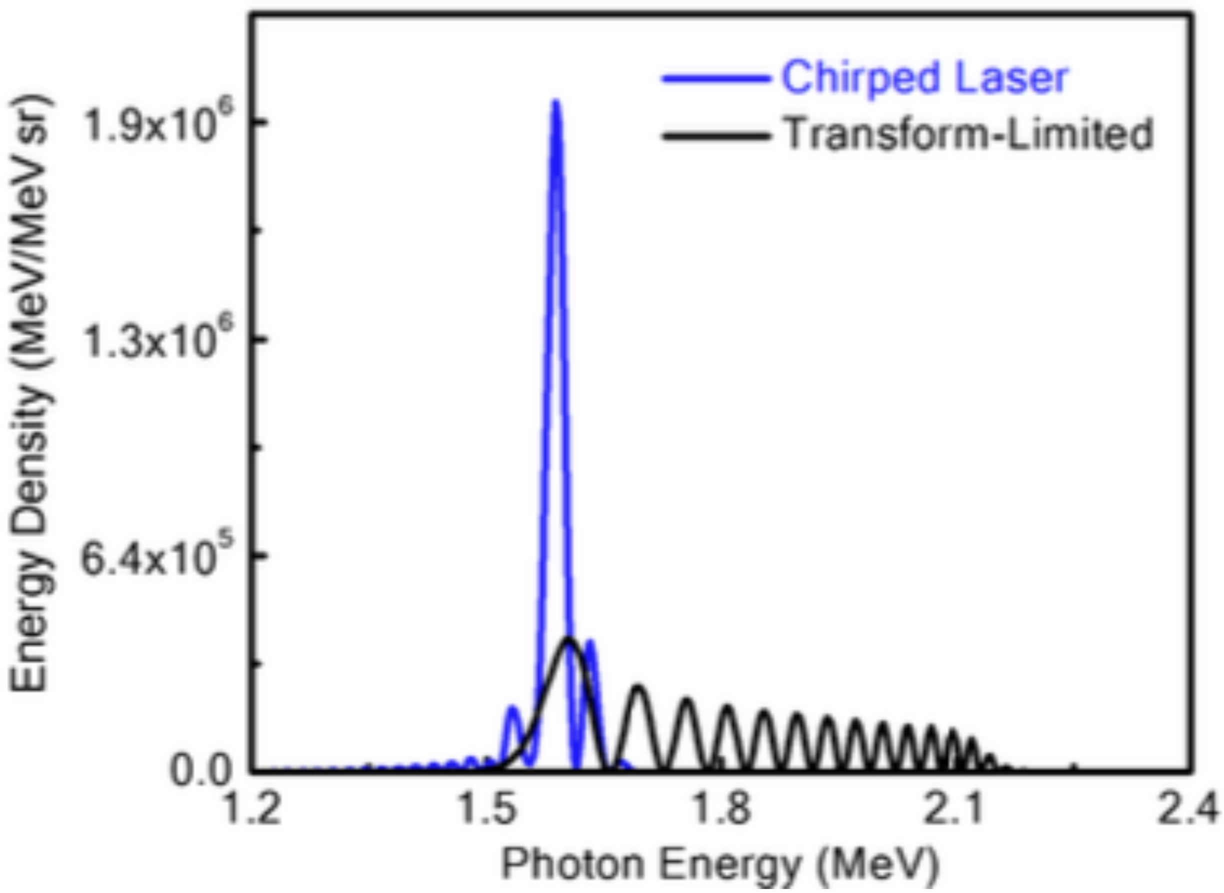

FIG. 47: Ghebregziabher et al. FM results: On-axis radiated energy density from the scattering of a 300 MeV electron by a 90 fs FWHM and 1.6×10^{18} W/cm^2 peak-intensity chirped laser pulse (blue line) and transform- limited pulse (black line). The photon flux per unit solid angle is approximately 4.1×10^4 photons/sr and 4.3×10^4 photons/sr for scattering with the chirped and transform-limited laser pulses, respectively [80].

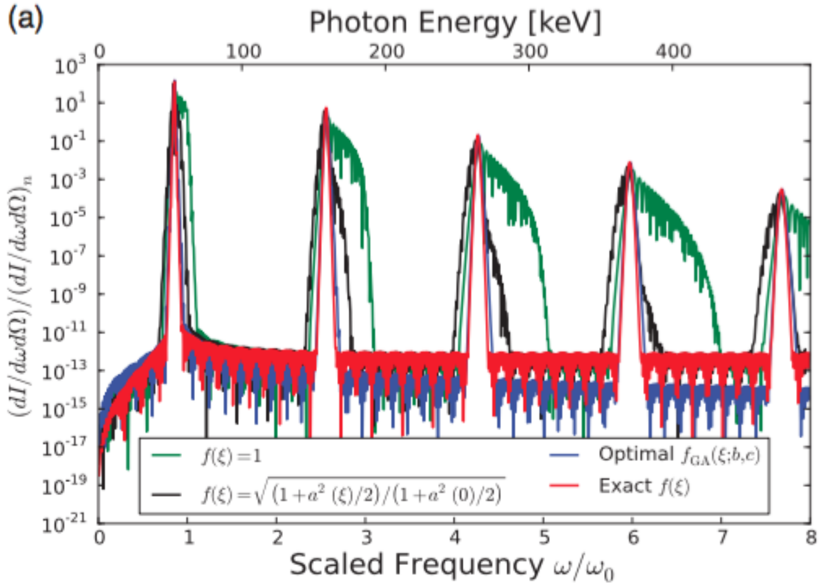

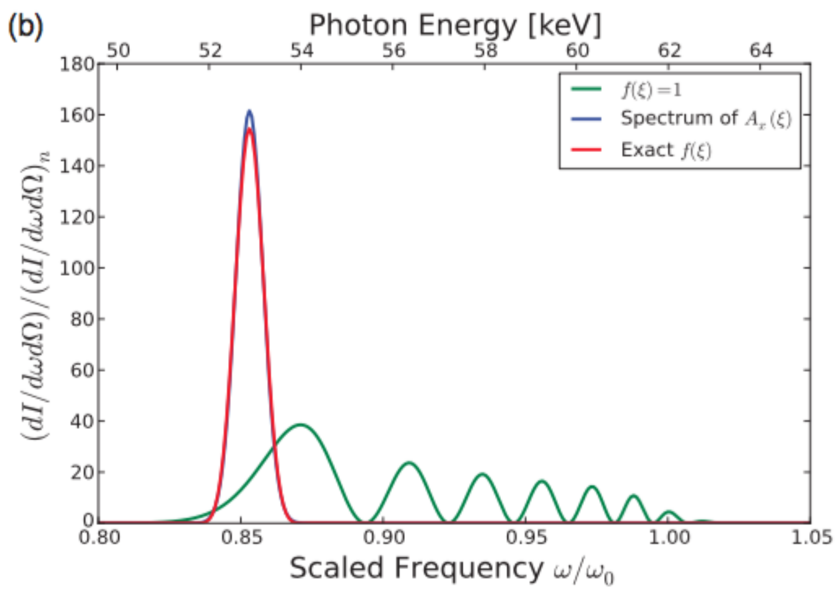

FIG. 48: (a) Normalized spectra of scattered radiation for the case without FM (green line), FM from Eq. (178) (black line), FM from optimal $f_{\rm GA}(\xi; b, c)$ (blue line), and the exact FM from Eq. (186) (red line). The shapes of the spectra, both nonmodulated and modulated, are independent on the scattering electron's energy. (b) Complete correction of spectral width is demonstrated by this comparison of the case with no FM (green line), the Fourier transform of the amplitude function (blue line), and the case with exact FM (red line). In both panels, a Gaussian envelope is used with $a_0 = 0.587$ and electron's $\gamma = 100$ as in Fig. (44)[81].

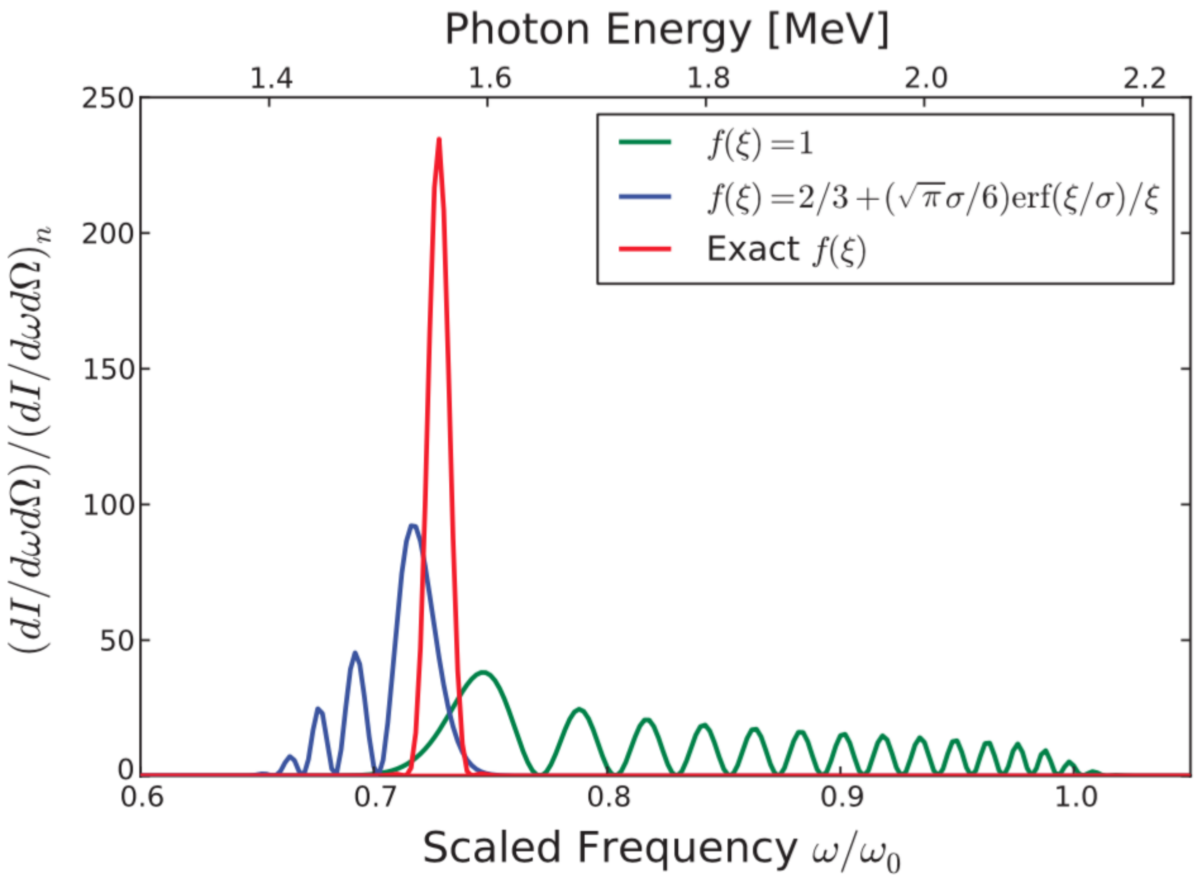

FIG. 49: Narrowing the radiation spectra by exact FM. Scattered spectral distributions calculated with no FM (green line), the GSU FM (blue line), and the exact FM (red line). A Gaussian envelope is used with $a_0 = 0.865$ as in Fig. (47). Note the linear scale and that only data in the first harmonic is displayed for both panels. The top x axis denotes photon energies for the case of $E_{beam} = 300$ MeV, $\lambda = 800$ nm, FWHM pulse duration of 90 fs, as in Fig. (47)[81].

compensates for ponderomotive broadening has been derived [81]. The bandwidth of the inverse Compton-scattered spectra may be reduced to the Fourier transform limit by this treatment, even for high-field strength collisions. This method does fail, however, at the highest field strengths (or for a laser pulse that is very long) where the emission of multiple photons per electron may occur. Also, this prescription is only valid in the Thomson limit.

For clarity of comparison, the potential may be written in terms of the FM function $f(\xi)$

$$\tilde{A}(\xi) = \frac{eA(\xi)}{mc} = a(\xi)\cos\left[\frac{2\pi\xi f(\xi)}{\lambda}\right]. \tag{173}$$

All of the chirping effects are contained within $f(\xi)$. In the case of an incident laser pulse without modulation, $f(\xi) = 1$. For a laser pulse centered at $\xi = 0$, it is necessary that $f(0) = 1$ because the emissions do not need correction at the maximum potential in the wave packet envelope. The number of subsidiary peaks N_τ within each harmonic n_h is proportional to the field strength squared and the temporal duration of the pulse T:

$$N_\tau = (2n_h - 1)\frac{c}{\lambda}T\int_0^\infty a^2(\bar{\xi})\mathrm{d}\bar{\xi}, \tag{174}$$

where

$$\bar{\xi} \equiv \frac{\xi}{\sqrt{2}\sigma}, \tag{175}$$

and σ is the pulse length. For a Gaussian distribution

$$a(\xi) = a_0 \exp\left[-\frac{\xi^2}{2\sigma^2}\right], \tag{176}$$

$n_h = 1$, and $N_\tau = \sqrt{2\pi}cTa_0^2/4\lambda \approx 0.24Ta_0^2$. Notice that under these conditions, the general equation for the number of subsidiary peaks, Eq. (174), reduces to the expression used by GSU, Eq. (171). The chirping prescription introduced by GSU, i.e. Eq. (172), may be constructed into this formalism

$$f(\xi) = \frac{2}{3}\left(1 + \frac{a^2(\xi)}{2a_0^2}\right). \tag{177}$$

This expression is only valid when FM occurs slowly, i.e. $[\xi f(\xi)]' = f(\xi) + \xi f'(\xi) \approx f(\xi)$, so the above equation becomes

$$f(\xi) = \sqrt{\frac{1 + a^2(\xi)/2}{1 + a_0^2/2}}. \tag{178}$$

As shown in Figure 48(a), the energy density spectrum generated from this FM dramatically reduces the ponderomotive broadening across all harmonics. In order to further improve the bandwidth of the scattered frequency, genetic optimization has been implemented to increase the peak height of the harmonics while simultaneously reducing the bandwidth [82]. The genetic optimization used a two-parameter family of functions of the form

$$f_{\mathrm{GA}}(\bar{\xi}; b, c) = \frac{c}{1 - (1 - c)\exp\left(-b\bar{\xi}^2\right)}. \tag{179}$$

The spectrum produced under the genetically optimized FM is also plotted in Figure 48(a), and it shows a marked improvement from Eq. (178). Analysis of the optimized b and c parameters revealed that c scales directly as $a_0^2/4$, and such a simple scaling suggests an underlying physics cause.

In cases where the FM is *not* slowly varying, i.e. $[\xi f(\xi)]' = f(\xi) + \xi f'(\xi) \neq f(\xi)$, the local values of the pulse frequency and wave number must be defined as

$$\omega(\xi) = \frac{\partial \Phi}{\partial t} = c\frac{\mathrm{d}\Phi}{\mathrm{d}\xi}, \tag{180}$$

and

$$k(\xi) = \frac{\partial \Phi}{\partial x} = \frac{\mathrm{d}\Phi}{\mathrm{d}\xi}, \tag{181}$$

where Φ is the incident wave phase. Lorentz transforming these localized parameters into the beam frame and then Lorentz transforming them back into the lab frame at a constant frequency yields the equation

$$(1+\beta^*)^2\gamma^{*2}\mathrm{d}\Phi/\mathrm{d}\xi = C = (1+\beta)^2\gamma^2\mathrm{d}\Phi/\mathrm{d}\xi(\xi = -\infty), \tag{182}$$

where C is some constant. This leads to the differential equation

$$\frac{\mathrm{d}}{\mathrm{d}\xi}\xi f(\xi) = \{1 + a^2(\xi)/2\}(\xi = -\infty). \tag{183}$$

With the boundary condition $f(0) = 1$, the above equation may be solved:

$$f(\xi) = \frac{1}{1 + a_0^2/2}\left(1 + \frac{\int_0^\xi a^2(\xi')\mathrm{d}\xi'}{2\xi}\right). \tag{184}$$

This is the general form for the exact high-field FM prescription in the Thomson limit. The function falls from 1 to $f(\pm\infty) = \{1 + a_0^2/2\}^{-1}$: f_{GA} closely traces this exact FM around the center of the pulse, i.e. $\xi = 0$, but it's exponential tails are unable to match the $1/\xi$ factor. This exact FM treatment, Eq. (184), is shown in Figure 48(a) (red plot). This solution is an improvement upon the initial chirping prescription in two important ways: first, this treatment corrects the ponderomotive broadening down to the Fourier limit; second, this treatment extends the correction though all harmonics of the emitted radiation. This FM is also independent of the electron energy which means the ponderomotive correction occurs for all electrons in the beam.

In Figure 48(b), spectral peak of the high-field, exact FM spectrum is compared to the Fourier transform of the Gaussian amplitude $a(\xi)$ (The Fourier transform has been red-shifted to the high-field peak for the purpose of comparison.). The bandwidths of these plots are identical. Since the

TABLE 4: Photon distribution functions for various pulse shapes.

Gaussian	$a_G = a_0 \exp[-\xi^2/(2(\sigma\lambda)^2]$
Lorentzian	$a_L(\xi) = a_0\sigma/[(\xi/\lambda)^2 + \sigma]$
Hyperbolic Secant	$a_S(\xi) = a_0 \operatorname{sech}(\sigma\xi/\lambda)$

Fourier transform limit represents the minimal bandwidth possible, it can be concluded that this general chirping method provides the optimal emissions for collisions in this energy regime.

Eq. (184) may be solved for the conditions reported by GSU:

$$f_{\rm GSU}(\xi) = \frac{2}{3}\left(1 + \frac{\sqrt{\pi}\sigma}{4\xi}\mathrm{erf}(\xi/\sigma)\right). \tag{185}$$

This result is very similar for the exact FM for a Gaussian envelope

$$f_{\rm exact,G}(\xi) = \frac{1}{1 + a_0^2/2}\left(1 + \frac{\sqrt{\pi}\sigma a_0^2}{4\xi}\mathrm{erf}(\xi/\sigma)\right). \tag{186}$$

Notice that the GSU prescriptions, Eq. (177) and Eq. (185), do not satisfy the condition $f(0) = 1$, so it is not possible for this FM to correct the nonlinear effects. It is interesting that for the condition $a_0 = 1$, $f_{\rm GSU}$ and $f_{\rm exact,G}$ are equivalent. This may explain why GSU were able to observe substantial narrowing of the emitted spectrum for there recorded field strength parameter: $a_0 = 0.865 \approx 1$ [81].

5.4.3 EXACT CHIRPING CALCULATION FOR PARTICULAR WAVE SHAPES

Chirping prescriptions for specific laser pulse distributions may be computed from Eq. (184), the general expression of the exact FM correction to ponderomotive broadening within the Thomson limit. In this section, the Gaussian, Lorentzian, and hyperbolic secant photon distribution will be explored. For each distribution the resulting FM function $f(\bar{\xi})$ will be calculated, and the chirped energy density spectra will be computed.

First, the energy density spectrum for the scattered photons, Eq. (54), will be constructed in terms of the scale-free spectrum. The scattered energy density in the beam frame can be expressed in terms of the beams energy distribution, $N(\gamma)$,

$$\left[\frac{\mathrm{d}^2E(\omega)}{\mathrm{d}\omega\mathrm{d}\Omega}\right]_{beam} = \int_0^\infty N(\gamma)\frac{\mathrm{d}^2E(\gamma,\omega)}{\mathrm{d}\omega\mathrm{d}\Omega}\mathrm{d}\gamma. \tag{187}$$

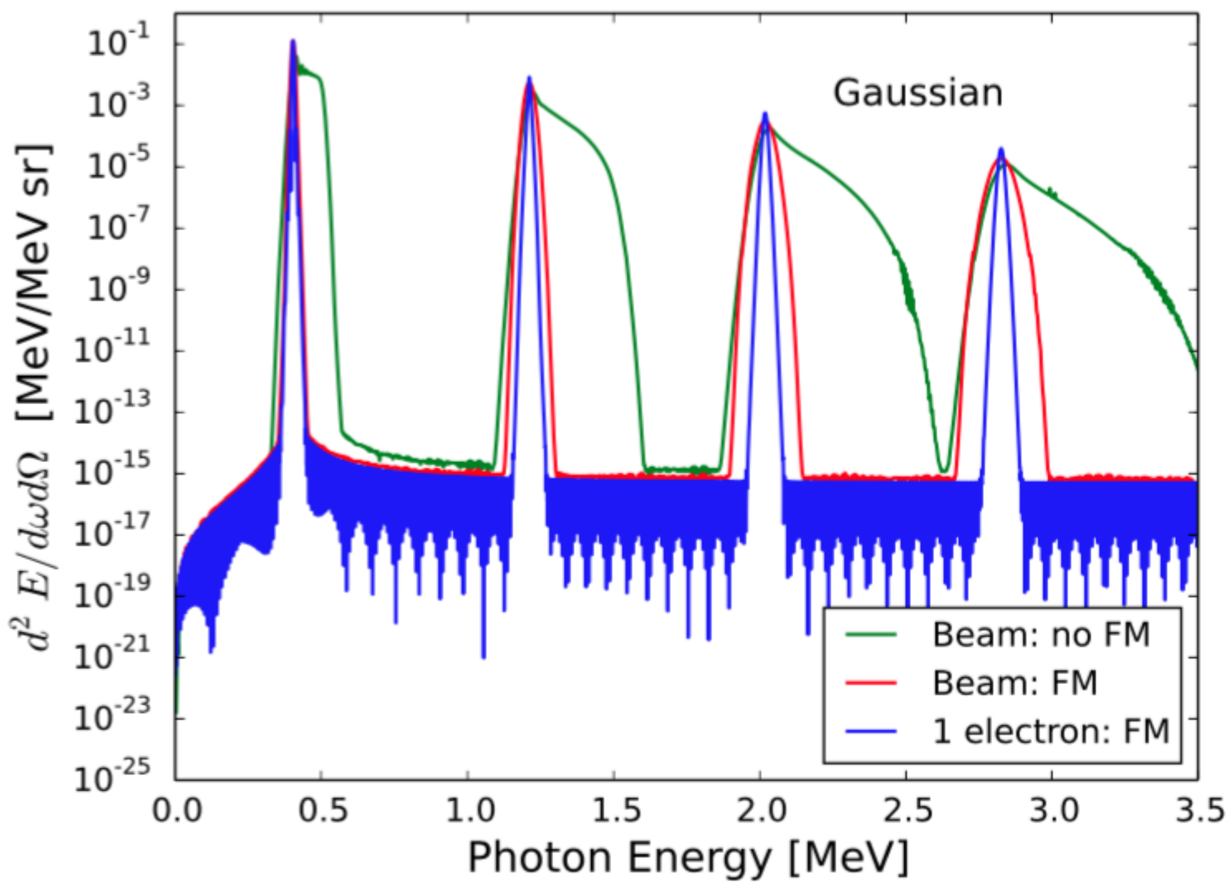

FIG. 50: Backscattered radiation of a Gaussian laser pulse with $\lambda = 1\ \mu$m, $a_0 = 0.707$ off a Gaussian electron beam with $Q = 100$ pC, $E_{beam} = 163$ MeV, and 1% FWHM energy spread: FM (red), non-FM (green), and the single electron FM case (normalized to FM) (blue)[83].

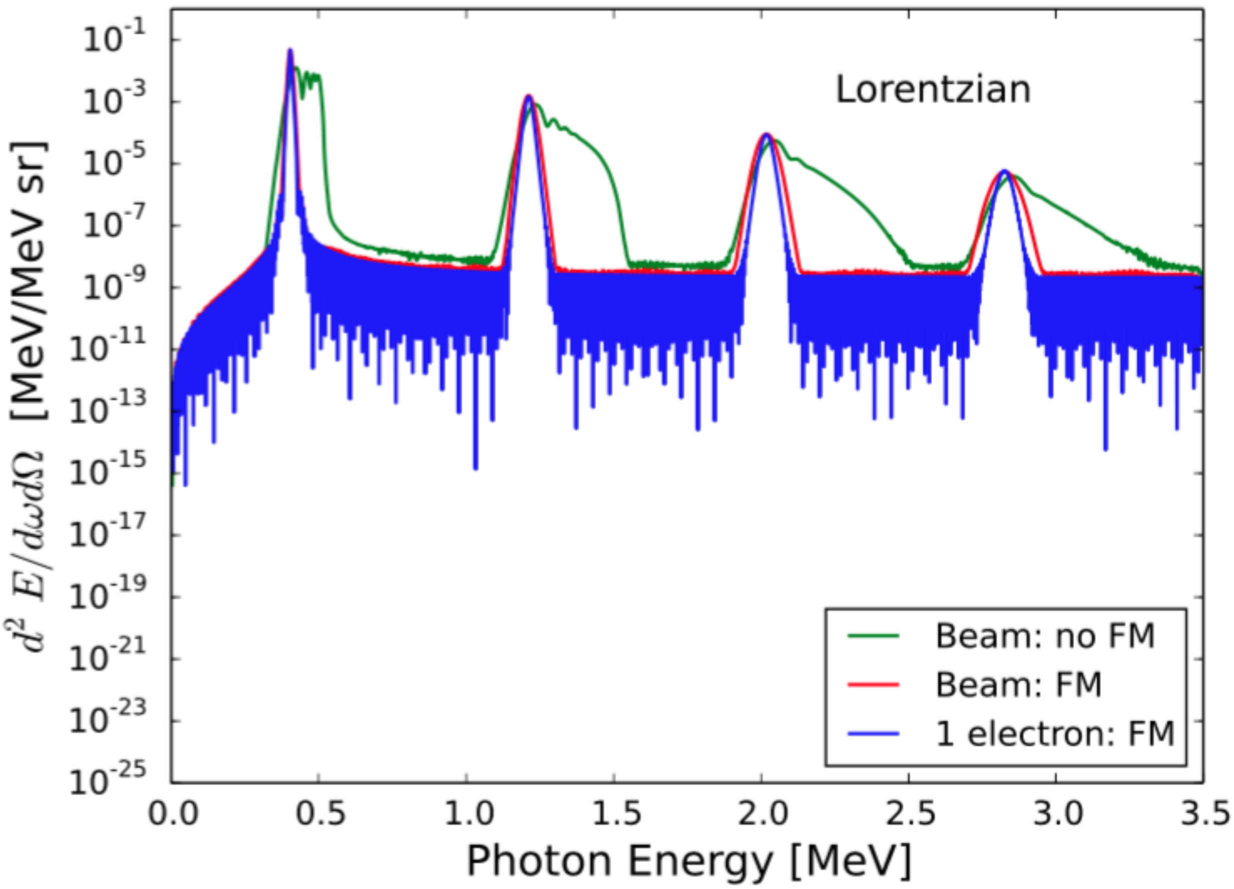

FIG. 51: Backscattered radiation of a Lorentzian laser pulse with $\lambda = 1\ \mu$m, $a_0 = 0.707$ off a Gaussian electron beam with $Q = 100$ pC, $E_{beam} = 163$ MeV, and 1% FWHM energy spread: FM (red), non-FM (green), and the single electron FM case (normalized to FM) (blue)[83].

The single-electron scattering spectrum in the lab frame may be written in terms of the spectrum in the beam fame

$$\frac{\mathrm{d}^2E(\gamma,\omega)}{\mathrm{d}\omega\mathrm{d}\Omega} = \left[\frac{\mathrm{d}^2E(\gamma)}{\mathrm{d}\omega\mathrm{d}\Omega}\right]_n \left[\frac{\omega}{\omega_0(\gamma)}\right]^2 \left|\frac{(1+\beta)\gamma D_1(\gamma,\omega)}{\lambda}\right|^2, \tag{188}$$

where $\omega_0(\gamma) = (1+\beta)^2\gamma^2 2\pi c/\lambda$ is the normalizing frequency, $[d^2E(\gamma)/d\omega d\Omega]_n = (1+\beta)^2\gamma r_e E_{beam}/c$ is the normalizing factor, λ is the normalizing wavelength of the incident pulse, $D_1(\gamma,\omega)$ is the transverse effective motion, and r_e is the classical electron radius. The effective motion may be rewritten as the scale-free scattering spectrum

$$\tilde{D}_1\left[\frac{\omega}{\omega_0}\right] \equiv \frac{(1+\beta)\gamma D_1(\gamma,\omega)}{\lambda}. \tag{189}$$

Now, the energy density spectrum can be written in terms of the scale-free scattering spectrum

$$\frac{\mathrm{d}^2E(\gamma,\omega)}{\mathrm{d}\omega\mathrm{d}\Omega} = \left[\frac{\mathrm{d}^2E(\gamma)}{\mathrm{d}\omega\mathrm{d}\Omega}\right]_n \left[\frac{\omega}{\omega_0(\gamma)}\right]^2 \left|\tilde{D}_1\left[\frac{\omega}{\omega_0}(\gamma)\right]\right|^2. \tag{190}$$

The benefit of reconstructing Eq. (54) in this way is that for any set of incident laser parameters– amplitude of the vector potential a_0, envelope shape, peak wavelength, and pulse width σ– only $\tilde{D}_1$ must be computed to change from one photon distribution shape to another. The resulting FM functions are calculated from solving Eq. (184) for each vector potential distribution function in Table 4:

$$f_G(\bar{\xi}) = \tilde{w}_f\left[1 + \frac{\sqrt{\pi}\sigma a_0^2}{4\bar{\xi}}\mathrm{erf}(\bar{\xi}/\sigma)\right], \tag{191}$$

$$f_L(\bar{\xi}) = \tilde{w}_f\left[1 + \frac{\sqrt{\sigma}a_0^2}{4\sqrt{2}\bar{\xi}}\left(\frac{\sqrt{2\sigma}\bar{\xi}}{\sigma+2\bar{\xi}^2} + \tan^{-1}\frac{\sqrt{2}\bar{\xi}}{\sqrt{\sigma}}\right)\right], \tag{192}$$

and

$$f_S(\bar{\xi}) = \tilde{w}_f\left[1 + \frac{a_0^2}{2\bar{\xi}^2}\tanh(\sigma\bar{\xi})\right], \tag{193}$$

where $\bar{\xi} = \xi/\lambda$. The scattered spectra for these wave shapes are plotted in Figures 50-52, and it is evident that, in all three wave shapes, Eq. (184) is quite effective in restoring the narrowband spectrum across all harmonics [83].

5.4.4 ANALYTIC SOLUTION FOR THE EXACT CHIRPED SPECTRUM

As shown in Figure 48(b), the first harmonic of the scale-free spectrum for a laser pulse under the exact FM prescription may be approximated by its Fourier transform

$$\tilde{D}_x\left(\frac{\omega}{\omega_0(\gamma}\right) = \frac{1}{2}\mathcal{F}\left\{a(\xi)\right\}\left(\frac{\frac{\omega}{\omega_0(\gamma)} - \tilde{w}_f}{\tilde{w}_f}\right), \tag{194}$$

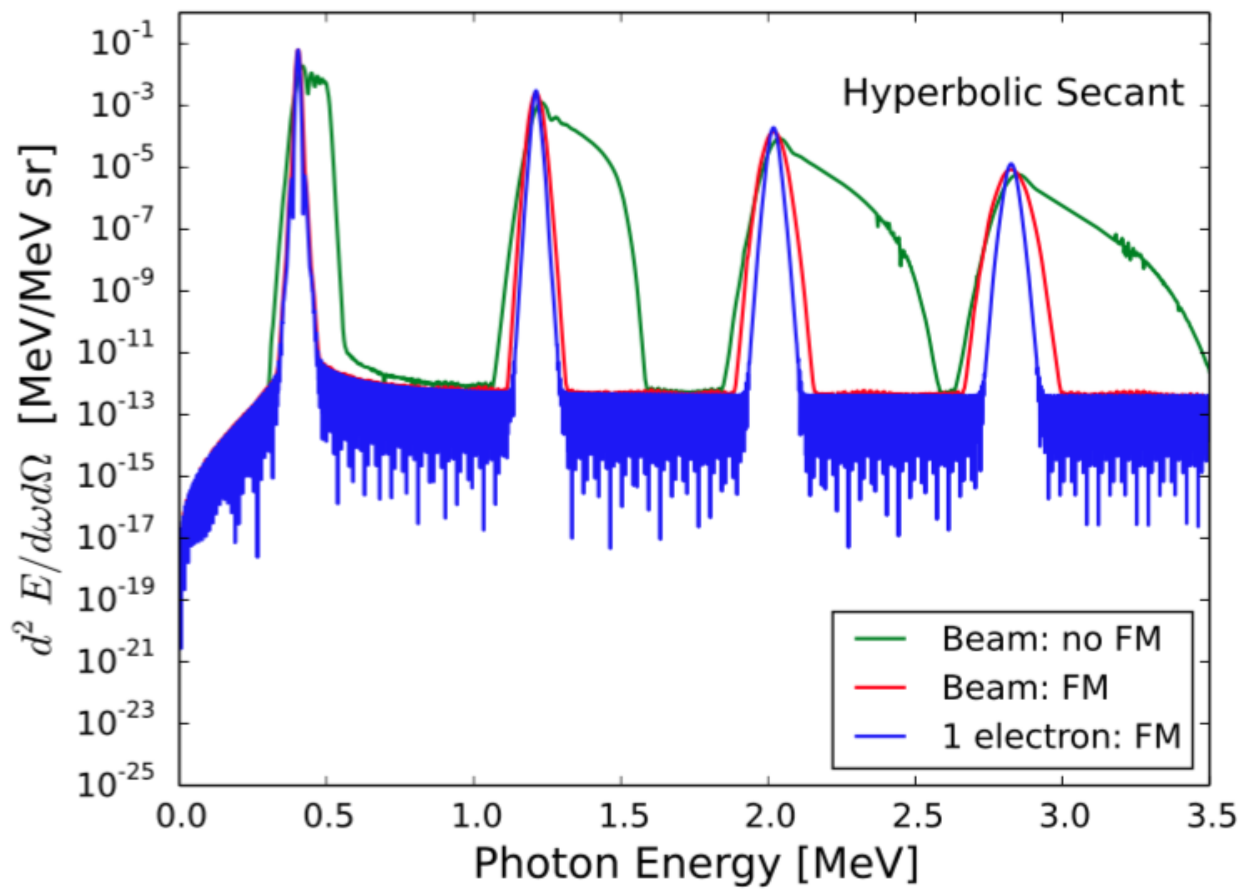

FIG. 52: Backscattered radiation of a hyperbolic secant laser pulse with $\lambda = 1\mu$m, $a_0 = 0.707$ off a Gaussian electron beam with $Q = 100$ pC, $E_{beam} = 163$ MeV, and 1% FWHM energy spread: FM (red), non-FM (green), and the single electron FM case (normalized to FM) (blue)[83].

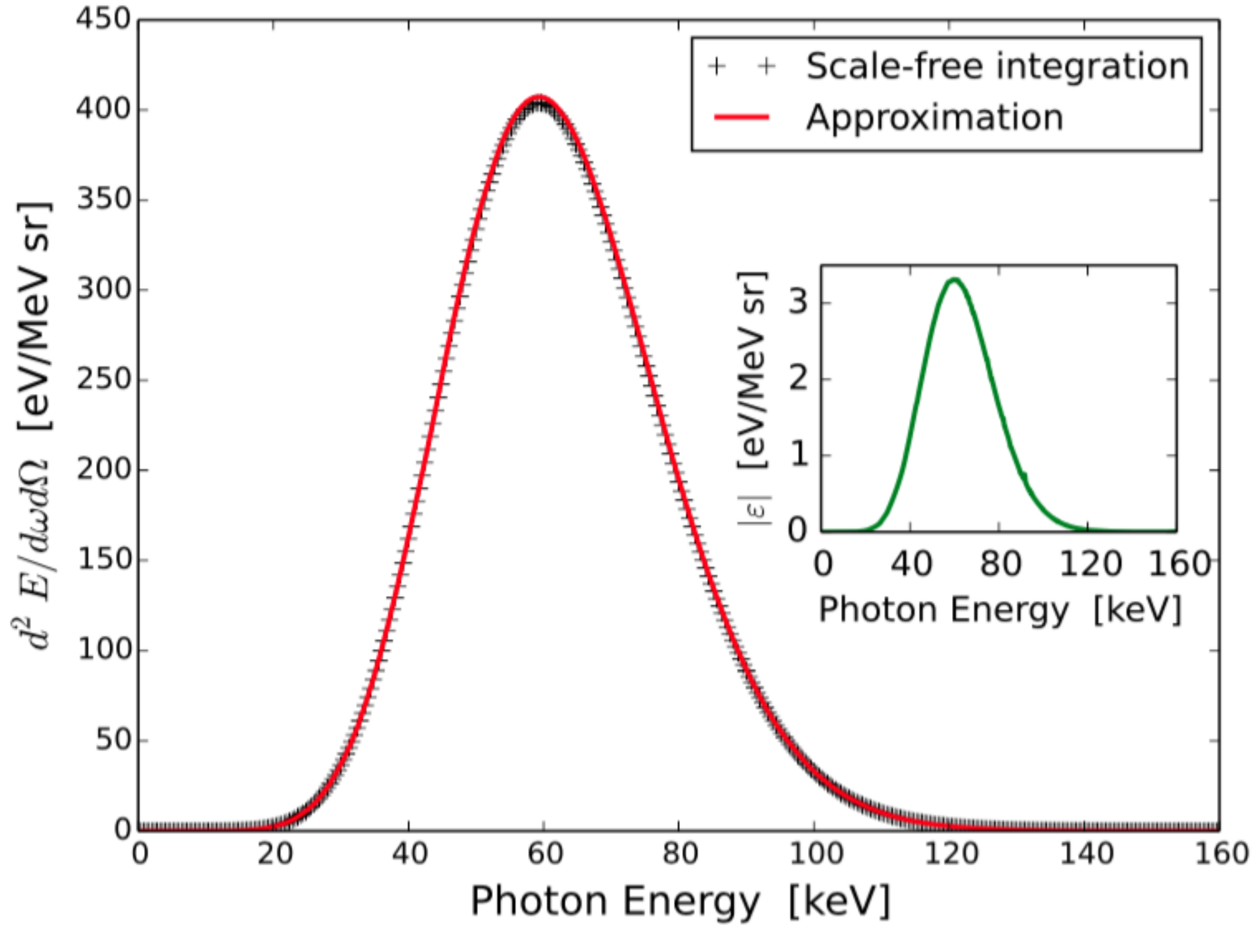

FIG. 53: Integration of a single scale-free spectrum $\tilde{D}_x$ and an electron beam with a 34% energy spread versus the analytical approximation derived from solving Eq. (205) for a Gaussian photon distribution (red line). The inset shows the absolute difference ϵ between the two results. Spectra are computed from scattering a FM Gaussian laser pulse with $\lambda = 800$ nm, $a_0 = 0.587$ off a Gaussian electron beam with $Q = 100$ pC and $E_{beam} = 51.1$ MeV [83].

where $\tilde{w}_f = 1/(1+a_0^2/2)$ is the scaling of the peak width. By taking the Fourier transforms of the vector potential distribution functions listed in Table 4, the transverse scale- free spectra may calculated:

$$\tilde{D}_{x,G}\left(\frac{\omega}{\omega_0(\gamma)}\right) = a_0\sigma\sqrt{\frac{\pi}{2}}\exp\left[-\frac{\left(\frac{\omega}{\omega_0}-\tilde{w}_f\right)^2}{2\bar{\sum}^2}\right], \tag{195}$$

$$\tilde{D}_{x,L}\left(\frac{\omega}{\omega_0(\gamma)}\right) = \frac{a_0\pi\sigma}{4}\exp\left(-\frac{\left|\frac{\omega}{\omega_0}-\tilde{w}_f\right|}{2\bar{\sum}}\right), \tag{196}$$

and

$$\tilde{D}_{x,S}\left(\frac{\omega}{\omega_0(\gamma)}\right) = \frac{a_0\pi}{2\sigma}\operatorname{sech}\left[\frac{\pi^2}{\bar{\sigma}}\left(\frac{\omega}{\omega_0}-\bar{w}_f\right)\right], \tag{197}$$

where $\sum = 1/2\pi\sigma$, $\bar{\sum} = \sum\tilde{w}_f$, and $\bar{\sigma} = \tilde{w}_f\sigma$.

The higher order harmonics may be derived from the following process: substitute Eq. (184) into Eq. (189); integrate by parts using the identity $\exp(i\alpha\sin\theta) = \sum J_n(\alpha)\exp(in\theta)$, where J_n is a Bessel function; finally, expand around the stationary phase point. The resulting expressions for the higher harmonics of the scale-free spectrum are defined by the following terms:

$$K_n(\alpha) = (-1)^n[J_n(\alpha) - J_{n-1}(\alpha)], \tag{198}$$

$$g(\xi) = a^2(\xi)(n-1/2)/\{2[1+1/2a^2(\xi)]\}, \tag{199}$$

$$\bar{\omega}_n = \omega/\omega_0 - 2(n-1/2)\tilde{w}_f, \tag{200}$$

$$A_n = K_n[g(0)], \tag{201}$$

$$\sum\nolimits_1 = \sqrt{-B_1^2/2\log[(B_1-1)/A_1]}, \tag{202}$$

$$\sum\nolimits_n = \sqrt{-B_n^2/2\log(B_n/A_n)}, \tag{203}$$

and

$$B_n = K_n[g(\sigma)]. \tag{204}$$

The analytic approximation of the scale-free spectrum may now be expanded to all harmonics by

$$\tilde{D}_x^1 = \frac{1}{2}\mathcal{F}\left\{a(\xi)\left(1 + A_1\exp\left[-\frac{\xi^2}{2\sum_n^2}\right]\right)\right\}\left(\frac{\bar{\omega}_1}{\tilde{w}_f}\right), \tag{205}$$

and

$$\tilde{D}_x^n = \frac{1}{2}\mathcal{F}\left\{a(\xi)A_n\exp\left[-\frac{\xi^2}{2\sum_n^2}\right]\right\}\left(\frac{\bar{\omega}_n}{\tilde{w}_f}\right). \tag{206}$$

As evident in Figure 53, this analytical approximation has excellent agreement with the exact scale-free solution [83].

5.4.5 3D LASER PULSE FREQUENCY MODULATION

Frequency modulation prescription have been expanded from the plane-wave approximation into the 3D incident laser field treatment for nonlinear Thomson scattering. Unfortunately, the benefits of chirping are diminished outside of the plane-wave approximation because the FM depends upon the field strength. Figure 54 shows the peak spectral density as a function of field strength for no FM, FM in the plane-wave approximation, and FM for the 3D laser treatment. Each electron experiences a path dependent field strength defined by Eq. (116):

$$\bar{a}_0 = a_0 \exp\left\{-\frac{x_0^2}{2\sigma_{x,l}^2} - \frac{y_0^2}{2\sigma_{y,l}^2} - \frac{z_0^2}{2\sigma_{z,l}^2}\right\} \exp\left\{\frac{\eta}{2\tilde{\sigma}_{z,l}^2}\right\}.$$

The FM may only be calculated for one specific field strength, so the scattered spectra will not be optimally corrected for each electron.

The optimal chirping for the 3D laser pulse model is [85]

$$f_{3\mathrm{D}}(Y;p) = \left(\frac{p}{3} + \frac{1}{Y}\int_0^Y \mathrm{d}Y' \left(s_1'(Y') + s_2'(Y')\right)\right), \tag{207}$$

where $A(Y) = a_0 \exp(-2Y^2)/2$, $Y = \xi/(\sigma\sqrt{2})$, and p is an arbitrary constant. The factor f_0 is a normalizing constant that is used to shift the scattered frequency without changing the shape of the spectral distribution. This constant is defined by the condition that when it is multiplied by the average angular frequency of the unmodulated laser $f_0\omega_0$ it must be equal to the angular frequency of the laser at the center of the pulse, i.e., when $\xi = 0$. In the plane-wave approximation, $f_0 = 1/(1 + a_0^2/2$, but f_0 must be found numerically for the 3D laser field treatment [72, 85].

5.5 VECTOR POTENTIAL AS AN INTERPOLATION OF A DISCRETE DATA SET

The latest version of the nonlinear Thomson code allows for the field of the incident laser pulse to be explicitly represented by the interpolation of a discrete data set input by the user [86]. This functionality allows the computational model to simulate spectra for cutting-edge, high-intensity lasers whose field vector envelopes do not neatly conform to some analytical representation. In order to make use of phase-space measurements, electric field formalism will be converted to vector potential as a function of ξ. In this section, the the treatment of the laser field will be expanded beyond the conventions of the formalism presented in this work so far in order to touch base with a broader field of researchers. Then the numerical methods used to interpolate the user input discrete data set are defined. This section concludes with a function test in which the new data interpolation function is bench marked against known analytical data.

5.5.1 LASER FIELD TREATMENTS

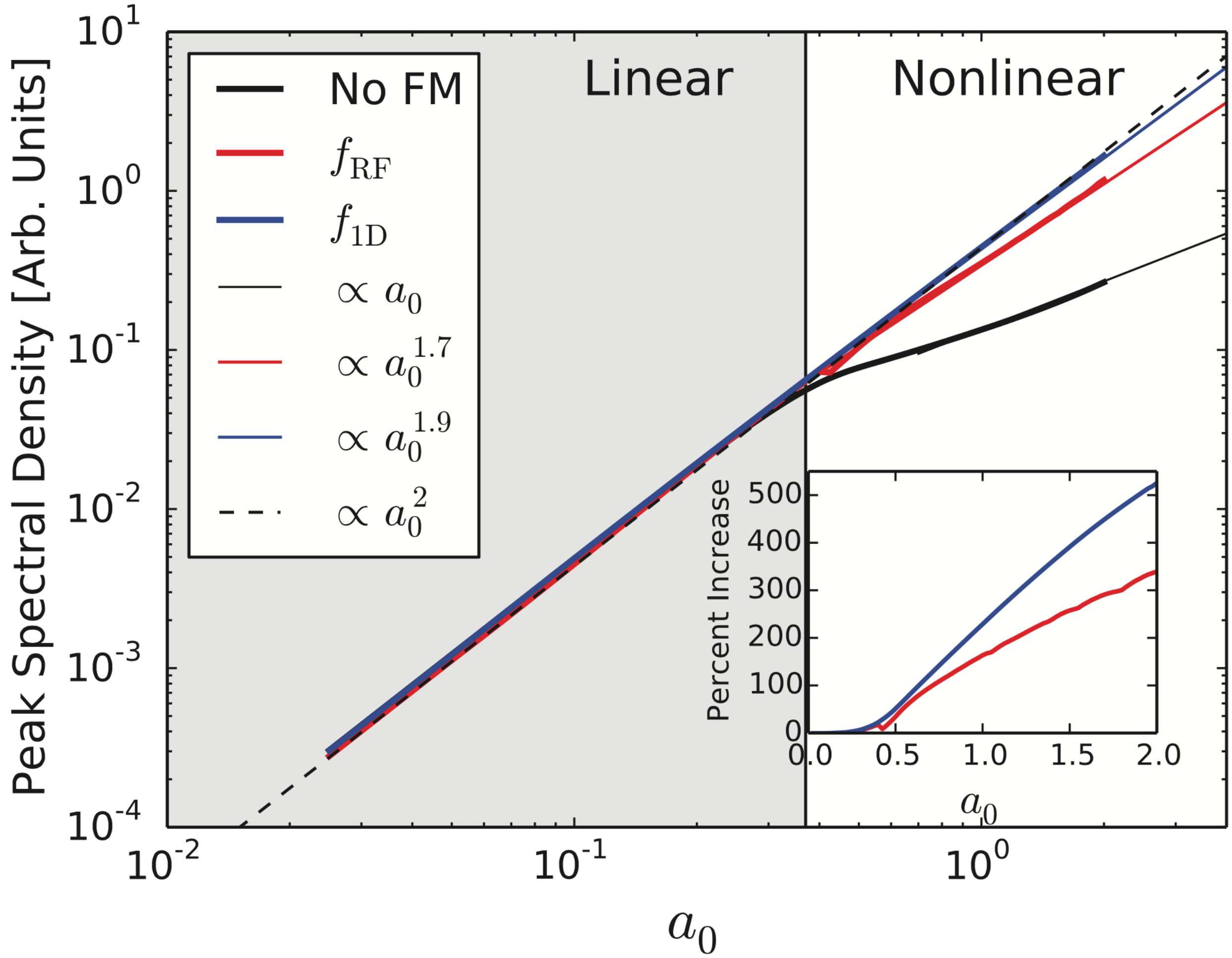

FIG. 54: The peak spectral density of back-scattered radiation for an on-axis electron passing through the laser as in the Dresden experiment [84], as a function of the laser field strength a_0, with 1D FM (red lines), RF FM (blue lines) and without FM (black lines). This is a 1D plane-wave limit in which FM is most effective. The inset shows the percent increase due to chirping [72].

The real, measurable component of an electric field $\epsilon(t)$ may be expressed in terms of its analytic signal $E(t)$ [87]:

$$\epsilon(t) = E(t) + E^*(t). \tag{208}$$

The the analytic signal of an ultrashort pulse must be defined on some interval time $[-T, T]$. The complex analytic signal may be generally expressed

$$E(t) = |E(t)| \exp[i\psi(t)] \exp(i\psi_0) \exp(-i\omega_0 t), \tag{209}$$

where $|E(t)|$ is the time-dependent envelope, $\psi(t)$ is the time-dependent phase, ω_0 is the carrier frequency, and ψ_0 is a constant called the carrier-envelope offset phase. The modulus squared of the signal is the instantaneous power of the laser as a function of time:

$$I(t) = |E(t)|^2. \tag{210}$$

The first time derivative of the phase ψ gives the instantaneous frequency of the electric field,

$$\Omega(t) = -\frac{\partial \psi}{\partial t}, \tag{211}$$

which accounts for the incidence of different photon frequencies at different times.

The frequency representation of the electric field may be calculated from the Fourier transform:

$$\tilde{E}(\omega) = |\tilde{E}(\omega)| \exp[i\phi(\omega)] = \int_{-T}^{T} \mathrm{d}t\, E(t) e^{i\omega t}. \tag{212}$$

Here $|\tilde{E}(\omega)|$ is the spectral amplitude. The spectral density is the square of the the spectral amplitude

$$\tilde{I}(\omega) = |\tilde{E}(\omega)|^2. \tag{213}$$

The spectral phase $\phi(\omega)$ describes the relative phases of the optical frequencies. The group delay is the first derivative of the spectral phase

$$T(\omega) = \frac{\partial \phi}{\partial \omega}. \tag{214}$$

As in Eq. (208), the real measurable component of the electric field in frequency space is

$$\tilde{\epsilon}(\omega) = \tilde{E}(\omega) + \tilde{E}^*(-\omega). \tag{215}$$

Only positive frequencies are permitted in $\tilde{E}$ because of the Fourier transform

$$E(t) = \frac{1}{2\pi} \int_0^{\infty} \tilde{E}(\omega) e^{-i\omega t} \mathrm{d}\omega. \tag{216}$$

The laser pulses propagate through free space without charges, so they are constrained to the condition

$$\int_{-T}^{T} \epsilon(t)\mathrm{d}t = \tilde{\epsilon}(0) = 0. \tag{217}$$

The vector potential may be calculated using Maxwell's homogeneous equation for electric field in terms of potentials:

$$\boldsymbol{E}(t) = -\nabla\Phi - \frac{\partial \boldsymbol{A}}{\partial t}. \tag{218}$$

.

5.5.2 NUMERICAL METHODS FOR THE DISCRETE DATA FUNCTIONALITY OF THE LINEAR THOMSON CODE

Eq. (142), Simpson's Rule, is implemented to complete the definite integrals of the Fourier transforms in Eq. (212) and Eq. (216)

$$\int_{x_0}^{x_2} f(x)\,\mathrm{d}x = \frac{h}{3}(y_0 + 4y_1 + y2) - \frac{h^5}{90} f^{(4)}(c),$$

where $h = x_2 - x_1 = x_1 - x_0$ and $x_0 < c < x_2$. In Figure 55, Simpson's rule is used to transform the real and imaginary components of the electric field in frequency space to times space.

Since there are no charges present, Eq. (218), the vector potential becomes the negative anti-derivative of the electric field

$$E(t) = -\frac{\partial A}{\partial t}. \tag{219}$$

The Fundamental Theorem of Calculus may be used in combination with Simpson's Rule to compute the vector potential:

$$-\int_{a}^{b} E(t)\mathrm{d}t = A(b) - A(a). \tag{220}$$

If the integration begins where the vector potential is zero, i.e., $A(-T) = 0$, then the vector potential may be found through Simpson's Rule

$$A(t) = -\int_{-T}^{T} E(t)\,\mathrm{d}t. \tag{221}$$

The restraint expressed in Eq. (217) can be used to choose an appropriate bounds for $[-T, T]$. In Figure 55, the vector potential in the bottom panel has been calculated by integrating the electric field in the middle panel.

The path parameter of the electron ξ is calculated from its definition:

$$\xi = z_0 + ct, \tag{222}$$

with $z_0 = 0$ since z_0, the fixed position where the measurements have been taken, is made to be the origin.

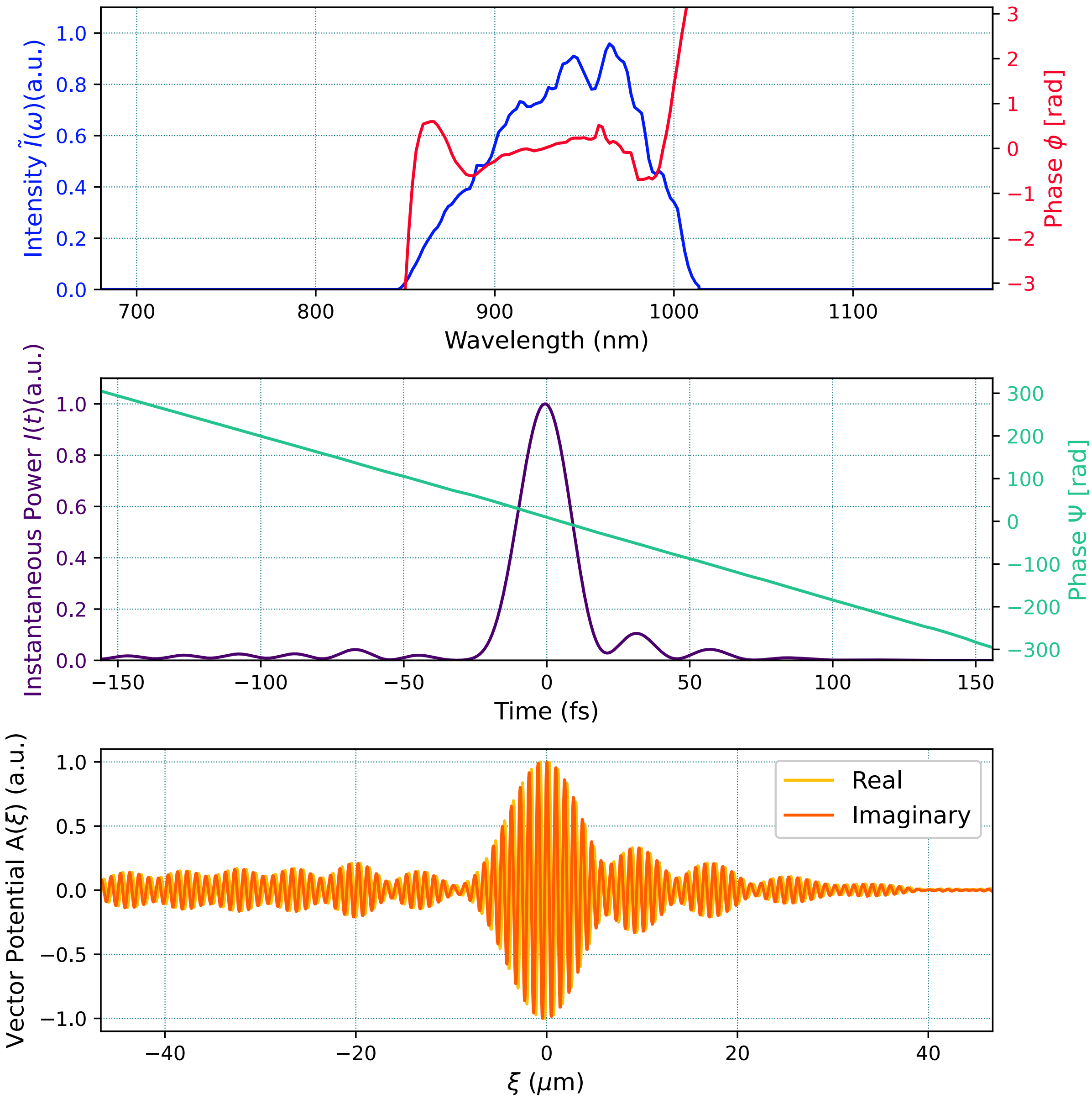

FIG. 55: The instantaneous power as a function of time plotted in the middle panel has been calculated from the frequency space phase and intensity data plotted in the top panel via the Fourier transform in Eq. (216). The real and imaginary components of the vector potential have been calculated using Maxwell's equation, Eq. (218).

5.5.3 DATA INTERPOLATION MODALITY TEST

This modality of the nonlinear Thomson code, i.e., the ability to read in laser envelope information from a discrete data set, has been benchmarked against the previous functionality of the code. To verify that the input data interpolation mode works properly, a simulation was conducted to test the the interpolation of the field strength envelope and the FM.. This first simulation used an incident laser pulse with an analytically generated Gaussian vector potential envelope $a_{\text{analytic}}(\xi)$, and the vector potential envelope data used in this simulation was exported as a discrete data set. This discrete data set was then used in a second simulation utilizing the input data interpolation function for the vector potential envelope $a_{\text{discrete}}(\xi)$ instead of the analytically generated vector potential envelope. The results of these simulations are presented in Figure 56. The analytic and discrete envelopes are the same in both cases, and the resulting spectra are in very strong agreement. This test concludes that the new discrete data set interpolation of the incident laser envelope modality of SENSE is functioning properly.

This update to the nonlinear Thomson computational model also includes the ability to input the frequency modulation (FM) function as an interpolation of a discrete data set. This FM interpolation mode has been benchmarked in exactly the same way the laser envelope input mode. A simulation was conducted using the parameters in which the laser pulse was subjected to a corrective FM [81]:

$$f(\xi) = \frac{1}{1 + a_0^2/2}\left(1 + \frac{\sqrt{\pi}\sigma a_0^2}{4\xi}\operatorname{erf}\left(\frac{\xi}{\sigma}\right)\right), \tag{223}$$

where a_0 is the field strength parameter of the incident laser pulse, σ is the longitudinal spread in the incident photons, and ξ is the spatial parameter that describes the electrons path through the field of the laser pulse. The first simulation used an analytically generated representation of Eq. (223) $f_{\text{analytic}}(\xi)$, and this FM data used was exported as a discrete data set. This discrete data set was then used in a second simulation utilizing the input data interpolation function for the FM $f_{\text{discrete}}(\xi)$ instead of the analytically generated FM. The results of these simulations are presented in Figure 57. The analytic and discrete FM the same in both cases, and the resulting spectra are in very strong agreement. This test concludes that the new discrete data set interpolation of the FM modality of SENSE is functioning properly.

Once these input data interpolation modes were both benchmarked, a final test was conducted to ensure that these new modes of operation function properly together. As before, an analytic simulation was conducted followed by a simulation in which both input interpolation modes were activated. The results of this test are shown in Figure 58. The analytic and data interpolation modes are in strong agreement.

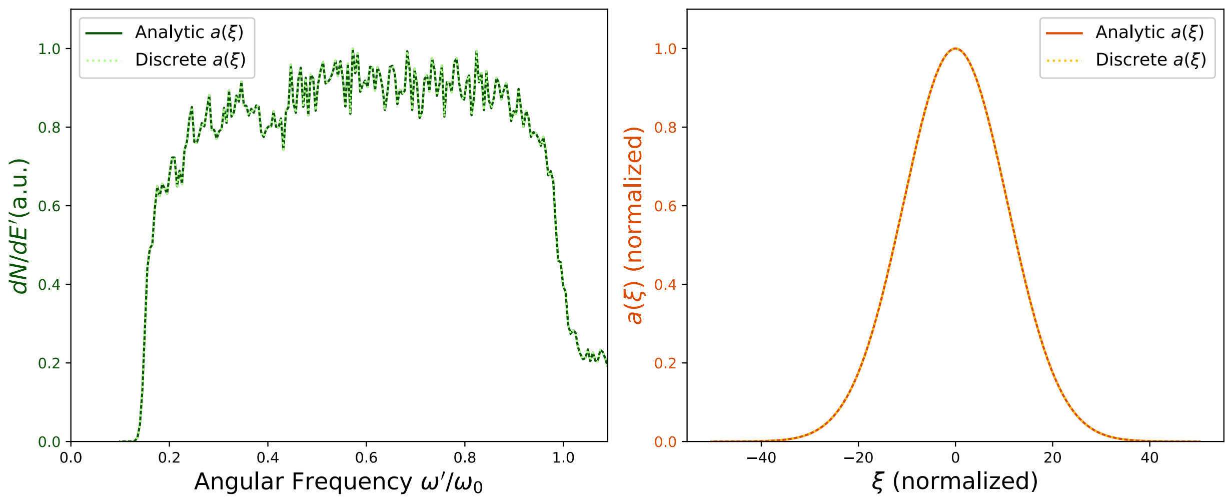

FIG. 56: Two Compton-scattered spectra are plotted on the left: one plot has been calculated using an a analytically generated representation of the incident laser pulse vector potential while the other plot was calculated using an interpolation of a discrete data set representation of the same incident laser pulse vector potential. The plot on the right shows these two representations of the vector potential envelope used by SENSE to calculate the spectra on the left. The comparison is designed to test the functionality of the new SENSE modality, and the strong agreement in the plots indicates that the amended code is functioning properly. The following collision parameters were also used in the simulations: $E_e = 5$ MeV; the electron energy spread is 0.1%; $\sigma_x = \sigma_y = 2.5$ μm; $\epsilon_x = \epsilon_y = 10^{-13}$ m rad; $\lambda = 935$ nm; $a_0 = 3.47$; $\sigma_{x,l} = \sigma_{y,l} = 2.55$ μm; $\sigma_{z,l} = 0.935$ μm; the circular, on-axis aperture is 1 m from the collision and has a radius of 10.2 mm.

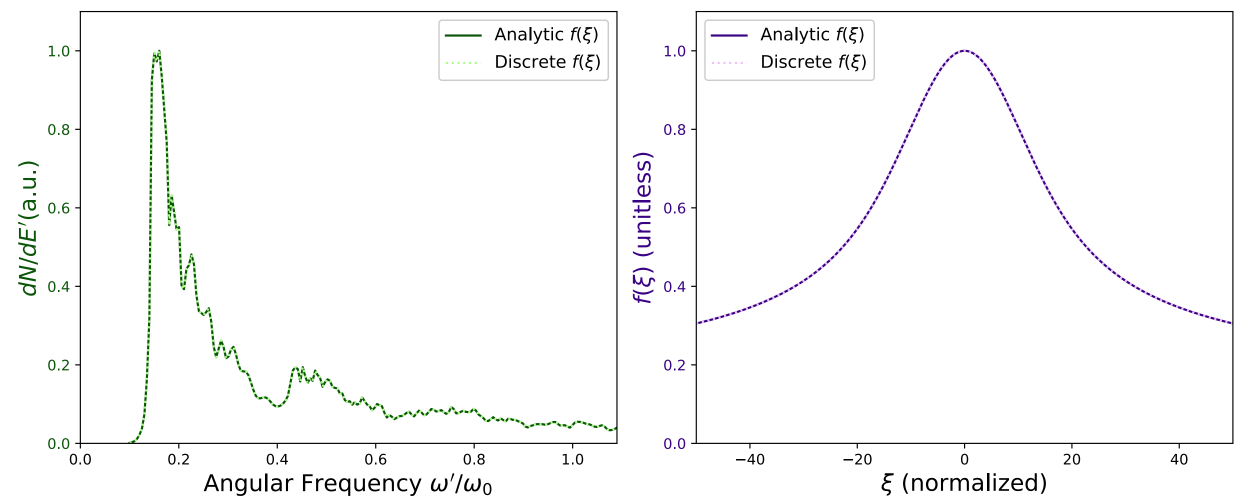

FIG. 57: Two frequency modulated Compton-scattered spectra are plotted on the left: one plot has been calculated using an a analytically generated representation of the frequency modulation function while the other plot was calculated using an interpolation of a discrete data set representation of the same frequency modulation function. The plot on the right shows these two representations of the frequency modulation function and used by SENSE to calculate the spectra on the left. The comparison is designed to test the functionality of the new SENSE modality, and the strong agreement in the plots indicates that the amended code is functioning properly. The following collision parameters were also used in the simulations: $E_e = 5$ MeV; the electron energy spread is 0.1%; $\sigma_x = \sigma_y = 2.5$ μm; $\epsilon_x = \epsilon_y = 10^{-13}$ m rad; $\lambda = 935$ nm; $a_0 = 3.47$; $\sigma_{x,l} = \sigma_{y,l} = 2.55$ μm; $\sigma_{z,l} = 0.935$ μm; the circular, on-axis aperture is 1 m from the collision and has a radius of 10.2 mm.

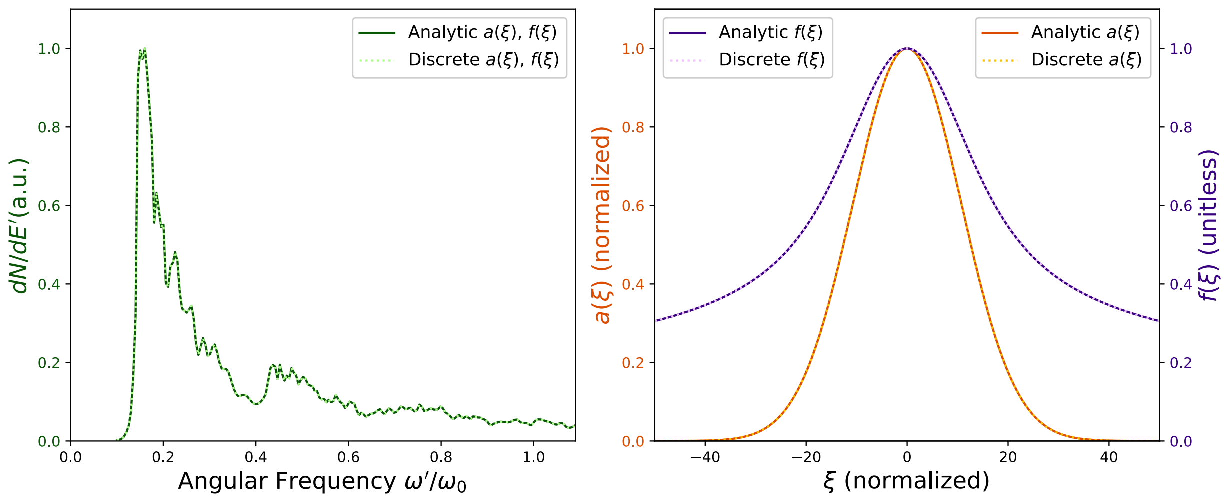

FIG. 58: Two frequency modulated Compton-scattered spectra are plotted on the left: one plot has been calculated using an a analytically generated representation of both the frequency modulation function and the incident laser pulse vector potential while the other plot was calculated using an interpolation of discrete data sets of both the frequency modulation function and the incident laser pulse vector potential. The plot on the right shows these two representations of the frequency modulation function and the vector potential envelope used by SENSE to calculate the spectra on the left. The comparison is designed to test the functionality of the new SENSE modality, and the strong agreement in the plots indicates that the amended code is functioning properly. The following collision parameters were also used in the simulations: $E_e = 5$ MeV; the electron energy spread is 0.1%; $\sigma_x = \sigma_y = 2.5$ μm; $\epsilon_x = \epsilon_y = 10^{-13}$ m rad; $\lambda = 935$ nm; $a_0 = 3.47$; $\sigma_{x,l} = \sigma_{y,l} = 2.55$ μm; $\sigma_{z,l} = 0.935$ μm; the circular, on-axis aperture is 1 m from the collision and has a radius of 10.2 mm.

CHAPTER 6

INVERSE COMPTON SCATTERING SIMULATIONS

In this chapter it will be shown how the ICCS3D and SENSE, the computational models presented in Chapters 4 and 5 respectively, have been implemented to advance the understanding of ICS light sources. The computational models of been benchmarked repeatedly against other theoretical models and experimental data. The impact of the incident laser field envelope shape upon the scattered spectra has been observed and studied. Although we have yet to see an experimental example of frequency modulation, the simulations have been used to demonstrate the possible spectral brilliance gains that could be achieved in existing sources through the use of chirping. These models have been used to evaluate the viability of novel, high-energy lasers in ICS applications. The onset of ponderomotive and Compton effects have been observed. These models have even been used to create diagnostic tools that can compute the beam dynamics of operational Compton sources. Our computational models have indeed been used to advance ICS research.

The simulations to be discussed are plotted with respect to their regime of operation in Figure 59. From the relatively low Compton parameter values on the x-axis, these simulations are almost entirely in the Thomson regime; the proposed Smart*Light from the Technical University of Eindhoven [32] approaches the cusp of the region where the Compton recoil begins to effect the scattered spectra. As we have studied many novel light sources proposed by the Laboratory for Laser Energetics at Rochester University (LLE), many of the simulations presented here our in the nonlinear regime. As previously stated, this work is limited to single-photon emissions, so all of the simulations fall beneath the radiation reaction limit. For ease of comparison, the maximum parameters of the studies presented in this chapter are listed in Table 5.

TABLE 5: Compton scattering parameters for the simulations presented in this chapter that determine the operating regime of the computational model [84, 88, 32].

Simulation	E_e [MeV]	γ	a_0	λ [nm]	X
Dresden	23	45	1.6	800	5.5×10^{-4}
MTW OPAL	20	39	3.5	810	4.7×10^{-4}
Smart*Light	31	60	0.19	800	7.3×10^{-4}
MuCLS	38	74	4.8×10^{-4}	1,064	6.7×10^{-4}
LLE Non-Analytic Pulse	5	9.8	3.5	940	1.0×10^{-4}

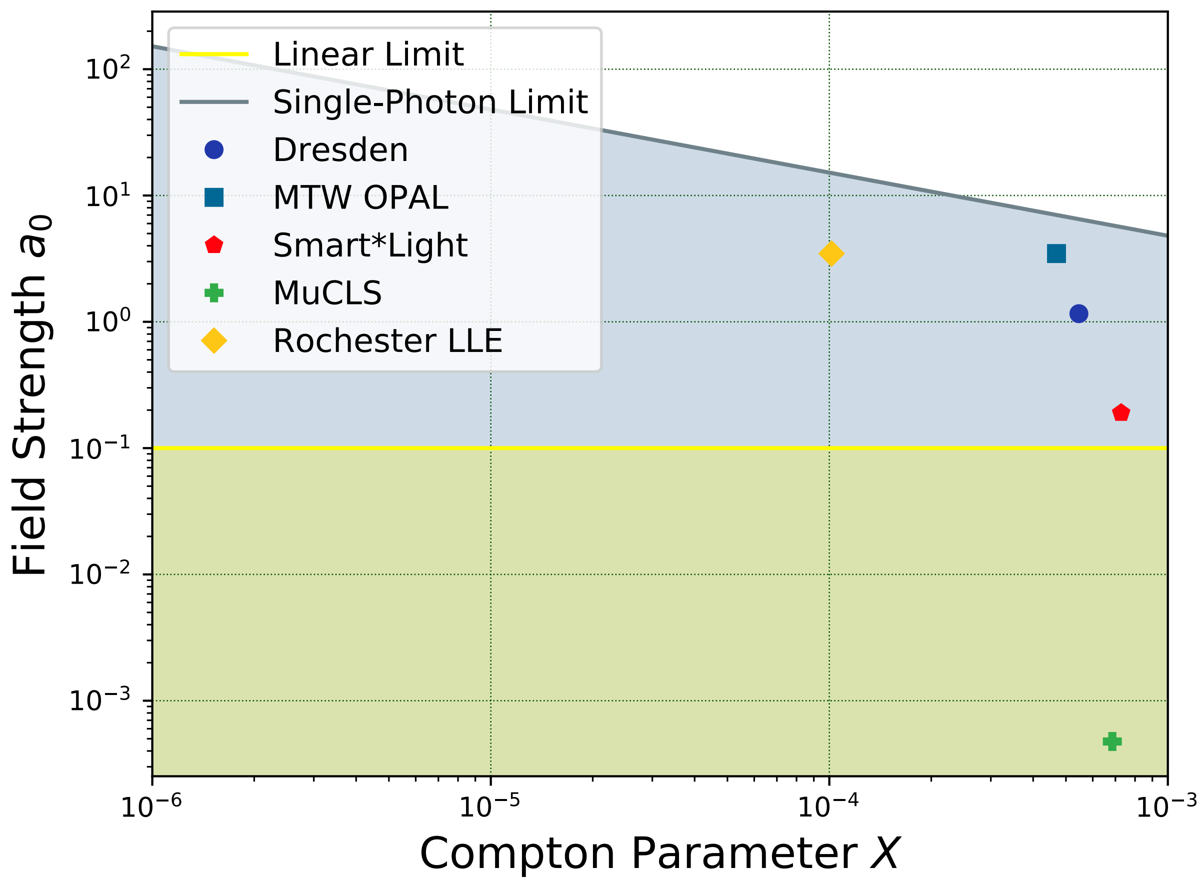

FIG. 59: Simulations generated using the computational models presented in Chapters 4 and 5, ICCS3D and SENSE, plotted with respect to the maximum field strength a_0 and the maximum Compton parameter X used during the simulations. Simulations lying in the yellow region are in the linear regime, and simulations above the yellow region are in the nonlinear regime. All of the simulations presented in this chapter fall beneath the grey line which is the radiation reaction limit, i.e., these simulations are within the single-photon emission regime.

6.1 DRESDEN

The quasiclassical computational model, SENSE [72], is compared to the quantum code CAIN [89] by replicating the Dresden experiments [84] that have been conducted in the nonlinear Thomson regime where electron recoil can be neglected. This study was a collaboration with our colleagues in Milan who ran the CAIN simulations. While both codes use Monte Carlo integrations, there is a fundamental difference between CAIN and SENSE. SENSE captures even the rarest scattering events by properly computing the scattering probabilities through the energy density spectrum derived in Chapter 5. CAIN, however, models the incoming laser beam scattering off each such electron from the sample with a fixed number of individual scattered particles. While this directly models what happens in an experiment, albeit on orders-of-magnitude smaller scales, it ensures that the rare events in nature will be equally rare in a simulation, leading to poor statistics in those regions. Accuracy in each portion of the spectrum computed by SENSE is equal: the precision is only determined by the resolution of the Monte Carlo integration. SENSE also offers a more sophisticated treatment of the incident laser field: the field shape may be modeled by any 3D analytic function, the field envelope may also be interpolated from a discrete data set, and FM may be modeled in the incident fields as well. CAIN does not have this functionality.

In all of our simulations the agreement between the results produced by CAIN and SENSE is remarkable, especially considering that they are based on two vastly different approaches. These simulations are plotted in Figure 60. For the largest values of the laser field, $a_0 = 1.6$, 1.0, the agreement between the experiments and simulations using CAIN is very good, and SENSE even better. However, for lower values, $a_0 = 0.5$, 0.05, there is a shift to the right in the simulations from both codes. Increasing the strength of the laser field from $a_0 = 0.5$ to 0.7 and from $a_0 = 0.05$ to 0.5 in SENSE simulation produces excellent fits to the data, comparable to those for the larger values of a_0. The discrepancy between the experiments and the simulations for the lower values of the strength of the laser field is likely due to a different geometry of collision.

As the transverse size of the laser pulse becomes much larger then the spot size of the electron beam, i.e., $r_x, r_y \to 0$ from Eq. 120) from Section 4.5.1, the path-dependent field strength parameter $\bar{a}_0$ begins to approach the maximum field strength a_0 for all electrons. This relation ship is plotted in Figure 61. In other words, vanishing ratios r_x, r_y lead to the 1D plane-wave model in which all electrons experience the same vector potential magnitude. The closer the beam sizes are to this 1D plane-wave limit, the more effective the FM becomes (as is shown in Figure 62).

6.2 ROCHESTER LLE: MTW OPAL

A series of simulations have been conducted for novel, high-intensity lasers proposed by the Laboratory for Laser Energetics (LLE) at the University of Rochester. These simulations were used to explore the possibility of using these devices for ICS. The parameters of the four lasers simulated are shown in Table 6. The normalized laser pulse length σ has been calculated from the

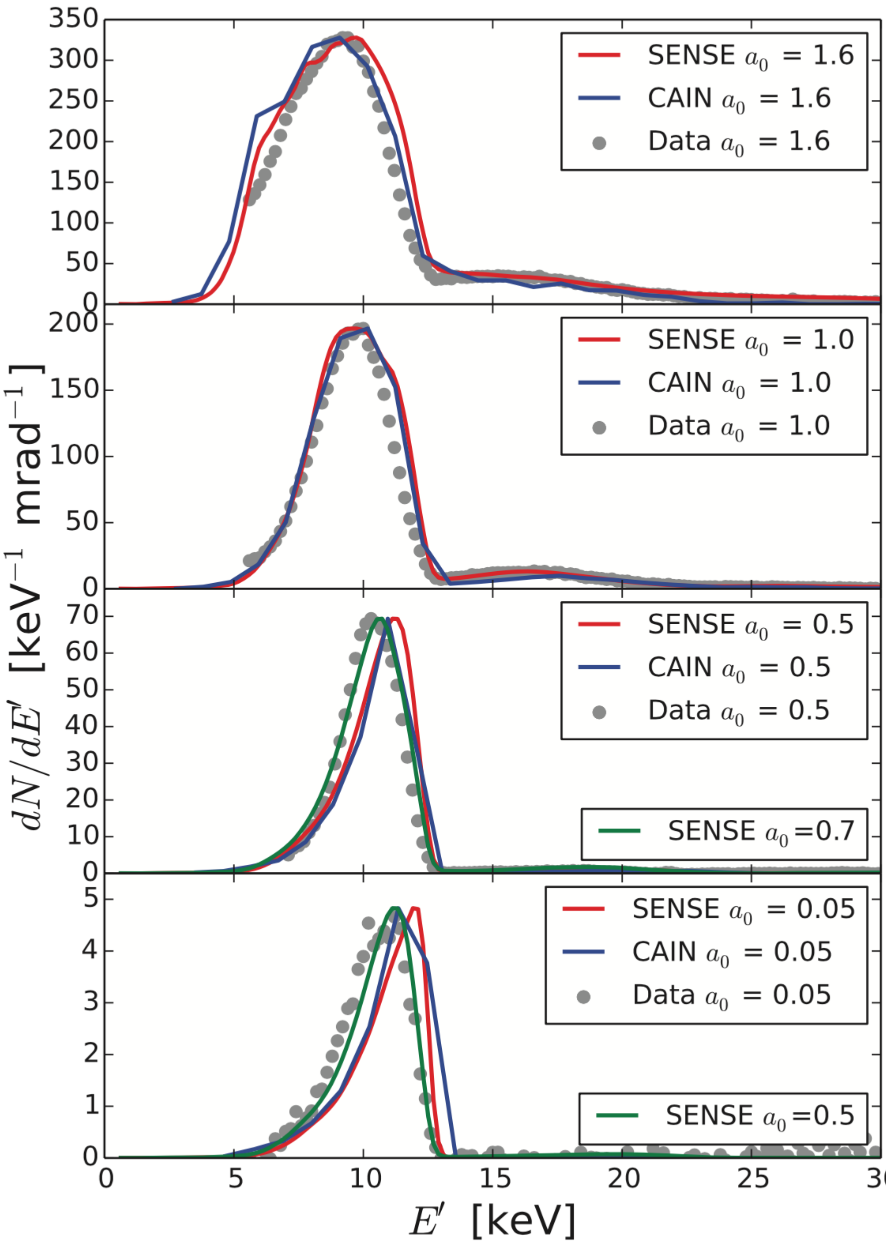

FIG. 60: Simulation of the Dresden experiment [84] data (gray circles) with CAIN (blue line) and with SENSE (red line) for parameters $a_0 = 1.6$, 1.0, 0.5, 0.05. Simulations with SENSE use circular aperture of $\theta_{\text{APERTURE}} = 0.004$. The other collision parameters are defined: the electron energy is 23 MeV; the electron energy spread is 0.175%; the electron spot size is the laser wavelength 800 nm; the electron beam horizontal spot size is $\sigma_x = 41 \pm 1.2$ μm; the electron beam vertical spot size is $\sigma_y = 81 \pm 2$ μm; the normalized horizontal emittance is $\epsilon_x = 20.3 \pm 1.1$ mm mrad; the normalized vertiacl emittance is $\epsilon_y = 18 \pm 6.6$ mm mrad; $\sigma_{x,l} = \sigma_{y,l} = 13.59$ μm; the laser pulse length is $\sigma_{z,l} = 4.5$ μm [72].

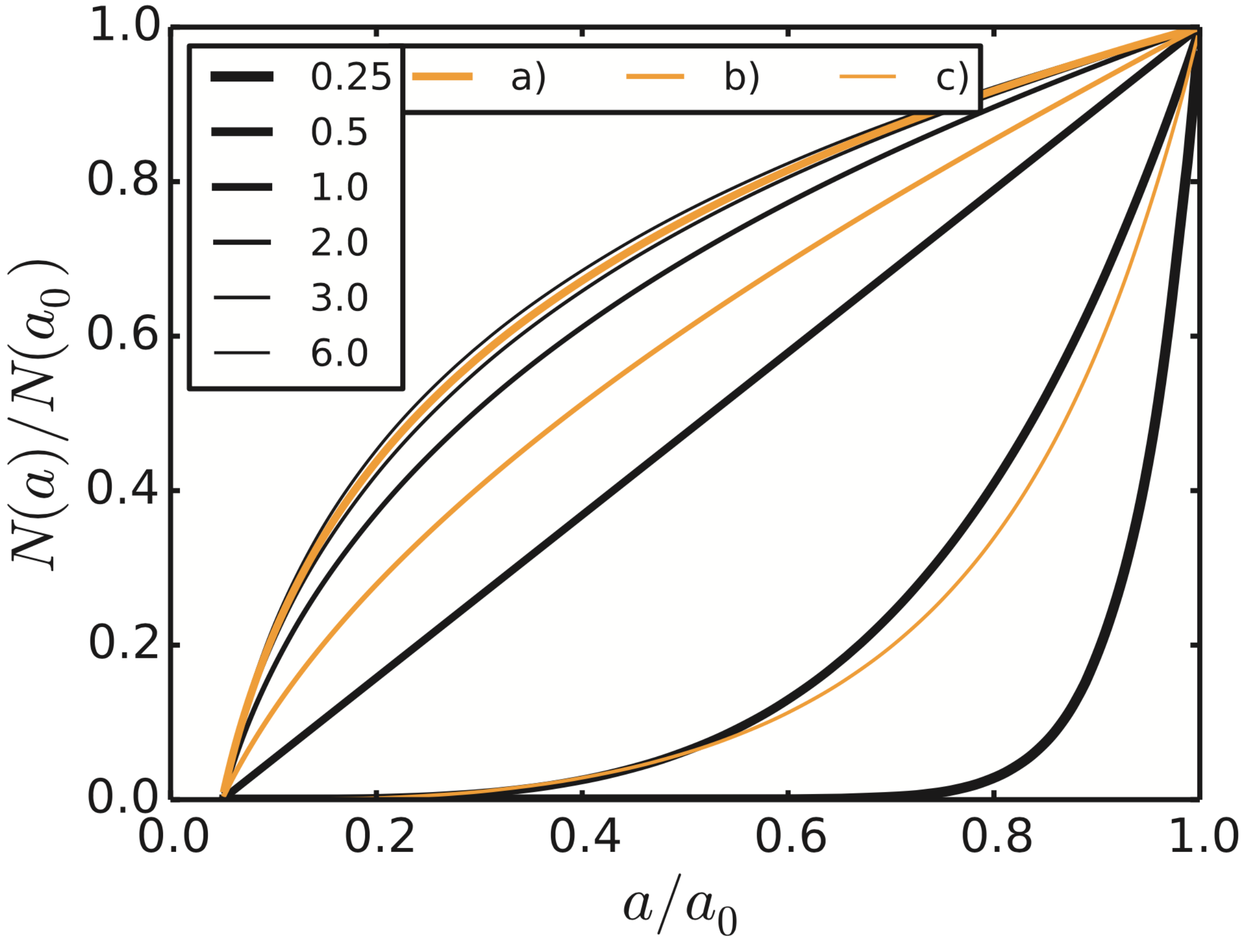

FIG. 61: Distribution of field strength values seen by the electron beam for various transverse ratios ($r_x = r_y = 0.25$, 0.5, 1, 2, 3, 6) in black. Shown in orange are the distributions corresponding to the plots in Figure 62: panel (a) with $r_x = 3$, $r_y = 6$, panel (b) with $r_x = 1$, $r_y = 2$, and panel (c) with $r_x = 0.3$, $r_y = 0.6$. A lower cutoff of $a > a_{min} = 0.05$ is imposed on the distribution [72].

TABLE 6: Laser parameters for the simulations presented in Section 6.2.

Device	a_0	λ [nm]	Length [fs]	Energy [J]	σ
MTW Opal(A)	3.47	810	15	7.5	2.36
Ω EP HESP(B)	1.65	1,054	15,000	1,000	1,820
Ω EP SP(C)	4.52	1,054	700	1,600	84.7
Ω EP SP(2)(D)	43.95	180	20	1,600	3.15

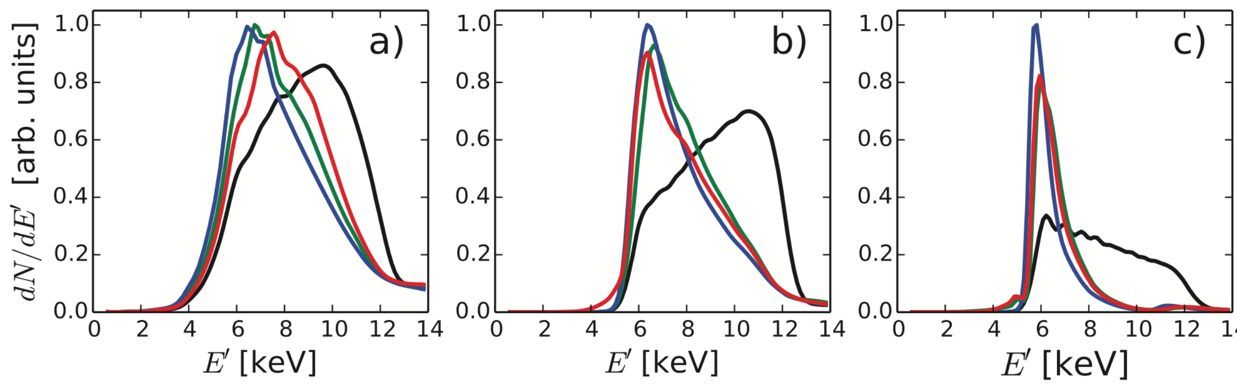

FIG. 62: Panels (a)–(c): simulation of the Dresden experiment [84] for $a_0 = 1.6$ using SENSE without FM (black lines) and with FM: optimal 1D plane-wave f_{1D} [81] (blue lines), optimal 3D laser pulse f_{3D} [85] (green lines) and RF FM [81] f_{RF} (red lines). The transverse electron beam size is nominal in (a), reduced by $\sqrt{10}$ in (b) and reduced by 10 in (c) [72].

FWHM temporal pulse width of the laser T:

$$\sigma = \frac{cT}{2.35\lambda}.$$

The lasers were proposed to be paired with a simple linac setup. There are two different configurations for the electron beam: the electron beam comes straight off the photoinjector gun, or the the electron beam is accelerated by a SLAC guide. Emittance has been taken to be of minimal value since we are to assume a 'perfect beam.' The parameters of the electron beam are shown in Table 7.

The simulations assume an on-axis, circular sensor aperture. In all cases, the aperture has a radius of $d\tan(1/10\gamma)$ where d is the distance between the sensor and the collision.

The simulations for MTW OPAL are displayed in Figure 63. As shown in the SI unit spectra for both simulated lasers, the increased electron energy dramatically blue shifts the radiated photon spectra. The geometry of the spectra, however, is unaffected by the increased energy as shown in the normalized plots.

The nonlinear Thomson code is only valid for the nonlinear Thomson regime. This computational model has been derived from the requirement that each electron only experiences one scattering event. As discussed in Section 3.5, each electron, on average, only experiences at most

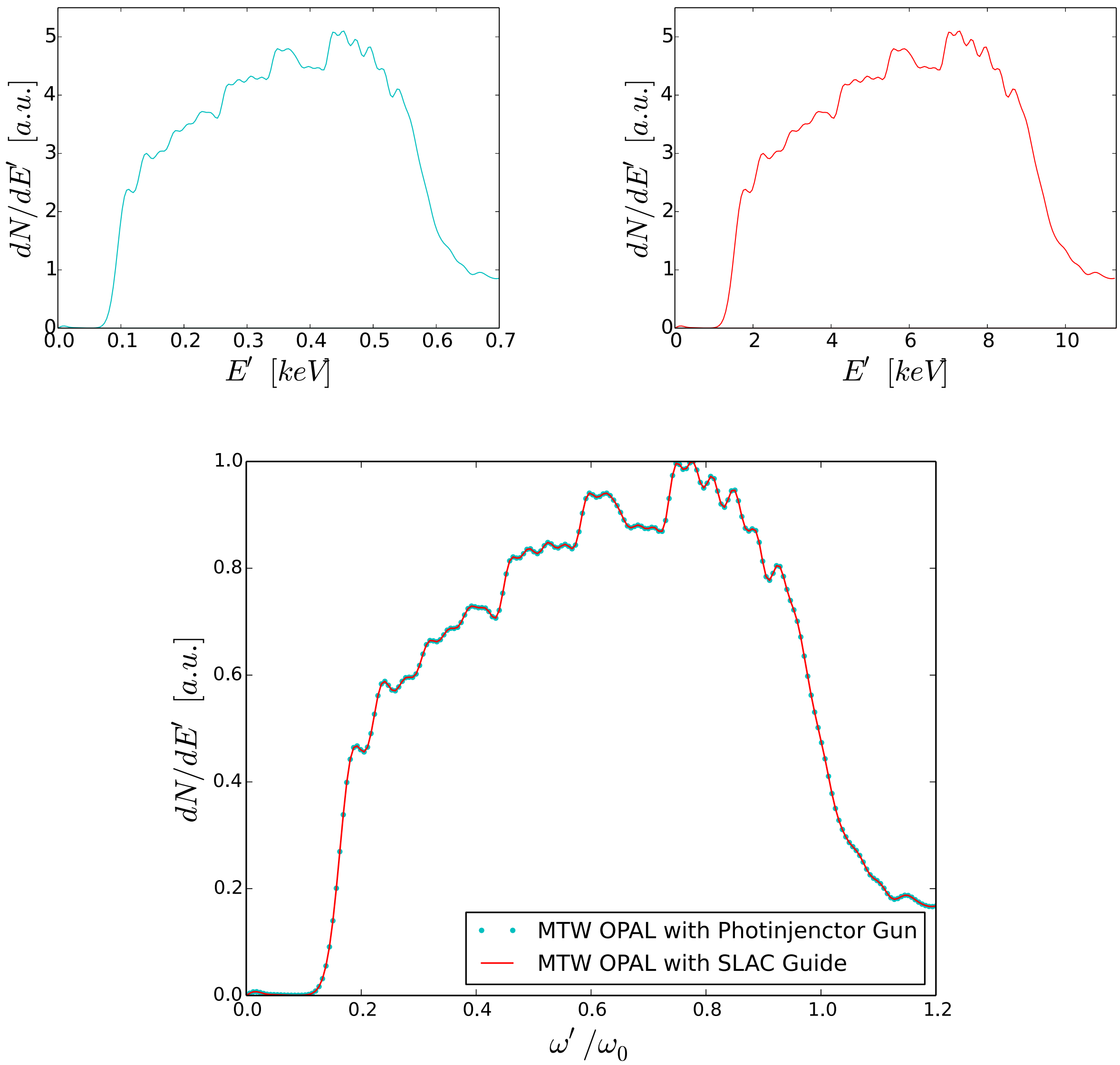

FIG. 63: Simulated Compton-scattered spectra generated by MTW OPAL. The top left plot shows the spectrum created by an electron beam from the photoinjector gun alone, while the top right plot show the spectrum created by an electron beam accelerated by the SLAC guide. Simulated Compton-scattered spectra generated MTW Opal. The bottom plot shows the peak-normalized, frequency-normalized spectra produced by both the photoinjector gun alone and the SLAC guide. The parameters for this simulation are shown in Tables 6 and 7. The scaling in the x direction is the same both plots as the aperture in both simulations scales with the energy of the electron beam $\theta_{\mathrm{A}} \propto 1/10\gamma$.

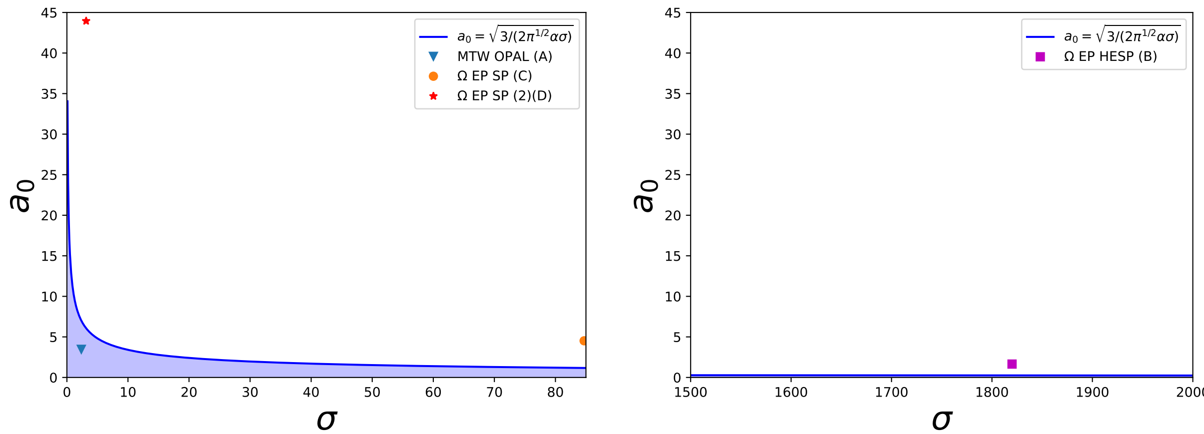

FIG. 64: Single emission field strength parameter a_0. The blue region of the plot illustrates the range of a_0 as a function of the normalized laser pulse length, $\sigma = \sigma_{z,l}/\lambda$, that is free of radiation reaction in the scattering electron. The input parameters for Section 6.2 are plotted above, and the parameter for the simulations are give in Tables 6 and 7.

TABLE 7: Electron beam parameters for the simulations presented in 6.2.

Device	Energy [MeV]	σ_E	σ_x [μm]	Charge [fC]
Photoinjector Gun (1)	5	0.1%	25	100
Gun & SLAC Guide (2)	20	0.1%	25	100

one scattering event. This condition is defined by the inequality

$$a_0 < \sqrt{\frac{3\lambda}{2\sqrt{\pi}\alpha\sigma_{z,l}}},$$

where λ is the incident laser wavelength, α is the fine structure constant, and $\sigma_{z,l}$ is the longitudinal photon distribution in the laser pulse. Figure 64 illustrates this limitation.

Unfortunately, the parameters for Ω EP HESP, Ω EP SP, and Ω EP SP(2) are in the region of radiation reaction, i.e., the electron emits multiple photons during a single collision event. These photon-electron collisions with radiation reaction have severely broadened spectra and lie outside the function of SENSE and ICCS3D. There is a brief discussion on this phenomenon in Section 7.4. While the proposed lasers have an impressive field strength and incredibly short pulse length, radiation reaction makes them less-than-ideal for the purpose of ICS. Even the MTW Opal which is squarely in the single-photon emission regime, suffers tremendous spectral broadening from ponderomotive effects. Without implementing frequency modulation or some other means of mitigating the nonlinear effects, these lasers will not be suitable for Compton light sources.

6.3 EINDHOVEN UNIVERSITY OF TECHNOLOGY: SMART*LIGHT

Our colleagues at the Eindhoven University of Technology are developing a compact, affordable tabletop Compton light source [32]. This light source makes use state-of-the-art low emittance electron guns, compact X-band accelerator technology and high-power pulsed lasers that have only recently become available and affordable. This ICS source, the TU/e Smart*Light, will serve extremely sensitive, on-site tool for non-destructive imaging and analysis that will be capable of many of the applications described in Chapter 1: phase contrast imaging, XRF. XRD, XRS, etc.

In a collaborative effort, both SENSE and ICCS3D simulated the proposed operating parameters of Smart*Light. Researchers at Eindhoven also conducted simulations. The objective of the simulations were two-fold. First and foremost, the main objective was to accurately model the spectra produced by the proposed ICS light source. The secondary purpose of the simulations was to benchmark a novel computational model against SENSE and ICCS3D [90]. The simulated spectra are all in agreement. Figure 65 shows the set of simulations generated in this study.

As one may note from Figure 59 in the beginning of this chapter, the parameters chosen for these simulations lie near the boundaries of both the linear/nonlinear limit and the Thomson/Compton limit. These boundaries are not discrete: the onset of the characteristics unique to these regimes, i.e., ponderomotive effects and the Compton recoil, increase slowly with the square of the field strength a_0^2 and the Compton parameter X respectively. Note that in the simulations, only SENSE is able to capture ponderomotive red shift.

Figure 66 shows an interesting way of increasing spectral brilliance by stretching the incident laser pulse [91]. Both plots displayed here were simulated by SENSE. It has been shown that the simple stretching of the laser pulse, while keeping the energy constant can significantly increase the peak spectral density of the scattered radiation.

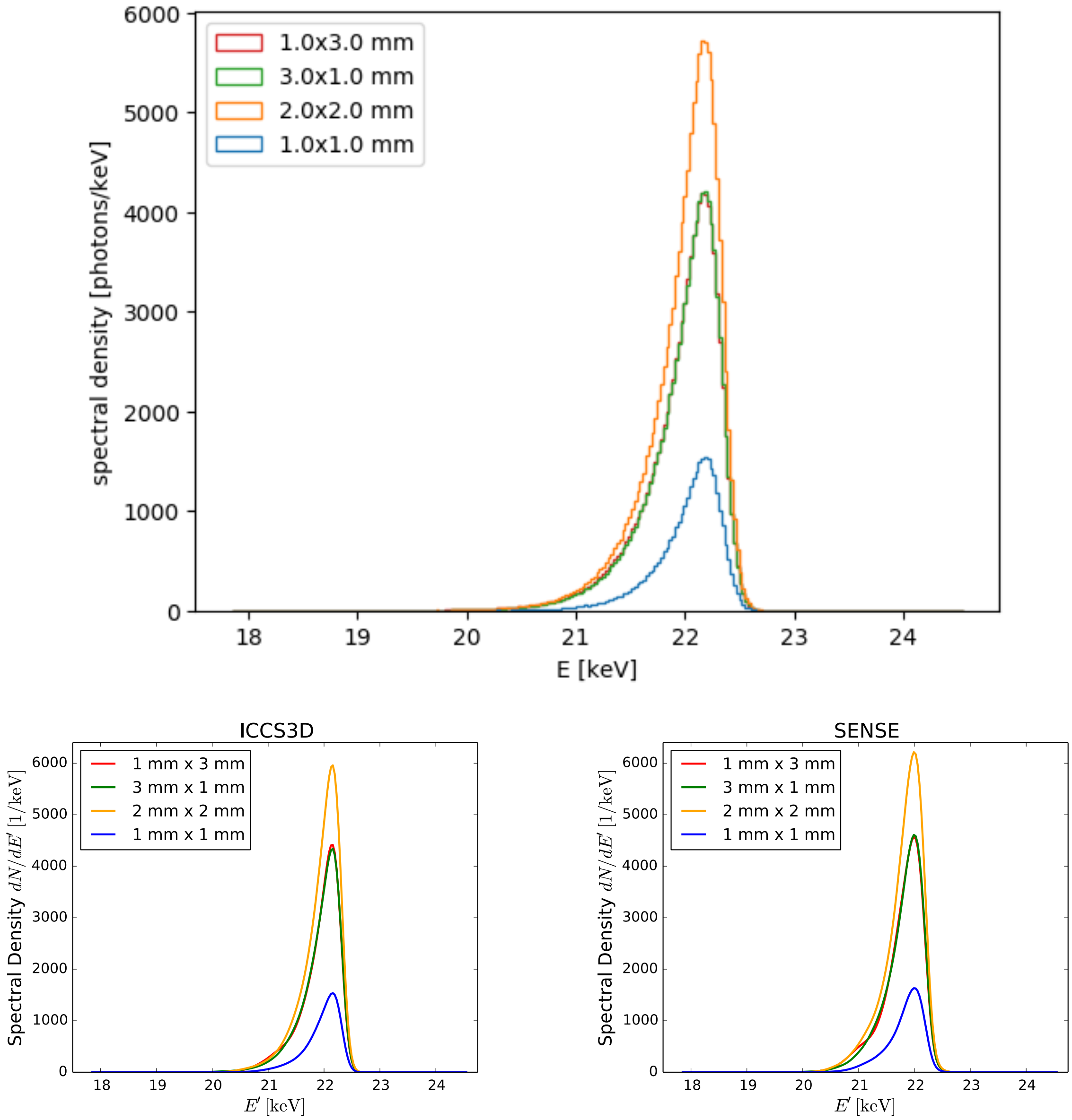

FIG. 65: Scattered spectra for the Smart*Light simulated with TUE linear Compton code (top), the linear Compton code ICCS (bottom left), and the non-linear Thomson code SENSE (bottom right). Non-linear red-shift of about $< 1/(1 + a_0^2/2)$ is not accounted for in the first two linear codes. The four different proposed aperture are simulated: 1 mm $\times$ 1 mm, 1 mm $\times$ 3 mm, 3 mm $\times$ 1 mm, 2 mm $\times$ 2 mm, all placed 1 m away from the collision point. The following collision parameters were also used in the simulations: the electron energy is 30.66 MeV; the electron energy spread is 0.01%; the electron beam spot size is $\sigma_x = \sigma_y = 6$ μm; the normalized circular emittance is $\epsilon_x = \epsilon_y = 0.5$ mm mrad; the laser wavelength 800 nm; the laser pulse spot size $\sigma_{x,l} = \sigma_{y,l} = 5$ μm; the laser pulse duration (FWHM) is 100 fs.

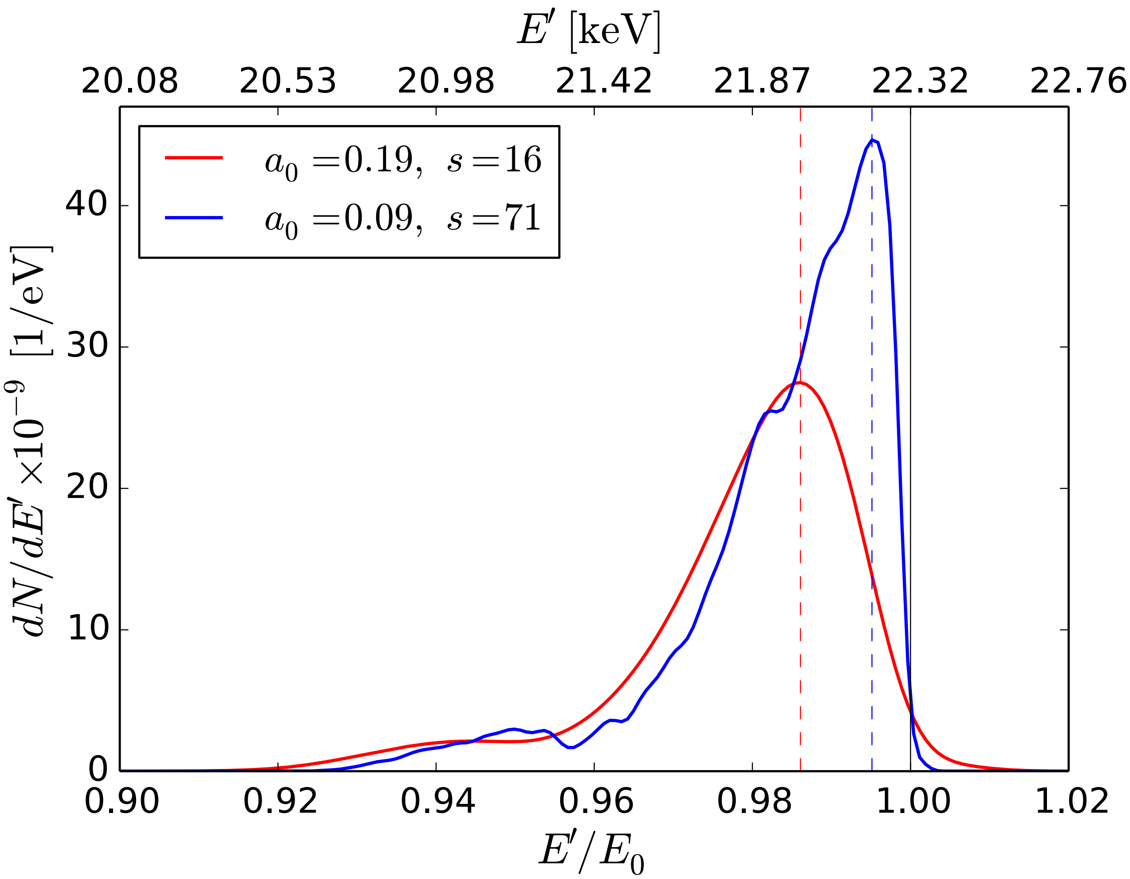

FIG. 66: Comparison of spectra produced using SENSE for the nominal Smart*Light design ($a_0 = 0.19$, shown in red) and the case where the total laser energy kept constant $E \propto a_0^2 s = const$, but the laser longitudinally stretched (blue line). In the linear case, the energy at which the peak spectral density is expected to occur is $E'/E_0 = 1$ (solid vertical line). Energies at which the peaks in the two spectra occur are shown in dashed lines. The rectangular aperture of 1 mm $\times$ 1 mm is used in the simulation. The following collision parameters were also used: the electron energy is 30.66 MeV; the electron energy spread is 0.01%; the electron beam spot size is $\sigma_x = \sigma_y = 6$ μm; the normalized circular emittance is $\epsilon_x \epsilon_y = 0.5$ mm mrad; the laser wavelength 800 nm; the laser pulse spot size $\sigma_{x,l} = \sigma_{y,l} = 5$ μm; the laser pulse duration (FWHM) is 100 fs.

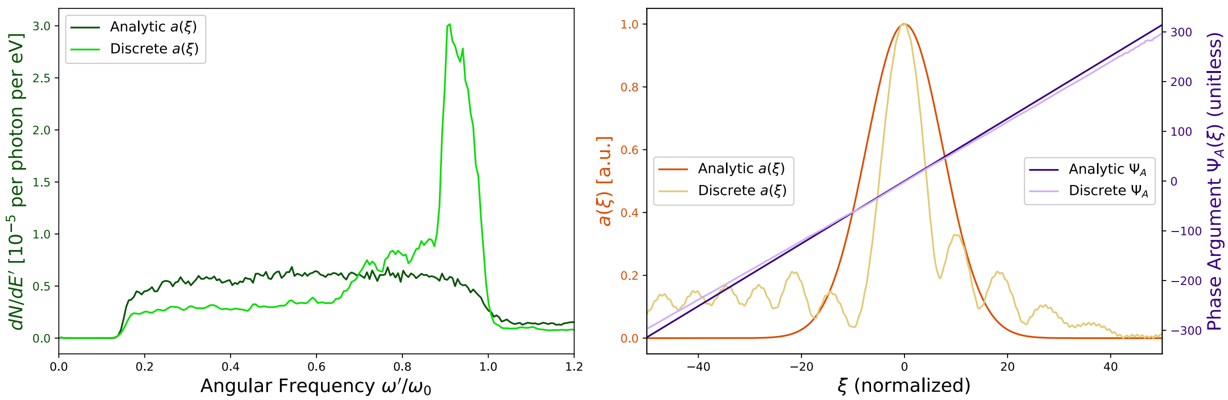

FIG. 67: Two Compton-scattered spectra are plotted on the left: one plot has been calculated using an a analytically generated representation of a Gaussian incident laser pulse vector potential ($\sigma = 5.261$) while the other plot was calculated using an interpolation of a discrete data set. The plot on the right shows these two representations of the vector potential envelope used by SENSE to calculate the spectra on the left. The following collision parameters were also used in the simulations: $E_e = 5$ MeV; the electron energy spread is 0.1%; $\sigma_x = \sigma_y = 2.5$ μm; $\epsilon_x = \epsilon_y = 10^{-13}$ m rad; $\lambda = 935$ nm; $a_0 = 3.47$; $\sigma_{x,l} = \sigma_{y,l} = 2.55$ μm; the circular, on-axis aperture is 1 m from the collision and has a radius of 10.2 mm.

6.4 ROCHESTER LLE: NON-ANALYTIC FIELD SIMULATION

Researchers in the field of high-energy lasers fields have a growing need for more sophisticated field treatments. Our colleagues at the Laboratory for Laser Enregetics (LLE) have developed high-intensity lasers whose vector potential envelopes do not conform to the analytic representations presented in Sections 4.5 and 5.2. In other words, there exists no analytic function $\tilde{A}(\xi)$ to properly represent the laser field envelope. The envelope is instead represented by a discrete data set that is derived through empirical measurement. Often these data sets are given in terms of frequency space intensity or instantaneous power in real space, as shown in Figure 55. The new modality also allows this form of input to be processed and prepared for SENSE.

The discrete laser envelope data input modality of the nonlinear Thomson code has been used to simulate a Thomson scattering event in which a nonlinear, ultra short laser pulse is incident up a relativistic electron bunch [86]. The ability to read in laser envelope information from a discrete data set has been used to simulate a photon pulse with specific frequency distribution. A secondary script has been written to calculate the vector potential envelope of the incident laser as a function of the electron path parameter ξ from the frequency representation of intensity and phase

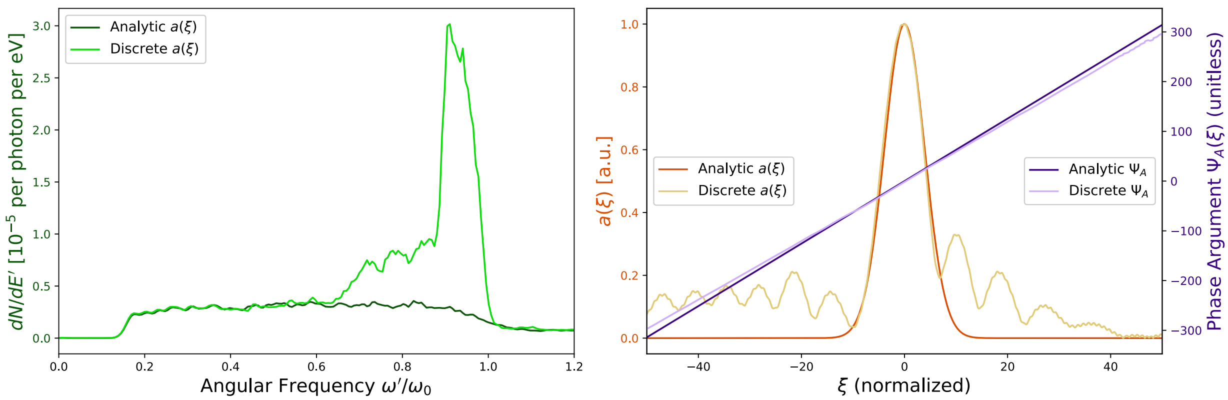

FIG. 68: Two Compton-scattered spectra are plotted on the left: one plot has been calculated using an a analytically generated representation of a Gaussian incident laser pulse vector potential ($\sigma = 2.75$) while the other plot was calculated using an interpolation of a discrete data set. The plot on the right shows these two representations of the vector potential envelope used by SENSE to calculate the spectra on the left. The following collision parameters were also used in the simulations: $E_e = 5$ MeV; the electron energy spread is 0.1%; $\sigma_x = \sigma_y = 2.5$ μm; $\epsilon_x = \epsilon_y = 10^{-13}$ m rad; $\lambda = 935$ nm; $a_0 = 3.47$; $\sigma_{x,l} = \sigma_{y,l} = 2.55$ μm; the circular, on-axis aperture is 1 m from the collision and has a radius of 10.2 mm.

characteristics of the photon pulse. Section 5.5.1 outlines the physics principles used to calculate the vector potential envelope from the frequency space data. Section 5.5.2 details the numerical methods used to compute the vector potential envelope. In order to illustrate the significance of including the detailed incident photon frequency distribution, the results of this simulation will be compared to a commonly used approximation, a Gaussian distribution, for the vector potential envelope.

The simulation shows that the frequency space intensity and phase argument from the top panel of Figure 55 generates a higher brilliance emission than an analytic Gaussian distribution of equal power. As Figures 67 and 68 both show, the incident laser field for this discrete data set is broken into a series of smaller peaks. The height of these peaks scale with the field strength parameter a_0 which means the vector potential from the discrete data set experiences a much smaller maximum field strength. The reduction in the field strength dramatically reduces the ponderomotive effects that undermine the brilliance of the analytic Gaussian envelopes. The simulations also indicate that the series of vector potential peaks in the discrete data set envelopes cause some degree of spectral broadening in the form of red shifted plateau-like tails. This broadening, however, is much less deleterious to spectral brilliance than the ponderomotive effects.

6.5 MUNICH COMPTON LIGHT SOURCE

The Munich Compact Light Source (MuCLS) is a facility operated by the Center for Advanced Laser Application (CALA) located at the Technical University of Munich (TUM). MuCLS is a joined project of the two premier Munich universities, TUM and Ludwig-Maximilian-Universität München (LMU)[92].

The facility boasts two X-ray light sources: an in-house developed X-ray beamline and the Lyncean Compact Light Source. The Lyncean Compact Light Source is an out-of-the-box ICS source. Our colleagues in Munich recently conducted the first X-ray absorption spectroscopy study using an inverse Compton source [88]. The study demonstrated the first proof-of-principle XAS study with an inverse Compton scattering light source. As stated in Chapter 1, the ICS source provided energy tunability, few percent bandwidth, and a very high brilliance for a laboratory setup. This MuCLS is particularly suited for routine XRS studies in the convenience of the on-site home laboratory. This ICS source is proposed to be a good candidates for XRF as well. The demonstrated pulse lengths of hard X-rays on the picosecond scale open a potential path for time-resolved studies investigating picosecond phenomena at high energies in a laboratory environment.

As the published results of the XAS study provided Compton scattered spectra in the linear regime, ICCS3D was used to simulated these reported spectra. As with the simulations presented earlier in this chapter, there is always value in benchmarking these computational models against experimental data. This followup study revealed that there was meaningful disparity between the reported spectrum and the simulated spectrum. Figure 69 shows the reported spectrum (green) compared to the ICCS3D simulation that uses the nominal parameters from light source manufacturer (grey). Lyncean specifies that the emittance in the light source electron beam is circular $\epsilon_x = \epsilon_y$. The scattered spectra, however, do not have the geometry characteristic of a circular emittance. The genetic algorithm (GA) was implemented along with ICCS3D to find the input parameters that best fit the experimental data. Specifically, the GA study optimized the fit over the following parameters: average electron energy, electron beam energy spread, and the horizontal and vertical emittance. This study found that the best fit was that of a non-circualr emittance. The resulting simulation is in very strong agreement with the experimental data.

As it is difficult to measure beam dynamics in situ on the Lyncean light source, a diagnostic tool has been developed that again combines ICCS3D and GA. This diagnostic software reproduces the above process for any spectra measured on the Lyncean light source: the GA begins with the nominal or best guess parameters and then optimizes the simulated spectra by manipulating the electron beam parameters. This new tool allows researchers some means to track the beam dynamics of the operation of the light source.

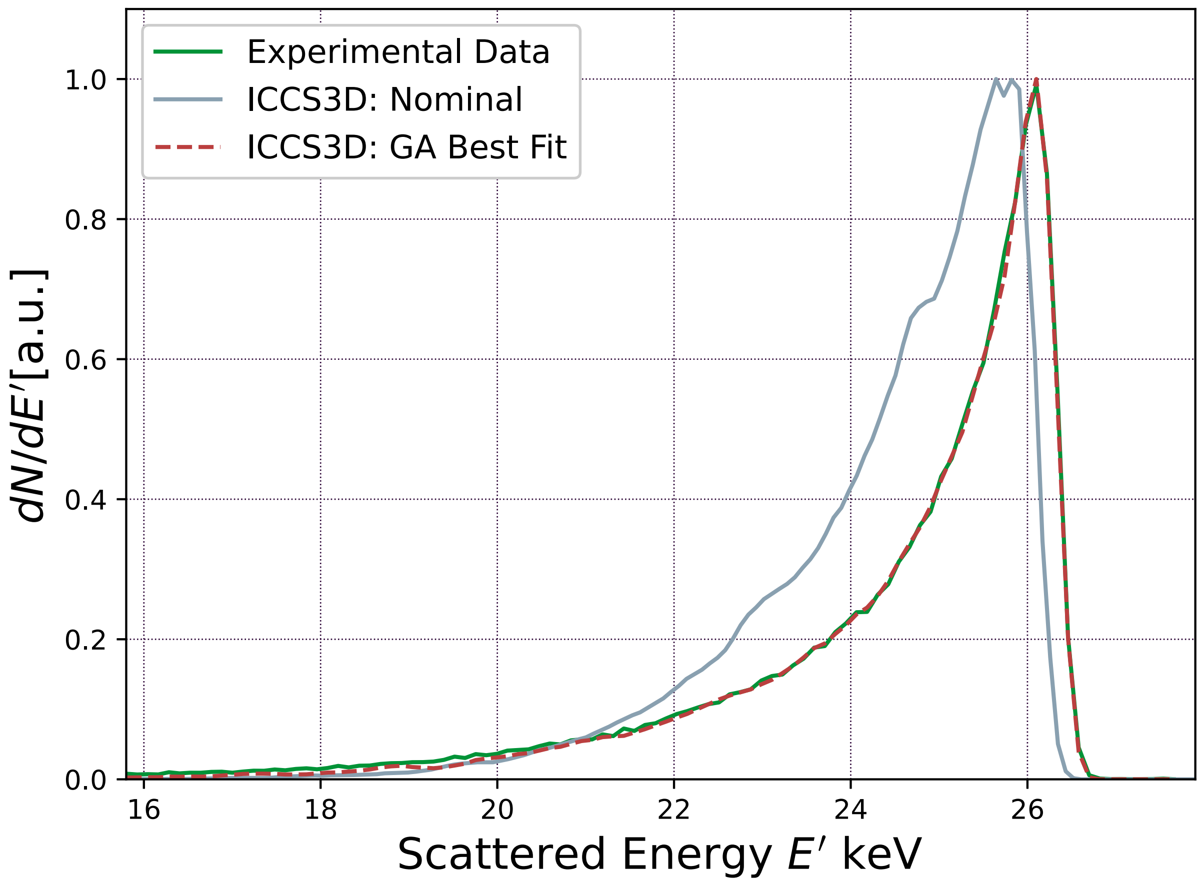

FIG. 69: Three plots are presented here: one spectrum (green) measured experimentally at the Munich Light Source (MuCLS) and two simulations generated by ICCS3D. The first simulation (blue plot) used the nominal parameters for the collision: $E_e = 38.4$ MeV; the electron energy spread is 0.26%; $\sigma_x = \sigma_y = 26$ μm; $\epsilon_x = 60.0$ mm mrad; $\epsilon_y = 60.0$ mm mrad; $\lambda = 1,064$ nm; $a_0 = 4.76 \times 10^{-4}$; $\sigma_{x,l} = \sigma_{y,l} = 90$ μm; the circular, on-axis aperture is 3 m from the collision and has a radius of 0.7 mm [88]. Given the difference in the two plots, a genetic algorithm was used to find the parameters that best fit the experimental data [82]. The second simulation (red dashed) is in very strong agreement with the experimental data. The following horizontal emittance and vertical emittance were optimized to fit the plot: $\epsilon_x = 16.1$ mm mrad; $\epsilon_y = 5.59$ mm mrad.

CHAPTER 7

CONCLUSION: THE NEED FOR ICS X-RAYS

The world needs access to high-brilliance X-rays. From art historians at the Louvre to the medical practitioners at your local hospital, improved accessibility to narrow bandwidth X-ray sources is a tide that raises all ships. Through materials science, medical imaging, and fundamental physics research, nearly every aspect of modern living is influenced by the research conducted with these high-energy photon emissions.

Massive SR facilities generate the highest quality X-ray emissions with respect to brilliance. Synchrotrons, synchrotrons with insertion devices, and FEL facilities certainly outperform ICS sources. These high-end emissions, however, come at a great cost. The accelerator facilities themselves demand a great deal of power, and their construction maintenance, and operation are quite expensive. This great expense limits the number of SR facilities in operation. Acquiring beam time is a competitive ordeal.

Bremsstrahlung X-ray sources may be more convenient and accessible than SR facilities, but the very brightest bremsstrahlung sources in the world have one ten-thousandth the spectral brightness of the most basic synchrotron. These sources trail the most sophisticated synchrotrons in brilliance by about eleven orders of magnitude- that is one hundred billionth the brilliance. What's worse is that these bremsstrahlung sources are not even tunable with respect to the frequency of the emitted radiation. Each bremsstrahlung device operates at very small range of scattered frequencies that is limited by the scattering material in the device. Though affordable and accessible, bremsstrahlung sources cannot be used for most of the research conducted with SR.

ICS sources provide a viable alternative to SR for much of the research being conducted at these facilities. ICS emissions are tunable, like SR. The intensity of the emissions generated via Compton scattering may be significantly less than those of SR facilities, but they are still, however, high enough for the non-destructive imagining analysis techniques commonly used by researchers. Advanced medical imaging and X-ray spectroscopy are already being conducted with Compton sources. Many institutions, such as ODU [2, 3] and TUE [32], have proposed constructing their own compact ICS sources. The mobility of a high-brilliance, compact X-ray source would offer advantages that are simply not possible via SR. Lidar applications or shipping vessel hull analysis are two examples where a mobile light source would be a tremendous advantage. While not necessarily mobile, some compact ICS sources are available commercially, such as the Compact Lyncean Light Source [93]. ICS sources are already creating new research opportunities across many fields of study.

7.1 ICS COMPUTATIONAL MODELS

In this work, a quasiclassical foundation has been built from first principles in order to better understand photon-electron collisions. Two computational models have been derived from this framework to simulated Compton scattering events. Modeling proposed ICS sources is an invaluable part of the development process as it is used to optimize the finished product and to motivate interest.

Compton scattering events can be generally classified by two parameters: electron beam energy and the intensity of the incident laser pulse. Photon-electron collisions with a relatively low laser intensity, i.e., with a relatively low field strength parameter a_0, are described as linear while collisions with higher intensities are non-linear. Photon-electron collisions with relatively low electron beam energy, i.e., with a relatively low Compton parameter X, are called Thomson scattering events while collisions with high X are called Compton scattering events. The first computational model presented in this work, ICCS3D operates in the linear Compton regime, and the second model presented here, SENSE, operates in the nonlinear Thomson regime.

Both models are limited to Compton scattering events in which only one photon is emitted per electron. The regime in which multiple photons are emitted per electron is known as the *radiation reactions* regime. Multiple photon emissions occur when the incident laser pulse has a very high intensity or when the incident laser pulse is sufficiently long. Radiation reaction calculations are beyond the scope of the work presented here.

These computational models compute the scattered spectra by numerically integrating an energy density spectrum $\mathrm{d}^2E'/\mathrm{d}\omega'\mathrm{d}\Omega$, which is a function that defines the total scattered photon energy E' per scattered photon frequency ω' that is scattered into a given solid angle $\mathrm{d}\Omega$. This energy density spectrum is integrated over the solid angle of a sensor aperture numerically since these energy density function cannot be integrated analytically.

The energy density spectrum for ICCS3D is derived from 4-vector conservation of momentum laws, the Klein-Nishina cross section, and a frequency representation of the electric field of the incident laser pulse. The computational model is coded in Python. The simulation is computed via parallel processing using the multiprocessing library. The integration itself is computed numerical using the `dblquad` function from the scipy library.

The energy density spectrum for SENSE is derived first by solving the Hamilton-Jacobi equation in order to find the equations of motion for the electron as it experiences the incident laser pulse. As a charged particle is accelerated it emits radiation, and this emitted radiation is calculated from the equations of motion to compute the energy density spectrum. This computational model is also scripted in Python and is computed through parallel processing. The solution to the Hamilton-Jacobi, however, is highly oscillatory and contains addition integrations. The integrals that arise from the equations of motion are solved numerically through an application of Simpson's Rule, and the integration over the solid angle is computed using Type I Monte Carlo integration.

7.2 CONTRIBUTIONS OF SENSE AND ICCS3D

The computational models ICCS3D and SENSE have made substantial contributions to the study of ICS. First and foremost, they have been used to connect the quasiclassical framework presented in this work to empirically measured experimental data. This agreement with the experimental data shows that the analysis is valid— at least for the range of parameters used within the experiments.

SENSE has been used to observe and quantify the ponderomotive effects upon the scattered spectra that arise from photon-electron collisions with high-intensity incident laser pulse. As these nonlinear effects dramatically undermine the narrowband nature of the emitted radiation, it is critically important to understand these effects in order to build ICS sources with optimal brilliance.

Similarly, ICCS3D has been used to study how higher energy collisions change the scaling laws of the sources of bandwidth in the scattered spectra. The Compton recoil also causes meaningful red shift in the spectra that must be accounted for in collisions involving high-energy electron beams.

The models have also been used to develop ways to theoretically recover bandwidth from these broadening effects. In the nonlinear regime, chirping, or the frequency modulation of the incident laser pulse has been proposed as a way to mitigate the effects of ponderomotive broadening in the emitted spectra. They also indicate show that this technique is especially effective in recovering brilliance in the plane-wave approximation. Simulations show that the brilliance recovered decreases as the ratio of the transverse sizes of the electron beam to the transverse size of the photon pulse increases. The models have also demonstrated that lengthening the photon pulse in time while keeping the over all energy of the pulse constant is another effective way to recover spectral brilliance by avoiding nonlinearities in the photon-electron collision.

Perhaps the most obvious use of the computational models has been to predict the quality of proposed ICS source setups. Several novel high-energy laser sources have been modeled in order to see if they would be useful in generating high-quality emissions via ICS.

7.3 QED COMPTON SCATTERING MODELS

This work focuses on quasiclassical calculations for ICS. QED-based models for Compton scattering have also been developed. The quasiclassical approach has served us well thus far as evident by the contributions to field of study made via SENSE and ICCS3D. For extreme parameters far outside the operational regimes of these models, however, it may be necessary to use QED analysis.

An analysis of ICS in the linear Compton regime has been developed [94]. This analysis describes the behavior of a classical and quantum particle in the presence of electromagnetic radiation. Vélez et al. have used this QED framework to analyze the Compton scattering events in the nonlinear Thomson and Compton scattering driven by single and arbitrarily short laser pulses. As the advancement of laser technology drives up the intensities of Compton scattering fields, it becomes necessary to extend the previously known laser-assisted scattering theories to the case of short and highly non-monochromatic fields. To this end, Boca and Florescu [95] generalized the non-linear Compton scattering, and Boca [96] paved the road for a full generalization of the Mott scattering.

Linear Compton scattering models have also been computed using methods of catastrophe theory. The simplest case can be controlled by the value of the linear chirp of the pulse. The findings of Kharin et al. require no full-scale calculations and have direct consequences for the photon yield enhancement of future nonlinear Compton scattering X-ray or γ-ray sources [97].

7.4 RADIATION REACTION

Expressions using both quassiclassical and QED analysis have been reported to define the spectral broadening induced by multi-photon emissions from the Compton-scattering event, i.e., these expressions capture the spectral impact due to radiation reaction in the electron [98]. When the radiation reaction is not included in the analysis, all the scattered energy falls within a small bandwidth when it should be scattered over a larger bandwidth. This, of course, is the reason that ICCS3D and SENSE should not be used for collisions in the radiation reaction regime. In the radiation reaction regime, a symmetrical envelope function emits a spectrum that is red shifted; the spectrum also contains areas with an uneven distribution interference fringes. The increase of interference fringes is due to the combination of the lower emitted frequencies and a larger travelled distance during the laser pulse interaction.

In order to expand the functional range of SENSE and ICCS3D, our continuing research will incorporate analysis of the radiation reaction into the quasiclasical formalism presented in this dissertation. Work has already begun to move in this direction. Experimental data has been published from a laser-wakefield ICS study designed to observe and analyze the onset of the radiation reaction in Compton-scattering events that utilize incident lasers of very high intensity or exceptional pulse length [99]. The electron and emitted γ-ray spectra were both measured simultaneously. This data was independently used to calculate the laser intensity during the interaction. Cole et al. used a quasiclassical and QED model to fit the data from the experiment. There is currently an on going effort to model these radiation reaction results using SENSE. The initial results are quite promising. Modeling radiation reaction with SENSE and ICCS3D will greatly expand the operational regimes of the codes.

BIBLIOGRAPHY

[1] https://tunl.duke.edu/research/our-research/beam-physics. Accessed: 2019-08-05.

[2] G. Krafft, E. Johnson, K. Deitrick, B. Terzić, R. Kelmar, T. Hodges, W. Melnitchouk, and J. Delayen. Phys. Rev. Accel. Beams, **19**:121302, (2016).

[3] K. Deitrick. Ph.D. thesis, Old Dominion University, 2017.

[4] R. Shankar. *Principles of Quantum Mechanics*, 2nd ed. (Plenum Press, New York, 1994).

[5] I. Falconer. Physics Education, **32**(4):226–231, (1997).

[6] G. Thomson and J. Thomson. in *Proc. R. Soc. A.*, **117**(778):600–609, (1928).

[7] C. Davisson and L. Germer. in *Proc. Natl. Acad. Sci. U.S.A.*, **14**(4):317–322, (1928).

[8] W. Bragg and W. Bragg. *X-rays and Crystal Structure.* (G. Bell and Sons LTD., 1915).

[9] J. Thompson, G. Braun, D. Tierney, L. Wessels, H. Schmitzer, B. Rossa, H. Wagner, and W. Dultz. Am. J. Phys., **86**(2):95–104, (2018).

[10] A. Chodos and J. Ouellette. APS News, **10**(10), Nov. 2001. https://www.aps.org/publications/apsnews/200111/history.cfm. Accessed: 2021-14-05.

[11] A. Assmus. *Early History of X-rays.* (SLAC National Accelerator Laboratory, Menlo Park, 1995).

[12] P. Suortti and W. Thomlinson. Physics in Medicine and Biology, **48**(13):R1–R35, (2003).

[13] S. Bayat et al. Physics in Medicine and Biology, **46**(12):3287–3299, (2001).

[14] T. Taba et al. European Radiology, **30**:2740–2750, (2020).

[15] G. Paternò, P. Cardarelli, M. Gambaccini, L. Serafini, V. Petrillo, I. Drebot, and A. Taibi. Physics in Medicine & Biology, **64**(18):185002, (2019).

[16] A. Sarnelli, C. Nemoz, H. Elleaume, F. Estève, B. Bertrand, and A. Bravin. Physics in Medicine and Biology, **50**(4):725–740, (2005).

[17] J. Dik, K. Janssens, G. Snickt, L. Loeff, K. Rickers, and M. Cotte. Anal. Chem., **80**(16):6436–6442, (2008).

[18] M. Shackley. *X-Ray Fluorescence Spectrometry (XRF) in Geoarchaeology*, 1st ed. (Springer, New York, NY, 2011).

[19] B. Beckhoff, B. Kanngießer, and N. Langhoff. *Handbook of Practical X-Ray Fluorescence Analysis*, 1st ed. (Springer, Germany, 2006).

[20] R. Schlotz and S. Uhlig. *Introduction to X-Ray Fluorescence (XRF)*, 1st ed. (Bruker AXS GmbH, Madison, 2006).

[21] G. Snickt et al. Anal. Chem., **84**(23):10221–10228, (2012).

[22] L. Loeff et al. Van Gogh Studies, (2012).

[23] M. Young. Rep. Prog. Phys., **75**(3):036504, (2012).

[24] J. Fink, E. Schierle, E. Weschke, and J. Geck. Rep. Prog. Phys., **76**(5):056502, (2013).

[25] G. Fonda and G. Collins. J. Am. Chem. Soc., **53**(1):113–125, (1931).

[26] G. Burns. *Space Groups for Solid State Scientists*, 2nd ed. (Academic Press, Boston, 1990).

[27] D. Raabey. http://www.dierk-raabe.com/dramatic-material-failure/oil-drilling-platforms/. Accessed: 2021-13-05.

[28] M. Eberhart. *Why Things Break: Understanding the World by the Way It Comes Apart*, 2nd ed. (New York : Harmony Books, 2003).

[29] M. Schuler. https://gcaptain.com/mol-comfort-incident-photos/. Accessed: 2021-12-05.

[30] J. Schijve. International Journal of Fatigue, **25**(8):679–702, (2003).

[31] https://www.element.com/nucleus/2016/5-disasters-caused-by-material-fatigue-and-what-we-learned-from-them. Accessed: 2021-13-05.

[32] J Luiten. *Smart*Light: a Dutch Table-Top Synchrotron Light Source.* (T.U. Eindhoven, Eindhoven, Netherlands, 2020).

[33] S. McDonald et al. Materials Characterization, **172**:110814, (2021).

[34] S. Teoh. International Journal of Fatigue, **22**(10):825–837, (2000).

[35] W. Ludwig et al. JOM, **62**(12):22–28, (2010).

[36] M. Herbig et al. Acta Materialia, **59**(2):590–601, (2011).

[37] A. King, W. Ludwig, M. Herbig, J. Buffière, A. Khan, N. Stevens, and T. Marrow. Acta Materialia, **59**(17):6761–6771, (2011).

[38] K. Wille. *The Physics of Particle Accelerators: An Introduction*, 1st ed. (Oxford University Press, Oxford, 2005).

[39] M. Otendal, T. Tuohimaa, U. Vogt, and H. M. Hertz. Rev. Sci. Instrum., **79**(1):016102, (2008).

[40] T. Skarzynski. Acta Crystallogr. Sec. D, **69**(7):1283–1288, (2013).

[41] H. Wiedemann. *Particle Accelerator Physics*, 4th ed. (Springer, U.S.A., 2015).

[42] N. Connor. https://www.radiation-dosimetry.org/de/was-ist-die-interaktion-von-betastrahlung-mit-materiedefinition/. Accessed: 2021-21-05.

[43] The Editors of Encyclopedia Britannica. *Bremsstrahlung*, *Encyclopedia Britannica*, (2018).

[44] J. Clarke. *The Science and Technology of Undulators and Wigglers.* (Oxford University Press, Oxford, 2004).

[45] J. Schwinger. in *Proc. Nat. Acad. Sci. U.S.A.*, **40**(2):132–136, (1954).

[46] H. Motz. J. Appl. Phy., **22**(9):1217–1217, (1951).

[47] S. Benson. Optics & Photonics News, **14**, (2003).

[48] M. Couprie and J. Filhol. Comptes Rendus Physique, **9**(5):487 – 506, (2008).

[49] C. Brau. *Free-Electron Lasers*, 1st ed. (Academic Press, San Diego, 1990).

[50] E. Johnson. in *Proceedings of IPAC 2018* (JACoW, Geneva, 2018), page 4351–4353.

[51] C. Pellegrini. The European Physical Journal H, **37**(5):659–708, (2012).

[52] A. Doerr. Nat. Methods, **15**(11):855, (2018).

[53] G. Krafft and G. Priebe. Reviews of Accelerator Science and Technology, **03**(01):147–163, (2010).

[54] J. Thomson. *Conduction of Electricity Through Gases*, 1st ed. (Cambridge University Press, Cambridge, 1903).

[55] Nobel Media. https://www.nobelprize.org/prizes/physics/1906/thomson/biographical/. Accessed: 2021-07-05.

[56] E. Johnson. Undergraduate thesis, Old Dominion University, 2015.

[57] N. Ranjan, B. Terzić, G. Krafft, V. Petrillo, I. Drebot, and L. Serafini. Phys. Rev. Accel. Beams, **21**:030701, (2018).

[58] J. Jackson. *Classical Electrodynamics* 3rd ed. (John Wiley & Sons, Inc., U.S.A.,1999).

[59] A. Compton. Phys. Rev., **21**:483–502, (1923).

[60] G. Krafft. Phys. Rev. Lett., **92**:204802, (2004).

[61] B. Terzić. *Non-Linear, Compton Project Summary.* (ODU, United States of America, 2019).

[62] C. Curatolo, I. Drebot, V. Petrillo, and L. Serafini. Phys. Rev. Accel. Beams, **20**:080701, (2017).

[63] The python programming language. https://www.python.org. Accessed: 2021-28-05.

[64] S. Behnel, R. Bradshaw, L. Dalcín, M. Florisson, V. Makarov, and D. Seljebotn. Cython: C-extensions for python. https://www.cython.org. Accessed: 2021-28-05.

[65] J. Hannah and J. Rowland. *Fourier Series, Transforms, and Boundary Value Problems*, 2nd ed. (Dover Publications Inc., Mineola, 2008).

[66] K. Krajewska, F. Vélez, and J. Kamiński. Phys. Rev. A, **91**:062106, (2015).

[67] Y. Yazaki. in Proc. Jpn. Acad. Ser. B Phys. Biol. Sci., **93**(6):399–421, (2017).

[68] O. Klein and Y. Nishina. Z. Physik, **52**:853, (1929).

[69] R. Feynman. *The Theory of Fundamental Processes*. (CRC Press, New York, 1961).

[70] G. Stedman and D. Pooke. Phys. Rev. D, **26**:2172–2174, (1982).

[71] D. Seipt, S. Rykovanov, A. Surzhykov, and S. Fritzsche. Phys. Rev. A, **91**:033402, (2015).

[72] B. Terzić, A. Brown, I. Drebot, T. Hagerman, E. Johnson, G. Krafft, C. Maroli, V. Petrillo, and M. Ruijter. EPL (Europhysics Letters), **126**(1):12003, (2019).

[73] R. Hajima. Nucl. Instrum. Methods A, **985**:164655, (2021).

[74] D. Griffiths. *Introduction to Quantum Mechanics*, 2nd ed. (Pearson Education Inc., Upper saddle River, 2005).

[75] W. Pauli. *Review of Relativity*. (Dover Publications, Mineola, New York, 1921).

[76] T. Sauer. *Numerical Analysis*, 2nd ed. (Pearson, Boston, MA, 2012).

[77] A. Fetter and J. Walecka. *Theoretical Mechanics of Particles and Continua*. (Dover Publications, Inc., Mineola, New York, 2003).

[78] H. Goldstein, C. Poole, and J. Safko. *Classical Mechanics*, 3rd ed. (Addison Wesley, Boston, 2001).

[79] L. Landau and E. Lifshitz. *Mechanics: Volume 1 Course of Theoretical Physics*, 3rd ed. (Butterworth-Heinemann, Oxford, 1976).

[80] I. Ghebregziabher, B. Shadwick, and D. Umstadter. Phys. Rev. ST Accel. Beams, **16**:030705, (2013).

[81] B. Terzić, K. Deitrick, A. Hofler, and G. Krafft. Phys. Rev. Lett., **112**:074801, (2014).

[82] A. Hofler et al. Phys. Rev. ST Accel. Beams, **16**:010101, (2013).

[83] B. Terzić, C. Reeves, and G. Krafft. Phys. Rev. Accel. Beams, **19**:044403, (2016).

[84] J. Krämer et al. Scientific Reports, **8**(1):1398, (2018).

[85] C. Maroli, V. Petrillo, I. Drebot, L. Serafini, B. Terzić, and G. Krafft. J. Appl. Phys., **124**(6):063105, (2018).

[86] E Breen. (Jefferson Lab, Summer R.E.U. Program, 2020).

[87] I. Walmsley and C. Dorrer. Advances in Optics and Photonics, **308**(1), (2009).

[88] J. Huang, B. Günther, K. Achterhold, Y. Cui, B. Gleich, M. Dierolf, and F. Pfeiffer. Scientific Reports, **10**(1):8772, (2020).

[89] P. Chen, G. Horton-Smith, T. Ohgaki, A Weidemann, and K. Yokoya. Nucl. Instrum. Methods A, **355**(1):107–110, (1995).

[90] Linda Stoel. (private communication, 2020).

[91] B. Terzić, G. Krafft, V. Petrillo, I. Drebot, and M. Ruijter. Europhysics Letters, **129**(6):62001, (2020).

[92] B. Günther et al. Journal of Synchrotron Radiation, **27**(5):1395–1414, (2020).

[93] Lyncean Technologies Inc. https://lynceantech.com/products/. Accessed: 2021-12-06.

[94] F. Vélez, J. Kamiński, and K. Krajewska. Atoms, **7**(1):34, (2019).

[95] M. Boca and V. Florescu. Phys. Rev. A, **80**:053403, (2009).

[96] M. Boca. Open Physics, **11**(9):1123–1134, (2013).

[97] V. Kharin, D. Seipt, and S. Rykovanov. Phys. Rev. Lett., **120**:044802, (2018).

[98] M. Ruijter, V. Kharin, and S. Rykovanov. J. Phys. B, **51**(22):225701, (2018).

[99] J. Cole et al. Phys. Rev. X, **8**:011020, (2018).

[100] G. Krafft & I. Bazarov. 4^{th} Generation Light Sources, E.R.L.s and Thomson Scattering, 2003. https://casa.jlab.org/publications/lecture_2003.shtml

[101] G. Arfken, H. Weber, and F. Harris. *Mathematical Methods for Physicists*, 7th ed. (Academic Press, Boston, 2013).

APPENDIX A

FOURIER TRANSFORM OF A 3D GUASSIAN LASER PULSE ENVELOPE

General form for vector potential that an electron experiences as it travels through a laser pulse is

$$A(\xi) = a(\xi)\cos\left(\frac{2\pi\xi}{\lambda}\right),$$

where ξ is a parameterized spatial variable that describes where the electron is within the laser pulse, $a(\xi)$ describes the localized magnitude of the field strength, and λ is the wavelength of the incident laser pulse. A Fourier transform is required to convert the vector potential into frequency space.

$$g(k) = \int_{-\infty}^{+\infty} A(\xi)e^{-ik\xi}d\xi. \tag{224}$$

The parameterized field strength for 3D Gaussian is defined in Eq. (115)

$$a(\xi) = \bar{a}_0 \exp\left\{-\frac{(\xi+\eta)^2}{2\tilde{\sigma}_{z,l}^2}\right\},$$

which leads to the Fourier transform:

$$g(k) = \int_{-\infty}^{+\infty} \bar{a}_0 \exp\left\{-\frac{(\xi+\eta)^2}{2\tilde{\sigma}_{z,l}^2} - ik\xi\right\}\cos\left(\frac{2\pi\xi}{\lambda}\right)d\xi. \tag{225}$$

Distribute $(\xi+\eta)^2$ and substitute $k = \omega/c$:

$$g(\omega) = \bar{a}_0 \int_{-\infty}^{+\infty} \left[\exp\left\{\xi^2\left(\frac{-1}{2\tilde{\sigma}_{z,l}^2}\right) + \xi\left(\frac{-\eta}{\tilde{\sigma}_{z,l}^2} - \frac{i\omega}{c}\right) - \frac{\eta^2}{2\tilde{\sigma}_{z,l}^2}\right\}\cos\left(\frac{2\pi\xi}{\lambda}\right)\right]d\xi. \tag{226}$$

For clarity of notation, the following substitutions will be used:

$$\cos\left(\frac{2\pi\xi}{\lambda}\right) = \frac{e^{i2\pi\xi/\lambda} + e^{-i2\pi\xi/\lambda}}{2}, \tag{227}$$

$$a = \frac{1}{\tilde{\sigma}_{z,l}^2},\ b_0 = \frac{\eta}{\tilde{\sigma}_{z,l}^2} + i\left(\frac{\omega}{c} - \frac{2\pi}{\lambda}\right),\ b_1 = \frac{\eta}{\tilde{\sigma}_{z,l}^2} + i\left(\frac{\omega}{c} + \frac{2\pi}{\lambda}\right),\ c = \frac{\eta^2}{2\tilde{\sigma}_{z,l}^2}, \tag{228}$$

$$g(\omega) = \frac{\bar{a}_0}{2}\int_{-\infty}^{+\infty} d\xi\left\{e^{-\left(a\xi^2+b_0\xi+c\right)} + e^{-\left(a\xi^2+b_1\xi+c\right)}\right\}. \tag{229}$$

The Gaussian integral has the solution

$$g(\omega) = \frac{\bar{a}_0}{2}\left\{\sqrt{\frac{\pi}{a}}e^{\left(b_0^2/4a\right)-c} + \sqrt{\frac{\pi}{a}}e^{\left(b_1^2/4a\right)-c}\right\}. \tag{230}$$

Define

$$c_0 = \bar{a}_0\sqrt{\frac{\pi\tilde{\sigma}_{z,l}^2}{2}}e^{-\eta^2/2\tilde{\sigma}_{z,l}^2}. \tag{231}$$

Substitute c_0 into the equation, and remove the previously used substitutions (a, b_0, b_1, c):

$$\begin{aligned} g(\omega) =& c_0\left[\exp\left\{\frac{\tilde{\sigma}_{z,l}^2}{2}\left(\frac{\eta^2}{\tilde{\sigma}_{z,l}^4} - \left(\frac{\omega}{c} - \frac{2\pi}{\lambda}\right)^2 + i\frac{2\eta}{\tilde{\sigma}_{z,l}^2}\left(\frac{\omega}{c} - \frac{2\pi}{\lambda}\right)\right)\right\}\right. \\ &\left. + \exp\left\{\frac{\tilde{\sigma}_{z,l}^2}{2}\left(\frac{\eta^2}{\tilde{\sigma}_{z,l}^4} - \left(\frac{\omega}{c} + \frac{2\pi}{\lambda}\right)^2 + i\frac{2\eta}{\tilde{\sigma}_{z,l}^2}\left(\frac{\omega}{c} + \frac{2\pi}{\lambda}\right)\right)\right\}\right]. \end{aligned} \tag{232}$$

Define

$$c_1 = c_0 e^{\frac{\eta^2}{2\tilde{\sigma}_{z,l}^2}} = \bar{a}_0\sqrt{\frac{\pi\tilde{\sigma}_{z,l}^2}{2}}. \tag{233}$$

Substitute c_1 into the equation:

$$\begin{aligned} g(\omega) =& c_1\left[\exp\left\{-\frac{\tilde{\sigma}_{z,l}^2}{2}\left(\frac{\omega^2}{c^2} + \frac{4\pi\omega}{c\lambda} + \frac{4\pi^2}{\lambda^2} + i\frac{2\eta\omega}{\tilde{\sigma}_{z,l}^2 c} + i\frac{4\pi\eta}{\tilde{\sigma}_{z,l}^2\lambda}\right)\right\}\right. \\ &\left. + \exp\left\{-\frac{\tilde{\sigma}_{z,l}^2}{2}\left(\frac{\omega^2}{c^2} - \frac{4\pi\omega}{c\lambda} + \frac{4\pi^2}{\lambda^2} + i\frac{2\eta\omega}{\tilde{\sigma}_{z,l}^2 c} - i\frac{4\pi\eta}{\tilde{\sigma}_{z,l}^2\lambda}\right)\right\}\right]. \end{aligned} \tag{234}$$

Redistribute the arguments of the exponent into second order polynomials with respect to ω:

$$\begin{aligned} g(\omega) =& c_1\left[\exp\left\{-\frac{\tilde{\sigma}_{z,l}^2}{2c^2}\left(\omega^2 + \omega\left(\frac{4\pi c}{\lambda} + i\frac{2\eta c}{\tilde{\sigma}_{z,l}^2}\right) + \left(\frac{4\pi^2 c^2}{\lambda^2} + i\frac{4\pi\eta c^2}{\tilde{\sigma}_{z,l}^2\lambda}\right)\right)\right\}\right. \\ &\left. + \exp\left\{-\frac{\tilde{\sigma}_{z,l}^2}{2c^2}\left(\omega^2 + \omega\left(-\frac{4\pi c}{\lambda} + i\frac{2\eta c}{\tilde{\sigma}_{z,l}^2}\right) + \left(\frac{4\pi^2 c^2}{\lambda^2} - i\frac{4\pi\eta c^2}{\tilde{\sigma}_{z,l}^2\lambda}\right)\right)\right\}\right]. \end{aligned} \tag{235}$$

For clarity of notation, the following substitutions will be used:

$$\tilde{\sigma}_\omega^{-2} = \frac{\tilde{\sigma}_{z,l}^2}{2c^2}, \tag{236}$$

$$B_0 = \frac{4\pi c}{\lambda} + i\frac{2\eta c}{\tilde{\sigma}_{z,l}^2},\; B_1 = -\frac{4\pi c}{\lambda} + i\frac{2\eta c}{\tilde{\sigma}_{z,l}^2}, \tag{237}$$

$$D_0 = \frac{4\pi^2 c^2}{\lambda^2} + i\frac{4\pi\eta c^2}{\tilde{\sigma}_{z,l}^2\lambda}, D_1 = \frac{4\pi^2 c^2}{\lambda^2} - i\frac{4\pi\eta c^2}{\tilde{\sigma}_{z,l}^2\lambda}. \tag{238}$$

In addition to the substitutions, the modulus squared will be taken on both sides of the equation to eliminate the imaginary portions of the expression:

$$\begin{aligned}|g(\omega)|^2 =& c_1^2 \left[\left(\exp\left\{-\tilde{\sigma}_\omega^{-2}\left(\omega^2+\omega B_0+D_0\right)\right\}+\exp\left\{-\tilde{\sigma}_\omega^{-2}\left(\omega^2+\omega B_1+D_1\right)\right\}\right)\right. \\ &\left.\times\left(\exp\left\{-\tilde{\sigma}_\omega^{-2}\left(\omega^2+\omega B_0^*+D_0^*\right)\right\}+\exp\left\{-\tilde{\sigma}_\omega^{-2}\left(\omega^2+\omega B_1^*+D_1^*\right)\right\}\right)\right].\end{aligned} \tag{239}$$

Multiply the two exponential sums:

$$\begin{aligned}|g(\omega)|^2 =& c_1^2 \left[e^{\left\{-\tilde{\sigma}_\omega^{-2}\left(2\omega^2+\omega\left(B_0+B_0^*\right)+\left(D_0+D_0^*\right)\right)\right\}}+e^{\left\{-\tilde{\sigma}_\omega^{-2}\left(2\omega^2+\omega\left(B_0+B_1^*\right)+\left(D_0+D_1^*\right)\right)\right\}}\right. \\ &\left.+e^{\left\{-\tilde{\sigma}_\omega^{-2}\left(2\omega^2+\omega\left(B_1+B_0^*\right)+\left(D_1+D_0^*\right)\right)\right\}}+e^{\left\{\tilde{-\sigma}_\omega^{-2}\left(2\omega^2+\omega\left(B_1+B_1^*\right)+\left(D_1+D_1^*\right)\right)\right\}}\right].\end{aligned} \tag{240}$$

For clarity of notation, the following substitutions will be used:

$$\omega_0 = \frac{1}{4}\left(B_0+B_0^*\right),\ \omega_1 = -\frac{1}{4}\left(B_0+B_0^*\right), \tag{241}$$

$$\delta_0 = \frac{D_0+D_0^*}{2} - \frac{\left(B_0+B_0^*\right)^2}{16},\ \delta_0 = \frac{D_1+D_1^*}{2} - \frac{\left(B_1+B_1^*\right)^2}{16}. \tag{242}$$

The complex addition may be completed to simplify the expressions:

$$B_0 + B_1^* = B_1 + B_0^* = 0, \tag{243}$$

$$G = \frac{D_0+D_1^*}{2} = \frac{4\pi^2c^2}{\lambda^2} + i\frac{4\pi\eta c^2}{\tilde{\sigma}_{z,l}^2\lambda} = \phi + i\theta, \tag{244}$$

$$G^* = \frac{D_1+D_0^*}{2} = \frac{4\pi^2c^2}{\lambda^2} - i\frac{4\pi\eta c^2}{\tilde{\sigma}_{z,l}^2\lambda} = \phi - i\theta. \tag{245}$$

The modulus squared of the Fourier transform becomes:

$$\begin{aligned}|g(\omega)|^2 =& c_1^2 \left[e^{\left\{-2\tilde{\sigma}_\omega^{-2}\left((\omega+\omega_0)^2+\delta_0\right)\right\}}+e^{\left\{-2\tilde{\sigma}_\omega^{-2}\left((\omega+\omega_1)^2+\delta_1\right)\right\}}\right. \\ &\left.+e^{\left\{-2\tilde{\sigma}_\omega^{-2}\left(\omega^2+G\right)\right\}}+e^{\left\{-2\tilde{\sigma}_\omega^{-2}\left(\omega^2+G^*\right)\right\}}\right].\end{aligned} \tag{246}$$

By expressing G in terms of θ and ϕ the expression may be simplified:

$$\begin{aligned}|g(\omega)|^2 =& c_1^2 \left[e^{\left\{-2\tilde{\sigma}_\omega^{-2}\left((\omega+\omega_0)^2+\delta_0\right)\right\}}+e^{-\left\{2\tilde{\sigma}_\omega^{-2}\left((\omega+\omega_1)^2+\delta_1\right)\right\}}\right. \\ &\left.+e^{-2\omega^2/\tilde{\sigma}_\omega^2}\left(e^{-\tilde{\sigma}_\omega^{-2}(\phi+i\theta)}+e^{-\tilde{\sigma}_\omega^{-2}(\phi-i\theta)}\right)\right].\end{aligned} \tag{247}$$

The ω and δ functions may also be simplified:

$$\omega_0 = \frac{2\pi c}{\lambda},\ \omega_1 = -\frac{2\pi c}{\lambda} = -\omega_0, \tag{248}$$

$$\delta_0 = \frac{4\pi^2 c^2}{\lambda^2} - \frac{4\pi^2 c^2}{\lambda^2} = 0,\ \delta_1 = \frac{4\pi^2 c^2}{\lambda^2} - \frac{4\pi^2 c^2}{\lambda^2} = 0, \tag{249}$$

$$|g(\omega)|^2 = c_1^2 \left[e^{\left\{-2\tilde{\sigma}_\omega^{-2}(\omega+\omega_0)^2\right\}} + e^{-\left\{2\tilde{\sigma}_\omega^{-2}(\omega-\omega_0)^2\right\}} + e^{-\tilde{\sigma}_\omega^{-2}(2\omega^2+\phi)} \left(2\cos\theta\right) \right]. \tag{250}$$

Since $\phi >> \omega_0 >> 1$:

$$|g(\omega)|^2 = c_1^2 e^{-\left\{2\tilde{\sigma}_\omega^{-2}(\omega-\omega_0)^2\right\}}. \tag{251}$$

Since $\tilde{E}(\omega) = \frac{mc}{e}\omega g(\omega)$, the modulus squared of the Fourier transform of the 3D Gaussian distribution vector potential is

$$\left|\tilde{E}(\omega)\right|^2 = \omega^2 a_\omega^2 \exp\left\{ \frac{-\left(\omega-\omega_0\right)^2}{2\sigma_\omega^2} \right\}, \tag{252}$$

where

$$a_\omega^2 = \frac{\pi m^2 c^2 \bar{a}_0^2 \tilde{\sigma}_{z,l}^2}{2e^2}, \tag{253}$$

$$\omega_0 = \frac{2\pi c}{\lambda}, \tag{254}$$

and

$$\sigma_\omega^2 = \frac{c^2}{2\tilde{\sigma}_{z,l}^2}. \tag{255}$$

APPENDIX B

HAMILTON-JACOBI SOLUTION: ELECTRON WITH 3D MOMENTUM

The solution presented here is for a linearly polarized incident laser pulse [100]. The photons are modeled as an infinite plane-wave propagating in the negative $\hat{z}$ direction:

$$\boldsymbol{A} = A_x(z + ct)\hat{x} \equiv A_x(\xi)\hat{x}, \tag{256}$$

where $\xi = z + ct$. Hamilton's principle function that solves Eq. (151) for this vector potential is

$$S = -k_0 ct + \boldsymbol{k} \cdot \boldsymbol{r} + F(\xi), \tag{257}$$

where k is the four-vector of the electron momentum in the new frame, i.e., the initial . The function F is defined by its first derivative with respect to ξ

$$\frac{\mathrm{d}F}{\mathrm{d}\xi} = \frac{1}{-k_0 - k_z}\left[\frac{m^2c^2 - k_0^2 - |\boldsymbol{k}|^2}{2} + \frac{e}{c}k_x A_x + \frac{e^2}{2c^2}A_x^2\right]. \tag{258}$$

As per the Hamilton-Jacobi equation, the energy of the electron as a function of ξ may be found by taking the the first derivative of S with respect to time

$$-E = \frac{\partial S}{\partial t} = -k_0 c + \frac{-c}{k_0 + k_z}\left[\frac{m^2c^2 - k_0^2 + |\boldsymbol{k}|^2}{2} + \frac{e}{c}k_x A_x + \frac{e^2}{2c^2}A_x^2\right] = -\gamma mc^2. \tag{259}$$

The Lorentz factor γ of the electron may be found by dividing both sides of Eq. (259) by $-mc^2$

$$\gamma = \frac{k_0}{mc} + \frac{1}{mc(k_0 + k_z)}\left[\frac{m^2c^2 - k_0^2 + |\boldsymbol{k}|^2}{2} + \frac{e}{c}k_x A_x + \frac{e^2}{2c^2}A_x^2\right]. \tag{260}$$

The velocity vector of the electron in terms of k and ξ may be solved using Hamilton's principle function S. The $\hat{x}$ component of the electron momentum p_x may be found via Eq. (145) by taking the first derivative of the function S with respect to x

$$\frac{\partial S}{\partial x} = p_x = k_x. \tag{261}$$

This must also be equal to the canonical electron momentum in momentum from Eq. (148)

$$k_x = \gamma m v_x - \frac{eA_x}{c}. \tag{262}$$

The $\hat{x}$ component of the electron velocity normalized by the speed of light v_x/c may be solved from the previous equation

$$\frac{v_x}{c} = \frac{k_x}{\gamma mc} + \frac{eA_x}{\gamma mc^2}. \tag{263}$$

The $\hat{y}$ component of the electron momentum p_y may be found via Eq. (145) by taking the first derivative of Hamilton's principle function S with respect to y

$$\frac{\partial S}{\partial y} = p_y = k_y. \tag{264}$$

This must also be equal to the canonical electron momentum in momentum from Eq. (148)

$$k_y = \gamma m v_y. \tag{265}$$

The $\hat{y}$ component of the electron velocity normalized by the speed of light v_y/c may be solved from the previous equation

$$\frac{v_y}{c} = \frac{k_x}{\gamma mc}. \tag{266}$$

Due to the polarization geometry, there is no oscillatory motion in $\hat{y}$. Unlike the electron motion in $\hat{x}$ as shown in Eq. (263), the motion of the electron in $\hat{y}$ does not contribute to the emitted dipole radiation.

The $\hat{z}$ component of the electron momentum p_z may be found via Eq. (145) by taking the first derivative of Hamilton's principle function S with respect to z

$$\frac{\partial S}{\partial z} = p_z = k_z + \frac{1}{-k_0 - k_z}\left[\frac{m^2c^2 - k_0^2 + |\boldsymbol{k}|^2}{2} + \frac{e}{c}k_x A_x + \frac{e^2}{2c^2}A_x^2\right]. \tag{267}$$

This must also be equal to the canonical electron momentum in momentum from Eq. (148)

$$k_z + \frac{1}{-k_0 - k_z}\left[\frac{m^2c^2 - k_0^2 + |\boldsymbol{k}|^2}{2} + \frac{e}{c}k_x A_x + \frac{e^2}{2c^2}A_x^2\right] = \gamma m v_z. \tag{268}$$

The $\hat{z}$ component of the electron velocity normalized by the speed of light v_z/c may be solved from the previous equation

$$\frac{v_z}{c} = \frac{k_z}{\gamma mc} + \frac{1}{\gamma mc(-k_0 - k_z)}\left[\frac{m^2c^2 - k_0^2 + |\boldsymbol{k}|^2}{2} + \frac{e}{c}k_x A_x + \frac{e^2}{2c^2}A_x^2\right]. \tag{269}$$

Time and the position of the electron in terms of k and ξ may be found by via Eq. (146). By taking the first derivative of Hamilton's principle function S with respect to k_0

$$\frac{\partial S}{\partial k_0} = \beta_0 = -ct + \frac{1}{(k_0 + k_z)^2}\int_{-\infty}^{\xi}\left[\frac{m^2c^2 - k_0^2 + |\boldsymbol{k}|^2}{2} + \frac{e}{c}k_x A_x + \frac{e^2}{2c^2}A_x^2\right]d\xi' + \frac{k_0 \xi}{k_0 + k_z}, \tag{270}$$

where β_0 is the initial time, i.e., $\beta_0 = 0$. Eq. (270) may be solved for time t

$$t = \frac{1}{c\,(k_0+k_z)^2}\int_{-\infty}^{\xi}\left[\frac{m^2c^2-k_0^2+|\boldsymbol{k}|^2}{2}+\frac{e}{c}k_xA_x+\frac{e^2}{2c^2}A_x^2\right]d\xi'+\frac{k_0\xi}{c(k_0+k_z)}. \tag{271}$$

Taking the first derivative of time t with respect to ξ gives

$$dt = \left(\frac{1}{c\,(k_0+k_z)^2}\left[\frac{m^2c^2-k_0^2+|\boldsymbol{k}|^2}{2}+\frac{e}{c}k_xA_x+\frac{e^2}{2c^2}A_x^2\right]+\frac{k_0}{c(k_0+k_z)}\right)d\xi. \tag{272}$$

The electrons position in $\hat{x}$ may be calculated by taking the first derivative of Hamilton's principle function S with respect to k_1

$$\frac{\partial S}{\partial k_1} = \beta_1 = x - \frac{1}{k_0+k_z}\int_{-\infty}^{\xi}\frac{eA_x}{c}d\xi' - \frac{k_x\xi}{k_0+k_z}, \tag{273}$$

where β_1 is the initial position of the electron in $\hat{x}$. Eq. (273) may be solved to express the electrons position in $\hat{x}$ in terms of k and ξ

$$x = x_0 + \frac{1}{k_0+k_z}\int_{-\infty}^{\xi}\frac{eA_x}{c}d\xi' + \frac{k_x\xi}{k_0+k_z}. \tag{274}$$

Taking the first derivative of x with respect to ξ gives

$$\frac{dx}{d\xi} = \frac{1}{k_0+k_z}\left(\frac{eA_x}{c}+k_x\right). \tag{275}$$

The electrons position in $\hat{y}$ may be calculated by taking the first derivative of Hamilton's principle function S with respect to k_2

$$\frac{\partial S}{\partial k_2} = \beta_2 = y - \frac{k_y\xi}{k_0+k_z}, \tag{276}$$

where β_2 is the initial position of the electron in $\hat{y}$. Eq. (276) may be solved to express the position of the electron in $\hat{y}$ in terms of k and ξ

$$y = y_0 + \frac{k_y\xi}{k_0+k_z}. \tag{277}$$

Taking the first derivative of y with respect to ξ gives

$$\frac{dy}{d\xi} = \frac{k_y}{k_0+k_z}. \tag{278}$$

The electrons position in $\hat{z}$ may be calculated by taking the first derivative of Hamilton's principle function S with respect to k_3

$$\frac{\partial S}{\partial k_3} = \beta_3 = z + \frac{1}{(k_0+k_z)^2}\int_{-\infty}^{\xi}\left[\frac{m^2c^2-k_0^2+|\boldsymbol{k}|^2}{2}+\frac{e}{c}k_xA_x+\frac{e^2}{2c^2}A_x^2\right]d\xi' - \frac{k_z\xi}{k_0+k_z}, \tag{279}$$

where β_3 is the initial position of the electron in $\hat{z}$. Eq. (279) may be solved to express the position of the electron in $\hat{z}$ in terms of k and ξ

$$z = z_0 - \frac{1}{(k_0+k_z)^2}\int_{-\infty}^{\xi}\left[\frac{m^2c^2-k_0^2+|\boldsymbol{k}|^2}{2}+\frac{e}{c}k_xA_x+\frac{e^2}{2c^2}A_x^2\right]d\xi' + \frac{k_z\xi}{k_0+k_z}. \tag{280}$$

Taking the first derivative of z with respect to ξ gives

$$\frac{dz}{d\xi} = -\frac{1}{(k_0+k_z)^2}\left[\frac{m^2c^2-k_0^2+|\boldsymbol{k}|^2}{2}+\frac{e}{c}k_xA_x+\frac{e^2}{2c^2}A_x^2\right]+\frac{k_z}{k_0+k_z}. \tag{281}$$

Now that the equations of motion have been solved for the electron passing through the field of an incident laser pulse, the Thomson scattered radiation of the electron may be calculated by applying fundamental principles of electrodynamics. Two important functions, the charge density of the electron ρ and the electric current density $\boldsymbol{J}$, will be built from the equations of motion. Since this calculation is for a single electron, the Dirac delta function will be used

$$\rho'\left(x',y',z',t'\right) = -e\delta(x'-x'(\xi(t)))\delta(y'-y'(\xi))\delta(z'-z'(\xi(t))). \tag{282}$$

The electric density current will also use the Dirac Delta function. The change in position will calculated using the derivatives of the coordinates with respect to ξ and the derivative of time with respect to ξ

$$\begin{aligned}\boldsymbol{J} =& \frac{dx'}{d\xi'}\frac{d\xi'}{dt'}\left(-e\delta(x'-x'(\xi(t)))\delta(y'-y'(\xi))\delta(z'-z'(\xi(t)))\right)\hat{x}\\ &+\frac{dy'}{d\xi'}\frac{d\xi'}{dt'}\left(-e\delta(x'-x'(\xi(t)))\delta(y'-y'(\xi))\delta(z'-z'(\xi(t)))\right)\hat{y}\\ &+\frac{dz'}{d\xi'}\frac{d\xi'}{dt'}\left(-e\delta(x'-x'(\xi(t)))\delta(y'-y'(\xi))\delta(z'-z'(\xi(t)))\right)\hat{z}.\end{aligned} \tag{283}$$

The radiation potentials may be calculated from the charge density and the electric current density. The electric potential from the electron is calculated through a Fourier transform into frequency space and a change of variables

$$\begin{aligned}\Phi\left(\boldsymbol{r}',t'\right) &= \int\frac{1}{R'}\rho'\left(\boldsymbol{r}'',t'-\frac{R'}{c}\right)dx''\,dy''\,dz''\\ ... &= -\frac{e}{2\pi c}\int\frac{e^{i\omega'\left(t''-\left(t'-\frac{R'}{c}\right)\right)}}{R'}dt''\,d\omega'\\ ... &= -\frac{e}{2\pi c}\int\frac{e^{i\omega'\left(\frac{1}{(k_0+k_z)^2}\int_{-\infty}^{\xi}\left[\frac{m^2c^2-k_0^2+|\boldsymbol{k}|^2}{2}+\frac{e}{c}k_xA_x'+\frac{e^2}{2c^2}A_x'^2\right]d\xi'+\frac{k_0\xi}{k_0+k_z}-\left(t'-\frac{R'}{c}\right)\right)}}{R'}...\\ &\quad...\left(\frac{1}{c\,(k_0+k_z)^2}\left[\frac{m^2c^2-k_0^2+|\boldsymbol{k}|^2}{2}+\frac{e}{c}k_xA_x'+\frac{e^2}{2c^2}A_x'^2\right]+\frac{k_0}{c(k_0+k_z)}\right)d\xi'\,d\omega',\end{aligned} \tag{284}$$

where $\boldsymbol{r}$ is the observation position and R' is the distance between the observer and the electron. The vector potential of the electron is calculated in the $\hat{x}$ and $\hat{z}$ components through a Fourier transform into frequency space and a change of variables:

$$\begin{aligned} A'_x(\boldsymbol{r}',t') &= \int \frac{J'_x(\boldsymbol{r}'',t'-\frac{R'}{c})}{R'c} dx''\, dy''\, dz'' \\ ... &= -\frac{e}{2\pi}\int \frac{v'_x(t'')e^{i\omega'\left(t''-\left(t'-\frac{R'}{c}\right)\right)}}{R'c} dt''\, d\omega' \\ ... &= -\frac{e}{2\pi}\int \frac{\frac{1}{k_0+k_z}\left(\frac{eA'_x}{c}+k_x\right)}{R'c}... \\ &\quad ...e^{i\omega'\left(\frac{1}{c(k_0+k_z)^2}\int_{-\infty}^{\xi}\left[\frac{m^2c^2-k_0^2+|\boldsymbol{k}|^2}{2}+\frac{e}{c}k_xA'_x+\frac{e^2}{2c^2}A'^2_x\right]d\xi'+\frac{k_0\xi}{c(k_0+k_z)}-\left(t'-\frac{R'}{c}\right)\right)} d\xi'\, d\omega', \end{aligned} \tag{285}$$

$$\begin{aligned} A'_y(\boldsymbol{r}',t') &= \int \frac{J'_y(\boldsymbol{r}'',t'-\frac{R'}{c})}{R'c} dx''\, dy''\, dz'' \\ ... &= -\frac{e}{2\pi}\int \frac{v'_y(t'')e^{i\omega'\left(t''-\left(t'-\frac{R'}{c}\right)\right)}}{R'c} dt''\, d\omega' \\ ... &= -\frac{e}{2\pi}\int \frac{\frac{1}{k_0+k_z}\left(k_y\right)}{R'c}... \\ &\quad ...e^{i\omega'\left(\frac{1}{c(k_0+k_z)^2}\int_{-\infty}^{\xi}\left[\frac{m^2c^2-k_0^2+|\boldsymbol{k}|^2}{2}+\frac{e}{c}k_xA'_x+\frac{e^2}{2c^2}A'^2_x\right]d\xi'+\frac{k_0\xi}{c(k_0+k_z)}-\left(t'-\frac{R'}{c}\right)\right)} d\xi'\, d\omega', \end{aligned} \tag{286}$$

and

$$\begin{aligned} A'_z(\boldsymbol{r}',t') &= \int \frac{J'_z(\boldsymbol{r}'',t'-\frac{R'}{c})}{R'c} dx''\, dy''\, dz'' \\ ... &= -\frac{e}{2\pi}\int \frac{v'_z(t'')e^{i\omega'\left(t''-\left(t'-\frac{R'}{c}\right)\right)}}{R'c} dt''\, d\omega' \\ ... &= -\frac{e}{2\pi}\int \frac{-\frac{1}{(k_0+k_z)^2}\left[\frac{m^2c^2-k_0^2+|\boldsymbol{k}|^2}{2}+\frac{e}{c}k_xA'_x+\frac{e^2}{2c^2}A'^2_x\right]+\frac{k_z}{k_0+k_z}}{R'c}... \\ &\quad ...e^{i\omega'\left(\frac{1}{c(k_0+k_z)^2}\int_{-\infty}^{\xi}\left[\frac{m^2c^2-k_0^2+|\boldsymbol{k}|^2}{2}+\frac{e}{c}k_xA'_x+\frac{e^2}{2c^2}A'^2_x\right]d\xi'+\frac{k_0\xi}{c(k_0+k_z)}-\left(t'-\frac{R'}{c}\right)\right)} d\xi'\, d\omega'. \end{aligned} \tag{287}$$

r' is the distance between the observer and the origin

$$r' = \sqrt{x'^2+y'^2+z'^2}. \tag{288}$$

In the far-field approximation, i.e., when the radiation is observed at a distance much greater than the wavelength of the emitted radiation, the distance between the observer and the electron may be approximated with a change of variable into polar coordinates

$$
\begin{aligned}
R' =& \sqrt{(x'-x'(\xi(t)))^2+(y'-y'(\xi(t)))^2+(z'-z'(\xi(t)))^2} \\
\approx& r'\left(1-\frac{x'x'(\xi)}{r'^2}-\frac{y'y'(\xi)}{r'^2}-\frac{z'z'(\xi)}{r'^2}\right) \\
\approx& r'\left(1-\frac{\sin\theta'\cos\phi'}{r'}\left[\frac{1}{k_0+k_z}\int_{-\infty}^{\xi}\frac{eA_x}{c}d\xi'+\frac{k_x\xi}{k_0+k_z}\right]\right. \\
&-\frac{\sin\theta'\sin\phi'}{r'}\left[\frac{k_y\xi}{k_0+k_z}\right] \\
&\left.-\frac{\cos\theta'}{r'}\left[-\frac{1}{(k_0+k_z)^2}\int_{-\infty}^{\xi}\left[\frac{m^2c^2-k_0^2+|\boldsymbol{k}|^2}{2}+\frac{e}{c}k_xA_x+\frac{e^2}{2c^2}A_x^2\right]d\xi'+\frac{k_z\xi}{k_0+k_z}\right]\right).
\end{aligned}
\tag{289}
$$

In this far-field approximation, the phase arguments of the radiation potentials, Eq. (284-287), may be calculated

$$
\begin{aligned}
t''-\left(t'-\frac{R'}{c}\right)=&\left[\frac{1}{c\,(k_0+k_z)^2}\int_{-\infty}^{\xi}\left[\frac{e}{c}k_xA_x+\frac{e^2}{2c^2}A_x^2\right]d\xi'+\frac{k_0\xi}{c(k_0+k_z)}\right]-\ldots \\
&\ldots\left(-\frac{\sin\theta'\cos\phi'}{c}\left[\frac{1}{k_0+k_z}\int_{-\infty}^{\xi}\frac{eA_x}{c}d\xi'+\frac{k_x\xi}{k_0+k_z}\right]+\ldots\right. \\
&\ldots-\frac{\sin\theta'\sin\phi'}{c}\left[\frac{k_y\xi}{k_0+k_z}\right]+\ldots \\
&\left.\ldots-\frac{\cos\theta'}{c}\left[-\frac{1}{(k_0+k_z)^2}\int_{-\infty}^{\xi}\left[\frac{e}{c}k_xA_x+\frac{e^2}{2c^2}A_x^2\right]d\xi'+\frac{k_z\xi}{k_0+k_z}\right]\right).
\end{aligned}
$$

It is convenient to rewrite this phase argument as factors of the vector potential integral

$$
\begin{aligned}
t''-\left(t'-\frac{R'}{c}\right)=&\frac{\xi}{c(k_0+k_z)}\left(k_0-k_x\sin\theta'\cos\phi'-k_y\sin\theta'\sin\phi'-\cos\theta' k_z\right)+\ldots \\
&\ldots+\left[\frac{k_x(1+\cos\theta')}{c\,(k_0+k_z)^2}-\frac{\sin\theta'\cos\phi'}{c(k_0+k_z)}\right]\int_{-\infty}^{\xi}\frac{eA_x}{c}d\xi'+\ldots \\
&\ldots+\left[\frac{1+\cos\theta'}{c\,(k_0+k_z)^2}\right]\int_{-\infty}^{\xi}\frac{e^2A_x^2}{2c^2}d\xi'.
\end{aligned}
\tag{290}
$$

For an electron with generalized three vector momentum, the equations of motion reveal that the electron motion in all three dimensions will cause emitted radiation. The total radiation emitted by the motion of the charged electron is given by Jackson [58]

$$
\frac{\mathrm{d}^2E'}{\mathrm{d}\omega'\mathrm{d}\Omega}=\frac{e^2\omega'^2}{16\pi^3\epsilon_0c^3}\left|\int_{-\infty}^{\infty}\mathbf{n}\times(\mathbf{n}\times\boldsymbol{\beta})\,e^{i\omega(t-\mathbf{n}\cdot\mathbf{r}(t)/c)}\,\mathrm{d}t\right|^2.
$$

The angular distribution of the scattered photons is found by solving the vector analysis above as in the USPAS workshop [100]. It must be shown, however, that the integrals converge over these new equations of motion.

The effective motion functions may be found by integrating the relativistic velocities, Eq. (274) and Eq. (280,) with respect to time via a change of variable to ξ as in Eq. (45):

$$\begin{aligned}
D_{\beta_x} =& \int_{-\infty}^{\infty} \beta_x i\omega' e^{i\omega'(t-\mathbf{n}\cdot\mathbf{r}(t)/c)}\,\mathrm{d}t \\
=& \frac{1}{k_0+k_z}\int\left[\frac{eA_x(\xi)}{c}+k_x\right]i\omega'... \\
&...\exp\left\{\frac{i\omega'}{c}\left(\frac{\xi}{k_0+k_z}\left(k_0-k_x\sin\theta'\cos\phi'-k_y\sin\theta'\sin\phi'-\cos\theta' k_z\right)+...\right.\right. \\
&...+\left[\frac{k_x(1+\cos\theta')}{(k_0+k_z)^2}-\frac{\sin\theta'\cos\phi'}{k_0+k_z}\right]\int_{-\infty}^{\xi}\frac{eA_x(\xi')}{c}d\xi'+... \\
&...+\left.\left.\left[\frac{1+\cos\theta'}{(k_0+k_z)^2}\right]\int_{-\infty}^{\xi}\frac{e^2A_x^2(\xi')}{2c^2}d\xi'\right)\right\}\,d\xi,
\end{aligned} \tag{291}$$

and

$$\begin{aligned}
D_{\beta_z} =& \int_{-\infty}^{\infty} \beta_z i\omega' e^{i\omega'(t-\mathbf{n}\cdot\mathbf{r}(t)/c)}\,\mathrm{d}t \\
& \frac{1}{(k_0+k_z)^2}\int\left[\frac{e}{c}k_xA_x(\xi)+\frac{e^2}{2c^2}A_x^2(\xi)+k_z(k_0+k_z)\right]i\omega'... \\
&...\exp\left\{\frac{i\omega'}{c}\left(\frac{\xi}{k_0+k_z}\left(k_0-k_x\sin\theta'\cos\phi'-k_y\sin\theta'\sin\phi'-\cos\theta' k_z\right)+...\right.\right. \\
&...+\left[\frac{k_x(1+\cos\theta')}{(k_0+k_z)^2}-\frac{\sin\theta'\cos\phi'}{k_0+k_z}\right]\int_{-\infty}^{\xi}\frac{eA_x(\xi')}{c}d\xi'+... \\
&...+\left.\left.\left[\frac{1+\cos\theta'}{(k_0+k_z)^2}\right]\int_{-\infty}^{\xi}\frac{e^2A_x^2(\xi')}{2c^2}d\xi'\right)\right\}\,d\xi'.
\end{aligned} \tag{292}$$

It is convenient to rewrite these effective motion functions $D_{x,z}$ in terms of the electron Lorentz factor γ, relativistic velocity β_i, electron mass m and the speed of light c by using the definition of the relativistic initial momentum of the electron $k_i = \gamma mc\beta_i$:

$$\begin{aligned}
D_{\beta_x} =& \frac{1}{\gamma(1+\beta_z)}\int\left[\frac{eA_x(\xi)}{mc^2}+\beta_x\right]i\omega \\
&\times\exp\left\{\frac{i\omega}{c}\left(\left[\frac{\xi\left(1-\beta_x\sin\theta\cos\phi-\beta_y\sin\theta\sin\phi-\beta_z\cos\theta\right)}{1+\beta_z}\right]\right.\right. \\
&+\left[\frac{\beta_x(1+\cos\theta)}{\gamma\left(1+\beta_z\right)^2}-\frac{\sin\theta\cos\phi}{\gamma(1+\beta_z)}\right]\int_{-\infty}^{\xi}\frac{eA_x(\xi')}{mc^2}\mathrm{d}\xi' \\
&+\left.\left.\left[\frac{1+\cos\theta}{2\gamma^2\left(1+\beta_z\right)^2}\right]\int_{-\infty}^{\xi}\frac{e^2A_x^2(\xi')}{m^2c^4}\mathrm{d}\xi'\right)\right\}\,\mathrm{d}\xi,
\end{aligned}$$

and

$$D_{\beta_z} = \frac{(1+\beta_z)}{(1-\beta_z\cos\theta)} \frac{1}{2\gamma^2\left(1+\beta_z\right)^2} \int \left[2\gamma\beta_x \frac{eA_x(\xi)}{mc^2} + \frac{e^2A_x^2(\xi)}{m^2c^4} + 2\beta_z(1+\beta_z)\right] i\omega$$
$$\times \exp\left\{\frac{i\omega}{c}\left(\left[\frac{\xi\left(1-\beta_x\sin\theta\cos\phi-\beta_y\sin\theta\sin\phi-\beta_z\cos\theta\right)}{1+\beta_z}\right]\right.\right.$$
$$+\left[\frac{\beta_x(1+\cos\theta)}{\gamma\left(1+\beta_z\right)^2} - \frac{\sin\theta\cos\phi}{\gamma(1+\beta_z)}\right]\int_{-\infty}^{\xi}\frac{eA_x(\xi')}{mc^2}\mathrm{d}\xi'$$
$$\left.\left.+\left[\frac{1+\cos\theta}{2\gamma^2\left(1+\beta_z\right)^2}\right]\int_{-\infty}^{\xi}\frac{e^2A_x^2(\xi')}{m^2c^4}\mathrm{d}\xi'\right)\right\}\,\mathrm{d}\xi.$$

It is also convenient to rewrite the equations using the normalized vector potential $\tilde{A}(\xi) = eA_x/mc^2$:

$$D_{\beta_x} = \frac{1}{\gamma(1+\beta_z)} \int \left[\tilde{A}_x(\xi) + \beta_x\right] i\omega$$
$$\times \exp\left\{\frac{i\omega}{c}\left(\left[\frac{\xi\left(1-\beta_x\sin\theta\cos\phi-\beta_y\sin\theta\sin\phi-\beta_z\cos\theta\right)}{1+\beta_z}\right]\right.\right.$$
$$+\left[\frac{\beta_x(1+\cos\theta)}{\gamma\left(1+\beta_z\right)^2} - \frac{\sin\theta\cos\phi}{\gamma(1+\beta_z)}\right]\int_{-\infty}^{\xi}\tilde{A}_x(\xi')\mathrm{d}\xi' \tag{293}$$
$$\left.\left.+\left[\frac{1+\cos\theta}{2\gamma^2\left(1+\beta_z\right)^2}\right]\int_{-\infty}^{\xi}\tilde{A}_x^2(\xi')\mathrm{d}\xi'\right)\right\}\,\mathrm{d}\xi,$$

and

$$D_{\beta_z} = \frac{(1+\beta_z)}{(1-\beta_z\cos\theta)} \frac{1}{2\gamma^2\left(1+\beta_z\right)^2} \int \left[2\gamma\beta_x\tilde{A}_x(\xi) + \tilde{A}_x^2(\xi) + 2\beta_z(1+\beta_z)\right] i\omega$$
$$\times \exp\left\{\frac{i\omega}{c}\left(\left[\frac{\xi\left(1-\beta_x\sin\theta\cos\phi-\beta_y\sin\theta\sin\phi-\beta_z\cos\theta\right)}{1+\beta_z}\right]\right.\right.$$
$$+\left[\frac{\beta_x(1+\cos\theta)}{\gamma\left(1+\beta_z\right)^2} - \frac{\sin\theta\cos\phi}{\gamma(1+\beta_z)}\right]\int_{-\infty}^{\xi}\tilde{A}_x(\xi')\mathrm{d}\xi' \tag{294}$$
$$\left.\left.+\left[\frac{1+\cos\theta}{2\gamma^2\left(1+\beta_z\right)^2}\right]\int_{-\infty}^{\xi}\tilde{A}_x^2(\xi')\mathrm{d}\xi'\right)\right\}\,\mathrm{d}\xi.$$

Since the laser pulse has a finite length, the normalized vector potential goes to zero as $\xi \to \pm\infty$. Therefore, the above integrals converge for the integrands that are factors of the normalized vector potential $\tilde{A}_x$. Furthermore, an convergence factor must be inserted into the equation to prevent the electron from radiating infinitely during the parts of the integral where the motion is linear, i.e., $\xi \to \pm\infty$:

$$\exp\left\{-\epsilon\left|\xi\right|\right\},\ \epsilon \to 0. \tag{295}$$

The integrands that are constant times the complex exponential, however, must be reconstructed in a form that converges over the bounds of integration. Integration by parts will be used to complete the integration

$$\int_a^b u \, \mathrm{d}v = uv|_a^b - \int_a^b v \, \mathrm{d}u. \tag{296}$$

Consider the integral

$$I = \int_{-\infty}^{-\infty} C_0 \, \exp\{-\epsilon\,|\xi|\} \exp\left\{C_1\xi + C_2 \int_{-\infty}^{\xi} \tilde{A}_x(\xi')\mathrm{d}\xi' + C_3 \int_{-\infty}^{\xi} \tilde{A}_x^2(\xi')\mathrm{d}\xi'\right\} \, \mathrm{d}\xi. \tag{297}$$

where C_0, C_1, C_2, and C_3 are constants relative to the integral. The u and v functions for integration by parts for the above integral are defined:

$$\begin{aligned}
u =& C_0 \exp\left\{C_2 \int_{-\infty}^{\xi} \tilde{A}_x(\xi')\mathrm{d}\xi' + C_3 \int_{-\infty}^{\xi} \tilde{A}_x^2(\xi')\mathrm{d}\xi'\right\}, \\
\mathrm{d}u =& C_0 \left[C_2\tilde{A}_x(\xi)\mathrm{d}\xi + C_3\tilde{A}_x^2(\xi)\mathrm{d}\xi\right] \exp\left\{C_2 \int_{-\infty}^{\xi} \tilde{A}_x(\xi')\mathrm{d}\xi' + C_3 \int_{-\infty}^{\xi} \tilde{A}_x^2(\xi')\mathrm{d}\xi'\right\}, \\
v =& \frac{1}{C_1} \exp\{C_1\xi\}, \\
\mathrm{d}v =& \exp\{C_1\xi\} \, \mathrm{d}\xi.
\end{aligned} \tag{298}$$

The integral may now be written

$$\begin{aligned}
I = C_0 &\exp\left\{C_2 \int_{-\infty}^{\xi} \tilde{A}_x(\xi')\mathrm{d}\xi' + C_3 \int_{-\infty}^{\xi} \tilde{A}_x^2(\xi')\mathrm{d}\xi'\right\} \frac{1}{C_1} \exp\{C_1\xi\} \exp\{-\epsilon\,|\xi|\}\Big|_{-\infty}^{\infty} \\
&\qquad - \int_{-\infty}^{-\infty} \frac{1}{C_1} \exp\{C_1\xi\}\, C_0 \left[C_2\tilde{A}_x(\xi')\mathrm{d}\xi' + C_3\tilde{A}_x^2(\xi')\mathrm{d}\xi'\right] \\
&\qquad\quad \times \exp\left\{C_2 \int_{-\infty}^{\xi} \tilde{A}_x(\xi')\mathrm{d}\xi' + C_3 \int_{-\infty}^{\xi} \tilde{A}_x^2(\xi')\mathrm{d}\xi'\right\} \mathrm{d}\xi \\
= -& \int_{-\infty}^{-\infty} \frac{C_0}{C_1} \left[C_2\tilde{A}_x(\xi')\mathrm{d}\xi' + C_3\tilde{A}_x^2(\xi')\mathrm{d}\xi'\right] \\
&\qquad \times \exp\left\{C_1\xi + C_2 \int_{-\infty}^{\xi} \tilde{A}_x(\xi')\mathrm{d}\xi' + C_3 \int_{-\infty}^{\xi} \tilde{A}_x^2(\xi')\mathrm{d}\xi'\right\} \mathrm{d}\xi.
\end{aligned} \tag{299}$$

The integral now clearly converges. This solution may now be applied to the constant portions of the integrands in the effective motion equations D_{β_x,β_z}:

$$
\begin{aligned}
D_{\beta_x} =& \frac{1}{\gamma(1+\beta_z)} \int \left[\tilde{A}_x(\xi) + \frac{-i\beta_x c(1+\beta_z)}{\omega\left(1-\beta_x \sin\theta\cos\phi - \beta_y \sin\theta\sin\phi - \beta_z\cos\theta\right)} \right. \\
&+ \left[\frac{\beta_x(1+\cos\theta)}{\gamma\left(1+\beta_z\right)^2} - \frac{\sin\theta\cos\phi}{\gamma(1+\beta_z)} \right] \tilde{A}_x(\xi')\mathrm{d}\xi' + \left. \left[\frac{1+\cos\theta}{2\gamma^2\left(1+\beta_z\right)^2} \right] \tilde{A}_x^2(\xi')\mathrm{d}\xi' \right] i\omega \\
&\times \exp\left\{ \frac{i\omega}{c} \left(\left[\frac{\xi\left(1-\beta_x\sin\theta\cos\phi - \beta_y\sin\theta\sin\phi - \beta_z\cos\theta\right)}{1+\beta_z} \right] \right. \right. \\
&\quad + \left[\frac{\beta_x(1+\cos\theta)}{\gamma\left(1+\beta_z\right)^2} - \frac{\sin\theta\cos\phi}{\gamma(1+\beta_z)} \right] \int_{-\infty}^{\xi} \tilde{A}_x(\xi')\mathrm{d}\xi' \\
&\quad \left. \left. + \left[\frac{1+\cos\theta}{2\gamma^2\left(1+\beta_z\right)^2} \right] \int_{-\infty}^{\xi} \tilde{A}_x^2(\xi')\mathrm{d}\xi' \right) \right\} \mathrm{d}\xi,
\end{aligned}
\tag{300}
$$

and

$$
\begin{aligned}
D_{\beta_z} =& \frac{(1+\beta_z)}{(1-\beta_z\cos\theta)} \frac{1}{2\gamma^2\left(1+\beta_z\right)^2} \\
&\times \int \left[2\gamma\beta_x\tilde{A}_x(\xi) + \tilde{A}_x^2(\xi) + \frac{-i2\beta_z(1+\beta_z)c(1+\beta_z)}{\omega\left(1-\beta_x \sin\theta\cos\phi - \beta_y \sin\theta\sin\phi - \beta_z\cos\theta\right)} \right. \\
&+ \left[\frac{\beta_x(1+\cos\theta)}{\gamma\left(1+\beta_z\right)^2} - \frac{\sin\theta\cos\phi}{\gamma(1+\beta_z)} \right] \tilde{A}_x(\xi')\mathrm{d}\xi' + \left. \left[\frac{1+\cos\theta}{2\gamma^2\left(1+\beta_z\right)^2} \right] \tilde{A}_x^2(\xi')\mathrm{d}\xi' \right] i\omega \\
&\times \exp\left\{ \frac{i\omega}{c} \left(\left[\frac{\xi\left(1-\beta_x\sin\theta\cos\phi - \beta_y\sin\theta\sin\phi - \beta_z\cos\theta\right)}{1+\beta_z} \right] \right. \right. \\
&\quad + \left[\frac{\beta_x(1+\cos\theta)}{\gamma\left(1+\beta_z\right)^2} - \frac{\sin\theta\cos\phi}{\gamma(1+\beta_z)} \right] \int_{-\infty}^{\xi} \tilde{A}_x(\xi')\mathrm{d}\xi' \\
&\quad \left. \left. + \left[\frac{1+\cos\theta}{2\gamma^2\left(1+\beta_z\right)^2} \right] \int_{-\infty}^{\xi} \tilde{A}_x^2(\xi')\mathrm{d}\xi' \right) \right\} \mathrm{d}\xi.
\end{aligned}
\tag{301}
$$

VITA

Erik Scott Johnson
Department of Physics
Old Dominion University
Norfolk, VA 23529

EDUCATION

- *Doctor of Physics* · 2016-2021, Old Dominion University, Accelerator Science Specialization, College of Sciences · Dissertation: *Quasiclassical Calculations of Compton Scattered Spectra*
- *Bachelor of Physics & Math*, Cum Laude · 2013-2016, Old Dominion University, Accelerator Science Specialization, College of Sciences · Thesis: *Computations of Compton Scattered Energy Spectra in the Linear Regime*
- *Associate of Science*, Cum Laude · 2003-2012, Tidewater Community College, Science Specialization

WORK EXPERIENCE

- *Research Assistant*, Department of Physics · 2016-2021, ODURF
- *Teaching Assistant*, Department of Physics · 2017-2019, Old Dominion University
- *Structural Craftsman*, 203$^{\text{rd}}$ Red Horse Squadron · 2000-2013, USAF

PUBLICATIONS

- G. Krafft, E. Johnson, K. Deitrick, B. Terzić, R. Kelmar, T. Hodges, W. Melnitchouk, and J. Delayen. Phys. Rev. Accel. Beams, **19**:121302, 12 (2016).
- E. Johnson. in *Proceedings of IPAC 2018* (JACoW, Geneva, 2018), page 4351–4353.
- B. Terzić, A. Brown, I. Drebot, T. Hagerman, E. Johnson, G. Krafft, C. Maroli, V. Petrillo, and M. Ruijter. Europhysics Letters, **126**(1):12003, 5 (2019).

Typeset using LaTeX.